Dissertation

submitted to the
Combined Faculties for the Natural Science and Mathematics
of the Ruperto-Carola-University of Heidelberg, Germany
for the degree of
Doctor of Natural Sciences

presented by
Dipl.-Phys. Sebastian Menk
born in Groß-Gerau
Oral examination: April 17$^{\text{th}}$, 2013

Vibrational Auto-Detachment of the Sulfur Hexafluoride Anion in a Low-background Cryogenic Ion Beam Trap

Referees:

Prof. Dr. Andreas Wolf

Priv.-Doz. Dr. Alexander Dorn

Kurzfassung

Schwingungsinduzierte, automatische Elektronenemission von Schwefelhexafluorid-Anion in einer untergrundarmen, kryogenen Ionenstrahlfalle

Die durch Molekülschwingungen ausgelöste Abtrennung von Elektronen (Vibrational Auto-Detachment, VAD) in angeregten $(SF_6^-)^*$-Molekülionen wurde in einer elektrostatischen, kryogenen Ionenstrahlfalle (CTF) untersucht. Die niedrigen Temperaturen von ∼12 K und Bedingungen extrem hohen Vakuums ermöglichten die Beobachtung der Neutralisationsrate über fast fünf Größenordnungen mit Messzeiten zwischen 500 μs nach der Ionenproduktion bis der Zerfall nach ∼100 ms verschwindet. Die präsentierten Untersuchungen führten zu einer bedeutenden Verbesserung im Vergleich zu früheren Beobachtungen dieses Zerfalls und gewährten dabei einen Einblick in den Zerfall zu späten Zeiten, die Rolle der Rotationsanregung und die Abhängigkeiten der Zerfallskurven von der Strahlungskühlung der SF_6^--Ionen.
Die Anwendung eines kürzlich in der Literatur präsentierten, mikroskopischen Modells des VAD-Prozesses offenbarte bei der Interpretation der vorliegenden Messungen erstaunlich gute Übereinstimmung; der stochastische Charakter des Zerfalls konnte hiermit bestätigt und frühere Modelle können ausgeschlossen werden. Des Weiteren konnte ein neuer Wert der adiabatischen Elektronenaffinität von SF_6 bestimmt werden, sowie typische Kühlzeiten von $(SF_6^-)^*$ für die Strahlungsstabilisation, welche mit dem VAD-Prozess zu späten Zeiten konkurriert.
Darüber hinaus konnte durch Photoanregung eine erneute, verzögerte Elektronenemission der gespeicherten SF_6^--Ionen induziert werden, welche die Beobachtung der Strahlungsstabilisation zu längeren Zeiten ermöglichte und die Identifikation des Fragmentationsprozesses von SF_6^- zuließ.

Abstract

Vibrational auto-detachment of the sulfur hexafluoride anion in a low-background cryogenic ion beam trap

Vibrational electron auto-detachment (VAD) of excited $(SF_6^-)^*$ was investigated using the electrostatic Cryogenic Trap for Fast ion beams (CTF), where low temperatures of ∼12 K and conditions of extremely high vacuum enabled the observation of the neutralization rate over almost five orders of magnitude, covering time scales from 500 μs after the ion production until the signal vanishes after ∼100 ms. The present study significantly improves earlier measurements of this decay and provides an insight into the decay behavior for late times, the role of rotational excitation and radiative cooling of the observed time dependencies.
Analyzing the present measurements with the help of a recent microscopic model for the SF_6^- VAD rate revealed astonishing agreement, confirming the stochastical character of the decay and excluding former models. Furthermore, a new value for the adiabatic electron affinity of SF_6 was determined and typical cooling times for the $(SF_6^-)^*$ radiative stabilization were obtained, which competes with the VAD-decay at late times.
Additionally, the continuation of the internal cooling was investigated by photo-excitation of the long-time stored SF_6^- ions by the observation of the delayed electron detachment; indications for the dissociation of SF_6^- could be identified.

Contents

Abbreviations and Symbols

CSR	Cryogenic Storage Ring
CTF	Cryogenic Trap for Fast ion beams
EA	(adiabatic) Electron Affinity
EIBT	Electrostatic Ion Beam Trap
IR	Infrared radiation
IVR	Intramolecular Vibrational Redistribution
KER	Kinetic Energy Release
MCP	Micro Channel Plate
SF_6	Sulfur hexafluoride
SF_6^-	Sulfur hexafluoride anion
$(SF_6^-)^*$	Sulfur hexafluoride anion excited above EA
PES	Potential Energy Surface
PES	Photo Electron Spectroscopy
VAD	Vibrational Auto-Detachment
VAE	Vertical Attachment Energy
VDE	Vertical Detachment Energy
VEX	Vibrational Excitation
VW	Vogt-Wannier electron capture process
XHV	Extremely High Vacuum

A, B	Singly degenerate vibrational mode (Mullikan symbol)
A, B, C	Rotational constants
β_T	β-function in the trap center
C_{4v}	Symmetry group of asymmetric SF_6^-
E	Doubly degenerate vibrational mode (Mullikan symbol)
E_D	Dissociation energy
E_R	Rotational energy
E_V	Vibrational energy
ϵ	Kinetic electron energy
f	Oscillation frequency of the trapped ions
$f_0(E,T)$	Initial vibrational energy distribution
$f_t(E,T)$	Vibrational energy distribution at time t
h	Planck's constant $(4.135667516(91) \times 10^{15}\,\mathrm{eV\,s})$
$h_0(J,T_R)$	Initial rotational energy distribution
k_B	Boltzmann's constant $(8.6173324(78) \times 10^5\,\mathrm{eV/K})$
$k(E)/k_{det}(E)$	Energy-dependent VAD rate function
$k_{diss}(E)$	Energy-dependent dissociation rate function

$k_{rad}(E)$	Energy-dependent radiative cooling rate
ν_i	Vibrational frequency
N_0	Initial number of ions
$N^{\ddagger}$	Sum of states in critical phase space area along the reaction coordinate
O_h	Octahedral symmetry group (SF_6)
$P(\epsilon)$	Transmission coefficient for an electron capture process
Q	Vibrational partition sum
Q_R	Rotational partition sum
$R(t)$	Neutralization rate
ρ^-	Density of states for the anion
ρ^0	Density of states for the neutral
s	Vibrational degrees of freedom ($3N-6$)
$\sigma(\epsilon)$	Electron capture cross section
σ_x, σ_y	Gaussian beam diameter
T	Triply degenerate vibrational mode (Mullikan symbol)
T_V	Vibrational temperature
T_R	Rotational temperature
τ	Time constant of an exponential decay function
U_i	Voltage of trap electrode i ($i = B$, D, E, F, G)
$W_{det}(E)$	Cumulative reaction probability at energy E
x, y, s	Transversal and longitudinal coordinates of the trap phase space
x', y'	Transversal angles of the trap phase space
x_{max}, x'_{max}	Maximum transversal position and angle of the trap phase space

Chapter 1

Introduction and motivation

Negative molecular ions (anions) are of particular interest in the wide research field of molecular reaction dynamics, with increasing demands for advanced measurements and theoretical modeling. Anions play an important role in molecular processes of e.g. ionic solutions, where their presence polarizes the electron cloud of neighboring molecules and leads to an opposite spatial orientation as compared to positive ions (cations) of the same species. Also the creation of molecular anions in the Earth's atmosphere is crucial to be understood, as they act as a catalyst for the formation and decomposition of molecules. Furthermore, negative molecular ions were observed in Titan's atmosphere [1], a satellite of the planet Saturn, and were included into its molecular ion chemistry. More remarkable was the recent discovery of small anionic carbon chains in interstellar clouds in unexpectedly high amounts [2–5], which raised the conclusion of further abundances of interstellar anions and a considerable importance in the astro-chemical modeling.

The existence of the negative ion state is not self-evident for any molecular or atomic system, in contrast to cations, but depends on the individual molecular structure. Outer electrons in anions are not bound by a Coulomb attractive potential as in neutrals or cations, but rather by a short-range induced dipole interaction with higher order dependencies than $1/r$ on the radial distances and a vanishing attraction for finite separation. Electronically excited configurations are rare in anions and Rydberg series are completely missing.

The binding energy of the electron, the electron affinity, is the essential property for the stability of a molecular anion, and is challenging to determine experimentally or theoretically. Total electronic binding energies of the neutral and anion ground state need to be calculated very precisely, and the difference yields the electron affinity, which is orders of magnitude smaller than the total energies. In contrast, experimentally this energy difference is directly determined; however, transitions between both ground states need to be ensured or have to be obtained by extrapolations. For instance, the fast electron removal by photon-detachment retains the molecular geometry of the anion, and the neutral ground state structure is only attained in a delayed relaxation process.

In the reverse process, when electrons are attached to molecules, at least the electron binding energy is gained and needs to be dissipated in order to stabilize the newly formed complex. In small systems, dissociation of the negatively charged molecular

complex follows, while in increasingly complex molecules, the excess energy can also induce vibrational excitations due to vibronic coupling. The energy gained in the attachment process will thus be hidden in the vibrational excitation.
A retransfer of this energy initiating a self-induced electron detachment was found to occur with large time delays of microseconds to milliseconds, remarkably long compared to typical electronic or even vibrational time scales. The stabilization of the newly formed anion by radiation (or by inelastic collisions with the environment) competes with the delayed detachment processes, and is important to be understood for chemical reaction models. To experimentally access these delayed processes, long time storage of molecular anions under isolated conditions is required, which also allows the time-dependent observation of the investigated delayed reaction.
Electrostatic Ion Beam Traps (EIBT) [6] provide perfect conditions to observe these delayed decays. Ions can be stored for long time scales, which are in particular feasible in an ultra high vacuum system, and different detection methods can be applied. EIBTs have been developed from multi-reflection time-of-flight mass spectrometers [7], where the ion's pathway is enhanced through several electrostatic mirrors. In EIBTs, two opposing mirror electrode arrays ensure stable periodic reflections with in principle unlimited confinement times and ion mass ranges. The high kinetic ion energy of a few keV per charge state stabilizes the trapping against external perturbations and provides short oscillation periods of microseconds with immense mass resolving powers becoming possible for the typical storage times of seconds by measuring the oscillation frequency.
This wide range in time scales is accessible for time dependent reaction dynamic measurements, also providing external access via lasers, detecting charge exchange reactions or fragmentation immediately by trap ion loss. The field free region between the mirrors offers well-controlled isolated conditions, which together with other mentioned properties further distinguishes this type of ion trap from other designs like Penning traps, Paul traps or other RF-trap variations. Also, much similarity to ion storage rings becomes apparent.
Unfortunately, the vacuum conditions in presently available EIBTs at room temperature limit the observation times to mostly for seconds, and also reactions with low intensities cannot be accessed. A pathway to reach a low-background and an extremely high vacuum (XHV) is cryo-condensation of residual gases. The Cryogenic Trap for Fast ion beams (CTF) [8], recently developed and put into operation at the Max-Planck-Institute for Nuclear Physics in Heidelberg, incorporates all the necessary features of a liquid helium cooled EIBT, and besides also allows to investigate ambient-temperature dependent reactions of the trapped ions down to ∼12 K. Accordingly, an enormous range of undisturbed ion observation times reaching from microseconds up to minutes is accessible for low intensity investigations and moreover, molecular vibrational ground states can be reached by radiative cooling.
For instance, the delayed decays of small anionic aluminum clusters (Al_x^-, x = 3-7) were recently investigated with the CTF under cryogenic operation and some of the results are summarized in Fig. 1.1. Here, the particle rate of neutralized aluminum anions is displayed as a function of the storage time and a power-law character of the decay is found for early times ($\propto t^n$, $n \leq -1$). Power-law decays of highly excited complex anions have been observed previously in investigations at

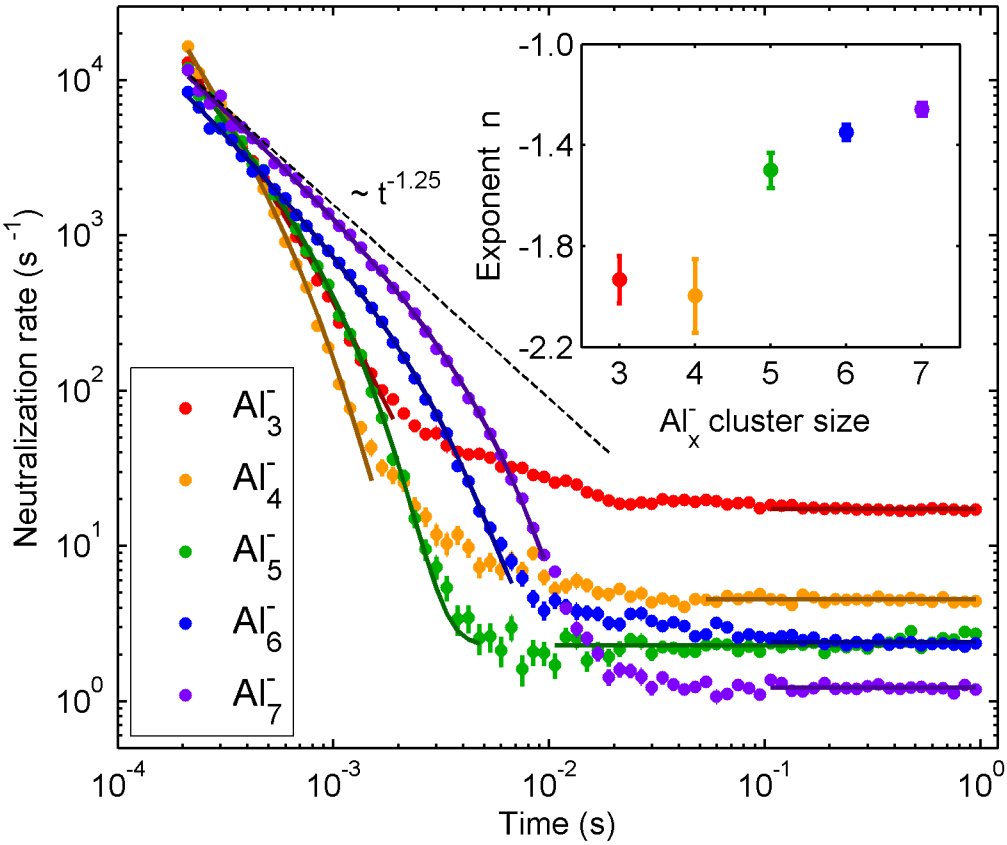

Figure 1.1: Neutralization rate of excited aluminum cluster anions Al_x^- (x = 3-7) as a function of the storage time. The exponent n of the initial power-law decay ($\propto t^n$) at early times changes with the cluster size as show in the inset. The deviations from the power-law at later times and the newly uncovered features close to the background rate at $\sim 10^{-2}$ s are presently difficult to explain by theoretical models and can be due to various influences such as electronic excitation, isomerization or competing fragmentation, possibly in combination with each other.

ion traps and storage rings [9–11], and are understood to result from the transfer of the vibrational energy back to the electron, a process also called Vibrational Auto-Detachment (VAD).

In the case of the aluminum clusters in Fig. 1.1, deviations from the power-law at later times as well as even more complicated time dependencies at very long delays ($\sim 10^{-2}$ s) have been uncovered, and call for explanations of the underlying physical processes. Excited electronic states, geometry changes (isomerization) with different vibrational properties, as well as unknown values for the electron affinity make a detailed analysis of the occurring processes presently difficult. Furthermore, competing processes to the detachment such as fragmentation, radiative energy loss or influences by rotational excitation make the aluminum clusters inappropriate as a model system to fundamentally understand the reaction concepts. Therefore, only phenomenological observations in terms of comparison of different cluster sizes are possible, as shown in Fig. 1.1, where the derived exponent n changes with the

complexity of the system approaching values of $n = -1$, which was also observed for even larger molecular systems.

For a better understanding of the decay properties at low rates becoming accesible with the low-background cryogenic devices, a system with well-known intrinsic properties was chosen in the present work. In particular, the anionic state of sulfur hexafluoride (SF_6^-) was investigated, which exhibits already complexities similar to the larger aluminum clusters in Fig. 1.1. In contrast to anionic clusters, however, comprehensive theoretically and experimentally knowledge on SF_6 and SF_6^- has already been collected over past years.
Sulfur hexafluoride (SF_6) is a synthetic molecule and has found rising interest in industry in the last couple of decades due to its various useful properties. The passive reaction character, the enhanced electron capture cross section and the strong infrared absorption capabilities are the most important properties to mention and are utilized in manifold applications [12, 13].
Increasing abundances of SF_6 in the Earth's atmosphere caused scientists to become aware that it represents one of the most potent greenhouse gases due to its infrared absorption ability [14]. The SF_6 degradation scenarios from the atmosphere include various reaction schemes, which rely on measurements and reaction modeling [15]. Direct destructive reactions involve positive ions such as O^+ or N_2^+ [16], UV absorption or dissociative electron attachment [13]. Other reactions depend on the prior formation of SF_6^-, which is accomplished partly by charge transfer with negative ions or by electron capture, where the dissipation of the gained energy in the latter reaction proceeds via collisions or radiation. These energy loss rates determine the lifetime of SF_6^- with respect to auto-detachment and thus, define the time window for destructive reactions, for instance with oxygen or atomic hydrogen. Other competing processes are radiative detachment or charge transfer back to SF_6. Hence, a detailed knowledge on various processes is required to improve the models and to make predictions more reliable.
The well-known, highly symmetric, octahedral structure of the neutral SF_6 led to detailed calculations of electronic, vibrational and rotational properties, and a slightly distorted asymmetric geometry was suggested recently for the anion [17, 18]. Even though the system exhibits a very symmetric structure, it is found to be complex enough for statistical models to be applied, leading to adequate descriptions, as will be discussed in this work.

The present work makes use of the storage of the SF_6^- anion in the Cryogenic Trap for Fast ion beams (CTF). Chapter 2 is dedicated to SF_6 and SF_6^-, their specific molecular properties as well as to transitions between them with particular emphasis on the electron detachment process. For this purpose, a recent state-of-the-art theoretical model is considered in much detail and observables relevant for the present measurements are derived. The CTF is presented in chapter 3, involving cryogenic design details, ion trapping properties and auxiliary components. In the course of this, special consideration is given to the ion source operation, as here important processes were found to influence the observations. Finally, the cryogenic detection system, the essential tool for these measurements, is introduced with a successive description of the laser setup. Chapter 4 then focuses on the measurements achieved

with the CTF, starting with an introduction to its operation and typically observed signals. The measurements of the vibrational auto-detachment of SF_6^- have accessed the long-time and low-intensity limits of this decay, revealed so far unobserved features, and inferred dependencies caused by radiative cooling, rotational excitation and the value of the adiabatic electron affinity. Furthermore, photo-excitation of the trapped SF_6^- anions enabled the observation of the delayed electron detachment and to access earlier decay times after the excitation process, thus revealing also signatures most likely arising from SF_6^- auto-dissociation.

Chapter 2

Electron detachment of SF_6^-

This chapter describes the basic properties and structures of the sulfur hexafluoride molecule SF_6 and its negative ion SF_6^- followed by a discussion of their transfer reactions, the electron attachment and detachment. From the literature, recent state-of-the-art-models [19–24] characterizing the energy dependence of the Vibrational electron Auto-Detachment (VAD) of excited $(SF_6^-)^*$ are summarized, and compared to more simplified approaches [10, 25, 26]. A detailed model is developed that simulates the total, neutral fragments producing, time-dependent decay rate of $(SF_6^-)^*$ and includes an averaging over their internal energy distributions. The resulting dependencies on the vibrational energy, the rotational excitation and variations of the value of the electron affinity of SF_6 are presented in detail. Furthermore, competing processes such as auto-dissociation and radiative cooling are put into perspective, where the first one is significant at very early observation times and the latter one dominates the long-time energy dissipation of the SF_6^- anions.

2.1 Electron affinities

Unlike to the creation of positive ions (cations) by removing electrons, not every atom or molecule accepts an additional electron. For atoms, the electron is attracted by a self-induced dipole moment interaction which is a short-range potential of the order of r^{-4} instead of a Coulomb potential in the case of positive ions or neutrals. Herewith also no infinite number of states are available as it is the case in a Coulomb field, and Rydberg series are missing. As a consequence in some cases only the fine- and hyperfine-structure of the ground state provides a bound state.
All noble gases are at first assumed to not build negative ions due to the shell closing; the same goes for alkaline earth metals (sub-shell closing). However, He^- has been found in a meta-stable excited state in the configuration $1s2s2p$ as well as Be^- in $2s2p^2$. For Ca^-, Sr^- and Ba^- also weakly bound states could be determined, but for the rest of the noble gases no anion formation is possible. On the other hand, halogens such as fluorine and chlorine exhibit very stable anions.
The electron binding energy of an atom is called the electron affinity (EA). It is the necessary energy to convert both ground states into each other and is given by

$$\mathrm{EA} = E_{tot}(\mathrm{A}) - E_{tot}(\mathrm{A}^-), \tag{2.1}$$

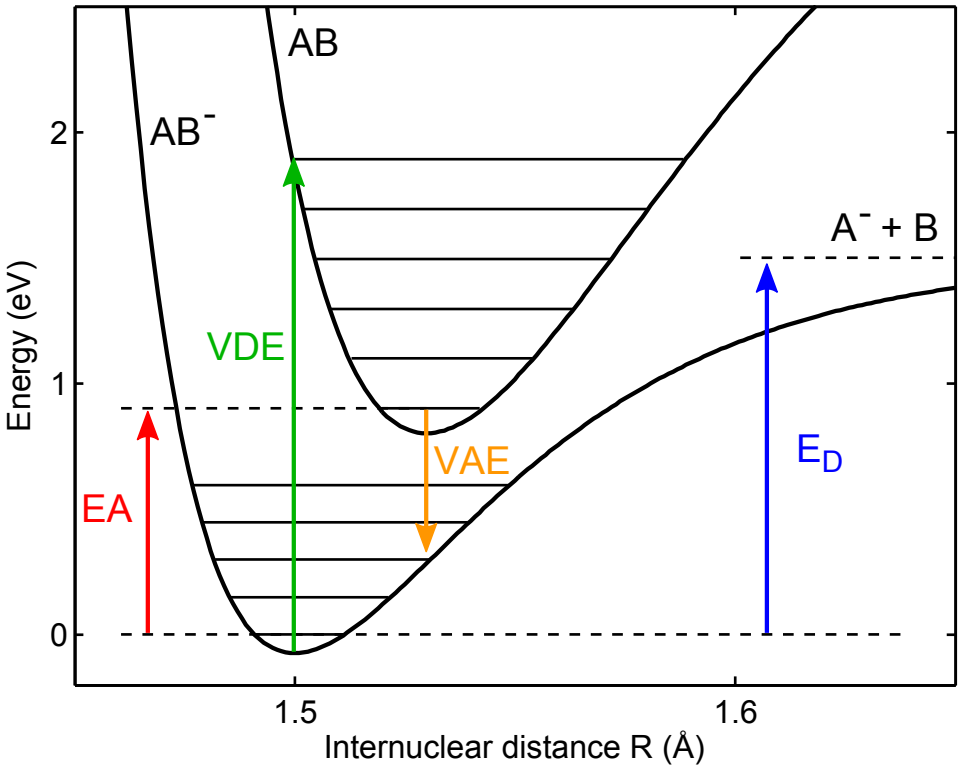

Figure 2.1: Schematic view on the potential energy curves for a typical molecule AB and its anion AB^- displayed as Morse potentials. The adiabatic electron affinity (EA) connects both ground states, here shown with different internuclear equilibrium distances R. The vertical detachment energy (VDE) is the lowest transition energy from the anionic ground state to the neutral, which retains its geometry. The reverse process, the lowest energy from the neutral ground state to the anion is the vertical attachment energy (VAE). Also depicted is the dissociation energy (E_D) inferring an infinite separation distance of this bond. Displayed dimensions are only to illustrate typical values (see also e.g.,[27]).

with the total ground states energies E_{tot} of the atomic neutral A and the anion A^-. The corresponding reaction is written as

$$A + e^- \rightarrow A^-. \tag{2.2}$$

For a theoretical determination of this value, both ground state energies have to be calculated to yield EA, which can become a challenging task even for small multi-electron systems. For light atoms such as carbon, the total electronic ground state energy exceeds already 1 keV, whereas the electron affinity is a quantity of at most a few eV. Thus, the ground states of A and A^- have to be calculated with high enough precision to get reliable values for EA.
Experimental methods are usually independent of the total electron binding energy, but measure directly the energy difference. One method is Photo Electron Spectroscopy (PES), where a laser beam of suitable photon energy $h\nu$ is used to detach

the electron and the excess energy is transferred to kinetic energy of the electron, which is then detected:

$$A^- + \gamma(h\nu) \rightarrow A + e^-, \tag{2.3}$$

$$E_{tot}(A^-) + h\nu = E_{tot}(A) + \epsilon(e^-). \tag{2.4}$$

Another method is the Laser Photo-detachment Threshold spectroscopy (LPT), where the wavelength of a narrow band laser is tuned to the threshold and the yield of neutrals is observed.
When considering negative molecular ions, the vibrational and rotational degrees of freedom require the definition of additional threshold quantities. An important difference to atoms is that the equilibrium geometries of the ground states are usually not equal (see Fig. 2.1) and a rearrangement of the nuclei has to take place. The equivalent of the electron binding energy in atoms is the adiabatic electron affinity (AEA) in molecules and connects both ground states in their equilibrium geometries. It can be considered as a very slow removal of the electron from the anion such that the nuclear configuration can always follow the momentary equilibrium and no energy is required for the geometrical change (adiabatic process). The adiabatic electron affinity is in the following shortly referred to as EA. As previously, a positive value of EA refers to a stable negative molecule. The threshold energy for a transition from the negative ground state to the lowest excited state in the neutral without changing the geometry is the Vertical Detachment Energy (VDE). The opposite direction, from the neutral ground state to lowest excited state in the anion at the neutral geometry, leads to the Vertical Attachment Energy (VAE). The negative of this quantity is also called the vertical electron affinity, but to avoid confusion with the adiabatic electron affinity EA, it will not be used.
The above definitions reveal the following relation which can also be seen in Fig. 2.1:

$$\mathrm{VDE} \geq \mathrm{EA}, \tag{2.5}$$

$$-\mathrm{VAE} \leq \mathrm{EA}. \tag{2.6}$$

Whether VAE is found to be positive or negative depends on the crossing point of both potential energy curves. It should be mentioned that the adiabatic electron affinity usually cannot be measured with the above mentioned spectroscopic methods as the instantaneous removal of the electron leads to a vertical transition. However, limits on the value of EA can be derived by extrapolations of the photo-electron yield in PES measurements to the highest observed electron energy, thus the lowest electron detachment energy (see e.g. [28]).

2.2 Properties of SF_6 and SF_6^-

Sulfur hexafluoride SF_6 is the heaviest known gaseous substance, it is non-flammable and chemically stable, thus not reacting with any other species under room temperature conditions. The industrial production proceeds via the exothermic reaction of $S_8 + 24F_2 \rightarrow 8SF_6$. The main applications of SF_6 are as gaseous dielectric [13] in high-voltage switches or other high voltages devices, where it acts as an insulating gas due to the high electron capture probability. For instance, it is used in Van

de Graaff accelerators to insulate the terminal charged to a couple of million volt from the surrounding tank. A rule of the thumb defines the discharge stability in vacuum to 1000 Volt per millimeter, which would make insulation distances of tens of meters necessary. This can be drastically reduced using SF_6 filled tanks. Other applications are found in plasma etching as an etchant provider [29], for medical imaging [12] and as a shielding gas, for instance, in the production of manganese using its passive reaction character.
Due to the various useful properties of SF_6, however, the rising production over the last decades led to an increasing abundance in the Earth's atmosphere [15]. Here, a further well-known property, the high infrared absorption ability, makes SF_6 to one of the most potent greenhouse gases [14]. In particular, it was estimated for a range of 100 years to have a more than 2×10^4 times higher Global Warming Potential (GWP) than CO_2 [30], which is the efficiency to act as a greenhouse gas. Model calculations for the SF_6 degradation from the atmosphere include reaction paths such as dissociative electron attachment to SF_6 and reactions of SF_6^- with other species as hydrogen or oxygen [15]. Thus, it is of crucial importance to understand the building processes of the anions and their subsequent degradation.

2.2.1 Adiabatic electron affinity

The adiabatic electron affinity of SF_6 is an essential property which is puzzling the scientific world since decades. The EA has been defined in Eq. (2.1) as the energy difference between the ground states of the neutral and the negative molecule. In contrast to the vertical detachment energy, the adiabatic electron affinity is important in chemical reactions, which usually take place near equilibrium conditions. It has been noted that the EA cannot be measured directly by Photo Electron Spectroscopy (PES) as this method addresses the vertical transitions between SF_6^- and SF_6. In PES the electron yield as a function of the photo-electron energy is determined, where according to Eq. (2.4) the highest electron energy provides an upper limit on EA. However, in the case of SF_6 a large discrepancy between both structures is known, which leads to a enhanced difference between vertical and adiabatic quantities. Indeed, in recent PES measurements of SF_6^- almost no photo-electron yield was observed for electron binding energies lower than $\sim$2 eV [5].
Early reported values of EA scatter largely between 0.6 eV [32] and 1.39 eV [33]. An experimental value was derived by Chowdhury (1985) [34] to 1.05 ± 0.1 eV; a couple of years later 1.07 ± 0.07 eV was experimentally determined by Chen (1994) [35]. Theoretical estimates for EA were performed by Gutsev and Bartlett (1998) [36] using extensive structure calculations to derive vibrational frequencies for the neutral and anion, yielding EA = 0.92 eV. Miller's calculation in 2003 [37] resulted in 1.21 eV assuming like the previous authors a symmetric structure of SF_6^-. A semi-experimental approach by Troe *et al.* (2007) [19–21] based on flowing afterglow measurements found a value of 1.20 ± 0.05 eV using the vibrational frequencies calculated by Gutsev and Bartlett.
Most recently, sophisticated coupled-cluster calculations by Eisfeld (2011) [17, 18] suggested an asymmetric ground state structure of SF_6^-, which will be further discussed below, and a value for EA of 0.9 ± 0.1 eV. Re-analyzing the experiments by

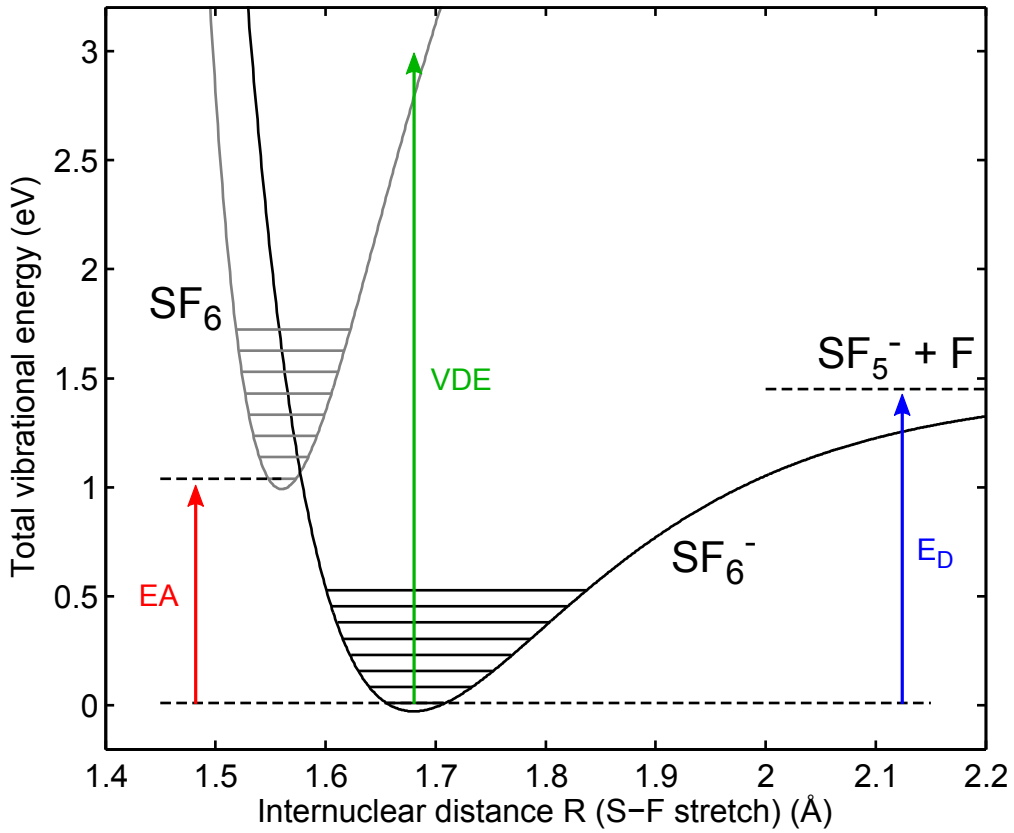

Figure 2.2: Schematic potential energy curves for SF_6 and SF_6^- using a Morse potential with the recent internuclear distances [17] (intermediate value for asymmetric SF_6^-, see table 2.1) and an adiabatic electron affinity EA of 1.03 eV and a dissociation energy E_D of 1.44 eV from Ref. [24], and a vertical detachment energy VDE of 3 eV (maximum of the electron yield in photo electron spectroscopy [5]). The first levels of the symmetric breathing vibrational mode ν_1 from table 2.1 are also illustrated. The crossing point of the two curves indicates a negative value for VAE as it is usually illustrated in literature for this system (see Ref. [5, 31]).

Troe (2012) using the new vibrational frequencies resulting from the suggested asymmetric structure of SF_6^- lead to an adiabatic electron affinity of 1.03 ± 0.05 eV [24], a value which was later supported by an independent calculation by Karton and Martin (2012) [38].
In figure 2.2, the schematic potential energy curves of the system are plotted using the internuclear distances for SF_6 and SF_6^- from Eisfeld [17], an EA of 1.03 eV and a dissociation energy E_D of 1.44 eV from Troe [24]. The level spacings of the symmetric breathing vibrational modes for SF_6 and SF_6^- are also indicated (compare table 2.1).
The VDE of SF_6^- is estimated to be around $\sim$3 eV from Photo Electron Spectroscopy [5], given by the broad maximum of the electron yield and hence, the highest Franck Condon overlap of the SF_6^- ground state with the neutral wave function at the ground-state bond distance of the negative species. A value of 3.27 eV

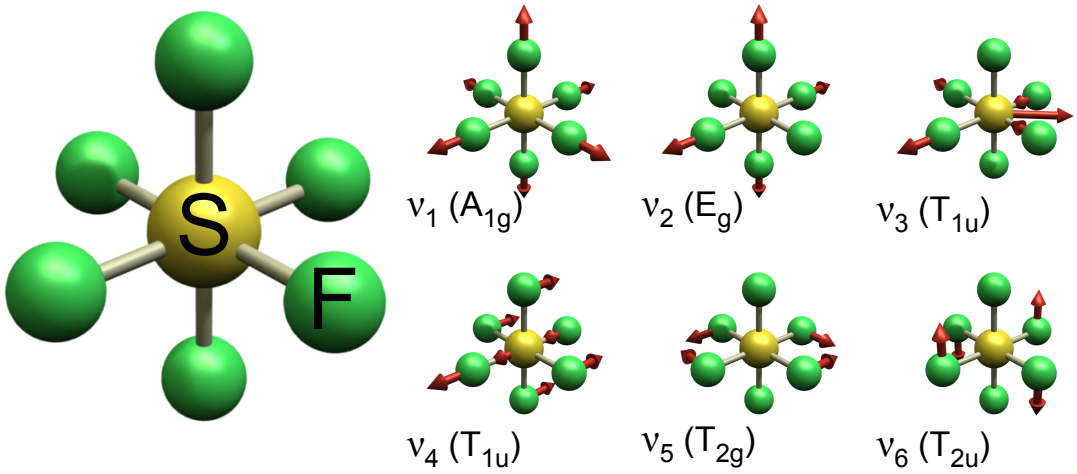

Figure 2.3: Structure of SF_6 and the 6 fundamental vibrational modes (see Ref. [43] or explanations in the text of Ref. [17])

for VDE was given by Eisfeld [17]. The dissociation threshold of the (S-F)-bond in SF_6^- was experimentally determined to 1.44 ± 0.05 eV [24], observing the reaction $SF_6^- \rightarrow SF_5^- + F$, which is in good agreement with a quantum chemical calculation also mentioned in Ref. [24].

2.2.2 Electronic structure and symmetry

Sulfur hexafluoride SF_6 is a compound of one sulfur atom and six fluorine atoms attached to it in all three dimensions in space with bonding angles of 90°, hence the geometric structure is given by an octahedron. Also the symmetric electron orbitals classify SF_6 into the symmetry group called O_h [39], which exhibits various symmetry operations like 3 C_4 rotational axes, 4 C_3 rotations, different mirror planes and also a center of inversion (sulfur). C_n denotes a rotation around $(360/n)$ degrees to map the molecule onto its own geometry.
The electronic ground state configuration of sulfur is $1s^2 2s^2 2p^6 | 3s^2 3p^4$, while the fluorine exhibits a $1s^2 | 2s^2 2p^5$ structure. Hence, the 6 outer electrons of sulfur have to be combined with 6 times 7 outer electrons of the fluorine. In the valence shell of F, two of the three p-orbitals are doubly occupied and saturated, while the third only singly occupied orbital is responsible for the binding. In this special electron configuration, due to the presence of the fluorine atoms, the $3s$ and $3p$-orbitals in sulfur build a (sp^3)-hybridization which is combined with two $3d$-orbitals and gives in summary a (sp^3d^2)-hybridization [40–42]. This hybridized orbital has places for a total of 12 electrons half of which are occupied. (sp^3)-hybridization is known from methane to create four symmetric bonds with equal angles and distances. However, in SF_6 under the additional influence of the two d-orbitals, the combined hybridized orbitals point to all three opposing directions in space on which the singly occupied p-orbital from the six fluorines are attached.
SF_6^- was recently been found to exhibit an asymmetric structure [17] in contrast to the neutral SF_6, which was also in discussion in earlier reports [44]. The previous

work by Gutsev and Bartlett predicted the additional electron to be spread over the entire molecule retaining the O_h structure after electron attachment. However, Eisfeld [17] found the electron to populate an antibonding σ^* orbital which is widely distributed over the molecule, however, partly concentrating towards one fluorine. The σ^* orbital is created between the 3s-orbital from sulfur together with the 2p-orbital of fluorine. Considering also the most probable dissociation channel into $SF_5^- + F$, SF_6^- can be considered as an SF_5^- containing 2/3 of the excess charge and a fluorine [17]. All the six potential minima, where the charge is directed to one of the fluorine, are separated from each other by a low energy barrier.
As a consequence of the asymmetry, SF_6^- falls into a different symmetry group namely the subgroup C_{4v} [39], where for instance the C_3 symmetry is no longer present. This also influences the degeneracies of the vibrational modes, as will be discussed below.
The electronic asymmetry also introduces different bonding distances for the (S-F) bond which are summarized in table 2.1. The equilibrium distance of the neutral is found to be at 1.5607Å in good agreement with previous values, but three different bond distances are given for the negative. The distances of the four S-F bonds perpendicular to the symmetry axis are at 1.6803Å already noticeably longer than in SF_6 (see Fig. 2.2). In the asymmetric direction 1.9324Å and 1.6027Å are calculated, respectively. This already demonstrates a large discrepancy between, for instance, the vertical detachment energy and the adiabatic electron affinity, and has consequences for the vibrational level densities and the rotational constants.

2.2.3 Vibrational frequencies

The neutral and the negative sulfur hexafluoride, which contain $n = 7$ atoms, have 15 vibrational degrees of freedom ($3n - 6 = 15$), which are partly degenerate. For the neutral SF_6 in O_h symmetry this results in 6 fundamental vibrational modes depicted in Fig. 2.3 and compiled in table 2.1 together with their degeneracies.
In the symmetric breathing mode A_{1g}, all fluorine atoms stretch the S-F bond simultaneously; this being the most symmetric movement and not degenerate. The nomenclature of the labels is defined by the degeneracy, where non-degenerate modes are A or B, being symmetric or anti-symmetric with respect to rotations about the principle axis, respectively. E is doubly degenerate and T triply, and the system is called Mulliken symbols [45] (or also [39]). Subscripts denote symmetry (g) or anti-symmetry (u) with respect to inversion. The degeneracies are not only given by the symmetry of the configuration of the nuclei, but also depend on the electronic orbitals which can have additional asymmetries.
As pointed out in Ref. [17], in an octahedral molecule only the T_{1u} modes can be infrared (IR) active as only they lead to a change in the dipole moment. In SF_6 only two modes have the T_{1u} symmetry and the higher frequency of 966 cm^{-1} (ν_3 mode) is well known for the highest IR activity in SF_6. Absolute integrated absorption intensities have been obtained experimentally for both T_{1u} modes [46].
Due to the asymmetry in this model of SF_6^-, all degenerate modes split up to build a total of 11 fundamental modes (see table 2.1). Concerning the IR activity, in the C_{4v} symmetry also A_1 and E modes can be IR active. The highest frequency

is found at 671.1 cm^{-1} ($\sim$83 meV) and also corresponds to a T_{1u} mode in the O_h group (compare table 2.1). In recent photo electron spectroscopy measurements [5], a strong absorbing line was found at 683(5) cm^{-1} which could not be assigned to any frequency in O_h, but could well be the 671.1 cm^{-1} transition predicted in C_{4v}. Also a feature at 440(10) cm^{-1} is reported which would fit to the 435.2 cm^{-1} second E mode from a T_{1u}.
A further difference to the previous assumption of a symmetric SF_6^- is the appearance of a very low energetic mode at 78.6 cm^{-1}. This should be kept in mind when deriving the density of states of SF_6^-, as the lowest frequencies dominate the amplitude and a drastic increase in the density of states compared to the O_h model is observed.

2.2.4 Rotational constants

The large difference in the equilibrium distances between SF_6 and SF_6^- is also reflected into the rotational constants (see Appendix A.1.4 and table 2.1). The value for the neutral is the highest and all three rotational constants are equal ($A = B = C$). This corresponds to a spherical top molecule reflecting the O_h symmetry. The rotational constants of SF_6^- are around 1/6th lower and very similar comparing both symmetries. Indeed, an averaged value over the rotational constants in the C_{4v} symmetry leads to 0.075325 cm^{-1} with less than one percent deviation from the old value. Although SF_6^- is a prolate symmetric top rotor ($A > B = C$), it can be assumed to be spherical considering the small difference.
One other point to note is that sulfur has four stable isotopes which are abundant according to: $^{32}_{16}$S (94.99%), $^{33}_{16}$S (0.75%), $^{34}_{16}$S (4.25%), and $^{36}_{16}$S (0.01%) [50]. Some effects of this have been for instance investigated in Ref. [49], but they are assumed to be not relevant for the present analysis and are not further considered.

Table 2.1: Collection of recent (S-F)-bond distances (Å), rotational constants (cm^{-1}) and vibrational frequencies (cm^{-1}) of SF_6 and SF_6^-. Bond distances are taken from [17], [47], [36] and [17]; rotational constants B from [48], [48] and [17]. Vibrational frequencies of SF_6 in O_h ground state symmetry [17, 49]; SF_6^- in O_h from [36] and in C_{4v} ground state symmetry [17]. Mode degeneracies are given in curly brackets.

	O_h	SF_6 (O_h)		SF_6^- (O_h)	SF_6^- (C_{4v})	C_{4v}
R_{eq} (S-F) (Å)		1.5607	1.5622 (7)	1.7167	1.9324 1.6803 1.6027	
Rot. const. (cm^{-1})		0.090686 {3}		0.074980 {3}	0.073919 {2} 0.078137 {1}	
Vib. mode (cm^{-1})		Eisfeld 2011 [17] (Theo.)	McDowell 1986 [49] (Exp.)	Gutsev 1998 [36] (Theo.)	Eisfeld 2011 [17] (Theo.)	
ν_1	A_{1g}	787.9 {1}	787.0 {1}	626 {1}	597.3 {1}	A_1
ν_2	E_g	654.8 {2}	654.8 {2}	447 {2}	506.9 {1} 479.8 {1}	A_1 B_1
ν_3	T_{1u}	966.0 {3}	964.0 {3}	722 {3}	757.7 {1} 671.1 {2}	A_1 E
ν_4	T_{1u}	617.7 {3}	620.0 {3}	306 {3}	224.9 {1} 435.2 {2}	A_1 E
ν_5	T_{2g}	526.4 {3}	524.4 {3}	336 {3}	371.8 {1} 240.0 {2}	B_2 E
ν_6	T_{2u}	349.5 {3}	355.1 {3}	237 {3}	263.7 {1} 78.6 {2}	B_1 E

2.3 Vibrational Auto-Detachment rate (VAD)

In this section, the basic model for the vibrational auto-detachment process is derived as it will be used to analyze the measurements presented in chapter 4. This process was observed by the detection of neutral SF_6 from the spontaneous electron emission of stored, excited SF_6^- ions. The corresponding reaction is given by

$$(SF_6^-)^* \rightarrow SF_6 + e^-, \tag{2.7}$$

where the asterisk $(*)$ denotes an internal excitation of SF_6^-.
The process of vibrational auto-detachment can take place if the energy in the vibrational modes of the anionic system exceeds the binding energy of the electron, that is the electron affinity EA. Pioneering work on the auto-ionization of neutrals and auto-detachment can be found in Ref. [51–53].
The basic process of VAD requires a transfer of vibrational energy to the electronic excitation with a subsequent electron emission. This requires a coupling between electronic and nuclear motion, which involves a breakdown of the Born-Oppenheimer approximation as here the electronic and vibrational energies are assumed to be conserved separately. The time scales for the energy transfer can cover a wide range of up to several milliseconds or even seconds, which are extremely long compared to the usually electronic (ps to fs) or vibrational (fs to ns) motion, and which depend on the excitation energy and the complexity of the considered system. Thus, long time scales are expected when the vibrational energy can be distributed over a large number of oscillators, reflected in a high density of states of the anionic system and a small number of final states in the neutral product configuration.
A schematic view on this process is illustrated in Fig. 2.4 using the potential energy curves of SF_6^- and SF_6. Several decay channels can be open to induce the detachment process. The total vibrational energy E in SF_6^- is required to exceed at least the adiabatic electron affinity EA; the remaining excess energy $E-\mathrm{EA}$ is shared between the vibrational excitation E_{vib}^0 of the neutral product SF_6 and the kinetic energy ϵ of the emitted electron. In figure 2.4 only the first levels of the symmetric vibrational breathing mode ν_1 in SF_6 (see table 2.1) are displayed as possible decay channels. A detailed approach to this process will be elaborated in the following section, which was developed by Troe [19–24].
Historically, in one of the first measurements by Edelson *et al.* [54] in 1962, the metastable character of $(SF_6^-)^*$ was found and a lifetime of $\sim$10 μs was determined. A time-of-flight (TOF) mass spectrometer was used with a SF_6^- drift time of only 18.5 μs, which obviously is only sensitive to a small time window of the decay. In general, the reported investigations can be classified into TOF measurements [33, 54–57] with sensitivities in the order of a few μs and ion cyclotron resonance (ICR) methods [58–60] which cover the range of milliseconds or higher. Accordingly, large discrepancies exist between reported lifetimes, which reach from a few μs to tens of milliseconds.
For an ICR measurement Odom *et al.* [59] stated already that the measured lifetime varies with the observation time, giving values between 50 μs to 10 ms, and multiple excited states were assumed with different decay constants to explain the observed time dependence. Moreover, Appelhans *et al.* [56] used a flight tube and even

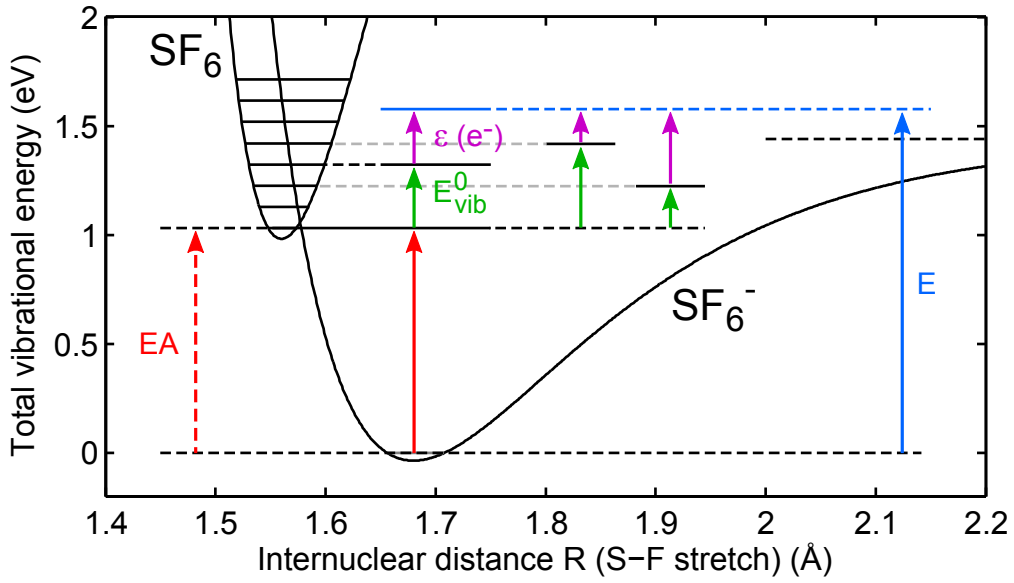

Figure 2.4: Schematic view on the potential energy curves of SF_6 and SF_6^- (see also Fig. 2.2) indicating the first levels of the symmetric vibrational breathing mode ν_1 in SF_6 (see table 2.1). In the VAD-decay, the excess energy $E - \mathrm{EA}$ for a given total vibrational energy E in SF_6^- can be shared between the kinetic energy ϵ of the electron and the vibrational excitation E^0_{vib} of the product SF_6.

observed variations in the lifetime for different ion source temperatures considering time ranges up to 23 μs.

In more recent results presented by LeGarrec *et al.* [57] in 2001, SF_6^- is created by a supersonic expansion cooled SF_6 gas jet attaching free electrons from photo-ionized sodium and the electron energy could be varied by the photon energy between 0 to 100 meV. A lifetime of 19.1±1.7 μs was found with the TOF method, however, without dependence on the electron energy.

In another experiment, electron transfer from Rydberg excited potassium atoms to SF_6 was used to produce SF_6^-, which were then stored in a Penning trap. After a variable delay, the remaining SF_6^- was ejected onto a detector [61]. Here, lifetimes between 1 and 10 ms were observed. Most recently, in a measurement with the electrostatic storage ring ELISA the observation of a power law decay with a time dependence of $\propto t^{-1.5}$ instead of an exponential decay was reported from the observation of the decay over the time span between hundred microseconds and ten milliseconds [25].

Present interpretations of the VAD process include the intramolecular vibrational redistribution (IVR) of the internal energy in SF_6^-, and explain the contradictory observations of the previous measurements. The VAD process extends over many decades in time corresponding to different internal excitations of the $(SF_6^-)^*$ instead of a few excited energy levels. However, it also became clear that the preceding observations probed not only the auto-detachment rate, but also depended on the internal energy distribution and thereby, the ion production process.

The approach which is applied here is based on the reversibility of the detachment and attachment processes and experimental results are included to derive the energy and time dependencies. The reader is referred to the Appendix B for a compilation of relevant concepts and formulas.

Troe's approach

The derivation of the reaction rate in the Rice, Ramsperger, Kassel and Marcus (RRKM) approach [62] is illustrated in detail in Appendix B.2. In equation (B.29), the probability for a transition is related to the sum of states $N^{\ddagger}(E - E_0)$ in the critical area along the reaction coordinate and the total phase space volume occupied at an energy E. Together with Planck's constant h, the reaction rate $k(E)$ for the detachment process is given as

$$k(E) = \frac{W_{det}(E - \mathrm{EA})}{h\rho^{-}(E)}, \tag{2.8}$$

where $N^{\ddagger}(E - E_0)$ is substituted by $W_{det}(E - \mathrm{EA})$, which includes the sum over all configurations that lead to a detachment, and $\rho^{-}(E)$ is the density of states of the anion.
More precisely, $W_{det}(E - \mathrm{EA})$ is the sum over all specific probabilities for each configuration, which induce a reaction (also called "cumulative reaction probability" [63]) and can be far greater than unity. The electron detachment process can be related to the electron attachment process via detailed balance, which is based on the microscopic reversibility of a reaction and implies an equilibrated, stationary configuration between reactants and products. However, to assume detailed balance, both processes have to be described by the same physical concept. Using the rates k the principle of detailed balance can be written for small intervals dE of the total energy E as

$$k_{detachment}\ \rho_{anion} = k_{attachment}\ \rho_{neutral+electron}. \tag{2.9}$$

Here, ρ_{anion} is the density of states for the anion and $\rho_{neutral+electron}$ refers to the configurations that the neutral and electron can have after the detachment. In the following, the density of states are denoted by $\rho^{-}(E)$ for SF_6^- and by $\rho^{0}(E)$ for SF_6, and they can be obtained by a summation over the vibrational energies (see Appendix A.1.3 and Fig. A.2).
Because of the assumed reversibility of the detachment process, we now consider the electron capture process to derive an expression for $W_{det}(E - \mathrm{EA})$ and substitute it into Eq. (2.8). The following model derivation has been carried out by Troe *et al.* [19–24] and is exemplified here to understand the further modification caused by rotational excitation and its application to the present experiments. The electron capture process to a neutral molecule takes place in a polarization potential of $-\alpha/2r^4$ induced by the incoming electron [64] which is a short-range potential when compared to the Coulomb field. The capture cross section $\sigma(k)$ can be written as

$$\sigma(k) = \frac{\pi}{k^2} \sum_{l=0}^{\infty} (2l + 1) P_l(k), \tag{2.10}$$

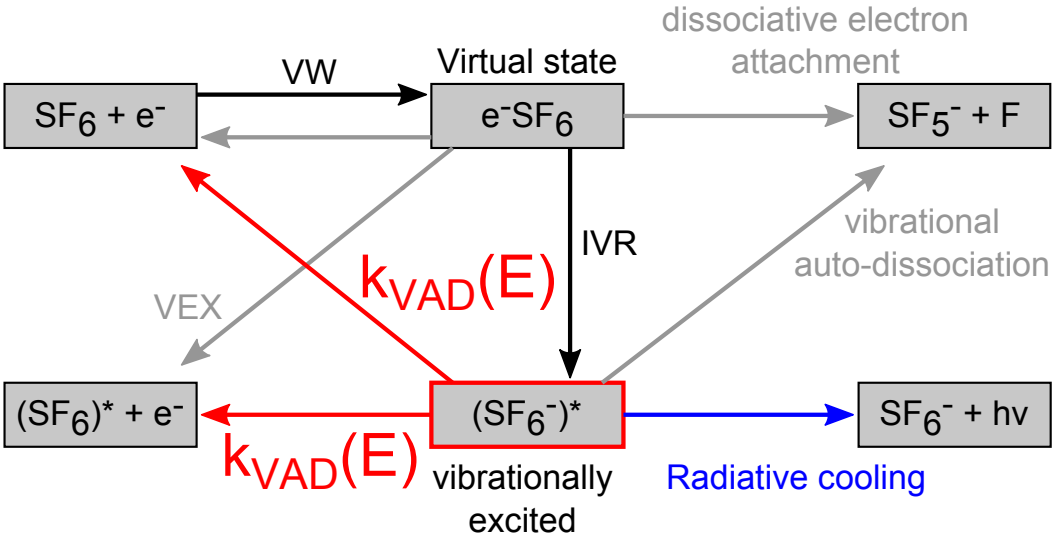

Figure 2.5: Reaction scheme for SF_6 + e^-: Electrons are captured by SF_6 into a virtual state according to the capture model by Vogt and Wannier (VW); intramolecular vibrational redistribution (IVR) transfers the gained energy into vibrational excitation obtaining vibrationally excited $(SF_6^-)^*$. Delayed vibrational auto-detachment (VAD) leads back to the initial state or to an excited $(SF_6)^*$. For higher collision energies between SF_6 and electron, vibrational excitation (VEX) by inelastic collisions competes with the production of $(SF_6^-)^*$.

where $k = \sqrt{2\mu\epsilon}/\hbar$ is the wavenumber of the electron, with the reduced mass μ of SF_6 and the electron ($\mu \approx m_e$), the kinetic electron energy ϵ, and $\hbar = h/2\pi$. The summation goes over all electron angular momenta l and this expression connects the maximum capture cross section of π/k^2 with a transmission coefficient $P_l(k)$. As simplification only s-wave capture ($l = 0$) has to be considered for SF_6 which, setting $P(\epsilon(k)) = P_0(k)$, leads to the capture probability of

$$P(\epsilon) = \frac{2\mu}{\pi\hbar^2}\,\epsilon\,\sigma(\epsilon). \tag{2.11}$$

A simple expression for the capture cross section for s-wave capture was derived by Klots in [65], see below. As a consequence of the microscopic reversibility of the process, $P(\epsilon)$ is also the transmission probability for the electron *detachment* process for a given kinetic energy ϵ of the emitted electron. Thus, the summation over all vibrational states $E_V^0(\{v_i\})$ in the product SF_6, which are accessible at a total vibrational energy E of SF_6^- (compare also Fig. 2.4), gives the requested cumulative reaction probability from Eq. (2.8) by

$$W_{det}(E - \mathrm{EA}) = \sum_i P(\epsilon(E, \{v_i\})), \tag{2.12}$$

where the electron energies are constrained by the relation $\epsilon(E, \{v_i\}) = E - \mathrm{EA} - E_V^0(\{v_i\}) > 0$. Here, $\{v_i\}$ denotes the ensemble of all quantum numbers characterizing the vibrational state of SF_6.

The validity of this assumption can be easily proven by applying the detailed balance relation from Eq. (2.9) to the detachment and attachment process by

$$k(E)\ \rho^-(E) = \int_0^{E-\mathrm{EA}} k_{att}(E,\epsilon)\ \rho^{el}(\epsilon)\ \rho^0(E-\mathrm{EA}-\epsilon)\ d\epsilon, \tag{2.13}$$

where $k_{att}(E,\epsilon)$ is the attachment rate as function of the total energy E and the electron energy ϵ (see also Fig. 2.4 for the energy balance). The free electron density of states $\rho^{el}(\epsilon)$ in Eq. (2.13) is given by

$$\rho^{el}(\epsilon) \ = \ \frac{1}{2}\ \frac{V}{2\pi^2}\left(\frac{2\mu}{\hbar^2}\right)^{3/2}\epsilon^{1/2}, \tag{2.14}$$

noting that the spin multiplicity has been removed by the additional factor of 1/2, as it was also not considered in the definition of $\rho^-(E)$. Using for the attachment rate $k_{att} = \sigma v/V$, with the capture cross section σ from Eq. (2.11), the electron velocity $v = \sqrt{2\epsilon/\mu}$ and the reaction volume V, Eq. (2.13) can be transformed into Eq. (2.8) by substituting

$$W_{det}(E-\mathrm{EA}) = \int_0^{E-\mathrm{EA}} P(\epsilon)\ \rho^0(E-EA-\epsilon)\ d\epsilon. \tag{2.15}$$

Instead of the summation in the prior definition of $W_{det}(E-\mathrm{EA})$, we obtain an integral over the electron energies, which is weighted by the density of states ρ^0 of SF_6 at the vibrational energy $E_V^0(\{v_i\}) = E - \mathrm{EA} - \epsilon$ and thus, accounts for the multiplicity with which a specific electron energy can occur considering the internal states of SF_6. The density of states ρ^0 of SF_6 can be imagined as a superposition of δ-functions at each vibrational state $E_V^0(\{v_i\})$ as it is also derived with the Direct Count method by Beyer and Swinehart [66, 67] (compare Appendix A.1.3 and Fig. A.2).

After accomplishing the link between the detachment rate $k(E)$ and the attachment process, the electron capture cross section has to be defined in a suitable representation. As mentioned before, Klots [65] found a simple expression for s-wave capture, which was further improved [68] and used to fit measured electron capture cross sections of SF_6 [19–24]. The analytic form of the transmission coefficient $P^{VW}(\epsilon)$, originating from Vogt and Wannier, reads as

$$P^{\mathrm{VW}}(\epsilon/eV) \approx 1 - 0.25\ \exp(-2.54\sqrt{\epsilon}) - 0.75\ \exp(-8.75\sqrt{\epsilon}), \tag{2.16}$$

taken from Ref. [23]. Specific properties such as the reduced mass between SF_6 and e^- and the polarizability α of SF_6 are included in the constants. Although this function describes the measured capture cross section for low energies up to $\sim$ 10 meV rather well, for higher energies the cross section is overshooting the experimental values.

Considering the process of electron capture as illustrated in Fig. 2.5, a virtual state e^-SF_6 is created which is unstable due to the gained energy of at least the electron

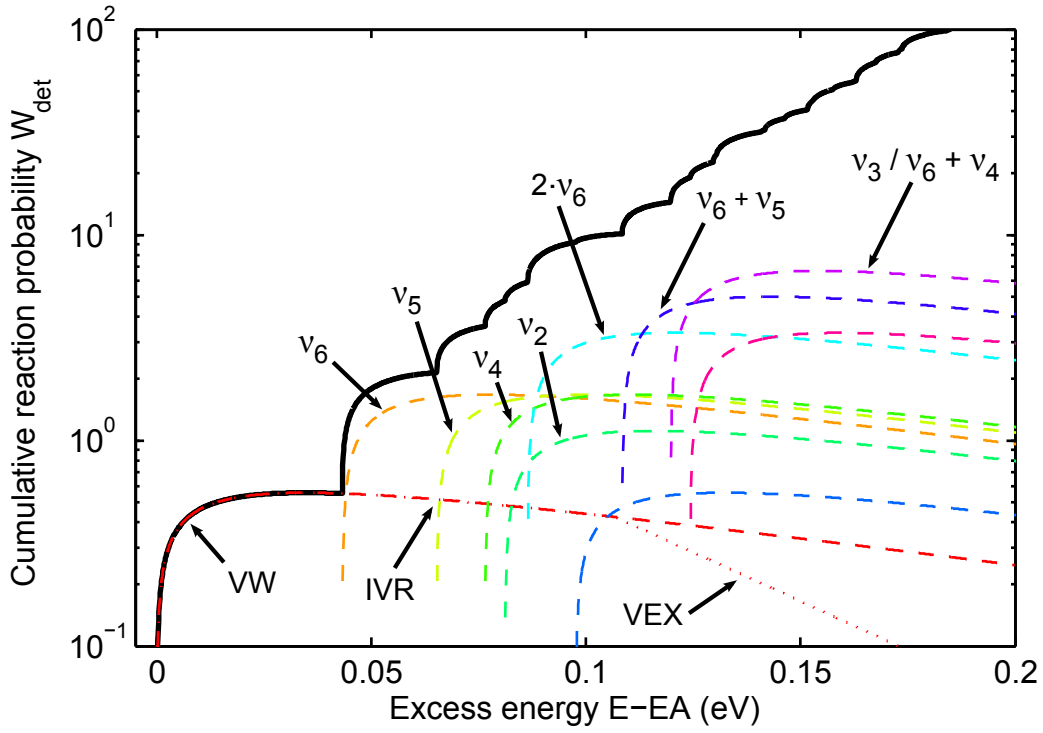

Figure 2.6: Composition of the cumulative reaction probability W_{det} for electron detachment: The lowest curve (red) corresponds to an excess energy of $E - \mathrm{EA} = \epsilon$ without vibrational excitation of SF_6 after the detachment. The dominating regions of the probabilities from VW, IVR and VEX are marked. The other curves show a detachment with vibrational excitation of $(SF_6)^*$ where the excess energy is given by $E - \mathrm{EA} = \epsilon + E_V^0(\{v_i\})$. The amplitudes results from the degeneracies of the different modes and their permutations for multiple excitations.

affinity during the attachment. The virtual state can either detach back to SF_6 and e^- or the excess energy is transferred to vibrational excitation due to a coupling process between electronic and nuclear motion. This process is called Intramolecular Vibrational Redistribution (IVR) and involves the exchange of energy between the vibrational modes, which are coupled due to the anharmonicities of the potentials. For higher electron energies, the time consuming IVR process becomes less probable, because the interaction time between electron and SF_6 decreases and IVR competes with the direct detachment. At even higher energies, there might be enough electron energy to excite $(SF_6)^*$ in an inelastic collision without attachment, which is called vibrational excitation (VEX). Both processes are described empirically [23] according to the shape of the experimental capture cross section by

$$P^{\mathrm{IVR}}(\epsilon/eV) \approx \exp(-6.48\ \epsilon), \tag{2.17}$$

$$P^{\mathrm{VEX}}(\epsilon/eV) = 1 \qquad \text{for } \epsilon \leq 0.094, \tag{2.18}$$

$$P^{\mathrm{VEX}}(\epsilon/eV) \approx \exp(-16.2\ (\epsilon - 0.094)) \qquad \text{for } \epsilon > 0.094, \tag{2.19}$$

where the value of 0.094 eV [23] is used to define the threshold energy for the VEX process.

Detailed balancing has been applied to relate the derived electron capture cross section to the detachment process, which relies on the reversibility of the reaction and both directions have to correspond to the same physical process. However, VEX involves inelastic scattering of the electron with SF_6, a process which does not seem to be present in the detachment reaction [19]. Thus, for the VAD process the contributions of VEX identified in the experimental capture cross sections are not considered and the total transmission coefficient to be inserted in Eq. (2.15) is

$$P(\epsilon) \approx P^{\mathrm{VW}}(\epsilon) \times P^{\mathrm{IVR}}(\epsilon). \tag{2.20}$$

The resulting cumulative reaction probability W_{det}, combining Eq. (2.15) and Eq. (2.20), is shown in Fig. 2.6 with the different contributions from excited modes of the product SF_6 after VAD. It should be noted that whether or not VEX should be included into the VAD process is still unclear, however, its inclusion would only lead to minor corrections.
The detachment rate of the VAD process is shown in Fig. 2.7 using an electron affinity of 1.03 eV as given by the latest model [23, 24], and will mostly be used in the following analysis. Figure 2.7 also illustrates the prior model results using an EA of 1.20 eV [19–22] and vibrational frequencies obtained by Gutsev and Bartlett for a symmetric SF_6^- (compare table 2.1). Additionally, the thermionic emission models from [10, 25, 26] are shown, which are shortly introduced below.

Thermionic emission model

The thermionic emission model is the microscopic counterpart to the macroscopic model describing the evaporative electron emission from hot surfaces, where the Richardson-Dushmann equation [69] describes the emitted electron current density $J \propto T^2 \exp(-E_0/k_B T)$ with the binding energy E_0 and the temperature T of the system. This equation was also applied to describe the VAD process of clusters [10]. A microscopic version of the Richardson-Dushmann equation can be derived from RRKM rates.
For this purpose, the cumulative reaction probability W_{det} is again written as an integral over the capture cross sections by combining Eq. (2.11) and Eq. (2.15). However, the electron energy is here assumed to be much smaller than the vibrational excitation of the resulting neutral ($\epsilon \ll E - \mathrm{EA}$), which does not really apply to small systems and energies close to the threshold. The density of states $\rho^0(E - \mathrm{EA} - \epsilon)$ is then expanded and related to a microcanonical temperature of the neutral: $1/k_B T_m = d\ln(\rho^0(E'))/dE'$. The integration over the electron energy ϵ leads to an expression that contains an average, energy-independent capture cross section σ_C and the detachment rate in the thermionic emission model [10] is then given as

$$k(E) = \frac{2\mu\sigma_C}{\pi^2\hbar^3}(k_B T_m)^2 \, \frac{\rho^0(E - \mathrm{EA})}{\rho^-(E)} = A \, \frac{\rho^0(E - \mathrm{EA})}{\rho^-(E)}. \tag{2.21}$$

Calculating the density of states with methods introduced in Appendix A using the vibrational frequencies, a constant $A = 10^{13}$ s^{-1} and EA = 1.20 eV leads to the thermionic emission rate for SF_6^-, which was used in Ref. [26], and this rate is included in Fig. 2.7.

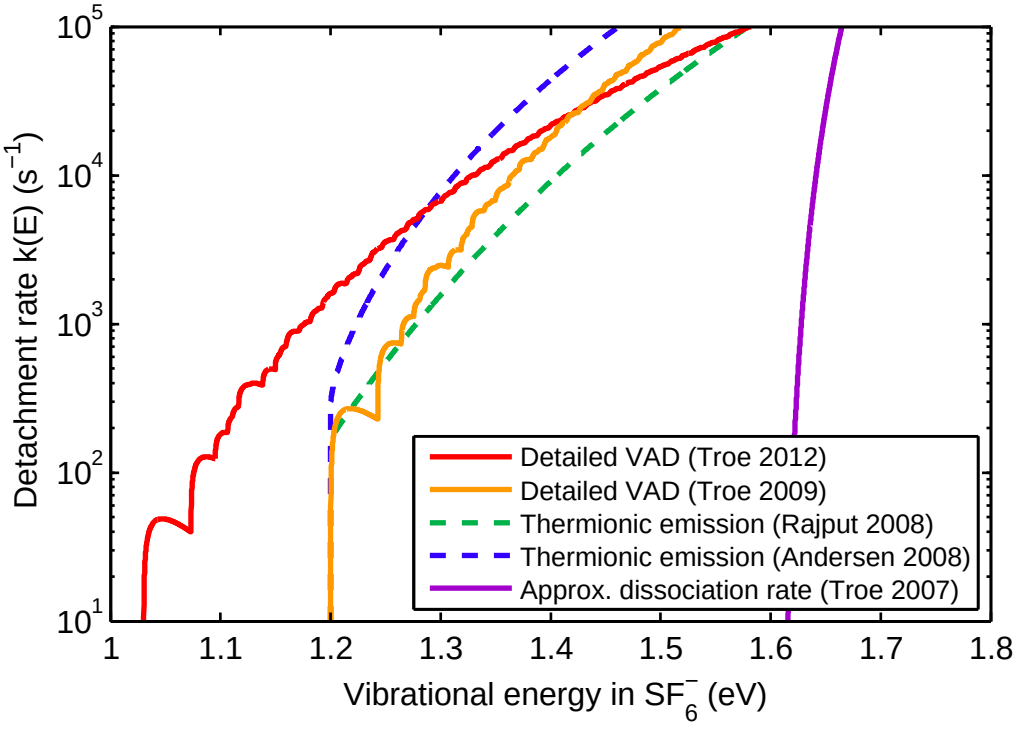

Figure 2.7: VAD detachment rates $k(E)$ for different models: Detailed VAD for EA = 1.03 eV from Ref. [24] (red curve), former model with EA = 1.20 eV from Ref. [22] (orange curve), thermionic emission model from Ref. [25] (dashed green) and from Ref. [26] (dashed blue). The dissociation rate taken from Ref. [20] is shown as comparison for $E_D = 1.61$ eV (purple).

A further approximation, applied especially when the real vibrational frequencies are unknown, is to assume that the density of states of the neutral and the anion are similar. The ratio of the density of states from Eq. (2.21) is then represented by an Arrhenius factor $\exp(-\mathrm{EA}/k_B T_e)$ and an expression similar to the Richardson-Dushmann equation for the detachment rate $k(E)$ is obtained with

$$k(E) = A\, e^{-\mathrm{EA}/k_B T_e}. \tag{2.22}$$

For the electron temperature T_e the so called heat bath correction [10, 70, 71] is applied as a link to the microcanonical temperature T_m: $T_e \simeq T_m - \mathrm{EA}/2C_m - \mathrm{EA}^2/12C_m T_m$, where C_m is the heat capacity of the neutral. The energy dependent microcanonical temperature was defined before in the text and for SF_6 derived as $T_m[\mathrm{K}] = 840E[\mathrm{eV}] + 270$ [25]. Together with a pre-factor of $A = 7 \times 10^{10}$ s^{-1} the dashed green thermionic emission curve in Fig. 2.7 is obtained, which was used in Ref. [25] to describe the VAD rate of excited $(SF_6^-)^*$.
It should be noted, that the pre-factor A in the thermionic emission formula is usually taken by an educated guess. Indeed, reducing the constant A by a factor of 2 as compared to the value used in Ref. [26], the more precise detachment rate derived by Troe is well reproduced for energies ∼100 meV above the threshold, but the rates at smaller energies are overestimated. In the even cruder approximation leading to

Eq. (2.22) the deviations are larger and cannot be compensated by changing the prefactor. The comparison shows that for small systems like SF_6^- and energies close to the threshold the accuracy of the thermionic emission model approach is rather limited.
For the present work, we will use the more precise detachment rate, because the simplified approaches from thermionic emission do not lead to a satisfying representation of the process; especially for low excitation energies close to the threshold. Furthermore, the detailed model will be analyzed and extended to different values of EA and to rotational excitation.

Competing decays

A competing process to VAD is the analogue decay by vibrational auto-dissociation, which is found to lead to a neutral fluorine atom and a negative SF_5^-. The dissociation threshold for this process was recently determined to be $E_D = 1.44 \pm 0.05$ eV [24], which is in good agreement with the value of 1.47 eV calculated by Kerkines, Morokuma and Bobadova-Parvanova. The latter value is cited in Ref. [24], but not yet published. The energy difference between electron affinity and dissociation energy was already reported in Ref. [20] to be $E_D - \mathrm{EA} = 0.41$ eV. In a former investigation, a value of $E_D - \mathrm{EA} = 0.43$ eV was determined [72].
The gross shape of the dissociation rate $k_{diss}(E)$ from Ref. [20] is depicted in Fig. 2.7 for a dissociation energy of $E_D = 1.61$ eV, which is the former value based on $\mathrm{EA} = 1.20$ eV and $E_D - \mathrm{EA} = 0.41$ eV [21]. Independent of the precise value of EA, the competition between VAD and auto-dissociation is only relevant at detachment rates $> 10^4$ s^{-1}, that is for times $1/k < 10^{-4}$ s after the production process of the hot SF_6^- anion.
In this work, the dissociation rate was approximated from Ref. [20] and will be scaled as follows for the new value of $E_D = 1.44$ eV and the recent vibrational frequencies of SF_6^- from Ref. [17]. The dissociation rate is assumed to have the same dependence on the vibrational density of states of SF_6^- as represented by the RRKM approach in Eq. (B.29) and thus, only enters in the denominator. As the vibrational frequencies of the neutral SF_6 vary only insignificantly (see table 2.1), $N^\ddagger(E - E_0)$ of Eq. (B.29) is assumed to be unchanged (E_0 is here the dissociation threshold E_D).
Hence, the dissociation rate $k_{diss}^{1.61}(E)$ from Ref. [20] is multiplied by the former density of states of SF_6^- $\rho_-^{1.20}(E)$, shifted to the new value of $E_D = 1.44$ eV and divided by the recent density of states $\rho_-^{1.03}(E)$ as follows

$$k_{diss}^{1.44}(E) = k_{diss}^{1.61}(E - 1.44 + 1.61)\,\frac{\rho_-^{1.20}(E - 1.44 + 1.61)}{\rho_-^{1.03}(E)}. \tag{2.23}$$

The so derived dissociation rate is compared to the VAD rate in Fig. 2.8, where the transition between both is found at a rate corresponding to around 10μs. Thus, dissociation will not be considered in the further model.
Another decay process competing in principle with the vibrational auto-detachment is radiative cooling of the SF_6^- ions by infrared (IR) radiation through IR active vibrational modes, which leads to a loss of excitation energy of the ion, and thus, to a shift of the excitation energy distribution to lower energies. The process will be

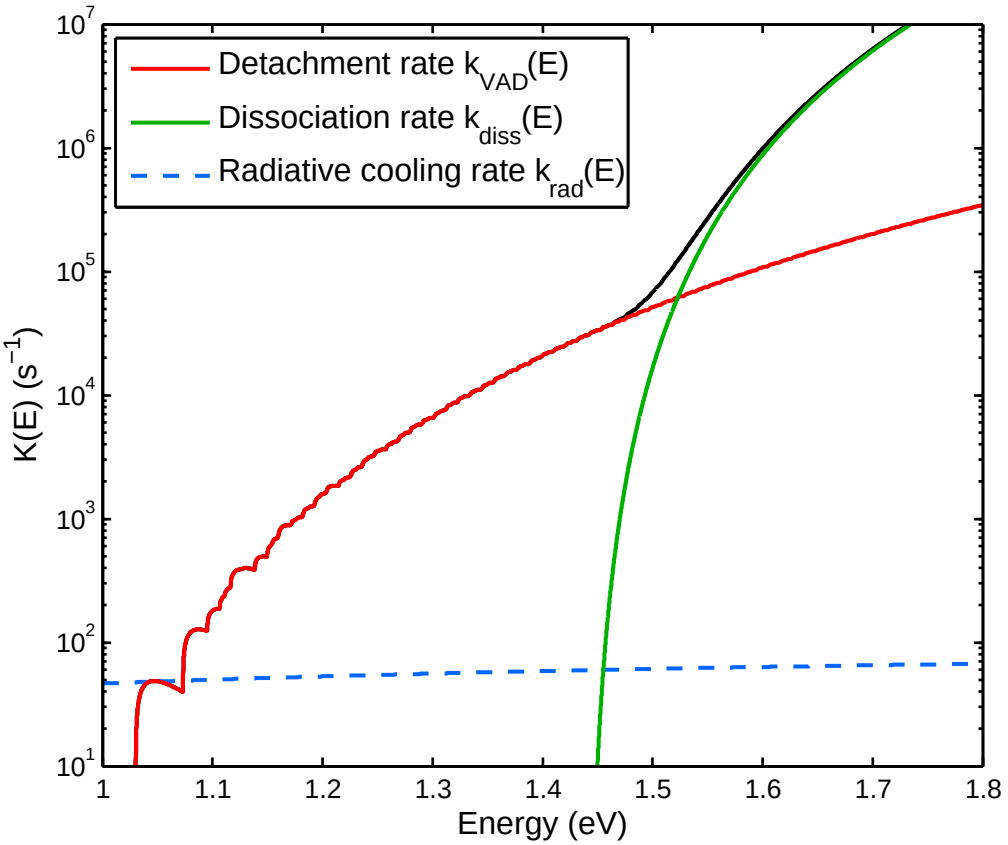

Figure 2.8: The detachment rate $k_{VAD}(E)$ for SF_6^- for EA = 1.03 eV and the auto-dissociation rate $k_{diss}(E)$ for $E_D = 1.44$ eV; approximated from Ref. [20] and scaled according to Eq. (2.8) (Both for $J = 0$). Also indicated is the radiative cooling rate $k_{rad}(E)$ for SF_6^-, which will be approximated in Sec. 2.5.1.

discussed in more detail in Sec. 2.5, where it will also be shown, that the decay rate k_{rad} is only weakly dependent on the excitation energies with values of $k_{rad} \sim 50$ s^{-1} at energies around the EA threshold. The comparison between k_{rad} and $k(E)$ in Fig. 2.8 shows that radiative cooling competes with the electron detachment rate only at energies very close to the detachment threshold, that is at times $1/k_{rad} \gtrsim$ 20 ms after the production of the hot SF_6^- ions.

2.4 The SF_6^- energy distribution and auto-detachment during initial cooling

In the measurements presented in chapter 4, SF_6^- anions produced in a hot ion source are stored in the CTF ion trap, and their VAD decay is observed by counting the neutral SF_6 molecules leaving the ion trap after electron detachment. The high kinetic energies of the SF_6^- anions enable a direct, time dependent detection of the neutrals as they propagate on with the same velocity as the mother ion $(SF_6^-)^*$ (recoil of the electron can be neglected), but are no longer confined by the electrostatic

mirrors of the trap. Thus, the number of neutral counts per time interval can be measured, which is referred to as the neutralization rate $R(t) = dN(t)/dt$, with t denoting the time after the initial ion excitation in the ion source.
The time range over which $R(t)$ has been observed in these experiments is limited to 500 μs $\leqslant t \lesssim$ 100 ms, where the lower limit is due to technical reasons, while at the upper limit the VAD rate is getting smaller than the rate caused by detector dark counts. As discussed in Sec. 2.3, VAD is determining the neutralization rate; only at the long time limit radiative cooling is expected to influence $R(t)$.
In the present section we will derive the neutralization rate $R(t)$ and discuss the influence of the various input parameters on the observed rates.

2.4.1 Energy distribution and neutralization rate

To derive $R(t)$, an ensemble of ions with fixed internal energy is assumed which decays independently of the distribution of the energy to the various vibrational modes, as the IVR mixes the configurations in times shorter than the characteristic time scales of the various decay modes. Thus, the VAD rate is expected to depend only on the total vibrational energy, as assumed before. Moreover, no exchange of energy between ions is supposed to takes place inside the ion trap during the measurement, i.e. all ions decay stochastically according to their initial internal energy.
A pure exponential decay behavior is obtained, if all ions would have the same internal energy. However, the probability of anions to have a certain excitation energy E after leaving the ion source is expected to be given by a broad energy distribution $f_0(E,T)$, the shape of which is determined by the parameters characterizing the source (summarized by T). Normalizing $f_0(E,T)$ according to

$$\int_0^\infty f_0(E,T)\, dE = 1, \tag{2.24}$$

the neutralization rate $R(t)$, caused by the VAD process is given by

$$R(t) = N_0 \int_{\mathrm{EA}}^\infty f_0(E,T)\; k(E) e^{-K(E)t}\, dE, \tag{2.25}$$

where N_0 denotes the total number of ions, and $K(E) = \sum_i k_i(E)$ is the total decay rate involving the sum over all decay processes i.
According to the steep increase of the VAD rate coefficient with E, ions with higher internal energy decay with higher rates and contribute mostly at early times and vice versa. The depletion of high energetic ions from the ensemble leads to a time dependent change of the energy distribution which is given by

$$f_t(E,T) = f_0(E,T)\; e^{-K(E)t} \approx f_0(E,T)\; e^{-k(E)t} \tag{2.26}$$

for $E \geq$ EA and $t > 10^{-4}$ s. Note that in writing down Eq. (2.25) and Eq. (2.26) the redistribution of the energy of the ions by radiative cooling has been neglected;

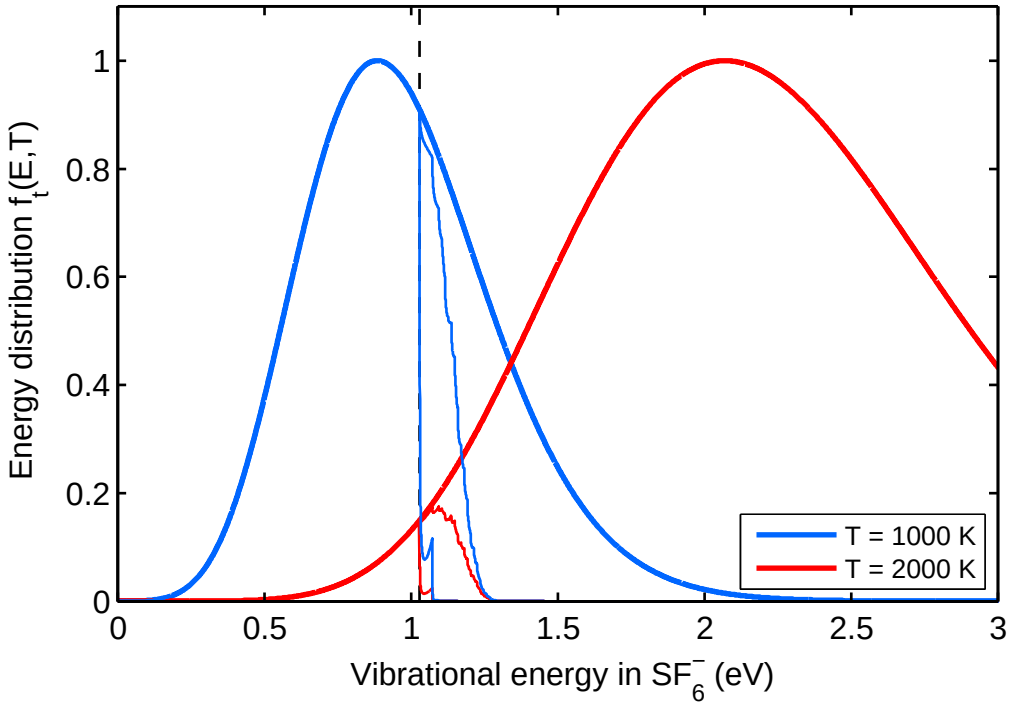

Figure 2.9: The initial vibrational energy distribution of SF_6^- for $T = 1000$ K (blue curve) and $T = 2000$ K (red curve) is shown with their time dependence due to the VAD process after 1 ms and after 50 ms according to Eq. (2.26).

as discussed in Sec. 2.3 this is a reasonable assumption for $E >$ EA (but see also Sec. 2.5). Moreover, the approximation leading to the right hand side of Eq. (2.26) is expected to be well fulfilled for observation times $t \gg 0.1$ ms since all states subject to auto-dissociation are already decayed and these ions are lost from the trap.
For the initial energy distribution $f_0(E,T)$, a (thermionic) canonical energy distribution is assumed, which in this case can be characterized by a single parameter, the canonical temperature T. More precisely, the canonical energy distribution refers to the temperature of the excited $(SF_6^-)^*$ ions and $f_0(E,T)$ is determined by the multiplicity of states $\rho^-(E)$ at each energy and the Boltzmann factor:

$$f_0(E,T) = \frac{1}{Q(T)}\,\rho^-(E)\,e^{-E/k_BT}, \tag{2.27}$$

$$Q(T) = \int_0^\infty \rho^-(E)\,e^{-E/k_BT}\,dE, \tag{2.28}$$

where $Q(T)$ is the canonical partition function to ensure the normalization of $f_0(E,T)$. Typical temperatures are in the order of 1000 K and more, to lead to high enough excitation to observe the VAD process. Figure 2.9 shows the initial energy distribution of SF_6^- for temperatures 1000 K and 2000 K, respectively, and their time dependence according to Eq. (2.26).
The neutralization rate resulting from Eq. (2.25) was calculated for various internal temperatures as shown in Fig. 2.10. The typical measurement for SF_6^- covers times

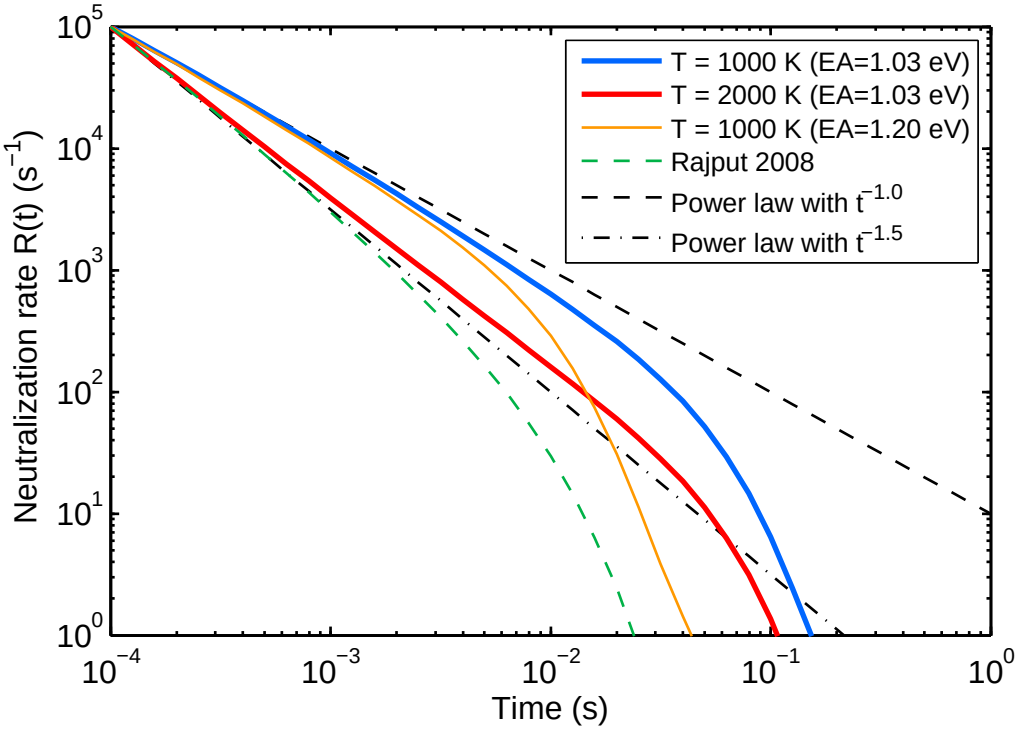

Figure 2.10: Neutralization rate for different initial temperatures of SF_6^-. For comparison, the neutralization rate calculated by Rajput *et al.* [25] is shown by the green dashed line; they used a Gaussian energy distribution with a center at 1.20+0.35 eV and a width of 0.17 eV.

from ∼300 μs to in principle minutes; however, the VAD decay is found both in these calculations (see Fig. 2.10) and in the experiment (see chapter 4) to vanish naturally after ∼100 ms. Even though a larger amount of the stored ion population decays already before the measurement starts, the initial temperature turns out to have significant influence on the neutralization rate, as can be seen in Fig. 2.10. In this double logarithmic plot, the neutralization rate as a function of the time will follow a straight line, if it is exhibiting a power-function dependence, i.e. if $R(t) \propto t^n$. As can be seen in Fig. 2.10, this is approximately fulfilled at early times, where n varies with T. At later times deviations from a power law are observed and the curve falls off more steeply.

A characteristic power law decay with n close to –1 has been observed in various experiments [9, 10, 73, 74] and is known as evaporation from small particles [70]. Here, the applied concept of thermionic emission for large cluster compounds was found to lead to reasonable good description of the decay.

This is seen as follows. Considering Eq. (2.25) and neglecting the energy dependence of $f_0(E,T)$ over the energy region where VAD is taking place, one finds

$$R(t) \propto f_0\, t^{-1} \int k(E)\, t\, e^{-k(E)t}\, dE, \tag{2.29}$$

pulling out t^{-1} from below the integral. The expression $k(E)te^{-k(E)t}$ exhibits only strong contribution to the integral for energies and times corresponding to $1/k \sim t$,

and the integral can be rewritten as integration over kt with the help of $d\ln(k)/dE = k'/k$, as illustrated for instance in Ref. [9]. This leads to

$$R(t) \propto t^{-1} \int (k/k')\, e^{-kt}\, d(kt) \propto t^{-1}, \tag{2.30}$$

where in the last step, it was assumed that (k/k') is constant. This is approximately fulfilled for large systems, where the detachment rate $k(E)$ can be described by Eq. (2.21). Expressing ρ^-/ρ^0 by using e.g. Eq. (A.18) or by an Arrhenius law ($\propto exp(-E_0/k_BT)$), in both cases the derivative k' and k are very similar functions and k/k' are only weakly energy dependent.
For SF_6^-, this approach is rather poor as the internal energy distribution $f_0(E,T)$ significantly changes the slope of the neutralization rate (see Fig. 2.10). The dashed and dash-dotted straight lines correspond to power-laws with t^{-1} and $t^{-1.5}$, and the SF_6^- neutralization rates are found in between. The deviation from the power law for later times sets in when the corresponding VAD rate reaches the detachment threshold EA (compare Fig. 2.7).
Figure 2.7 also shows that for the neutralization rate using the previous value for the detachment threshold EA = 1.20 eV (orange curve), a much earlier fall-off is observed. Finally, also the thermionic emission model from Rajput *et al.* [25] is indicated in Fig. 2.7, where a different excitation process for $(SF_6^-)^*$ was assumed (as for this measurement a cold cathode plasma ion source was used). Electrons are assumed to be captured by SF_6 gas molecules at room temperature (∼300 K) and thus, the corresponding energy distribution is assumed to be shifted by the binding energy EA. Furthermore, this energy distribution was approximated by a Gaussian distribution located at an energy $E = 1.20 + 0.35$ eV and a width of 0.17 eV, which was found to give a good agreement with the data from Ref. [25]. One should note that in this approach all ions would decay via the VAD process and no ions should be left after the stagnation of the decay, which in fact contradicts the observation in Ref. [25]. This will be considered in more detail in chapter 4.

2.4.2 Dependencies of the neutralization rate $R(t)$

The neutralization rate $R(t)$ is the key experimental observable during the initial storage of the SF_6^- ions (see chapter 4). Therefore, its dependencies on some input parameters and approximations will be discussed here.

Electron affinity

Recalling the determination steps for the VAD rate $k(E)$, for the cumulative reaction probability $W_{det}(E-EA)$ experimentally adapted capture probabilities $P(\epsilon)$ and the density of states of SF_6, ρ^0, at $E - EA - \epsilon$ were used. Furthermore, in combination with the density of states of SF_6^-, $\rho^-(E)$, the VAD rate $k(E)$ is derived with Eq. (2.8). To obtain all mentioned quantities, a precise knowledge on the value of the electron affinity is not required, as EA only enters as a shift of the energy scale into $W_{det}(E-EA)$. However, as this quantity is divided by the steeply rising density of states, the energy shift by EA plays a crucial role for the amplitude of $k(E)$. The first maximum in Fig. 2.6 for W_{det} corresponds to transitions without excitation in SF_6 and has a

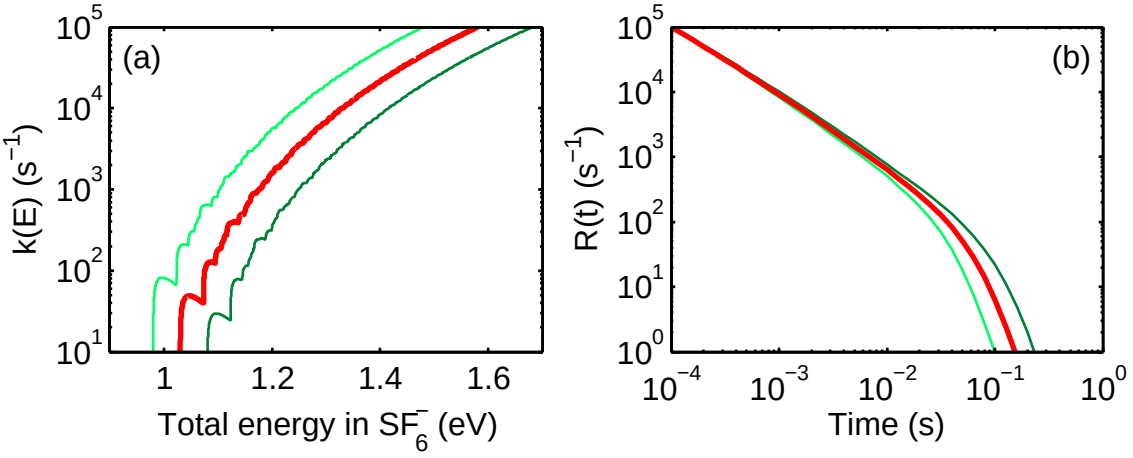

Figure 2.11: (a) VAD rates coefficients and (b) neutralization rates for $(SF_6^-)^*$ with EA = 1.03 eV (red), EA = 0.98 eV (light green), EA = 1.08 eV (dark green) using an initial vibrational temperature of 1000 K.

value of ∼0.6, the corresponding density of states closely above the threshold of 1.03 eV can be seen in Fig. A.2 and lead to $h\rho^- \sim 4 \cdot 10^{-15} \cdot 3 \cdot 10^{12}\, s^{-1}$. Combined, an amplitude of $k \sim 50\, s^{-1}$ is derived which corresponds to the first maximum of the red curve in Fig. 2.11.
Small variations in the electron affinity of only 0.05 eV, which is the given uncertainty of the latest value of EA, changes this maximum of the amplitude of $k(E)$ to around ∼85 s^{-1} and ∼30 s^{-1}, respectively. This is also shown in Fig. 2.11(a) for EA = 0.98 eV (light green) and 1.08 eV (dark green) and the corresponding neutralization rate (for an initial temperature of 1000 K) in Fig. 2.11(b). The stagnation time of the decay is clearly defined by the value of EA, whereas the slope for early times stays constant. Thus, a determination of the electron affinity with the help of the stagnation time seems to be possible, however, other effects influence this end point time as well.
The location of the fall-off in the neutralization rate is determined by the amplitude of the VAD rate close to the threshold, and only indirectly via the height of the first maximum of $k(E)$ on the threshold energy EA.

Rotational excitation

Rotational excitation has been included only in the most recent calculations [19] of the VAD-rate. We consider its inclusion here, as it can also have an influence on the observed neutralization times. The integration of rotational energy into the formalism of RRKM theory is described in Appendix B.2, and the reaction rate $k(E, J)$ as a function of the total rovibrational energy E and the angular momentum number J is derived in Eq. (B.35). Here, the rotational energy $E_R(J)$ has to be subtracted from the total energy E to derive the vibrational energy $E_V = E - E_R(J)$.

In the present work, the formalism of spherical top molecules is used for both SF_6 and SF_6^- to determine $E_R(J)$, since even in the asymmetric C_{4v} form of SF_6^- the rotational constants for different axis are very similar to each other (compare ta-

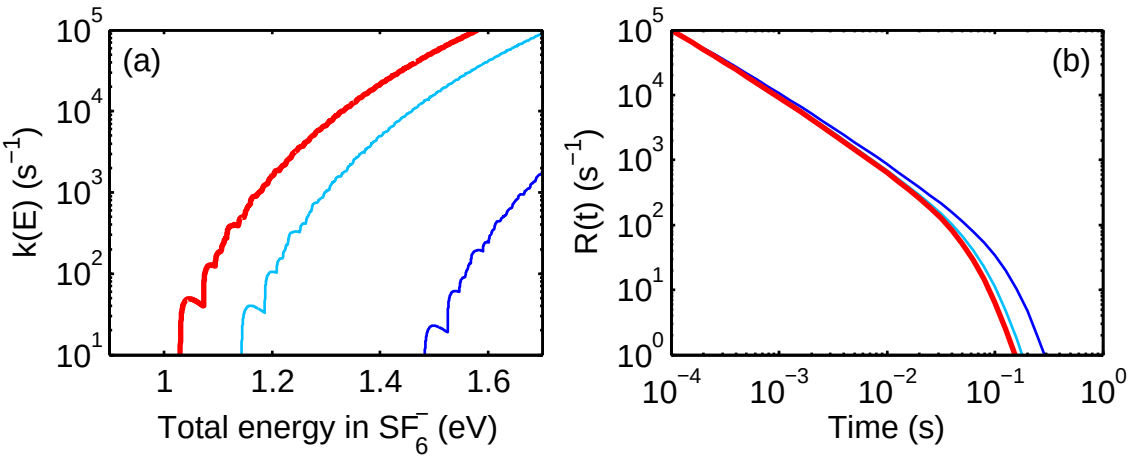

Figure 2.12: (a) VAD rates coefficients and (b) neutralization rates for $(SF_6^-)^*$ with EA = 1.03 eV and $J = 0$ (red), $J = 100$ (light blue) and $J = 200$ (dark blue) using an initial vibrational temperature of 1000 K.

ble 2.1). Moreover, the angular momentum J is assumed to be conserved in the detachment reaction, which was already implicitly applied when considering only the s-wave electron capture cross section in calculating $P(\epsilon)$. Only minor changes in the angular momentum can be induced by the electron, due to the small electron mass, the short range polarization potential, and the enhanced s-wave capture probability for low electron velocities.
On the other hand, the equilibrium distances of the S-F bond for SF_6 and SF_6^- show strong differences resulting in rotational constants differing by about a factor of 5/6. Thus, for a given J the rotational energies are different, which results in $\Delta E_R(J) = E_R^0(J) - E_R^-(J) \geq 0$ in the present case.
The energy balance is then given by

$$E \;=\; E_V^- + E_R^-(J) \;=\; \mathrm{EA} + E_V^0 + E_R^0(J) + \epsilon(e^-), \tag{2.31}$$

which is also illustrated in Fig. 2.13. An effective J-dependent electron affinity might be defined by $\mathrm{EA}(J) = \mathrm{EA} + \Delta E_R(J)$, below which no reaction can take place.
Thus, the effective electron affinity leads to a similar influence on the VAD amplitude as a change of EA, however, the energy shift in Fig. 2.12(a) is found to be larger as here the excitation energy of SF_6^- including the total internal rovibrational energy is plotted.
In analogy to Eq. (2.25), the neutralization rate for a constant J is given by

$$r(t, T_V, J) = N_0 \int_{\mathrm{EA}(J)}^{\infty} f_0(E - E_R^-(J), T_V)\; k(E, J) e^{-k(E,J)t}\; dE. \tag{2.32}$$

To describe the probability of anions to be produced in the ion source with a given rotational angular momentum J, we use a canonical rotational distribution charac-

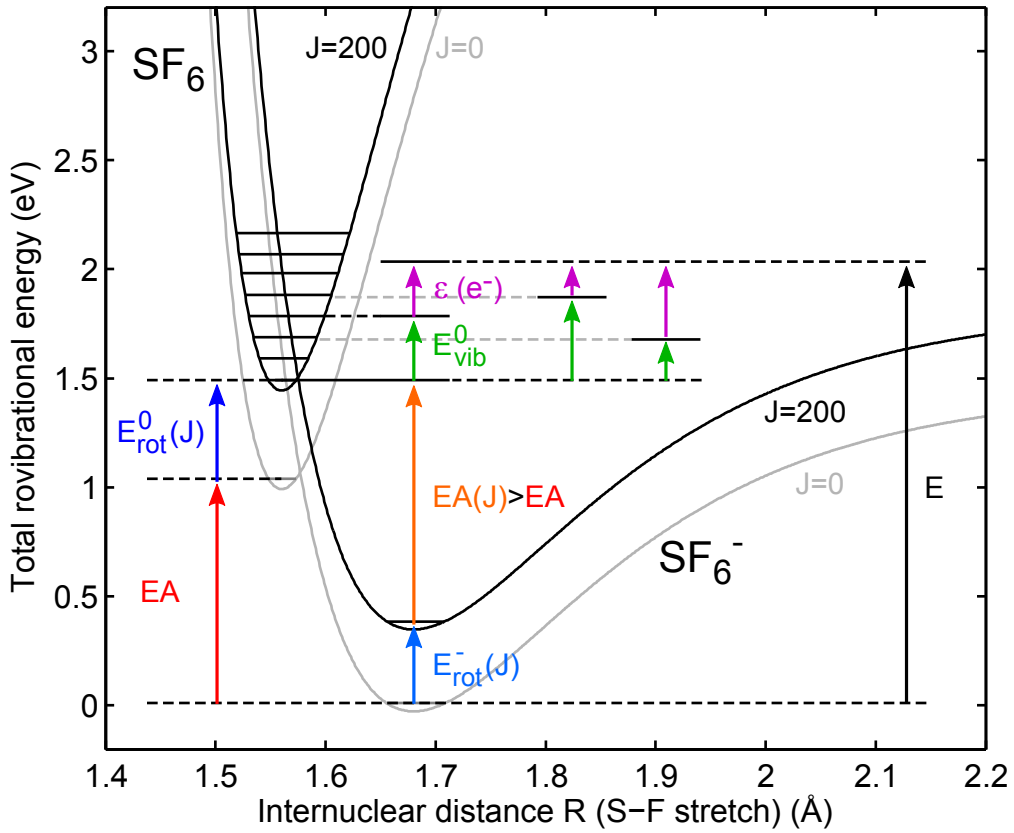

Figure 2.13: Schematic view on the potential energy curve for SF_6 and SF_6^- to illustrate the influence from rotational excitation on the effective electron affinity EA(J): Curves with rotational excitation (black) are shifted by the rotational energies $E_R^0(J)$ and $E_R^-(J)$, respectively, for $J = 200$. Note that the shift for SF_6^- is smaller than for SF_6.

terized by a rotational temperature T_R, i.e.

$$h_0(J, T_R) = \frac{1}{Q_R(T_R)} \, (2J+1)^2 \, e^{\frac{-\langle B^- \rangle J(J+1)}{k_B T_R}}, \tag{2.33}$$

$$Q_R(T_R) = \sum_{J=0}^{\infty} (2J+1)^2 \, e^{\frac{-\langle B^- \rangle J(J+1)}{k_B T_R}}, \tag{2.34}$$

where $\langle B^- \rangle$ denotes the average rotational constant of the asymmetric SF_6^- and $(2J+1)^2$ is the degeneracy for a molecule with spherical top structure (see Appendix A.1.4). Analog to the vibrational distribution, the rotational partition sum $Q_R(T_R)$ accounts for the normalization of $h_0(J, T_R)$, which is then used to derive the neutralization rate with independent vibrational and rotational temperatures:

$$R(t, T_V, T_R) = \sum_{J=0}^{\infty} h_0(J, T_R) \, r(t, T_V, J). \tag{2.35}$$

The maximum of the rotational energy distribution $h_0(J, T_R)$ is given by $J_{max} =$

$\sqrt{k_B T_R/\langle B^- \rangle} - 1/2$ and gives $J_{max} = 96$ for 1000 K and $J_{max} = 135$ for 2000 K, respectively. The average rotational constant $\langle B^- \rangle = 0.075325 cm^{-1}$ of SF_6^- was derived with the values from table 2.1.
Figure 2.12(b) illustrates the influence of rotational excitation on the neutralization rate for a rotational angular momentum of $J = 100$ and $J = 200$, respectively. Similarly to the increase of EA, the fall-off of the neutralization rate is shifted to longer times, when rotational excitation is included.

Radiative cooling

As discussed in Sec. 2.3, radiative cooling has to be taken into account in the neutralization rate $R(t)$ only at times $t \gtrsim 1/k_{rad} \sim 20$ ms, that is when states close to the threshold energy EA start to dominate the $R(t)$ signal ($E - \mathrm{EA} \lesssim 50$ meV, see figures 2.7 and 2.8). Radiative cooling does not lead to a loss of ions from the trap, but only to a loss of internal energy and thus to a redistribution of $f_t(E, T)$. This will be discussed in more detail in the next section. However, the effect on the neutralization rate $R(t)$ from thermally excited $(SF_6^-)^*$ can be taken into account by observing that the most likely energy taken away by the IR-photon is ∼83 meV (Sec. 2.2.3). Thus, the ion undergoing a radiative cooling step will acquire an energy $E < \mathrm{EA}$, and can no longer decay by emitting an electron; the ion is not lost from the trap, but from the ensemble which can contribute to the VAD process. Thus, the radiative cooling effect on $R(t)$ can be approximated within reasonable accuracy by replacing $e^{-K(E)t}$ in Eq. (2.25) by $e^{-(k(E)+k_{rad})t}$.
Radiative cooling constants are derived in Sec. 2.5.1 below. Figure 2.14 illustrates the influence of the radiative cooling constants k_{rad} on the neutralization rate, assuming values of 20 s^{-1} and 50 s^{-1}, respectively. In contrast to the influence from rotational excitation by the angular momentum J, radiative cooling leads to a faster drop in $R(t)$ as k_{rad} increases.

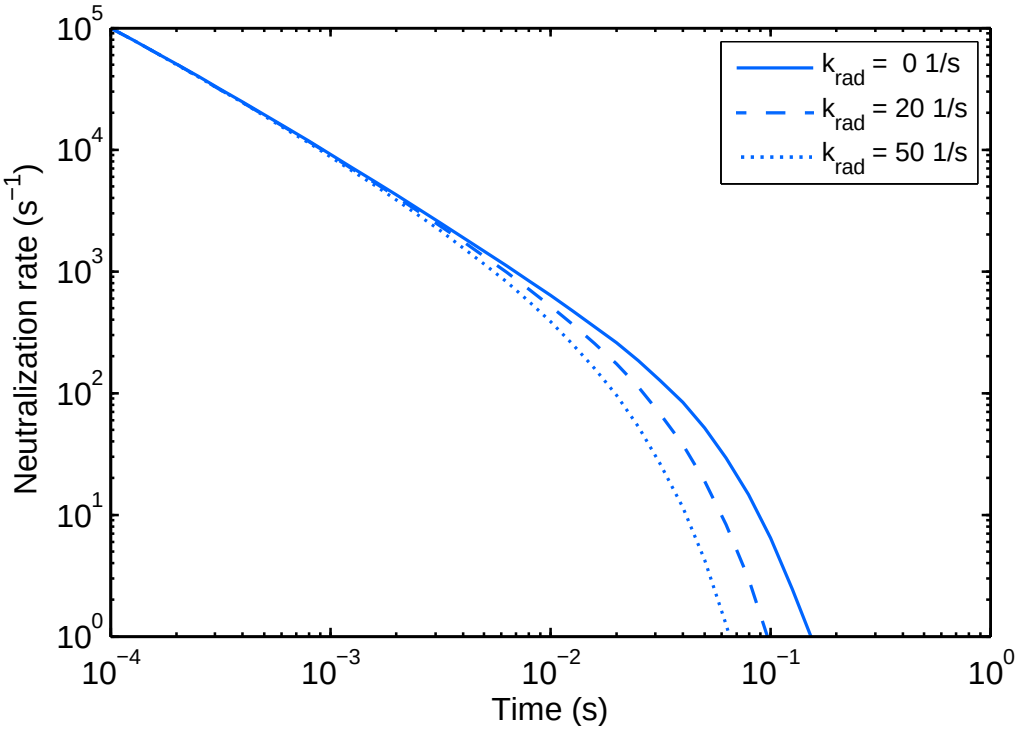

Figure 2.14: The neutralization rate for an initial temperature of 1000 K is shown accounting for radiative cooling by an exponential decay with decay constant k_{rad} (see text for details).

2.5 The SF_6^- energy distribution during long-time storage

This section describes neutralization models for laser excited SF_6^- in an electrostatic ion beam trap. The mayor difference to the previous model is the increase of the internal energy of the trapped SF_6^- by a laser pulse, which is then observed as an enhanced neutral count rate on the detector. Although the laser energy is well defined, the distribution of the excitation energy of the SF_6^- at the time of the laser shot is unknown as described below.
A second important difference is the sensitivity in these studies to much earlier times scales of the neutralization process. For the VAD from thermal excited $(SF_6^-)^*$ from the ion source, observation times later then a few hundred microseconds are accessible, whereas shorter times are concealed by the ion injection or by other ion loss processes at early storage times. In contrast, after laser excitation of the stored ions, no early time constrains are present for the observation of the neutralization rate. However, an uncertainty of half a trap oscillation in the ion decay time is existing as the neutrals after the decay propagate on with unchanged velocity and impinge simultaneously on the detector. Nevertheless, short timescales of up to 5 μs are accessible and thus, the process of dissociation of SF_6^- might be a competing process at these early times.
A representation of the dissociation rate $k_{diss}(E)$ was given in Ref. [20], but for a dissociation energy E_D of 1.61 eV, which is defined by the energy difference of 0.41 eV to the electron affinity EA of 1.20 eV. For the recent EA of 1.03 eV and hence a dissociation energy E_D of 1.44 eV, the auto-dissociation rate $k_{diss}(E)$ was here approximated in Eq. (2.23) and compared to the VAD rate in Fig. 2.8, where the transition between both is found at a rate corresponding to around 10 μs. Thus, for short times after the laser excitation both processes might have to be taken into account, but it should also be pointed out that the dissociation rate is not known such precisely and also its rotational dependence is neglected here.
The inclusion of dissociation is obtained by a sum of the decay rates of both processes. However, the neutral fluorine fragment propagates on with a significantly lower energy of 870 eV. The detection efficiency of the fluorine is found to be approximately a factor of 5 lower for energies below 1 keV compared to 6 keV [75, 76] and can be included in the derivation of the neutralization rate. Even if the fluorine is not detected, a faster decrease of the neutralization rate will be observed due to the additional depletion of the internal energy population by auto-dissociation.

2.5.1 Radiative cooling

Another difference to the previous thermally excited $(SF_6^-)^*$ neutralization is that the internal energy distribution of the ions is determined after a certain storage (relaxation) time, as here the ion excitation energies are shifted above the EA by the absorbed photon energy. The initial thermal distribution above the EA decreases due to the VAD process and ions with energies below EA are considered as stable with respect to VAD (and also dissociation). However, the internal energy of the latter ions further decreases due to radiative cooling and a stable distribution is

obtained after a certain cooling time.
The radiative cooling proceeds via the emission of radiation from IR-active vibrational modes, which are defined by a changing dipole moment during the nuclear vibrational movement. For the neutral SF_6, two degenerate sets of IR-active vibrational frequencies are found, denoted by ν_3 and ν_4 in table 2.1, where the first one is known to have the highest IR absorption potential, which for instance makes SF_6 to a considerable greenhouse gas in the atmosphere.
The radiative emission rate for a specific vibrational mode ν_{if} is given by the Einstein coefficient for spontaneous emission A_{if} (see also Eq. (A.12)), and reads as

$$A_{if}(s^{-1}) = 3.14 \times 10^{-7} \, |\boldsymbol{\mu}_{if}|^2(D) \, \nu_{if}^3(cm^{-1}), \tag{2.36}$$

where $|\boldsymbol{\mu}_{if}|$ is the dipole matrix element. Using measured integrated infrared intensities for mode ν_3 in SF_6 from Ref. [46], a value for the dipole matrix element of $\sim$0.438 D is determined. Using the frequency of 966 cm^{-1} of ν_3, an emission rate of $\sim$54 s^{-1} is obtained. The second IR-active mode ν_4 exhibits an orders of magnitude lower dipole matrix element and also has a lower vibrational frequency.
For SF_6^-, the integrated infrared intensities have not been measured, but the vibrational frequency of 671.1 cm^{-1} corresponding to the same fundamental vibrational mode as ν_3 in SF_6, and was recently also found in photo-electron spectroscopy [5]. The frequency is lower as for the neutral, but the dipole matrix element can be expected to be higher as an additional charge is present and the bond distances are larger in SF_6^-. Thus, a comparable radiative emission rate to SF_6 might be obtained (as also pointed out in Ref. [61]).
A calculation of the integrated infrared intensity of this mode was performed by Lugez *et al.* [77] assuming a vibrational frequency of 640 cm^{-1} and an O_h symmetry of SF_6^-. Thus, with the dipole matrix element of $\sim$0.611 D, a value of $A_{10} = 31$ s^{-1} is obtained for the Einstein coefficient for spontaneous emission. In the recent calculation by Eisfeld, frequencies of 671.1 cm^{-1} (doubly degenerate) and 757.7 cm^{-1} are found for this vibrational mode (see table 2.1). Thus, the degeneracy of the T_{1u} mode is partly lifted. Here, we consider it plausible that both frequencies have very similar transition properties. Hence, an average value of 700 cm^{-1} for the IR-active mode will be used and the Einstein coefficient is scaled from Lugez' result according to the frequency dependence from Eq. (A.12): $A_{10}^{(3)} = 31 \text{ s}^{-1} \times (700/640)^3 = 40 \text{ s}^{-1}$. As expected, the value is smaller than the one for SF_6 due to the lower frequency, but however not by as much as a factor of 3 as expected from the frequency dependence of Eq. (A.12).
However, radiative cooling in a complex molecule depends not only on the radiative emission rate of each mode, but also on the population of this mode. Intramolecular vibrational redistribution (IVR) leads to a chaotic distribution of the energy E over the different fundamental vibrational modes, a process assumed to be much faster than the radiative cooling or VAD. Hence, at each energy there are always configurations possible, where a specific mode is populated. All vibrational configurations at an energy E can be assumed to be stochastically passed through, where the total number of configurations is given by the density of states $\rho(E)$. In contrast, the number of configurations, where one specific vibrational mode, e.g. an IR-active one, is at least once occupied, is the density of states at an energy reduced by the

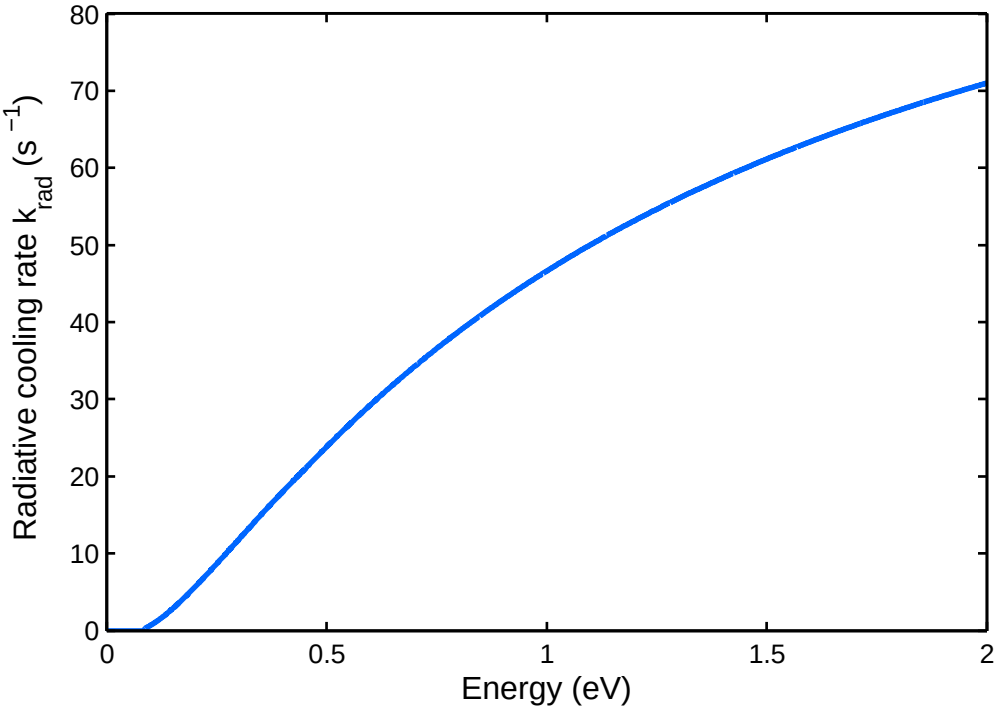

Figure 2.15: Estimated radiative cooling rate $k_{rad}(E)$ for SF_6^- according to Eq. (2.38) using an averaged, three times degenerated vibrational frequency ν_3 of 700 cm^{-1} (see table 2.1 for SF_6^- in C_{4v} symmetry).

vibrational energy of this mode: $\rho(E-h\nu_i)$. The probability, that this specific mode ν_i is stochastically populated, is the ratio between the two density of states.
The radiative cooling rate $k_{rad}(E)$ is for this reason given as a sum over all n vibrational frequencies ν_i as

$$k_{rad}(E) = \sum_{i=1}^{n} g_i \, A_{10}^{(i)} \, \frac{\rho(E - h\nu_i)}{\rho(E)}, \tag{2.37}$$

where g_i is the degeneracy of each fundamental vibrational mode and A_{10}^{i} its Einstein coefficient for spontaneous emission.
In the specific case of SF_6^-, an averaged value of 700 cm^{-1} was approximated for the doubly degenerate mode at 671.1 cm^{-1} and the single mode at 757.7 cm^{-1}, which correspond to the strongest IR-active vibrational mode ν_3 in the O_h symmetry (compare table 2.1). Using a value of $A_{10}^{(3)} = 40$ s^{-1} for this mode and neglecting the other modes, Eq. (2.37) simplifies to

$$k_{rad}(E) = g_3 \, A_{10}^{(3)} \, \frac{\rho(E - h\nu_3)}{\rho(E)}, \tag{2.38}$$

where $g_3 = 3$.
In figure 2.15 the resulting radiative cooling rate $k_{rad}(E)$ is displayed using Eq. (2.38) with the frequency $\nu_3 = 700$ cm^{-1} ($\sim$87 meV). Thus, for energies around the threshold EA, where the radiative cooling process becomes a competing process to VAD,

the cooling rate exhibits a value of about 45 s^{-1}. This value can be expected to be relevant for the long-time-dependence of the initial VAD-decay in the previous section and is also compared to the VAD-rate and dissociation rate in Fig. 2.8.

2.5.2 Cooling of the internal energy distribution

We will also consider the derived radiative cooling rate of the SF_6^- ions for the further cooling process, when the initial auto-detachment decay is over. The SF_6^- internal energies then lie below EA∼1 eV. At these lower energies the probability that the infrared-active mode is occupied decreases and tends towards zero (see Fig. 2.15), when the energy of 87 meV of the vibrational mode is reached and no further cooling is possible according to this model. However, for these low energies the previous assumption of IVR might not be valid and the remaining energy can also be stored in non-IR-active modes without a coupling to IR-active ones.
To further elaborate the radiative cooling process of ions stored in the CTF-trap, the time dependence of the energy distribution has to be derived. Ions performing radiative emission are not lost from the stored ion ensemble, but rather found at lower energies in the distribution. When radiative cooling is involved, the time dependence of the energy distribution $f_t(E)$ can be described in general by the following differential equation:

$$\frac{df_t(E)}{dt} = -\sum_{i=1}^{n} k_{rad}^i(E) f_t(E) \; + \; \sum_{i=1}^{n} k_{rad}^i(E + h\nu_i) f_t(E + h\nu_i), \tag{2.39}$$

where the summation goes over the total number of vibrational modes n. The first term represents the depletion of the occurrence of ions with energy E in the distribution and the second term accounts for the re-population from higher states. Vibrational transitions involving $\Delta v = 2$ or higher are not considered here.
The absorption of radiation in Eq. (2.39) from the surroundings was neglected as the reported measurements were performed at cryogenic trap operation at about 12 K. For comparison, the absorption rate can be obtained by $k_{abs} = B_{01}\rho(\nu) = A_{10}[\exp(h\nu/k_B T) - 1]^{-1}$, where B_{01} is the Einstein coefficient for absorption, $\rho(\nu)$ is the spectral energy density and T is the ambient temperature. Using $A_{10}^{(3)} = 40$ s^{-1} and the vibrational frequency of 700 cm^{-1} of the averaged IR-active mode in SF_6^-, a rate of $k_{abs} \sim 1.5$ s^{-1} for 300 K and $k_{abs} \sim 10^{-35}$ s^{-1} for 12 K is obtained, respectively. Thus, under cryogenic conditions photon absorption can be neglected compared to the radiative emission rate.
When only one mode ν contributes to the cooling, the previous equation simplifies to

$$\frac{df_t(E)}{dt} = -k_{rad}(E) f_t(E) \; + \; k_{rad}(E + h\nu) f_t(E + h\nu), \tag{2.40}$$

which we will use for the ion storage times $t > 10$ ms to obtain the long-time cooling behavior. For times $t \leq 10$ ms, the time development was approximated by

$$\frac{df_t(E)}{dt} = -K(E) f_t(E), \tag{2.41}$$

with $K(E) = k(E) + k_{diss}(E)$. This assumed simplification can be justified by considering the amplitudes of the different rates, which were compared in Fig. 2.8.

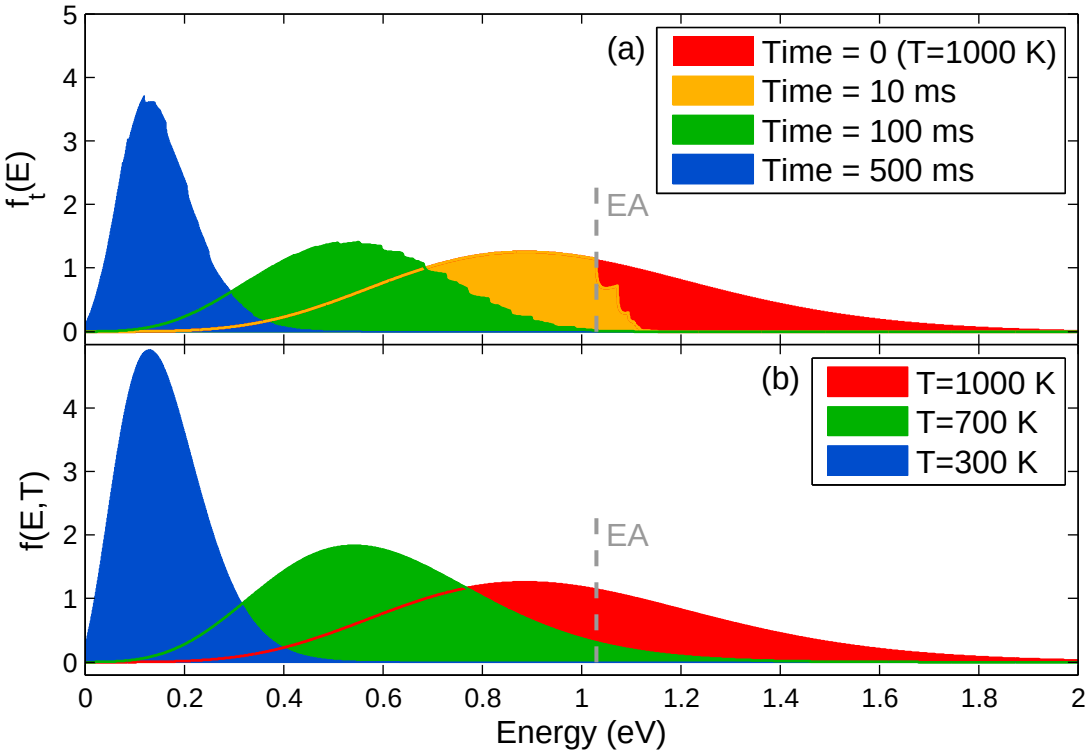

Figure 2.16: (a) Time-dependent vibrational energy distributions obtained with the cooling model according to Eq. (2.40) and Eq. (2.41) for cooling times 0, 10 ms, 100 ms and 500 ms with an initial energy distribution at 1000 K and EA = 1.03 eV. (b) Vibrational energy distributions for different temperatures of 1000 K, 700 K and 300 K according to Eq. (2.27). Cooling times and remaining temperatures can thus be related to each other. Initial energy curves are normalized to the total energy integral; curves for times $t > 0$ in (a) are lower due to the ion loss from the VAD-decay in the first 10 ms.

For the present case of SF_6^-, we have solved the system of coupled differential equations numerically with an initial energy distribution $f_t(E)$ following Eq. (2.27) and Eq. (2.28) and the radiative cooling rate $k_{rad}(E)$ from Eq. (2.38). The result assuming an initial ion temperature of 1000 K is illustrated in Fig. 2.16(a) for cooling times of 0, 10 ms, 100 ms and 500 ms according to the time periods from Eq. (2.40) and Eq. (2.41). For comparison, in Fig. 2.16(b) internal energy distributions are shown in the case that the distribution can be described by a temperature T. It is obvious that for cooling times $\gtrsim$100 ms the resulting distribution from radiative cooling can be well approximated by a thermal distribution of a given temperature. This remarkable result shows that the cooling times can be directly related to a remaining temperature in the investigated molecular system.
Whether this distribution is really obtained after the given cooling time depends on the validity of the IVR assumption for lower energies, and here also the density of states might not be represented by a smooth curve. These cooling distributions, either represented by a temperature or in the cascade radiative cooling model, are

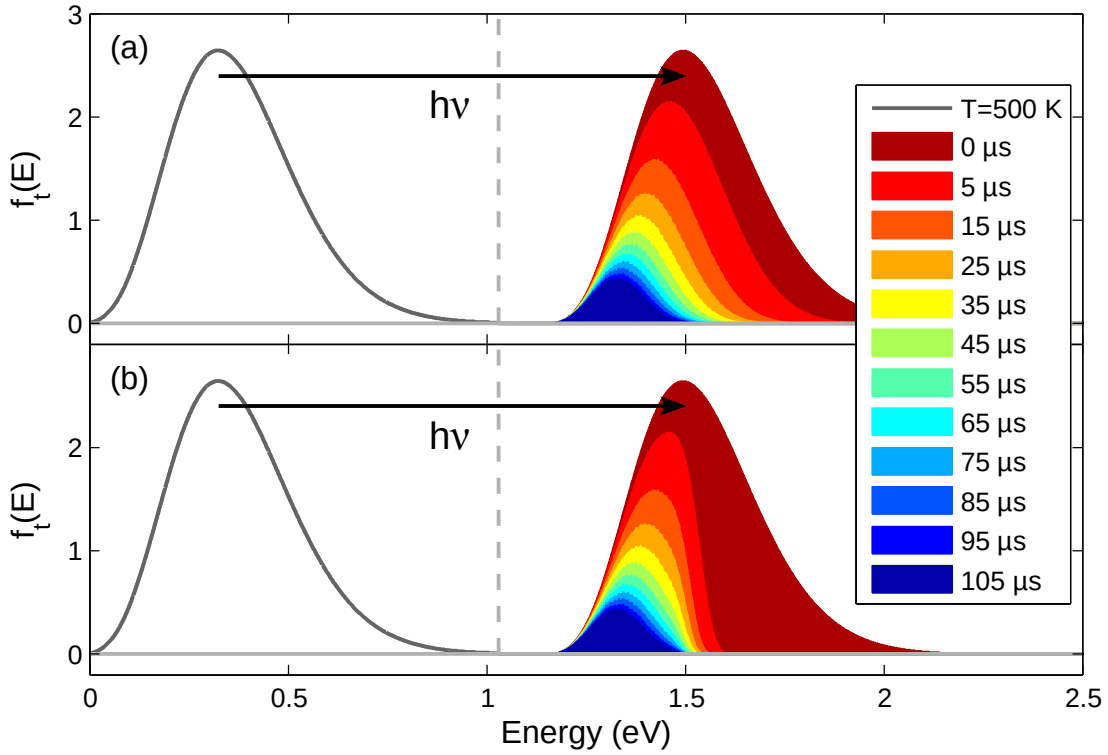

Figure 2.17: Time-development of the internal energy distribution of SF_6^- ions after laser excitation by $h\nu = 1.165$ eV photons. Before the laser shot the internal energy distribution is assumed to be a thermal distribution for $T = 500$ K (black curves). The time dependence is calculated (a) assuming $k_{diss} = 0$ and (b) including $k_{diss}(E)$. The shifted distribution by the photon energy exhibits an enhanced depletion at its high energy part when dissociation is involved. However, for times $\gtrsim$50 μs the remaining distributions show similar shapes.

applied in the photo-excitation process described below.

2.5.3 Delayed detachment of SF_6^- after photo-excitation

In the photo-excitation process, the momentary energy distribution of the stored ions can be probed by the observation of the neutral yield from VAD or dissociation. The energy distribution of a small fraction of ions, which absorb a photon, is shifted by the photon energy towards higher energies. The experiment is performed with a pulsed laser exciting the ions at different times of the ion storage. The photon energy was chosen such that each photon absorption process leads to an ion decay excluding repeated excitation. Moreover, the photon absorption probability $P_{h\nu}$ for a photon energy $h\nu$ is assumed to be independent of the initial excitation energy as always a large amount of final states are available.

The neutralization rate due to VAD and auto-dissociation is defined by

$$R_{h\nu}(t,t_i) = N_0 \int_{EA}^{\infty} P_{h\nu}\; f_{t_i}(E-h\nu)\; k(E)\; e^{-[k(E)+k_{diss}(E)]t}\, dE, \tag{2.42}$$

where in this case only the detachment products (SF_6) are assumed to be detected. As previously the time t denotes the time after the excitation process, which is here the photon absorption. The time t_i is the total ion storage time before the i^{th} laser pulse, at which the time dependent energy distribution f_{t_i} has to be evaluated, but at the energy $E - h\nu$ before the photon absorption.
In the case that only the auto-dissociation products would be detected, which is the neutral fluorine, the neutralization rate is given by

$$R^{diss}_{h\nu}(t,t_i) = N_0 \int_{\mathrm{EA}}^{\infty} P_{h\nu}\; f_{t_i}(E-h\nu)\; k_{diss}(E)\; e^{-[k(E)+k_{diss}(E)]t}\, dE, \tag{2.43}$$

where $k_{diss}(E)$ is zero below the dissociation threshold E_D.
The combined total neutralization rate $R(t,t_i)$ can then be written as

$$R(t,t_i) = \epsilon\; R_{h\nu}(t,t_i) + \epsilon_{diss}\; R^{diss}_{h\nu}(t,t_i), \tag{2.44}$$

where ϵ and ϵ_{diss} are the detection efficiencies for the VAD and auto-dissociation products, respectively.
The time-development of the internal energy distribution after laser excitation is given by

$$f_t(E) = f_{t_i}(E-h\nu)\; e^{-[k(E)+k_{diss}(E)]t}, \tag{2.45}$$

and a comparison of the distribution between $k_{diss} = 0$ and for included $k_{diss}(E)$ is illustrated in Fig. 2.17, where the remaining energy distribution $f_t(E)$ at different times t after laser excitation is shown for an initial distribution $f_{t_i}(E)$ for 500 K at the time t_i of the laser shot. In the absence of the auto-dissociation channel in Fig. 2.17(a) the high energy part of the distribution maintains for longer times as in the case with included dissociation (b), which is due to the higher amplitude of the dissociation rate coefficients (compare Fig. 2.8).
Both models are compared to the measurements in chapter 4, where the neutralization rate for times $\lesssim$5 μs after the laser excitation is combined as the prompt neutral signal and for times later than 5 μs as the delayed neutralization. The prompt signal might also contain contributions from direct photo-detachment, however two-photon absorption processes of the stored SF_6^- can be neglected as will be evaluated in in chapter 4.

Chapter 3

Experimental setup and methods

In this chapter, the Cryogenic Trap for Fast ion beams (CTF) will be introduced, which was constructed at the Max-Planck Institute for Nuclear Physics in Heidelberg, Germany. At first, the principles of Electrostatic Ion Beam Traps (EIBT) will be highlighted, which involve the trap design, stable trapping conditions, and transversal and longitudinal ion trapping properties. Afterward, the CTF as a novel combination of this trap-type for cryogenic operation will be introduced, which includes the cryogenic design and cooling concepts. After a brief introduction of the ion injection beam line, essential auxiliary components and processes such as the ion production in the employed ion source, the particle detection system as well as the laser setup will be elaborated.

3.1 The electrostatic Cryogenic Trap for Fast ion beams (CTF)

The Cryogenic Trap for Fast ion beams (CTF) was constructed as a cryogenic test facility for the Cryogenic Storage Ring (CSR), which is currently being assembled at the Max-Planck Institute for Nuclear Physics in Heidelberg [78, 79]. The CTF consists of an Electrostatic Ion Beam Trap (EIBT) [6] placed in a cryostat, which is in the present study cooled by cold helium gas ($\sim$4 K) from a closed circuit refrigeration system. One of the major goals of the CTF was the verification of an extremely high vacuum (XHV) reaching down to residual gas densities of a few thousand particles per cm^3, which corresponds to a pressure of $<10^{-13}$ mbar for a room temperature environment ($\sim 10^{-15}$ mbar at 10 K). In addition, tests of the cooling and isolation concept have been successfully performed leading to temperatures of about 10 K on the trap vacuum system and below 2 K on the cooling units (using superfluid helium in the prior cooling concept), which are designated areas for cryo-condensation of hydrogen. A comparison between measurements on the residual gas related loss rates of trapped nitrogen cations N_2^+ under warm and cold conditions of the CTF could verify a vacuum of $(8 \pm 4) \times 10^{-14}$ mbar in the trapping area; further details are given in Ref. [8].

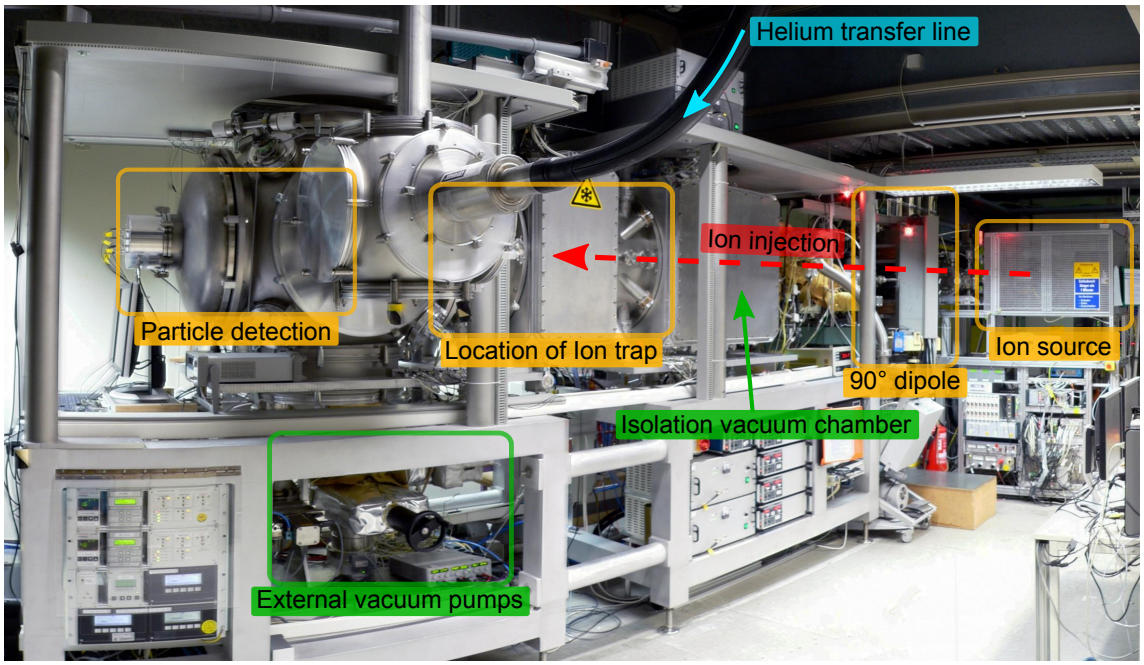

Figure 3.1: A photo of the CTF in the new laboratory

3.1.1 Ion trapping in Electrostatic Ion Beam Traps (EIBT)

In an Electrostatic Ion Beam Trap (EIBT), ions at kinetic energies of a few keV per charge state are confined only by electrostatic fields. According to Earnshaw's theorem [80], charged particles cannot be maintained in a stable stationary equilibrium with pure electrostatic fields; however, this is only valid for particles at rest. In an EIBT ions experience a time varying field due to their high speed and can be trapped for seconds or even minutes (limited by the vacuum conditions).
The trap is built like an optical resonator with two stacks of electrostatic mirror electrodes on opposing sides (see Fig. 3.3). To inject ions, the entrance mirror potential is grounded during the ion passage and quickly raised in hundreds of nanoseconds. As a typical time scale, tens of microseconds oscillation times occur in the trap for an ion beam of a few keV.
One advantage of this type of ion trap is the high ion speed. Neutralized fragments from ions produced by any process will immediately escape from the trapping area with a high kinetic energy and can be detected by Micro Channel Plates (MCP) or similar particle detectors. Thereby, the production rate of the reaction products is measured, as opposed to the depletion of the parent particles as sometimes applied for reaction studies in other trap types. In addition, the electrostatic design sets in principle no limit to the stored ion mass and any heavy ion which can be accelerated to an energy of a few keV can be trapped.

History of EIBT

This type of ion trap was developed by Zajfman *et al.* [6], from the example of similar setups referred to as multi pass time-of-fight mass spectrometer in earlier works [7]. Here, an ensemble of nearly mono-energetic ions is reflected between

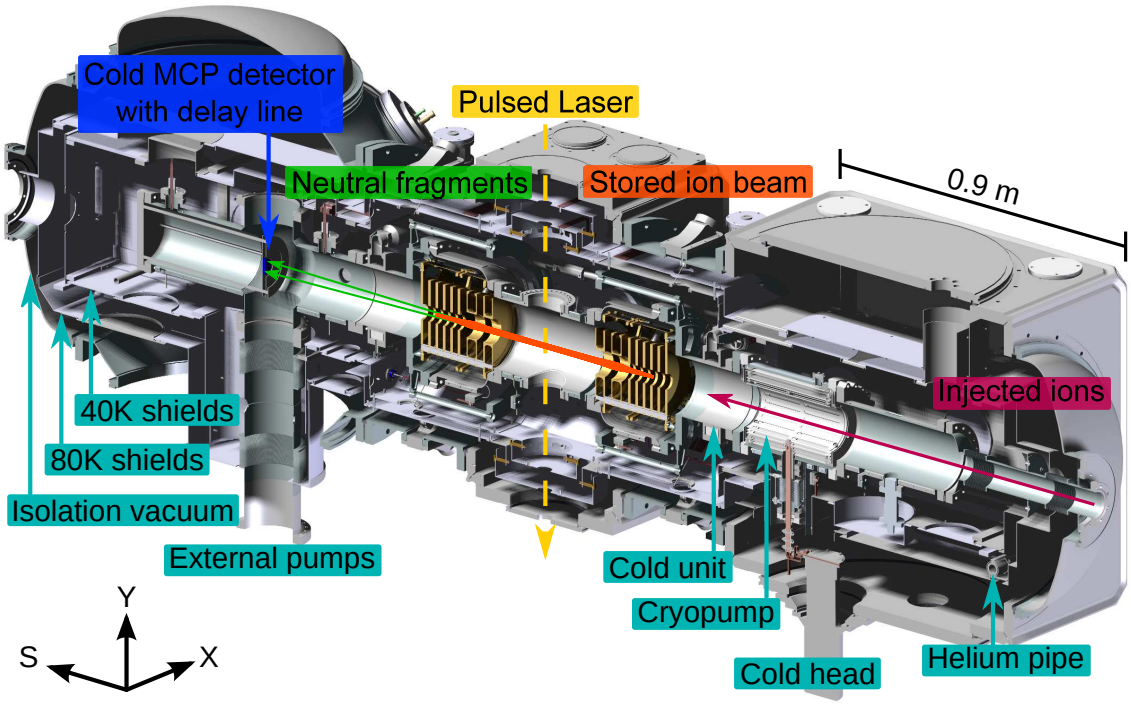

Figure 3.2: Longitudinal cross section of the CTF

a limited number of mirrors, which increases the ions' path length and separates them by the time of flight difference according to their mass to charge ratios. The development of fast high voltage switches enabled the usage of only two opposing mirrors trapping ions on a closed trajectory. Nowadays, the switching of voltages up to 20 kV in half a microsecond is not a limiting aspect.
Ion beam traps at the Weizmann Institute in Israel [6], were developed to investigate atomic, molecular and cluster ions in a table-top setup, keeping experimental features available as in larger magnetic ion storage rings. This idea also triggered the development of small electrostatic ion storage rings with diameters of about three meters [81–83]. The development of ion traps of this type was also motivated by the usage to characterize large ions from electrospray ionization sources [84], which proceeded in parallel to Ref. [6]. It should also be mentioned that trapping of ions in electrostatic fields can be traced back to the Kingdon ion trap in 1923 [85], where the ions perform a helical movement around a wire, which has a potential different to the co-axially surrounding cylinder.
A couple of these ion trap-types are in operation using femtosecond laser-induced dissociation in Belfast [86], for the preparation and accumulation of ions at a free electron laser in Hamburg [87] or as an isotope separator for high precision mass measurements [88], to mention a few of the manifold applications. The CTF extends the large potential to extremely high vacuum conditions to investigate ions with long lived states or very rare processes, as well as a nearly isolated area from black-body radiation [8].

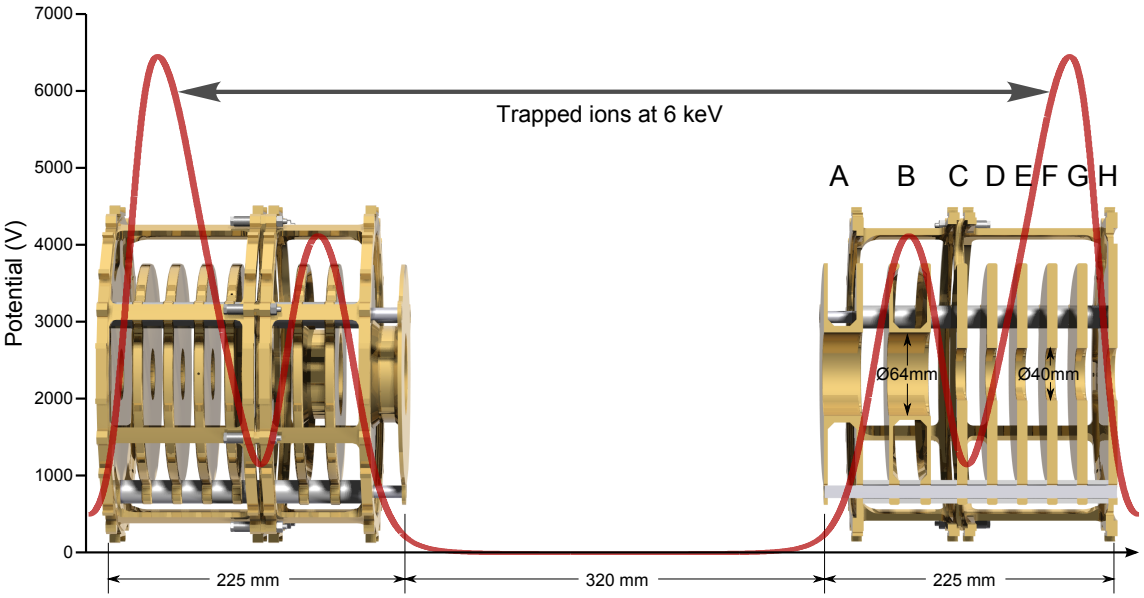

Figure 3.3: The two opposing CTF mirror electrodes including a overlaid simulated potential for a 6 keV ions beam.

Stability

Criteria for stable trapping in EIBT can be transferred [6] from optical resonators. The relation between focal length f and distance between the mirrors L is given by

$$0 \leq \left(1 - \frac{L}{2f}\right)^2 \leq 1 \quad \Leftrightarrow \quad \frac{L}{4} \leq f \leq \infty, \tag{3.1}$$

which can be easily fulfilled with the typical trap design.
An important part of each trap is the focusing lens, called einzel lens in ion optics, which is composed out of the three innermost electrodes of each mirror stack (compare Fig. 3.3). Only the central electrode (B) of these three is set to a high voltage, whereas the other two are grounded (A and C). Depending on the polarity of the electrode voltage with respect to the ion charge, the ions are first decelerated and then accelerated or vice versa, resulting in a combination of defocusing and focusing, which can be shown to lead to a net focusing effect.
The next four electrodes (D-G) create the reflection potential where the ion beam quickly slows down and nearly comes to rest, while expanding in transversal direction. This has to be compensated by the lensing electrode B to guide the ion beam into the opposing mirror and fulfill the stability criterion.

Trajectories and phase space

To further characterize the trapping conditions, it is useful to introduce the transversal phase space and for the longitudinal direction the slip factor η which will be explained below.
The phase space is usually defined as a six dimensional space between the position and the momentum components of a stored ion. The coordinate s describes the

axial or longitudinal direction; x and y are the transversal directions. As the trap is radially symmetric, only one of the transversal directions has to be considered. Instead of using the actual coordinates of each particle, the deviation to the synchronous particle is used, which is the particle being exactly on the design trajectory and with the kinetic energy E_0.
Also the transversal momentum p_x is replaced by the directional deviation x' which is related to the actual angle ϕ_x and to p_x by

$$\phi_x = \arctan\left(\frac{x}{s}\right) \approx \frac{dx}{ds} = x', \tag{3.2}$$

$$x' = \frac{dx}{ds} = \frac{dx/dt}{ds/dt} = \frac{p_x}{p_s} \approx \frac{p_x}{p}. \tag{3.3}$$

The approximation is valid as the angles are typically below one degree (≈ 17 mrad). The transversal phase space can be considered at any longitudinal position s, but usually the trap center is used. Figure 3.4 shows the transversal phase space in the trap center simulated with SIMION [89] for ions with a kinetic energy of 6 keV and the standard trap voltages ($U_B = 5536$ V, $U_D = 2140$ V, $U_E = 3995$ V, $U_F = 6400$ V, $U_G = 7817$ V).
In the transversal phase space at a fixed location in the trap, e.g. the trap center, ions are moving on ellipses, while an exchange between transversal position x and angle x' takes place, similar to the exchange of kinetic and potential energy. To obtain Fig. 3.4, the ion trajectory in the trap was simulated for ions with initially different transversal positions x in the trap center, but with $x' = 0$, and recording the coordinates after each oscillation. Outside of the plotted area no stable trajectories were observed and the maximum expansion of the phase space is given by $x_{max} \approx 4.6$ mm and $x'_{max} \approx 14$ mrad. The trap acceptance A [90] is defined by the area of the maximum transversal phase space (divided by π), and is for the specific case of an upstanding phase space ellipse (as in Fig. 3.4) given by

$$A = x_{max}\, x'_{max} \approx 64\,\text{mm mrad}, \tag{3.4}$$

and is a machine property. A phase space ellipse is called upstanding, if it is aligned to the coordinate axes, which is here the case due to the symmetry of the trap. In general the phase space ellipse is tilted during the ion propagation in the trap.
In contrast, the expansion of the ion beam, the emittance ϵ, is defined in a similar way, but usually a Gaussian profile in the x and x' direction of the beam is assumed [90]. Furthermore, the value of the 2σ-emittance is typically provided, which is given by

$$\epsilon_x^{2\sigma} = 4\,\sigma_x\,\sigma_{x'}, \tag{3.5}$$

and is the area of the phase space ellipse at a height of $\exp(-4/2)$ of the maximum of the two-dimensional Gaussian distribution ($\propto \exp\{-(x^2/2\sigma_x^2 + x'^2/2\sigma_{x'}^2)\}$). The emittance is defined by the ion source or can be limited by apertures in the ion injection beam line. The maximum amount of ions that can be trapped is obtained by comparing the ion beam emittance ϵ_x to the trap acceptance A.

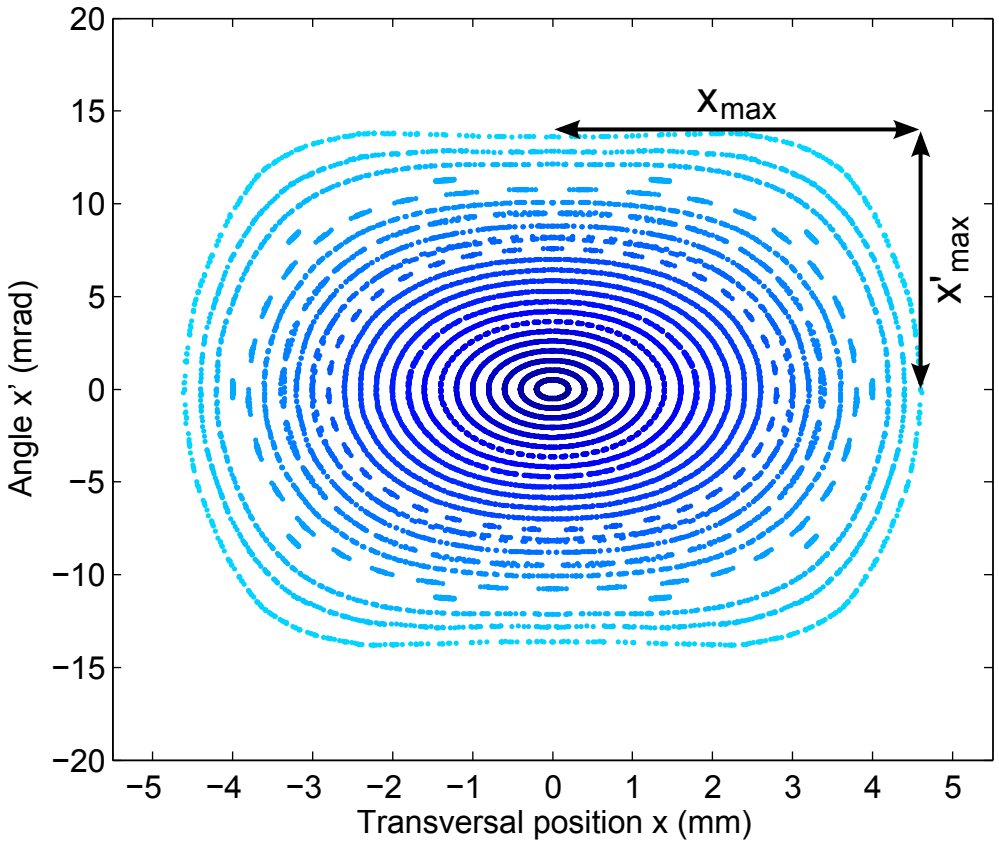

Figure 3.4: Simulated transversal phase space at the trap center of the CTF with 6 keV ions and trap electrode voltages of $U_B = 5536$ V, $U_D = 2140$ V, $U_E = 3995$ V, $U_F = 6400$ V, $U_G = 7817$ V.

Longitudinal beam dynamics

In the longitudinal beam direction, the trapped ion dynamics can be characterized by two cases: a completely filled trap with a constant ion density or a bunched beam, where the ion density varies strongly along the beam. A short, trapped ion bunch has the advantage of a localized charge and gives the opportunity to measure its position over time. The oscillation frequency of the ion bunch can be monitored by the periodically induced mirror charge on a pickup, which is a small ring electrode near the trap center (compare Fig. 3.10). Due to the relation $f \propto 1/\sqrt{m}$ for a constant ion energy, a precise measurement of the ion mass m is obtained from the frequency f. However, due to the uncertainties of the exact kinetic ion energy and the prediction of the theoretical oscillation frequency, usually a relative measurement of the mass is applied, where at least a resolution of $\delta m/m \approx 10^{-4}$ can be achieved [91].
To obtain high frequency and mass resolution, the ion bunch has to retain in its shape for a sufficient time to reduce δf by the uncertainty product in the Fourier-transform $\delta f \delta t \approx 1$. This can be realized by using the so called "self-synchronized" trapping mode, where the ion bunch is held together by the special, energy-dependent shape of the trapping potential. This mode has already been addressed in various papers

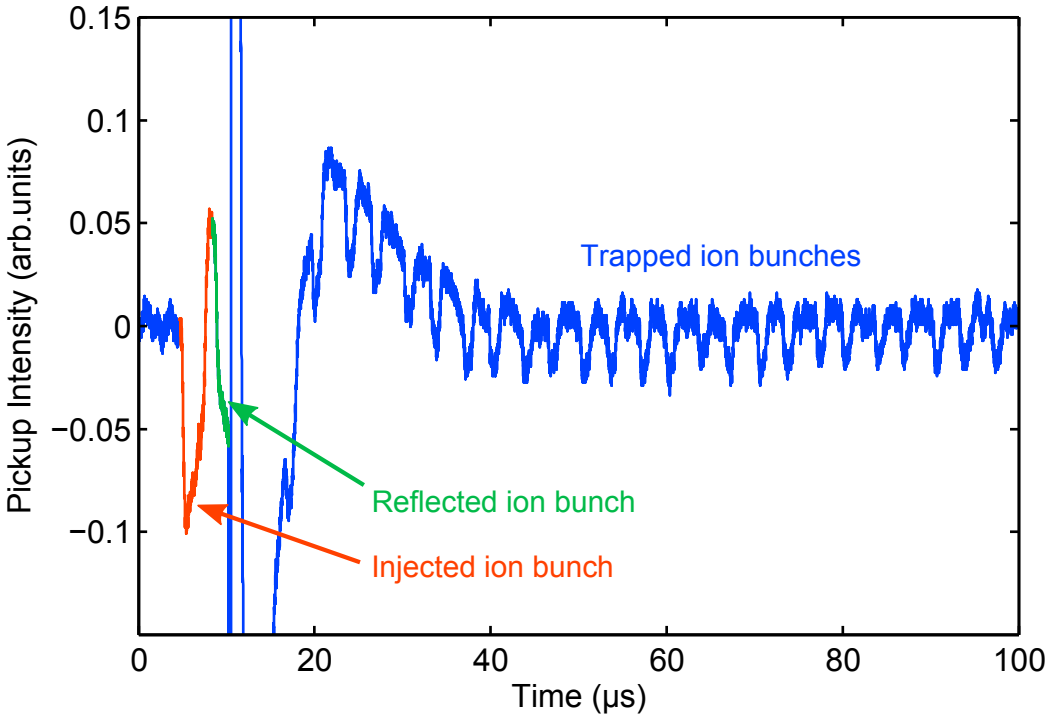

Figure 3.5: The first induced ion bunch signals of the ion injection of an 3 μs long, 6 keV O^- bunch monitored with the beam pickup in the trap (see also Fig. 3.10).

(see, e.g., Ref. [92–94]).
The ion bunch expands in time due to the spread of the kinetic energies and the repulsive Coulomb forces between the ions. The expansion is prevented in the self-synchronizing mode by the energy-dependent oscillation path lengths, which are created by the shallow trapping potential at the returning point of the ions (see Fig. 3.3). A constant oscillation frequency can thus be accomplished, which is independent of the kinetic energy of the ions. The trapping potential can even be used to reverse the energy-dependence on the frequency. For instance, the faster ions will have a longer oscillation frequency and will fall back in the ion bunch. Here, they are decelerated by the repulsive force between the ions and thus, the energy spread is reduced. A detailed investigation of the dispersion of an ion bunch in an EIBT for long storage times has been performed with the CTF. The loss of ions from the bunch, not from the trap itself, could be observed for up to 12 seconds of the ion storage, which was only accessible due to the long storage lifetime of the trapped ions. Different influences on the decay were identified such as intrabeam scattering or the expansion of the ion bunch although the trap was operated in the self-synchronizing mode. Further details can be found in Ref. [95].
In figure 3.5, the ion bunch signals from the first few trap oscillations after an injection are shown for the case of a 3 μs long O^- bunch with 6 keV energy. The trapped ions bunch signal was obtained from the induced mirror charge on the cylindrical pickup electrode close to the center of the trap (compare Fig. 3.10) and the amplified signal is then observed on an oscilloscope.
The first dip in the signal in Fig. 3.5 corresponds to the first passage of the injected

bunch through the pickup, the second is after the reflection on the exit trap mirror. However, this latter signal contains significant electronic cross-talk from the switched entrance mirror. This also causes an upwards shift of the signal baseline, which is superimposed by the trapped bunch signal. Careful observation of the signal reveals a slight variation between the time difference of neighboring dips, which comes from the pickup not being situated exactly in the trap center. The frequency spectrum of the periodic bunch signal can be obtained by a numerical Fourier transform and is illustrated for trapped SF_6^- ions and other ion masses in Fig. 4.2.

3.1.2 Basic components of the CTF

In the CTF, an electrostatic ion beam trap was combined with the advantages of cryogenic temperatures, which are an extremely high vacuum through cryo-condensation of residual gases as well as a background radiation free environment. The CTF consists of a 3 m long straight experimental vacuum chamber (see Fig. 3.2), referred to as the cold chamber, which is cooled by with cold (>4 K) helium gas in two locations to around 12 K under cryogenic operation. The centerpiece is the 77 cm long electrostatic ion beam trap, which was introduced in detail in the previous section. The cold vacuum chamber is surrounded by two aluminum radiation shields, also cooled by helium, and the outer one is covered with 20 layers of multi-layer insulation. The whole assembly is placed in an outer separate vacuum system to isolate the cold chamber from convective heat flow. Heat transfer through conduction is minimized by a stainless-steel wire construction on which the cold chamber is attached to the isolation vacuum chamber and by the use of edge-welded bellows for the ion injection beam line and connections to room temperature vacuum pumps.
To achieve at room temperature ultra-high-vacuum (UHV) conditions with pressures of the order of 10^{-11} mbar (for instance for preparative measurements and for comparing results at room temperature to cryogenic ones), the entire experimental vacuum system is bakeable to ∼300°C. To prevent the multi-layer insulation, which is installed on top of the outer radiation shield, to reach temperatures above 120°C, these shields are equipped with a water cooling system out of copper pipes. This is only operated and filled with water during the bake-out period and left under isolation vacuum during normal operation.
Especially for the room temperature operation, a bakeable charcoal-based cryopump is used with a Leybold CP 140T single-stage cold head, which can be disconnected from the cryopump for the bake-out. Furthermore, the experimental vacuum is pumped by a 500 l/s Pfeiffer turbo molecular pump and an ion getter pump (Varian Star Cell), which both can be shut off from the trap vacuum system by all-metal vacuum valves during the cryogenic operation. In addition, the main pumping of hydrogen at room temperature is accomplished by non-evaporative getter (NEG) strips from SAES Getters (model ST707/CTAM/30D), which are partly covering the inside of the vacuum chambers. For their chemical activation and purification, the chambers are baked to 320°C, in one location even to 400°C. However, under cryogenic conditions the chemical binding process of hydrogen and other gases stagnates due to the lack of thermal energy. Here, the pumping is almost exclusively performed by cryosorption and cryocondensation on the helium cooling units.

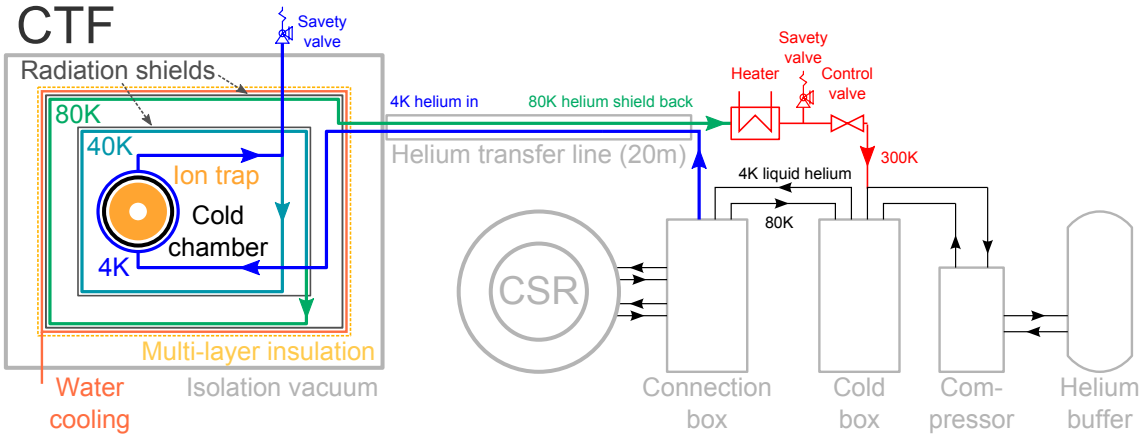

Figure 3.6: Schematic view on the new CTF cooling concept: Helium at 4 K is transferred from the connection box to the CTF in a coaxial pipe system isolated by the warmer helium back flow. Subsequently, the helium cools the cold chamber of the CTF, the 40 K and 80 K shields. The back flow is heated up to room temperature and transferred to the helium buffer.

Further details about the cryogenic design are given in the next section about the cryogenic helium supply line and can also be found in Ref. [96, 97].

3.1.3 Helium supply line and cryogenic design

At first, one has to note that according to the design of the CTF in the first period of operation, two separate helium pipe circuits with 4 K liquid and 2 K superfluid helium were used. The 4 K pipe system is consecutively connected to the two layers of radiation shields with design temperatures of 40 K and 80 K. The 2 K pipe system is thermally connected to the cold chamber by copper strips and particularly in two locations, the cooling units, the helium has direct contact to the outside of the experimental vacuum chamber.
Because of the transfer of the CTF to a new laboratory, required for making space for the assembly of the CSR next to the refrigeration system, the cryogenic connection scheme was slightly modified. In the new concept the 2 K and 4 K circuits are connected in series and supplied with cold (>4 K) helium gas, which is transferred to the new laboratory by a coaxial flexible helium transfer line from Nexans with a length of 20 m.
The 4 K helium is liquefied in the cold box (see Fig.3.6) by a Brayton cooling process and transferred afterward to the connection box, which works as the link to the CSR and here the further refrigeration to 2 K superfluid helium by a Joule-Thomson expansion is accomplished. From here the liquid helium is led into the CTF transfer line via a coaxial pipe system. In the transfer line, the helium is guided in the inner pipe surrounded by multi-layer insulation and an isolation vacuum. The helium back flow from the CTF at about 80 K is transferred coaxially, thereby shielding the 4 K helium, and it is again surrounded by a second layer of insulation and an isolation vacuum.
The helium back flow has to be heated up by an electrical heater to be returned

into the room temperature helium buffer. The mass flow through the whole system is regulated by a room temperature control valve directly behind the heater. A mass flow of $\dot{m}_{\mathrm{He}} = 2.3$ g/s of the liquid helium at 4 K can be delivered by the refrigeration system from which 1.0 g/s are reserved for the 2 K superfluid circuit for the CSR and 1.3 g/s for the 4 K shield system. In case of a parallel operation of CTF and CSR, the CTF could get at most a tenth of the mass flow that is 0.13 g/s at 4 K for the transfer line.
The energy balance for the transfer line was calculated by using the available cooling power and considering the energy loss. The enthalpy of vaporization for helium at 4.2 K is $\Delta H_V = 20.78$ J/g [98]. The cooling power only by the vaporization of the liquid helium is given by $P_V = \Delta H_V \cdot \dot{m}_{\mathrm{He}} = 2.70$ W. The loss in the transfer line is specified to 0.02 to 0.03 W/m and the Johnston-type coupling, which is used to connect the transfer line to the refrigeration system, needs 1.0 W. The combined worse-case loss is thus 1.6 W and considering the cooling power this still leads to ∼40 % of liquid helium reaching the CTF.
However, so far the CTF was always cooled without the CSR and more cooling power was available. Nevertheless, no evidence of liquid helium in the CTF with the transfer line was observed neither with a helium level probe nor by reaching the low temperatures of around 4 K. The achieved low temperatures of ∼12 K on the cold chamber of the ion trap are comparable to temperatures of the previous operation with the 2 K circuit. Thus, a similar radiation background for the trapped ions is obtained and also storage lifetimes in the order of hundreds of seconds could be measured with various anions such as SF_6^-, which does not set limits on the performed measurements.

3.1.4 Ion injection beam line

The ion preparation and beam transport takes place in the injection beam line (see Fig. 3.7), which extends over more than 4 m from the ion source to the trap center. The production and acceleration to the final kinetic energy of the ions (usually 6 keV) takes place in the ion source. The detailed ion source processes are highly important for the interpretation of the internal ion excitation and therefore will be addressed in a separate section below. Leaving the ion source, the ion beam is focused by an einzel lens consisting of three ring shaped electrodes, where the outer ones are grounded and the middle one is set to a potential. The ions are initially extracted from the source with an energy of 20 keV and then simultaneously focused and decelerated by the einzel lens to the final kinetic energy of 6 keV. Using this configuration, the ion yield from the source was optimized.
The ion source is followed by a deflecting element that also serves as a beam chopper, and then followed by a 90° dipole magnet. This steerer consists of two horizontal plates at which usually a voltage difference of roughly ±100 V is applied. One of these potentials can quickly be switched between this steering voltage and a deflection voltage of 1 kV. Thus, the beam is blocked by a deflection to the chamber wall and for each injection the ions can only pass for a few microseconds.
Horizontally, the ion beam is mass selected by the double focusing dipole magnet using two sets of horizontal and vertical slits before and after the magnet. The

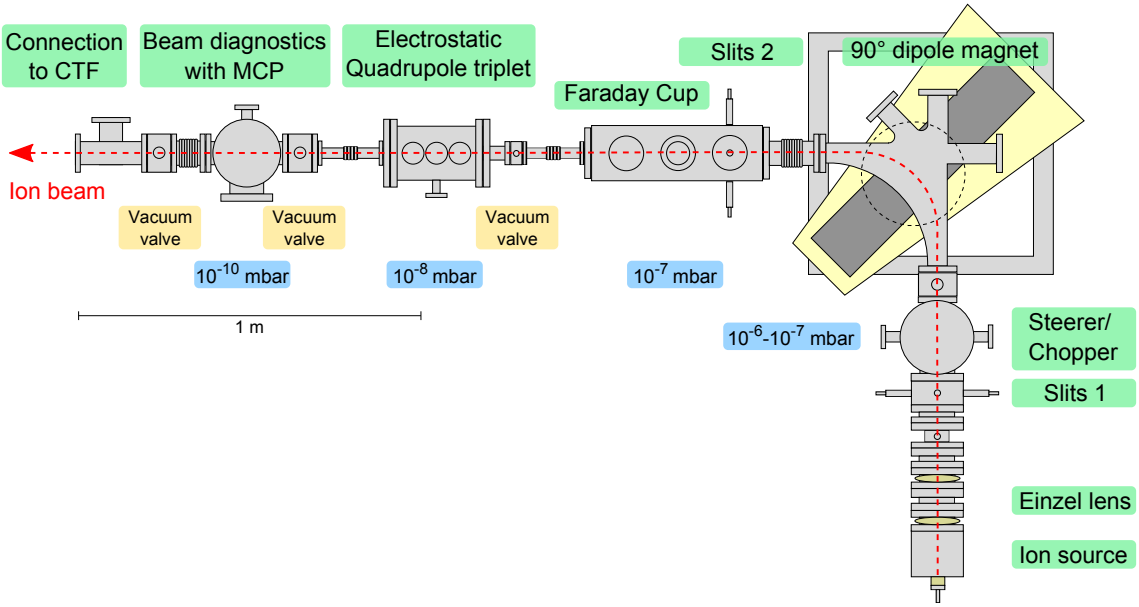

Figure 3.7: CTF ion injection beam line with the positions of ion optical elements and typical pressures for the different vacuum chambers.

beam current is measured with a Faraday cup directly behind the second pair of slits. The mass resolution of the magnet can be written as $\Delta m/m = 2x_s/D_x = 2 \times 10^{-3}$ (x_s/mm) using the dispersion function $D_x \approx 1$ m at the second focus point and a constant kinetic energy and charge. Setting the slits to a width of 1 mm, the mass resolution of SF_6^-, for instance, is around $\Delta m \approx 0.3$ which is sufficient to separate the masses. However, for the injection of ions into the CTF usually larger slits are used to yield higher beam intensities as the possible contamination from other species can also be monitored by measuring the frequency spectrum with the pickup.
The ion beam is afterward prepared to match the trap acceptance with an electrostatic quadrupole triplet. The four electrode voltages of the last quadrupole can be controlled separately and hence, a steering of the beam can also be accomplished. The last vacuum chamber before entering the cryogenic region houses a destructive beam profile measurement unit [99]. Here, an aluminum plate can be moved into the beam path and secondary electrons are created by the impinging ions. These electrons are accelerated onto a stationary micro channel plate (MCP) by a voltage of 1.5 kV applied to a grid in front of the plate. The beam profile is then imaged by a phosphor screen behind the MCP and a CCD-camera outside the vacuum through a glass window.

3.2 Negative ion sources

In this section a short introduction about ion sources will be given, focusing on the production of negative ions particularly for larger molecules or clusters and on the employed cesium sputter ion source.

3.2.1 General introduction to ion sources

In the context of this work, the internal excitation of the molecular ions plays an important role which is why the source principles will be addressed sequentially from the hot to the colder ion production. In commonly used sources for moderate size of atomic or molecular anions, electrons are emitted from a cathode, accelerated and attached to the gaseous particles. The electron emission can either be performed by the impact-induced electron emission from a cold-cathode or with the help of a heated filament. The electron emission current density J is related to the temperature T and the work function ϕ_s of the material by the Richardson-Dushmann equation [69], which is $J = AT^2\exp(-e\phi_s/k_BT)$, where A is a material dependent constant.
One may differentiate between an electron bombardment ion source and a discharge plasma source, where in the first one ions are created by electron impact, but the density is too low to form a plasma. In contrast, in discharge sources like Penning ion sources or duoplasmatrons, a plasma is formed consisting of electrons, positive ions and also negative ions. These sources are usually used for the production of highly intense positive beams, but a careful extraction of negative ions is also feasible; in some cases the much lighter electrons are pulled out of the extracted beam by an additional deflection potential. Static magnetic fields are also applied in many sources to confine the electrons radially and increase the electron and ionization density. The plasma can easily acquire temperatures of >1000 K, which results in high internal excitation of molecular ions in terms of vibrational and rotational energy.
Molecular ions with high internal energies can also be produced in sputter ion sources [100], where negative ions are formed by contact to electron donating materials instead of free electrons. The sputtering itself can either be performed by impact of accelerated positively charged ions or by an intense laser beam. The sputtering process and electron attachment will be explained in detail in the next section.

Coming to the production of colder ions and heavier ion complexes, three important principles have to be mentioned namely the *supersonic expansion* ion source, the *electrospray ionization* and the Matrix-Assisted Laser Desorption Ionization (*MALDI*).
Starting with the *supersonic expansion*, invented in the 1970s by Levy [101, 102], a high pressure gas is expanded through a small nozzle into a low pressure region, usually a vacuum system. In the resulting supersonic jet, a large number of collisions between the gas particles occur leading at first to a highly directed beam where the thermal external energy in terms of transversal kinetic energy is transformed into an accelerated gas flow. The kinetic temperature in the co-moving frame of this flow is reduced significantly as compared to the temperature at the nozzle. In case

of molecular gas, this isentropic expansion also leads to a decease of the internal excitation starting with the cooling of the rotations and followed by the vibrations. Cooling of molecular gases is mostly performed by introducing a small amount of a few percent of the molecular species, the seeded gas, into a carrier gas, which can be any rare gas; usually helium or argon. Since the isentropic expansion factor $\gamma = C_V/C_P$, the ratio of the heat capacities, is highest for atomic gases with a value of 5/3, also the highest flow velocities can be achieved. Thus, an enhanced amount of the thermal energy is converted to the directed flow and leaves a low temperature in the co-moving frame of the expanded gas. The small fraction of the seeded, molecular gas is forced by collisions to the higher velocity of the carrier gas, which further cools the internal degrees of freedom of the molecules. The high density in the expansion also enables the formation of clusters, where in contrast to the translational or internal cooling three-body collisions are needed to carry away the energy. A good introduction to supersonic expansion can be found in Ref. [103]. Electrons can be attached to the molecules by introducing them from a heated filament to the expanded gas jet. In this arrangement, the acceleration of the anions to high kinetic energy should be implemented after the expansion process in a low pressure regime in order to protect the ions from a collisional re-excitation. On the other hand, each electron capture process transfers at least the energy of the electron affinity into the molecular ion. The attachment should thus be performed as early as possible within the expansion process in order to cool this additional energy input and obtain cold ions.

Compared to sputter or plasma sources, *electrospray ionization* and *MALDI* are soft non-destructive vaporization and ionization methods. Here, an already existing molecular complex, such as a biological molecule, is brought without destruction into the gas phase and is also charged up during this process. Clustering is also possible in these sources, but usually not desired as the complex should be investigated under isolated conditions. The inventors of the two methods shared half of the Nobel Prize for Chemistry in 2002 namely John Fenn for the electrospray ionization [104] and Koichi Tanaka for the development of MALDI [105, 106].

In the *electrospray ionization*, a strong electric field is created at the tip of a capillary filled with a solvation of the molecule of interest. The field of a few kV generates at the tip a so called Taylor cone composed of an enhanced amount of charged molecules from the solvent. Ions are emitted, once the repulsion of the charged molecules on the surface approaches the surface tension of the solution, and they are accelerated by the electric field. A recent overview can be found in Ref. [107].

In the *MALDI* method, the desired molecule is co-crystallized into a matrix compound, usually a crystallized UV-absorbing weak organic acid. Desorption is performed by laser radiation, where most of the irradiated energy is absorbed by the matrix and causes the co-crystallized molecules to vaporize indirectly. Additionally, the matrix acts as a proton donor or acceptor, leading to charged molecular complexes to be investigated.

The applied method to produce negative molecular ions or clusters in this work, was cesium sputtering and will be explained in detail in the following section.

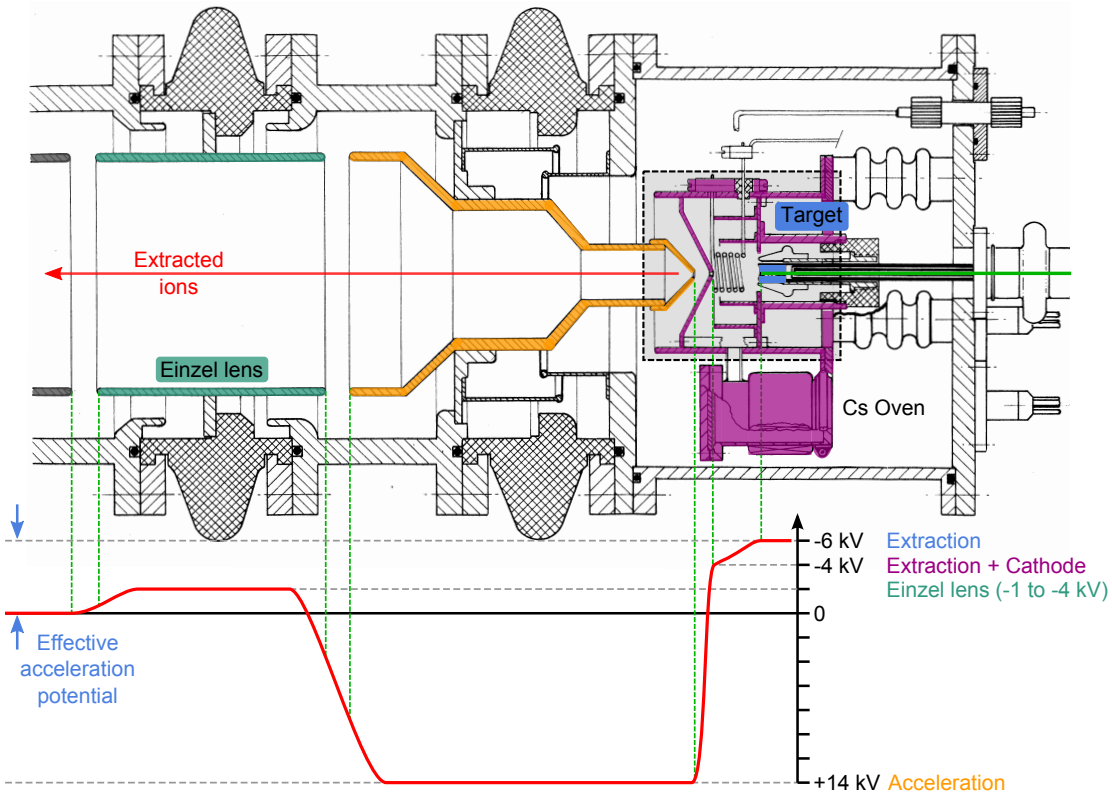

Figure 3.8: Cross section of the MISS ion source including extraction electrode and integrated einzel lens: Sputtered ions are created on the target at a potential of −6 kV (blue). They are at first accelerated by the cathode potential between the target and source housing (purple), then to 20 keV in the gap to the extraction electrode and decelerated and focused simultaneously in the einzel lens. The center of the MISS is shown in detail in Fig. 3.9.

3.2.2 Negative sputter ion source MISS

This section describes the production of negative ions from a cesium sputter ion source, more precisely a MISS (Multi-purpose Ion Sputter Source or Metal Ion Sputter Source). This type of source was first introduced by Middleton in the 1980s and the MISS modification used in Heidelberg comes closest to the Type VII in his original work [100]. Realizations of this source type mostly vary in the shape and position of the filament, which defines the acceleration potential for the cesium cations, and in the supply method for the cesium vapor.
A cross section of the MISS setup applied in this work including the extraction electrode and the integrated einzel lens, is shown in Fig. 3.8. The sputtered ions are created on the target at a potential of −6 kV (blue). They are at first extracted by the cathode potential between the target and source housing (purple) and then accelerated to a kinetic energy of 20 keV in the gap to the extraction electrode (orange). A deceleration to 6 keV and simultaneous focusing of the ion beam takes place in the following einzel lens. The initial faster extraction of ions with 20 keV was found to give a higher ion yield because of lower space charge effects. The schematic applied potential distribution is also shown in Fig. 3.8.

Figure 3.9 shows the centerpiece of the MISS: Condensed cesium vapor on the ionizer filament is thermally ionized to form Cs^+, and accelerated onto the target. The sputtered material then captures an electron from adsorbed cesium on the target. Thus, the basic process is surface ionization in both cases, the production of positive cesium and negative sputtered ions.
In more detail, cesium is vaporized in an oven, typically heated to about 100°C. The boiling point of cesium is 671°C (melting point at 28.44°C); however, under low pressure a sufficient amount of cesium is vaporized and condenses on the inner source chamber including the filament and target. The cesium is then ionized by losing an electron to the heated tungsten filament. The positive ion yield is given by the Boltzmann energy distribution as $(g_+/g_0)\exp[e(\phi_s - I_p)/k_BT]$, where ϕ_s is the work function of the filament, I_p the ionization potential of cesium and g_+/g_0 statistical factors. Tungsten as filament material is used because of its very high work function of 4.55 eV [108] and the high temperature resistance enabling to further increase the ion yield by heating. Typically the filament temperatures are between 1000 K and 2000 K.
The so called sputtering process is the generation of gas phase particles from the target surface by elastic collisions with the energetic cesium ions hitting the sputter target (≈1-3 keV). Depending on the impinging ions, one or more particles can be released and beside the predominant production of atoms also larger compounds and clusters are created. A small fraction will also be charged and the negative ion yield is proportional to $\exp[-e(\phi_s - \mathrm{EA})/k_BT]$, with EA being the electron affinity of the sputtered particle. Typical target work functions are $\phi_s(\mathrm{Al}) = 4.06 - 4.26$ eV for aluminum and $\phi_s(\mathrm{Mo}) = 4.36 - 4.95$ eV for molybdenum [108] (dependent on the surface orientation of the crystal). However, the target is always covered by condensed cesium, which has a work function of $\phi_s(\mathrm{CS}) = 1.95$ eV and primarily works as the electron donator in this process. In addition, it has been shown that the effective work function is even lower in a partly covered cesium layer (surface coverage ∼60 %) [109–111].
The production of negative ions from a gas target using the same type of source has been performed for various species, creating either a compound ion of the target material and the gas, e.g. BO^-, MgO^-, AlO^- or the gas only like for HF_2^- and O_2^-. For this purpose, the gas is introduced through a drilled target and in case of purely gaseous ions a very refractory target like molybdenum is used, hence reducing the amount of unwanted ions and also the risk of blocking the gas injection hole after some time of operation.
For the production of negative sulfur hexafluoride, SF_6 gas is introduced through a drilled molybdenum target. The process of ion production is not fully understood, but there are some hints that SF_6^- must be created close to the target surface. Adsorbed SF_6 on the target could be desorbed and capture an electron from the condensed cesium, which is a process similar to the sputtering from a solid target. Also electron capture from the gas phase might be a plausible explanation, as SF_6 does not have to be resolved beforehand and the electron density close to the gas injection hole could be sufficient high. A capture process further away from the target can be excluded because the ions would not experience the same acceleration potential and hence, would be extracted with a lower kinetic energy. A shifted

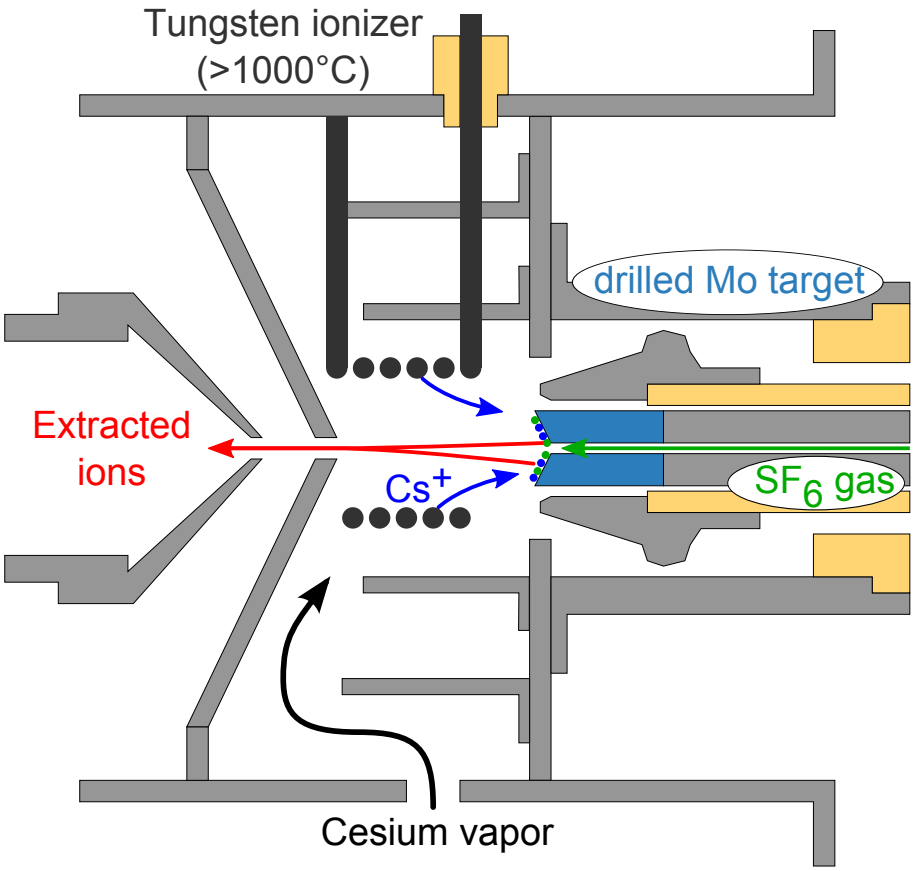

Figure 3.9: Schematic close-up view on the centerpiece of the MISS ion source (gray shaded area in Fig. 3.8): Condensed cesium vapor from an oven condenses on the heated tungsten ionizer, where it is thermally ionized and accelerated by the cathode voltage onto the target. The sputtered material which is released can capture an electron from neutral condensed cesium on the target surface. The newly formed negative ions are accelerated by the cathode voltage and afterward by the extraction voltage to a kinetic energy of 20 keV.

energy or reduced sharpness compared to ions produced from a solid target was not observed neither in the mass spectrum of the dipole magnet nor in the oscillation frequency of the stored ions in the trap.

3.2.3 Excitation of anions in sputter ion sources

One important issue in the framework of this thesis is the internal excitation of the produced ions, especially vibrational and rotational excitation. This deposed energy can usually be much higher than the dissociation energy or electron affinity in the case of anions. Measurements of sputtered neutrals as Cs_2, K_2 and Na_2 were performed by Fayet *et al.* [112] using one- and two-photon ionization spectroscopy to analyze the internal energy. Temperatures between 1000 K and 1500 K have been found with similar values for vibrations and rotations. More recent measurements were carried out by Wucher *et al.* [113] employing fragmentation lifetime measurements for very short time scales from ns to μs. Here, vibrational and rotational

temperatures of 3100 K and 5600 K, respectively, have been determined for Ag_2. Larger clusters showed higher internal energies but similar estimated temperatures. Further investigations on the clusters Me_n, Fe_n^+ and Nb_n^+ also showed increasing average internal energy with the cluster size and resulting temperatures of the order of 3000 K [114].
In terms of these measurements, the dependency on the kinetic energy of the sputtering ions was studied using an energy range from 500 to 5000 eV with Ar^+ and Xe^+. Besides an increase in the ion yield with higher impact energy, no dependency on the internal energy has been observed, concluding that the higher energetic ions penetrate deeper into the target surface and the energy is here distributed over a larger volume. Further measurements have been performed employing a photonionization efficiency (PIE) method and comparing to the ion production from a supersonic expansion as discussed in Ref. [115]. Recent temperatures are located in the range between 2000 to below 1000 K and a more detailed model was developed [116].

3.2.4 Ion-gas collisions in the ion sources

The initial internal excitation of SF_6^- was found to vary with the vacuum pressure in the chopper chamber (see Sec. 4.2), which to some extent reflects the ion source pressure due to the constant pumping speed. Estimates of this pressure and resulting collision rates of ions with gas molecules are derived here.

Estimated pressure in the ion source

The small source volume housing the target and filament is assumed to have the most influence on ion collisions. Due to the low velocity of the ions they spend a long time in this volume and additionally, the high pressure leads to a large number of collision partners. This area is only connected to the subsequent vacuum system by a small hole in the skimmer of around 1.5 mm diameter and a length of 2 mm. The following setup is shown in Fig. 3.7 and Fig. 3.8, between the einzel lens and chopper chamber a small hand valve for venting the source and a pair of beam slits are situated. During operation the chopper pressure is between 10^{-6} to 10^{-7} mbar. As simplification a large volume with known pressure p_1, reflecting the chopper chamber, is assumed which is connected to a small volume of unknown pressure p_2 by an orifice. The connection between the two pressures for a molecular flow is given by

$$q_{pV} = L\Delta p, \tag{3.6}$$

where q_{pV} is the volume flow equal to the pumping speed of the vacuum pump (250 l/s). The conductivity L of the orifice can be written as

$$L = \frac{\bar{c}}{4} AP, \tag{3.7}$$

with the mean velocity $\bar{c}$ of the gas, the cross section of the orifice A and the transmission probability P through the orifice. For a thin orifice P is just unity, but here the diameter and length are comparable and the transmission probability for a

pipe is given by

$$P = \left(1 + \frac{3}{8}\frac{l}{r}\Phi\right)^{-1}, \tag{3.8}$$

with length l, radius r and a correction factor Φ of around 1.24 for a ratio of $l/r = 8/3$ [117].
The mean gas velocity $\bar{c}$ can be determined from the Maxwell speed distribution at a temperature of $T = 20°\mathrm{C}$ (≈273 K):

$$\bar{c}(\mathrm{SF_6}) = \sqrt{\frac{8k_BT}{\pi m}} \approx 206\,\mathrm{m/s}, \tag{3.9}$$

which assumes that the collision partner for the ions is predominantly SF_6. Furthermore, the temperature of the injected SF_6 gas was used (20°C) instead of the source temperature of around 250°C because the collisions will mainly occur in the injected SF_6 gas flow. Using Eq. (3.6) and the above determined values the source pressure p_2 is given by

$$p_2 = p_1\left(1 + \frac{q_{pV}}{\frac{\bar{c}}{4}AP}\right) \approx 6 \times 10^3\ p_1. \tag{3.10}$$

Collision rates

The mean free path and the collision rate can be calculated by assuming hard spheres for both collision partners:

$$\frac{dN(x)}{dx} = -k_C \cdot N(x), \tag{3.11}$$

$$N(x) = N_0 \cdot e^{-k_C x} = N_0 \cdot e^{-n\sigma x} = N_0 \cdot e^{-x/\lambda}. \tag{3.12}$$

Hence, the mean free path λ and the collision rate k_C are related by

$$k_C = n\sigma = \lambda^{-1}, \tag{3.13}$$

with the particle density $n = p/(k_BT)$ in the source and the collisional cross section σ, which is estimated from the geometrical cross section of SF_6^- and SF_6. For this purpose, the equilibrium distances between the S-F bond are used from the most recent calculation [17], which gives for SF_6 a distance of 1.56 Å. The asymmetric SF_6^- anion has the largest extension along the remaining symmetry axis, with lengths of 1.9 Å and 1.6 Å [17], respectively, for the two opposing bonds. Assuming a radius of $r_1 = 1.56$ Å for SF_6 and a maximum radius $r_2 = 1.75$ Å for SF_6^-, the geometrical cross section is given by

$$\sigma = \pi(r_1 + r_2)^2 \approx 34.4 \times 10^{-20}\mathrm{m}^2. \tag{3.14}$$

The resulting source pressures p_2, mean free path lengths λ and collision rates k_C are summarized in table 3.1 for typical values of the pressure p_1 measured in the chopper chamber.
The path length inside the source between target and extraction electrode, where the pressure is highest, is around 20 mm. For a low pressure of 10^{-7} mbar, only

Table 3.1: Summary of the estimate of the pressure p_2 in the ion source chamber for different pressures in the chopper chamber p_1. Mean free path lengths λ and collision rates k_C were approximated for SF_6^- ions with SF_6 for the pressure p_1.

p_1 (mbar)	p_2 (mbar)	λ (mm)	k_C (mm^{-1})
1×10^{-7}	6.1×10^{-4}	193	0.005
5×10^{-7}	3.1×10^{-3}	38	0.026
1×10^{-6}	6.1×10^{-3}	19	0.052
5×10^{-6}	3.1×10^{-2}	3.8	0.264

10 % of the ions will experience one or more collisions, whereas for the highest shown pressure in table 3.1 five collisions per ion is the average.
One has to note the many simplifications made in this estimation. For instance, in estimating the pressure ratio the shape of the extraction electrode and einzel lens have not been taken into account and also the temperature difference between ion source and the following vacuum system has been neglected. However, one can assume that the calculation should be correct within one order of magnitude. This shows that a difference in the number of collisions between the two extreme cases of pressures measured in the chopper chamber is plausible. The observed variations in the internal excitation of the SF_6^- ions (see Sec. 4.2), which are produced highly excited in the ion source, can thus be attributed to additional excitation by collisions at the different pressure regimes.

3.3 The cryogenic delay line detector

The CTF detection system (see Fig. 3.13) for neutral particles consists of two micro channel plate (MCP) [118] detectors (40 mm diameter) in a chevron arrangement, attached to a position sensitive delay line anode [119]. It is located behind the electrostatic mirror at the trap end opposite of the injection at a distance of 871 mm from the trap center, where it accepts particles emitted at the trap center into a cone with $\pm 1.3°$ ($\approx$23 mrad) opening angle (see Fig. 3.10). Thus, the whole trap acceptance in the trap center ($x_{max} \approx 4.6$ mm and $x'_{max} \approx 14$ mrad) is covered by the detector. However, during the deceleration of the stored ions towards the electrodes their emittance increases and not all neutrals produced there can be detected. In addition, the detection efficiency for MCPs decreases with lower kinetic energy of the particles as described in the following.
MCPs consist of a plate of highly resistive material perforated by several hundred thousand cylindrical channels of a few micrometer diameter, which are tilted typically by an angle of around 8° against the plate face. A voltage on the order of 1000 V per MCP is applied between both sides; for the operation of a chevron configuration (two MCPs behind each other) or a Z-stack (three MCPs) an accordingly higher voltage is used. Energetic particles hitting the front of the MCP create secondary electrons, which are accelerated into the channels by the applied voltage, where further collisions of these electrons with the channel walls can lead to an en-

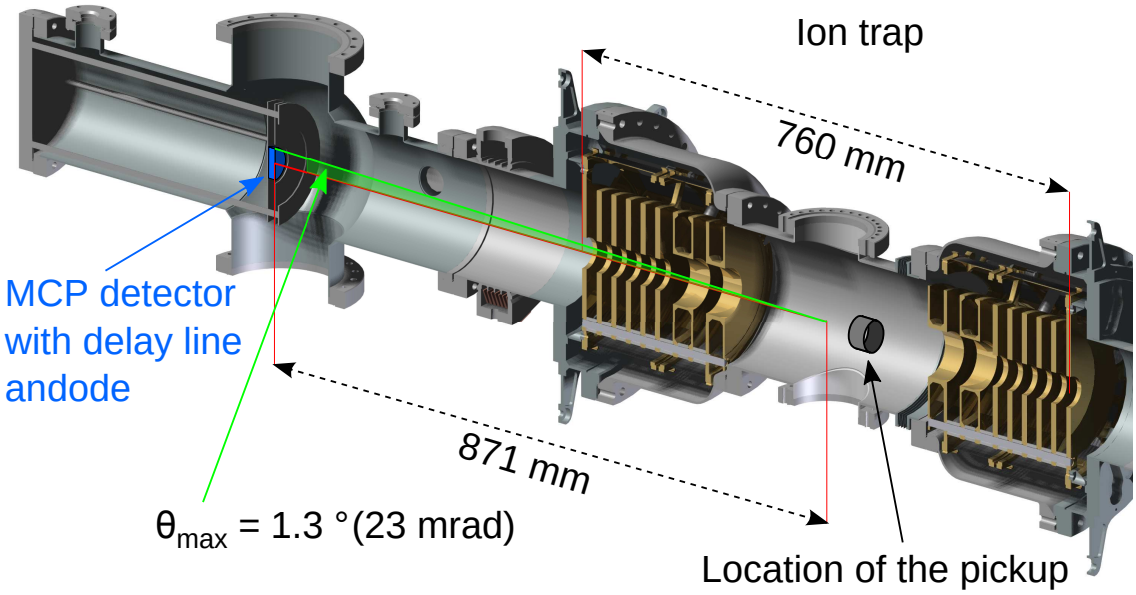

Figure 3.10: Location of the detector with respect to the ion trap

hancement of the electron output signal by a factor of 10^6-10^8. In the chevron and Z-stack configurations the MCPs are rotated by 180° against each other so that no straight passage of particles through the entire assembly is possible.
The detection efficiency of MCPs has been measured, for instance in Ref. [75, 76], where especially the energy range of 0.5 to 5 keV was covered including charged and neutral particles. The efficiency was found to depend only on the kinetic energy and not the particle mass. However, only impacts of single atoms as opposed to molecules have been investigated. For neutral particles, a plateau for high energies of a few keV is found with an efficiency of ∼50 % which towards lower energies decreases to ∼10 % at 1000 eV.
This CTF detection system is located inside the cryostat reaching temperatures of 40−50 K under cryogenic operation. The electrical resistance of MCPs is found to increase steeply with lower temperatures [120] leading to longer dead times of the triggered electron multiplication channels. By applying a voltage of 2000 V to the Chevron MCP at room temperature, a resistance of 26 MΩ was determined, whereas under cryogenic conditions (47 K on the closest sensor) no current above the sensitivity of 1 μA of the gauge was observed, which indicates a resistance of at least 2 GΩ. The temperature dependence of this MCP was also measured in more detail in Ref. [121].
The layers of the delay line detector with applied voltages are shown in Fig. 3.11. Neutral particles impinge from the top, where the two grids in front of the MCP can be used to repel charged particles. Thus, the first grid is set to +1000 V and then the potential gradually decreases to −2450 V on the MCP front.
Negatively charged ions from the injection are blocked by the exit mirror of the ion trap and will not reach the detector. However, during operation without grid voltage, it was found that slow particles seem to arrive on the detector at times between 100 μs to 1 ms after the injection. These particles might come from a part

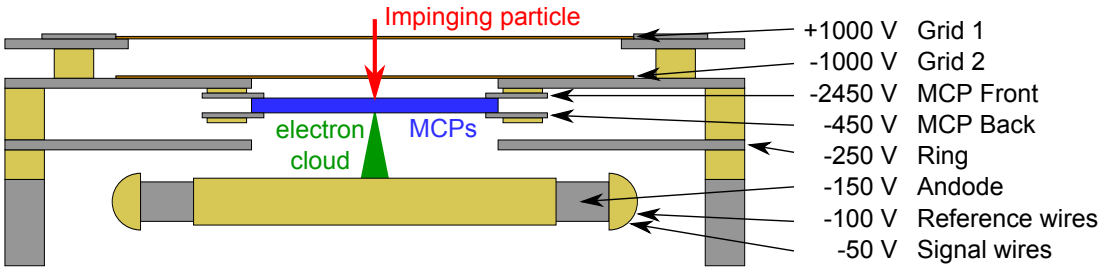

Figure 3.11: View on the different layers of the detector and the applied voltages

of the injected ion bunch hitting the vacuum chamber walls and creating a slow diffuse flow of fragments. When applying +1000 V to the first grid almost all of the slow signal could be suppressed leading to the conclusion, that predominantly the charge exchange processes that take place at the chamber walls are created by positive slow ions.

3.3.1 Principle of a delay line anode detector

The delay line anode [122] is used to gather 2D-position and timing information of the impinging particles on the detector. Placed behind the MCP, the amplified electron cloud is attracted by a voltage applied to a long helically wrapped wire (see Fig. 3.12). When the cloud is picked up by the wire, the collected amount of charge splits up and propagates to both wire ends. The difference in arrival time of the signal at both ends of the wire coil contains the position information and is measured with a high resolution time-to-digital converter (TDC) (here with 25 ps time resolution). The correct scaling factors between time and position are usually determined by a calibration measurement.
In more detail, the wire is wound into a coil with an oblong cross-section and with an equidistant spacing of 1 mm between neighboring wire rounds around the anode. To gather two dimensional information two crossed wire coils are wound around the same carrier with an insulating gap between the two coil layers. To reduce noise, each coil is wound from two parallel wires, with one wire (the reference) being biased with a less attractive voltage to direct electrons as compared to the second wire (the signal). Thus, locally induced noise is picked up by the signal and reference wires and can be filtered out by subtracting the two signals afterward. The applied voltages are also illustrated in Fig. 3.11, where a voltage difference of 2000 V is applied between both sides of the MCP and the potential decreases to the reference and signal wires, which are at −100 V and −50 V, respectively.
The propagation time differences between the arrival times of the electron signal on both ends of each wire are given by

$$\Delta t_x = t_{x_2} - t_{x_1}, \tag{3.15}$$

$$\Delta t_y = t_{y_2} - t_{y_1}, \tag{3.16}$$

where x and y are the horizontal position and the vertical position, respectively. To transform the time difference to a position, a transversal propagation time of the signals can be defined. When the electron signal has propagated for one turn of

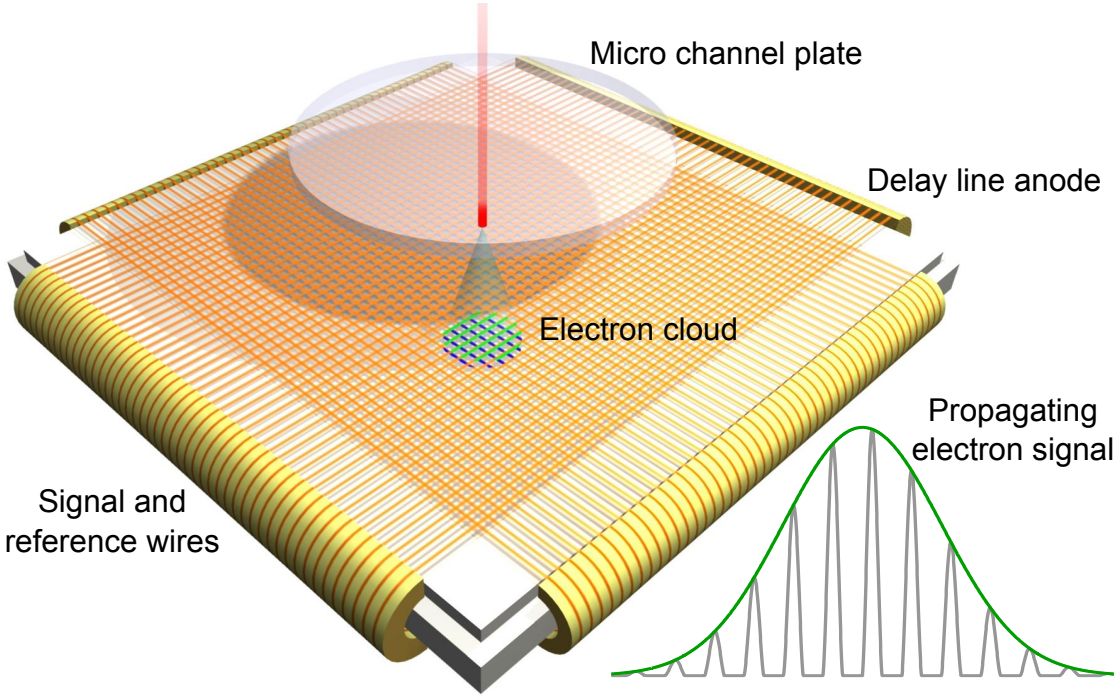

Figure 3.12: Schematic view on the delay line anode. The propagating electron signal becomes a smooth function due to the temporal spread of the signal and the immediate dispersion.

the coil the transversal gain in position is just the distance between the windings of 1 mm, thus the single pitch propagation velocity $v_{sp,i}$ $(i = x, y)$ along the two dimensions of the MCP backplane is defined as

$$v_{sp,x} = \frac{1}{L_{sp,x}} c' \approx 0.572 \ \frac{\text{mm}}{\text{ns}}, \tag{3.17}$$

$$v_{sp,y} = \frac{1}{L_{sp,y}} c' \approx 0.595 \ \frac{\text{mm}}{\text{ns}}. \tag{3.18}$$

The length of one winding L_{sp} is slightly different between both dimensions, because the winding for the y direction (as defined here) is closer to the anode and hence, the coil circumference is smaller so that the single pitch propagation velocity becomes higher. c' denotes the propagation velocity which is close to the speed of light. The given values for the single pitch propagation along a wire have been determined by a calibration measurement which is described below.
With the single pitch propagation velocity and the time difference, the position is given by

$$x = (1/2)\ v_{sp,x}\ \Delta t_x \ + \ x_0, \tag{3.19}$$

$$y = (1/2)\ v_{sp,y}\ \Delta t_y \ + \ y_0, \tag{3.20}$$

where the factor 1/2 comes from the fact that the electron signal propagates simultaneously in both directions. Later on to filter out noise, a cut on the sum of the two time signals $T = t_2 + t_1$ can be applied, as the time sum is a constant position-

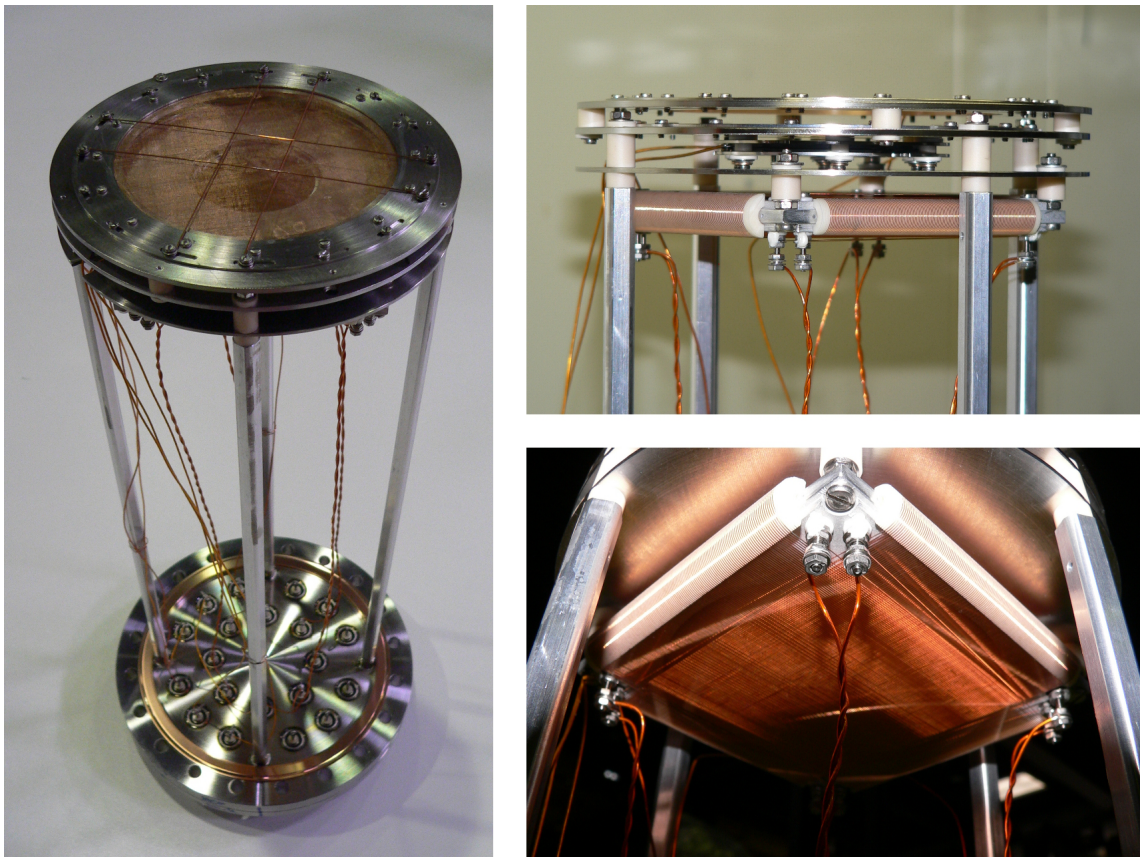

Figure 3.13: Photos of the detector: The picture on the left side shows the whole detector with the mounting flange and feed-throughs; on top the deflection grids and calibration wires can be seen. A view on the MCP and delay line assembly is shown on the right.

independent value making sure that the signals originate from the same location.

The position resolution of a delay line anode is not limited by the spacing of the wires, as the center of mass of the electron cloud is automatically interpolated to a position lying in general between the wires. The electron signal is schematically shown in Fig. 3.12, where due to the time extension of the electron cloud and the immediate propagation of the collected electrons, a smooth signal distribution is produced (and not a spiked curve from each wire segment). Thus, the TDC resolution sets a limit on determining the maximum of that distribution and the time difference $\delta(\Delta t) = \sqrt{2}\delta t$, which is for the used TDC 25 ps. The position accuracy is usually limited by the calibration of v_{sp}, for which a mask with well known equally spaced holes is installed in front of the detector. With the aid of particles from an ion beam or alpha source the measured shadow from the mask on the detector can be scaled to reflect the correct dimensions.
In the case of this cryogenic detector, no movable mask could be installed. Instead a permanent set of wires are mounted in front of the detector whose angles and mutual distances are well known (compare left picture in Fig. 3.13). The wires are tilted by 11.25° and the distance including wire thickness is known to <0.5 mm. Figure 3.14

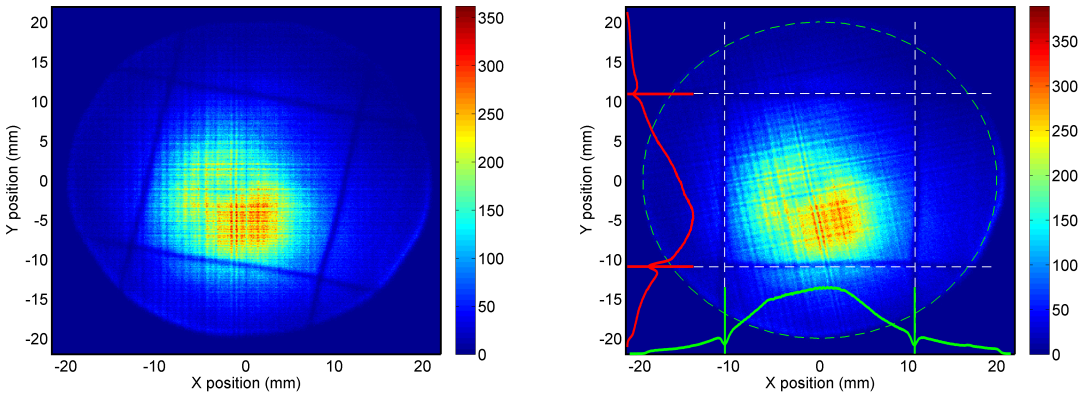

Figure 3.14: The left side shows the 2D-intensity of neutrals from a stored SF_6^- in the trap; the right side is after the rotation by 11.25° overlaid by the expected position of the calibration wires. The red and green lines show the projection of the intensity distribution onto the respective axis.

shows 2D-intensity plots of neutral particles with and without the reconstructed calibration wire positions. For the calibration, the figure was tilted by the angle of 11.25° and the summation of the signal in each dimension was performed yielding a minimum at the position of the wire.
The position resolution obtained with this calibration can be approximated by

$$\frac{\delta(s)}{s} = \sqrt{2\left(\frac{\delta(t)}{t}\right)^2 + \left(\frac{\delta(v_{sp})}{v_{sp}}\right)^2} \approx \frac{\delta(v_{sp})}{v_{sp}} \approx \frac{\delta(\Delta w)}{\Delta w} \approx (1.5 \pm 0.5) \times 10^{-2}, \quad (3.21)$$

where Δw is the wire distance, which has an experimental error that is much larger than the uncertainty in the time measurement. Thus, considering the size of the detector of 40 mm diameter the resolution is ∼0.5 mm for this calibration method.

3.3.2 Signal processing

This part describes all electronic signals used by the CTF detection system. The detector signals and supply voltages are guided via Kapton-isolated wires to the experimental vacuum feedthroughs, whereas twisted pairs are used for each pair of signal and reference wires. The connection to the isolation vacuum feedthroughs is more critical in terms of heat input onto the cold chamber. Due to low voltages on the signal and reference wires (see Fig. 3.11), standard cryogenic twisted-pair wires could be used, which are Kapton-isolated stainless steel wires with a diameter of 0.1 mm for low heat conductance and specified for a voltage difference of 400 V. In addition, for protection against accidental damage during installation they are guided in Teflon tubes, and they are thermally anchored on the 40 K shields by clamping them between aluminum plates.
An electronic box directly mounted on the outside of the isolation vacuum flange (see Fig. 3.1) provides all necessary voltages for the MCP and delay line anode system by a resistance chain and also couples out the MCP and the delay line signals from the high-voltage lines. In the process, the voltage from the reference wire is electronically

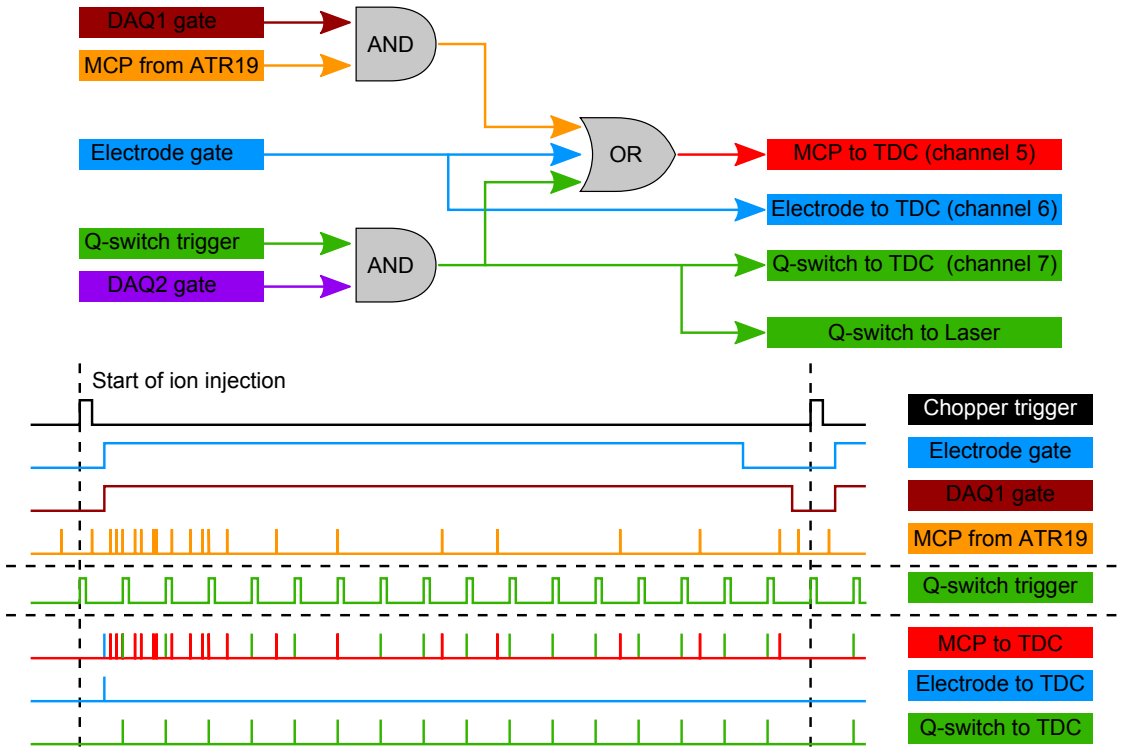

Figure 3.15: Logical connection and schematic view of the electric signals: The measured MCP signals (orange) and the Q-switch trigger enabling the laser (green) can be gated by DAQ1-gate (dark red) and DAQ2-gate (purple), respectively. Resulting signals are transferred to different channels of the TDC. The schematic view on the signals shows one injection cycle, where the chopper trigger initiates the ion injection, and the electrode gate defines the ion storage duration. The MCP signal to the TDC (red, channel 5), which is the trigger to record an event in the TDC, contains the trigger information from the MCP, the electrode trigger (channel 6) and the Q-switch trigger (channel 7). They can be distinguished from particle events in the later analysis by a coincidence with the signal of channels 6 and 7, and are used to obtain these trigger times. For further information see text.

subtracted from that on the signal wire. From here the signals are transferred to an amplifier/trigger module (RoentDek ATR19), where the MCP signal and the four delay line signals are amplified and converted to a NIM-conformal pulse by constant fraction discriminators (CFD). The signal is processed by several analog and digital electronic modules mounted in a NIM-Crate (compare Fig. 3.15). The MCP signal is afterward transferred to a PC Counter/Timer PCI card (National Instruments NI PCI-6602) with a time resolution corresponding to 80 MHz, and was used for the data acquisition without position information to obtain only the detector count rate.

The position sensitive recording of the data is performed with a fast TDC-PCI-card, where the four delay line signals and the MCP signal are connected. The TDC consists of 8 input channels measuring the signal times with a resolution of 25 ps. The MCP signal is connected to the trigger channel (here channel 5), which enables

the data acquisition to record an event. The time differences of the four delay line signals with respect to the trigger signal are recorded in the input channels 1 to 4, which are the times $t_{x_1}, t_{x_2}, t_{y_1}$ and t_{y_2} in Eq. (3.15) and Eq. (3.16). For each event also the absolute time since the measurement started is logged. However, for multiple ion trapping cycles in one measurement run, the ion storage time with respect to the ion injection into the trap is required. Hence, the electrode signal, which is used to switch the mirror electrode voltages of the trap, is connected to channel 6 of the TDC to record the exact time of the beginning of each injection. Since only one channel of the TDC can be configured as the trigger channel, the electrode signal is simultaneously supplied to channel 5 using an OR-gate in the NIM-crate. Thus, an event is always recored when the electrodes are switched and this signal can be distinguished from particle counts by the coincidence with channel 6 (see Fig. 3.15).
Similarly, the Q-switch trigger, which enables the laser, is connected to channel 7 and is also combined with the signal to the trigger channel 5. The Q-switch trigger changes the quality factor (Q-value) of an attenuator in the laser's optical resonator, and enables the creation of a laser pulse for photo-excitation measurements. Thus, the exact time information from each laser pulse is determined. Furthermore, the DAQ1-gate in Fig. 3.15 is used to select only a specific time frame of the MCP signal for the data acquisition; and DAQ2-gate can disable the creation of laser pulses for competitive measurements. The conversion between different signal types like NIM or TTL has been omitted in Fig. 3.15, as well as transformations between signal edges to short trigger pulses as it is necessary to obtain the electrode trigger.

3.3.3 Detector saturation tests

The performance of the detector under cryogenic conditions in terms of the maximum count rate measurable without saturation was investigated in separate measurements. Saturation of MCP detectors occurs when the rate of particles triggering a particular channel exceeds the inverse of its recovery time, which is dependent on the resistance of the MCP. The resistance was found to increase from 77 MΩ at room temperature to above 2 GΩ at cryogenic temperatures, which agrees with the findings of Ref. [121]. The resulting lower current available for recharging triggered channels leads to longer recovery times, and saturation is expected to occur at lower count rates.
To characterize this saturation effect, a rate measurement with different ion beam intensities and detector temperatures was performed. A 250 μs long O^- pulse was passed to the trap, from which only the count rate from the neutral particles produced en route to the trap was observed, so that the ion beam was not stored, but reflected by the first mirror.
The result of this measurement is shown in Fig. 3.16, for estimated temperatures of the detector of 220 K, 120 K and 70 K, respectively, performed during the cooldown of the CTF. The temperature was measured at the vacuum flange at which the detector is mounted (see Fig. 3.13 and Fig. 3.10). The actual temperature of the detector might be higher as the detector was positioned on purpose above the connection to the room temperature vacuum pumps.

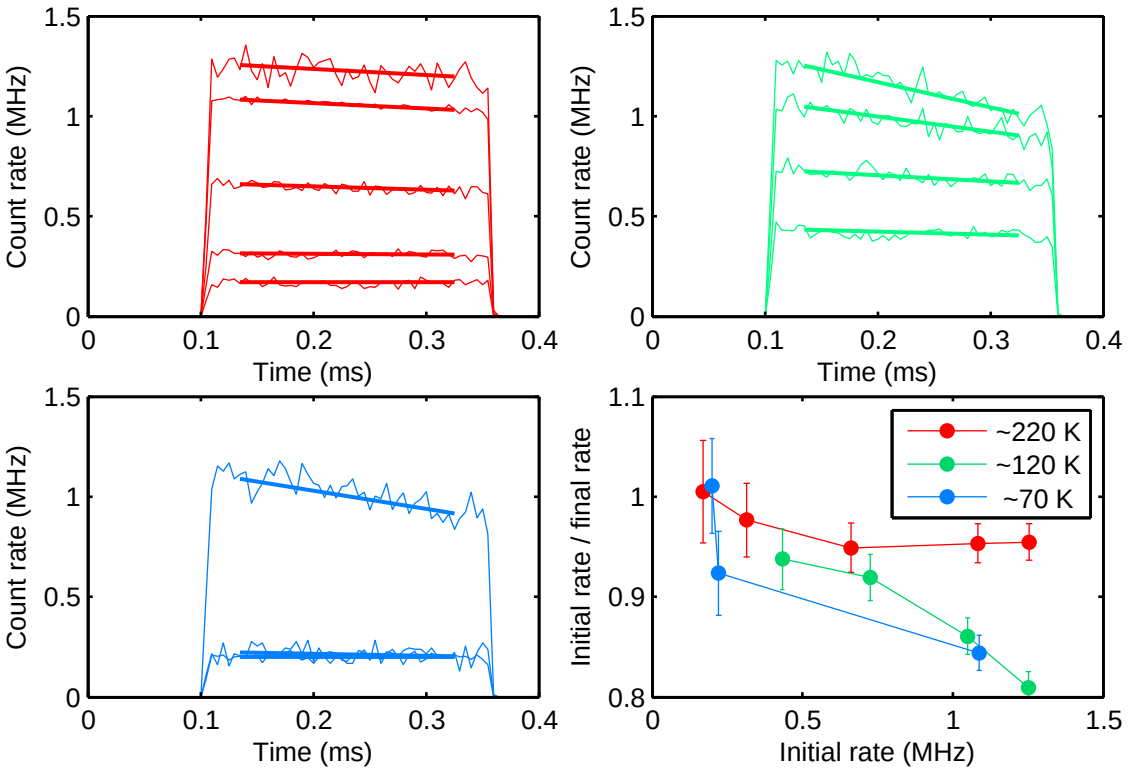

Figure 3.16: Detector count rate measurements with neutral particles from a 250 μs O^- pulse at different intensities and temperatures (see color coding). Saturation effects increase for high rates and lower detector temperatures. The ratio of the count rates at the beginning and end of the pulse gives a measure for the reduction of the detection efficiency. Rates below 1 MHz are found to exhibit saturation effects of <10 %.

The ratio of the average count rates at the beginning and end of the pulse was used to determine the reduced detection efficiency. The signal was found to clearly decrease at high particle rates above 1 MHz. The measurement shows that a maximum count rate of 1 MHz is tolerated under cryogenic operation with a detection efficiency of >90 % over a time of 0.25 ms. Furthermore, in the SF_6^- experiments, high count rates in the order of 100 kHz occur only in the first few hundred microseconds of the ion storage, because afterward the ion decay rate rapidly decreases.

3.4 Laser setup

A pulsed laser setup was applied for photo-excitation measurements with the stored ion beam in a crossed beam configuration using a pulsed Nd:YAG laser (Continuum Powerlite 8050) with a repetition rate of 50 Hz. The fundamental wavelength of 1064 nm (1.165 eV, infrared) was either directly used for low energy excitation or the second harmonic at 532 nm (2.33 eV, green) was pumping a NarrowScan dye laser from Radiant Dyes. At 1064 nm the laser pulses are about 15-20 ns long; at 532 nm 8-10 ns.
The laser beam is guided from the laser laboratory to the CTF by means of several mirrors. At first, the beam is prepared and widened up by a set of apertures and lenses to about a diameter of 1-1.5 cm to match the size with the stored ion beam and to reduce the power density falling on the sapphire laser window on the cryogenic vacuum chamber (compare Fig. 3.4). Transferred to the CTF, the laser beam is guided through two vacuum windows before exciting the stored ion beam and exiting the vacuum system through a second set of windows. Outside the vacuum, the laser beam is dumped in a caloric power meter monitoring the average power.
The total transmission including reflection losses of the outer glass window sealing the isolation vacuum (T_1) and of the sapphire window on the cold vacuum chamber (T_2) were measured at a wavelength of 1064 nm to

$$T_1 = 0.925 \pm 0.008 \ \text{(Glass window)}, \tag{3.22}$$

$$T_2 = 0.886 \pm 0.009 \ \text{(Sapphire window)}. \tag{3.23}$$

With this information, the actual infrared laser power I_{trap} in the trap center can be estimated from the power meter measurement I_{dump} to be

$$I_{trap} = \frac{1}{T_1 T_2} \, I_{dump} \approx 1.22 \cdot I_{dump}. \tag{3.24}$$

Typically, laser powers I_{dump} between 100 to 800 mW were used at 1064 nm in the experiments, resulting in up to 1 W or 20 mJ per pulse at 50 Hz in the trap center. The dye laser was operated with Sulforhodamine B covering a wavelength range from 585 nm to 610 nm, but usually 600 nm (2.04 eV, orange) was used. For slightly lower energies, the laser dye DCM covered a range from 600 nm to 660 nm and was mainly used at a wavelength of 635 nm (1.95 eV). The laser powers from the dye were significantly lower reaching at most 100 mW on the power meter.
However, for the reported experiments with SF_6^- only the fundamental photon energy at 1.165 eV was used. The higher energies were also applied for photo-excitation measurements with SF_6^-, but no delayed electron detachment signal could be observed, concluding that the SF_6^- ions were excited to a too high internal energy (compare Sec. 4.3).

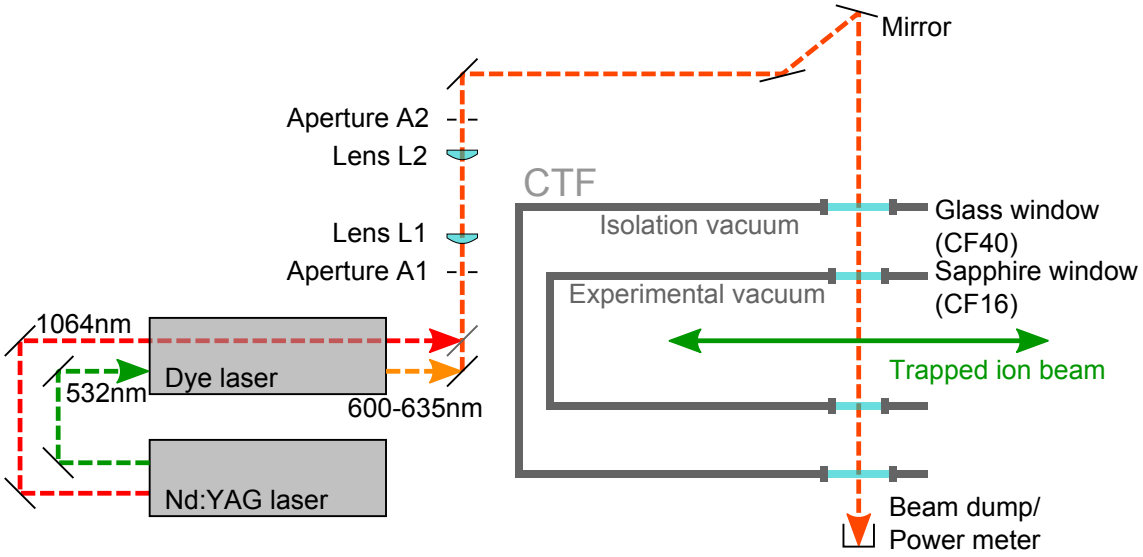

Figure 3.17: In the CTF laser setup the photon energies from the Nd:YAG laser can be used either directly or to pump a dye laser in the case of the 532 nm beam. The laser beam is expanded in a Galilean telescope consisting of two lenses and any resulting halo is removed by apertures resulting in a parallel beam of about 1-1.5 cm diameter, which is guided into the CTF through viewports on both the isolation and experimental vacuum chamber and crossed with the stored ion beam.

3.5 Phase space imaging via photo-detachment

The position sensitive, cryogenic delay line detector in the CTF was constructed and taken into operation particularly with regard to the use of similar detectors in the presently assembled Cryogenic Storage Ring (CSR). Here, the position and time information for ions and electrons will be used to gain full 3D reaction information in the reaction-microscope and similarly for neutral fragments in dissociative recombination measurements using the electron cooler. Investigations under cryogenic conditions on the dark count rates, the saturation count rate limits were performed, which have been summarized in the previous section.
However, the availability of the new detector also made it possible in the present work to perform measurements on the ion beam properties in an EIBT by detecting neutral particles from the trap as a projection of the phase space occupied by the ions stored in the trap. Characterizing the effects on such measurements from the trap parameters or the ion injection allows a comparison to simulations and, in this respect, to obtain well controlled trapping conditions for extracting, for instance, signatures of molecular dissociation. A Kinetic Energy Release (KER) within a dissociating reaction will increase the angle between the fragments, particularly for those emitted perpendicularly to the ion's flight direction. Hence, a larger position spread of the detected neutrals may open the possibility to distinguish neutralization by electron detachment from dissociation.
The trap phase space was already introduced in Sec. 3.1.1 considering the transversal positions $x(s)$ and the angles $x'(s) = dx/ds$ of the trapped ions, both as a function of s, the longitudinal direction in the trap. The simulated phase space in the trap center using the electrode voltages in self-synchronizing mode is given in Fig. 3.4, from which the maximum transversal phase space volume, the trap acceptance A, can be obtained (Eq. (3.4)).
The position sensitive detection of the neutrals represents a projection of the occupied trap phase space on the detector, as the produced neutrals propagate on with their momentary velocity. However, the shape and volume of the phase space changes in the course of the ion oscillation in the trap and hence, the detected neutral signal is obtained as a superposition of neutrals from ions at any location of the trap. These neutrals can be created for instance by spontaneous ion decay or induced by residual gas collisions. The first part here will be dedicated to those reactions.

3.5.1 Residual gas collision induced phase space measurement

In a room temperature investigation, a 6 keV O^- beam was trapped and the neutral counts, which were mainly induced by residual gas collisions, were recorded including the position information. Neutral position images are presented in Fig. 3.18 as a function of the horizontal and vertical position x and y, respectively, where the intensity is provided in linear arbitrary units with red being the highest intensity for each plot. For the following figures the scale will not be displayed, however, it is always defined in the same way. In figure 3.18(a), O^- was trapped for 1 s in the

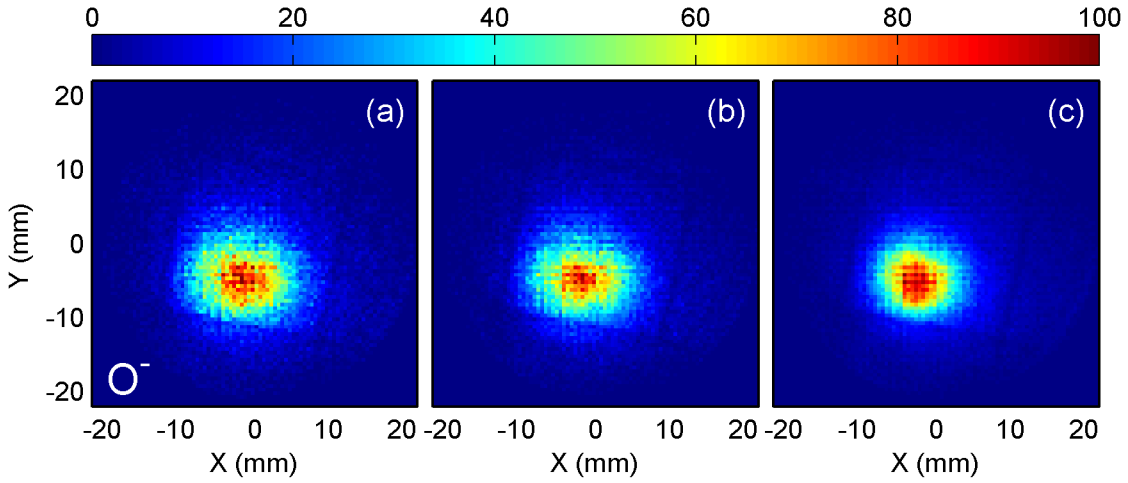

Figure 3.18: Neutral position image from trapped O^- ions summed for storage times between 0.01 s and 1 s: (a) trapping mode I (self-synchronizing), (b) with the voltages on the electrodes B reduced by 100 V, and (c) trapping mode II with further lowered electrodes B by 100 V. A successively narrower spot is observed. Trapping modes are also summarized in table 3.2. The color scale is always in arbitrary units, where red is the highest intensity for each single plot. In the following plots the scale will not be displayed, but is defined always in the same way.

usually applied self-synchronizing mode (mode I). This mode has been optimized in previous studies to a high ion trapping capacity and for excellent ion bunch retaining properties. With a weaker intensity than in the central spot, most of the 40 mm MCP detector surface is illuminated by the neutrals, also unveiling the calibration grid with a 12.25° tilt (compare also Fig. 3.14). The large spread of this background profile leads to the conclusion that heavy residual gas scattering must influence the trapped ion trajectories.

When the voltage on the trap internal einzel lens (electrode B in Fig. 3.3) is lowered from 5536 V by 100 V and 200 V, respectively, a successively smaller spot of neutrals is observed as shown in Fig. 3.18(b) and (c). A further reduction of the voltage on B leads to a strong decrease in the number of trapped ions and insufficient statistics for a good measurement. The obtained trapping mode in (c) provides the desired properties in terms of an improved localization of the neutral spot with a still sufficient number of trapped ions, and is in the following referred to as mode II.

As a next step, for mode II, the stability of the neutral position image as a function of ion injection parameters is analyzed, which is important for the reproducibility of the trapping conditions. The focusing of the injected ion beam is manipulated by lowering the ion source einzel lens from the standard voltage of 3000 V (a), to 2500 V (b) and finally also to 0 V (c), depicted in Fig. 3.19, still trapping O^- in mode II. Minor effects are observed for small variations between (a) and (b). However, in Fig. 3.19(c) without the einzel lens focusing the neutral position image clearly looses its sharpness. Thus, the ions in the trap phase space seem to be more uniformly distributed compared to the focused injection. It is interesting to see that the neutral fragment imaging serves as a tool to optimize the focusing and injection distribution.

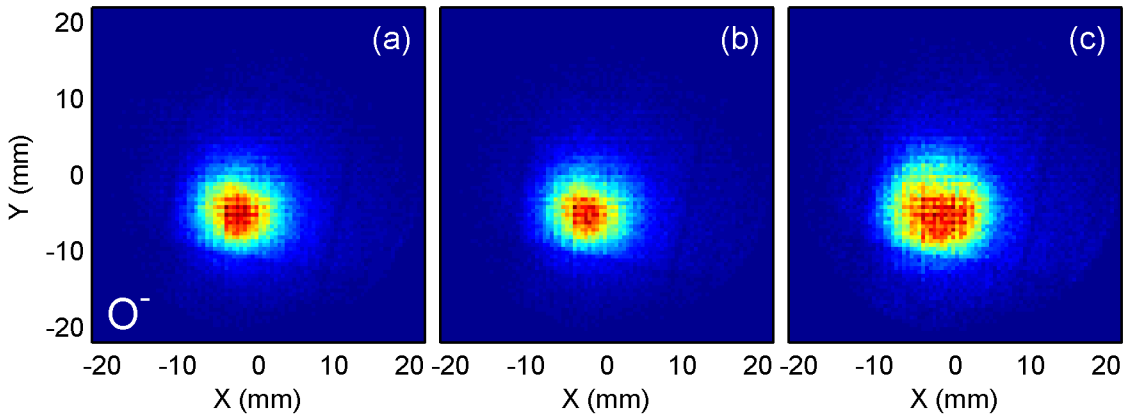

Figure 3.19: (a) Neutral position image from trapped O^- in mode II, (b) Reduced ion source einzel lens voltage from 3000 V to 2500 V leading to a less focused injected ion beam, and in (c) without the focusing effect from the einzel lens (0 V).

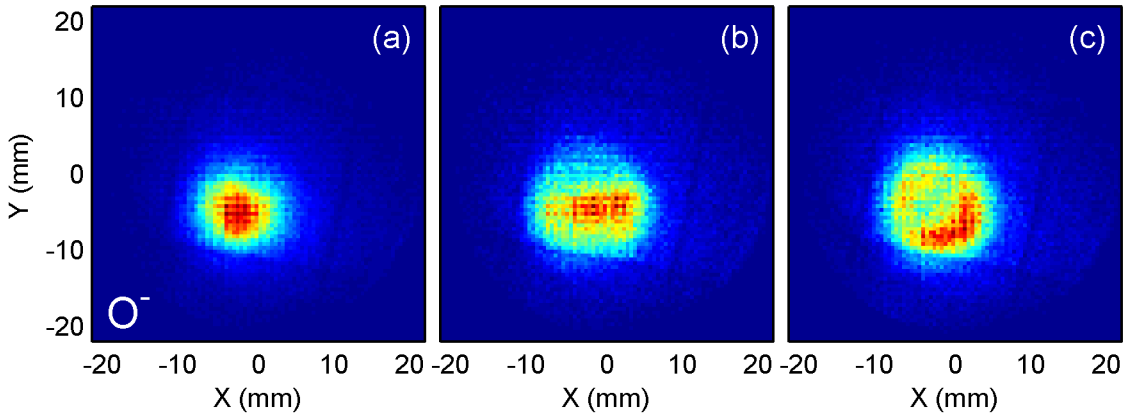

Figure 3.20: (a) Neutral position image from trapped O^- in mode II, (b) injected ion beam was steered to the right using the third quadrupole, (c) steered ion beam to the bottom

The phase space can also be occupied asymmetrically when the injected ion beam is deflected towards one side. This was realized by changing the third electrode pair of the electrostatic quadrupole triplet (see Fig. 3.7 for its location), and deflecting the beam towards the right side as illustrated in Fig. 3.20(b). The injected ion beam is only matched with the right side of the phase space and populates it symmetrically along the y axis. Similar effects are found when the beam is deflected downwards, as it is shown in Fig. 3.20(c), however, here the phase space seem to be matched on the bottom right side and a diagonal occupation is observed.
On the one hand side, the observation nicely demonstrates, that the trap phase space can be decreased by varying the trap voltages and differently occupied by the ion injection. However, on the other hand, careful ion injection is required to provide a symmetric population of the phase space, which could otherwise obstruct the observation of dissociation. In the following, detailed information on the size and shape of the occupied phase space will be obtained by using the projected neutral

signal on the detector via photo-detachment of the trapped ions.

3.5.2 Photo-detachment induced phase space measurement

In the previous measurements with O^-, the neutral signal was given as a superposed signal from different trap locations, and is not feasible for an exact determination of the occupied phase space. To fix the position and time at which neutrals are created, laser pulses were used to photo-detach the stored ions in the trap center. Moreover, to reduce the residual gas collisions from the previous study, the following measurements were performed under cryogenic conditions, thus with one or two orders of magnitude lower vacuum pressures in the trap.
O_2^- was found to exhibit perfect features for such an experiment. Besides its high production yield in the utilized ion source, the electron affinity is found in an ideal range for photo-detachment. The latest calculation provides a value of EA = 0.448±

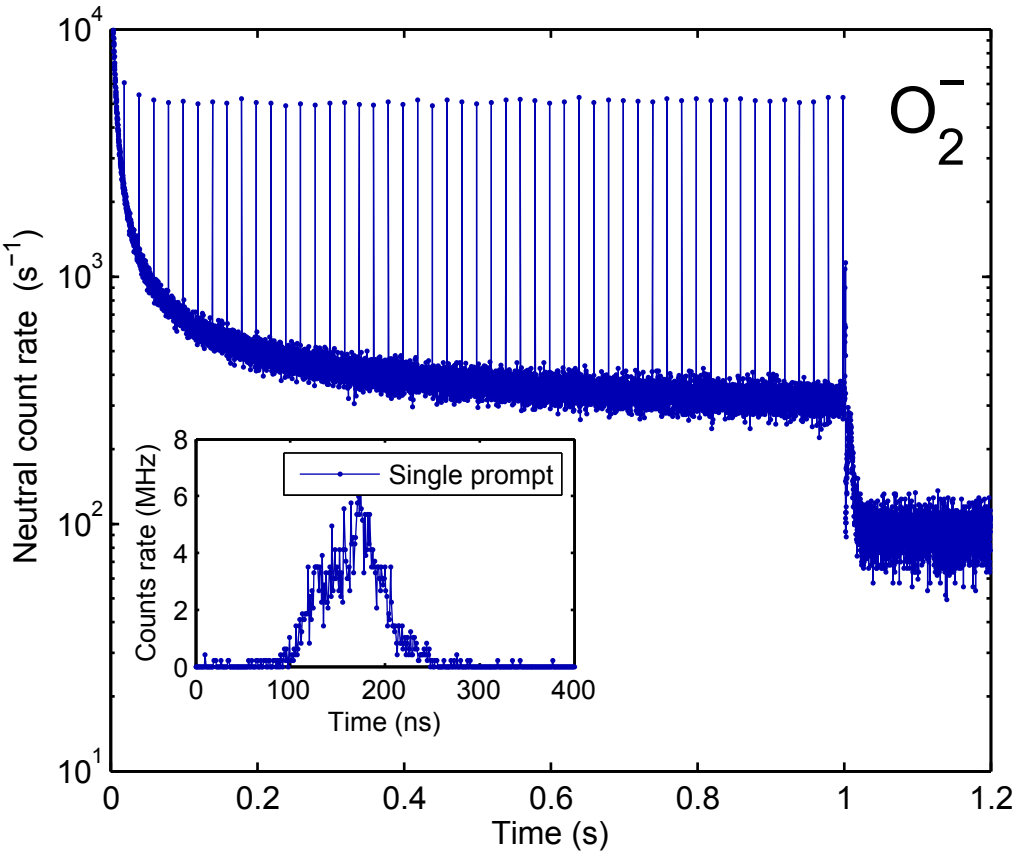

Figure 3.21: Neutral count rate from a trapped 6 keV O_2^- ion beam under cryogenic trap conditions: The equidistant neutral signals from photo-detached O_2^- with a laser energy of 1.165 eV is observed. The shape of the decay curve is due to a VAD process from thermally excited O_2^-. The inset shows one single neutral signal from the photo-detachment using a high resolution binning of 1 ns. The width can be used to determine the laser diameter and beam overlap (see text).

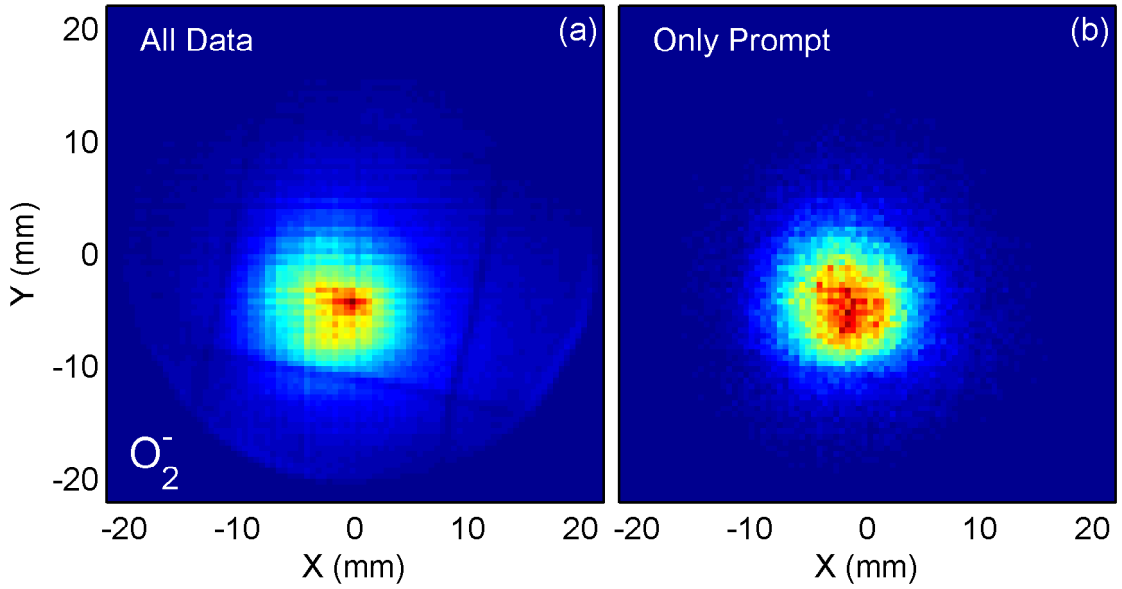

Figure 3.22: Neutral position image for trapped O_2^- from Fig. 3.21: (a) all counts between 0.01 s and 1 s of the ion storage; (b) only the signal from the photo-detached O_2^- in the trap center by a time cut around the prompt peaks.

0.006 eV [123] which is also in excellent agreement with previous calculations and measurements. The quantity is low enough for photo-detachment by the employed laser wavelength of 1064 nm (1.165 eV), but also high enough to provide a stable anion.
The O_2^- dissociation energy of $E_D = 4.104 \pm 0.006$ eV [123] exhibits a fairly high value and thus, the observed signals are not obstructed by a possible kinetic energy release within the decay. Also electronically excited states of O_2^- below the neutral ground state of O_2 have not been observed, which might otherwise influence the neutral ion yield over time. However, a vibrational auto-detachment signal is observed from excited O_2^-, whereas for auto-dissociation the energy threshold is assumed to exceed the excitation.
One has to note that a contamination by in parallel trapped sulfur anions S^- with the same atomic mass of 32 u cannot be excluded. However, the higher electron affinity of sulfur of EA = 2.077103 ± 0.000003 eV [124] suppresses the effect of these ions (although it would even not disturb the present study).
Figure 3.21 reveals the neutralization signal from the VAD decay for a trapped O_2^- beam overlaid by the neutrals from photo-detached O_2^-. The pulsed Nd:YAG laser was operated at a wavelength of 1064 nm (1.165 eV) using an average laser power of 490 mW and a constant pulse repetition rate of 50 Hz with pulse length of 15 to 20 ns.
The inset in Fig. 3.21 presents a high resolution signal of 1 ns from a single peak of the direct neutrals from the photo-detachment. The width of the peak of about 90 ns and can be used to obtain the diameter of the laser beam in longitudinal trap direction. The fraction of trapped ions which is irradiated by the laser pulse and neutralized propagates on with its former velocity corresponding to 6 keV in the

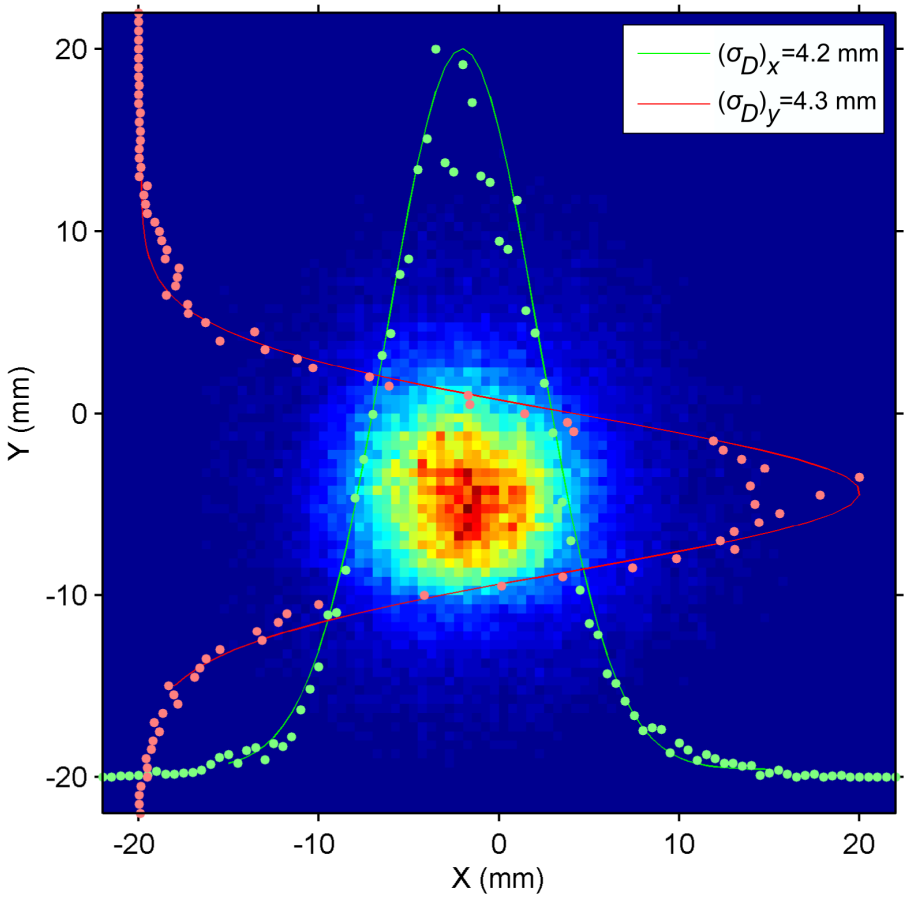

Figure 3.23: Enlarged view from Fig. 3.22(b) with overlaid x and y profiles by summing counts between ±2 mm around the center in the respective perpendicular direction. From the applied Gaussian fits a distribution width of $(\sigma_D)_x = 4.2$ mm and $(\sigma_D)_y = 4.3$ mm is derived.

trap center. For O_2^- at this energy the velocity is 190 mm/μs, which in the analysis leads to a laser diameter of ∼17 mm. However, uncertainties in the time are given by the duration of the laser pulse of about ∼20 ns and by the energy uncertainty of the ions. The latter one is assumed to be ∼12 eV [125] from the ion source and thus, a velocity uncertainty of ∼0.3%, and a time uncertainty of ∼18 ns after the drift distance of 870 mm to the detector is obtained. All distributions are assumed to be Gaussian and the widths are added quadratically. This leads to a temporal width of ∼86 ns from the laser and ion beam overlap only, and a slightly smaller laser beam diameter of ∼16 mm is obtained, although the largest error is expected from the energy uncertainty.

Without the additional photo-detachment the position image of the neutralization rate is a superposition of neutrals of the VAD-decay, of collisional-induced ion loss and can originate from any location of the trap phase space. In contrast, when a time cut is applied and only the direct photo-detachment signals (prompt) from the trap center are selected, an undisturbed spatial profile of the neutral signal from

O_2 after photo-detachment is obtained. These profiles are compared in Fig. 3.22, where (a) gives the total count rate between 0.01 to 1 s of the ion storage and (b) is obtained by a microsecond time cut around each prompt signal. The broad background spectrum, which extends even to the calibration grid in (a), completely disappears in (b) and a very symmetric neutral spot is obtained.
An enlarged view on the prompt distribution is shown in Fig. 3.23 with an overlaid profile in x and y direction. Each profile was created by summing over a slice with a width of ± 2 mm from the maximum of the distribution in the corresponding perpendicular direction. A Gaussian distribution was found to give the best match with the profile and widths of $(\sigma_D)_x = 4.2$ mm and $(\sigma_D)_y = 4.3$ mm were determined from the Gaussian fit ($\propto \exp\{-(x - x_0)^2/2\sigma_x^2\}$).
As a first conclusion one finds that the observed Gaussian profile also reflects the occupation of the trapped ions in the transversal phase space as the projection from the trap center retains the shape of the profile. Furthermore, from the very symmetric distribution and its size (considerably smaller than the laser beam diameter estimate above), one can conclude that the laser beam must have irradiated the full diameter of the trapped ion beam. The laser beam is injected in the y direction (compare Fig. 3.2 or Fig. 3.17), and in case of an only partly overlap with the ion beam, the x extension of the distribution would be reduced, but the y direction would maintain unchanged.

3.5.3 Calculation of the phase space projection

The projection of the detected beam width σ_D and the initial ion beam width in the trap σ_T can be related to each other by introducing the β-function, which is a trap specific parameter for a given set of electrode voltages and can be determined from simulations of the trap phase space. For the measurement with O_2^-, the trap voltages from table 3.2 for trapping mode II were used; mode I is the usually applied self-synchronizing mode.
The corresponding transversal phase space simulated for the trap center for the position x and the angle x' is shown for trapping mode II in Fig. 3.24 including exemplary ion trajectories as a function of the longitudinal position s on the left. The β-function [90] can be determined as

$$\beta_T = \left(\frac{x_{max}^2}{A_x}\right) = \left(\frac{x_{max}}{x'_{max}}\right) \approx 0.725\,\text{m (Mode II)}, \tag{3.25}$$

where x_{max} and x'_{max} are the maximum position and angle of the trap phase space, respectively, and in the second step, $A_x = x_{max}\, x'_{max}$ was used for the acceptance of an upstanding phase space ellipse. Here, the size of the acceptance was assumed to have the same extension as the largest, inner part of the phase space which still exhibits an elliptic, only slightly distorted shape. Here values of $x_{max} = 5.8$ mm and $x'_{max} = 8$ mrad are obtained. The outer ion trajectories are expected to be metastable, and ions cannot be stored for long durations. Detailed information on ion beam optics can be found in Ref. [90].
For a free drift without influencing electromagnetic fields, which is the case for

Table 3.2: Different ion trapping modes for 6 keV beam energies with corresponding electrode voltages and beam parameters are presented. Beam values for mode III give the maximum of the island and its maximum angle (compare Fig. 3.24).

Trapping Mode	U_B	U_D	U_E (V)	U_F	U_G	x_{max} (mm)	x'_{max} (mrad)	β_T (m)
I (self-synchronizing)	5536	2140	3995	6400	7817	4.6	14	0.329
II	5336	2140	3995	6400	7817	5.8	8	0.725
III (Ring mode)	5300	2140	3995	7000	7817	∼7	∼6	

neutrals after the photo-detachment of O_2^-, the β-function transforms as

$$\beta(s) = \beta_T + \frac{s^2}{\beta_T}, \tag{3.26}$$

where s is the longitudinal position. Together with the relation $\sigma(s) = \sqrt{\epsilon\beta(s)}$ (which holds [90] both at the trap center and at the detector position), one obtains the ion beam size in the trap center as

$$\sigma_T = \sigma(s)\,\frac{1}{\sqrt{1+\frac{s^2}{\beta_T^2}}}, \tag{3.27}$$

where $\sigma(s)$ is the beam size at position s.
With an average beam width on the detector of $\sigma_D = 4.25$ mm from Fig. 3.23, the corresponding β-function from table 3.2 for mode II and a detector distance of $s_D = 0.871$ mm from the trap center, one obtains the trapped ion beam width and angle in the trap center:

$$\begin{aligned} \sigma_T &= \sigma_D \cdot 0.64 \approx 2.72\,\text{mm}, \\ \sigma'_T &= \sigma_D \cdot 0.88 \approx 3.75\,\text{mrad}, \end{aligned} \qquad \text{(Mode II)}$$

where for the angle $\sigma'_T = \sigma_T/\beta_T$ was used.
Typically, the 2σ-emittance is provided in accelerator or ion storage ring physics [90], and contains 86.5 % of the total ion beam (see also Eq. (3.5)). Accordingly, the 2σ-emittance is here given by $\epsilon^{2\sigma} = 4\,\sigma_T\,\sigma'_T = 41$ mm mrad and is found to be slightly smaller than the trap acceptance of $A = x_{max}\,x'_{max} = 46$ mm mrad. The corresponding phase space ellipses for the assumed trap acceptance and the derived beam emittance are illustrated in Fig. 3.24.
However, the derived and characterized trap settings still provide a too dispersed neutral distribution on the detector. On the one hand side small variations in the distribution from a possible kinetic energy release will be obscured by the angular uncertainty. On the other hand, also a reproducible, symmetric ion injection into the trap center is required, which cannot be verified if an unknown molecular system is investigated due to the superposition with the kinetic energy release.

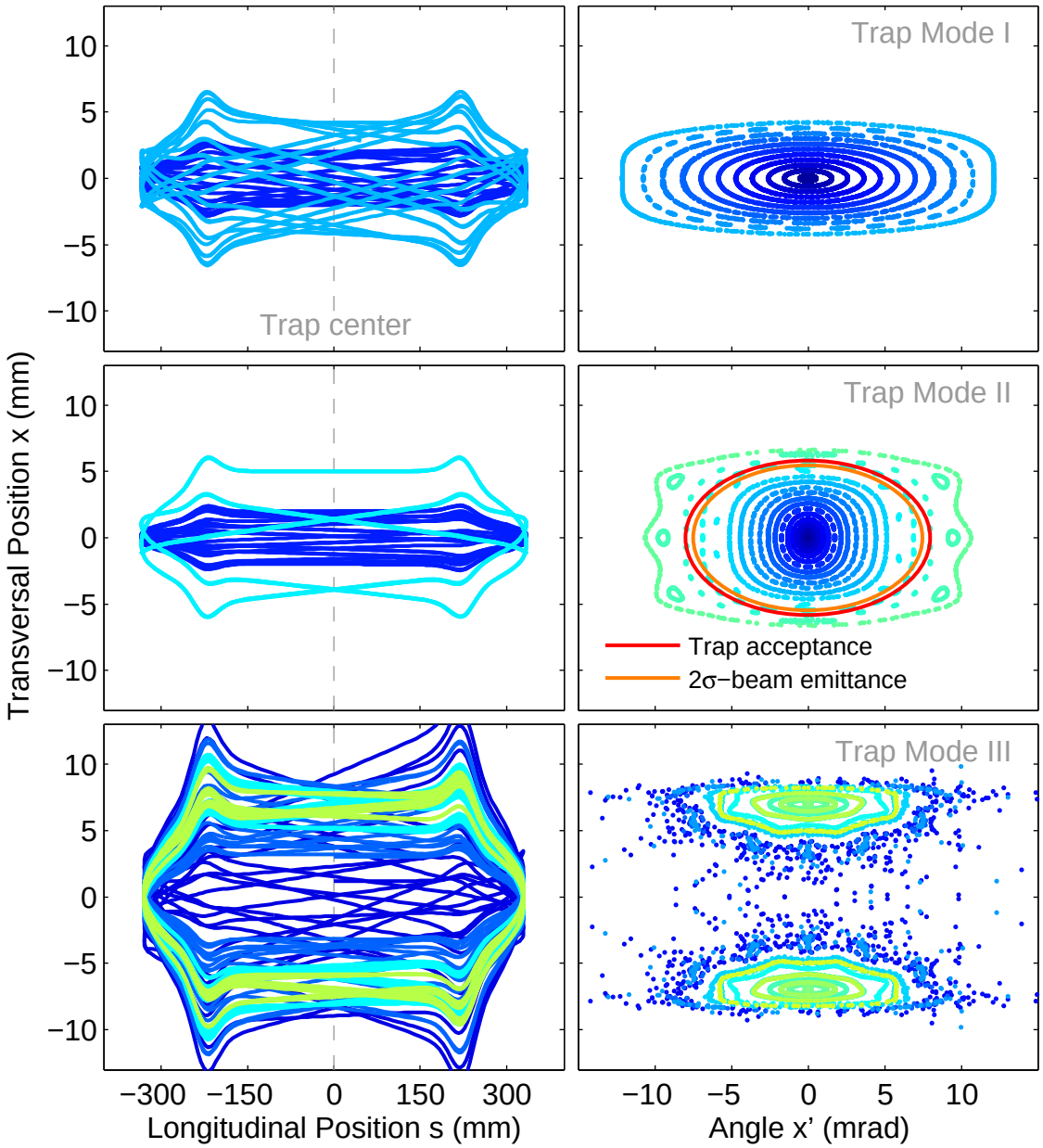

Figure 3.24: Comparison of different simulated trapping modes from table 3.2: On the left exemplary ion trajectories are shown as a function of the longitudinal trap position s and the transversal position x. On the right side is the corresponding phase space; here rotated compared to typical representations to match with the ordinate for x on the left side. For trap mode II the reprojected values for σ_T and σ'_T from the Gaussian fit from Fig. 3.23 are indicated as a red ellipse.

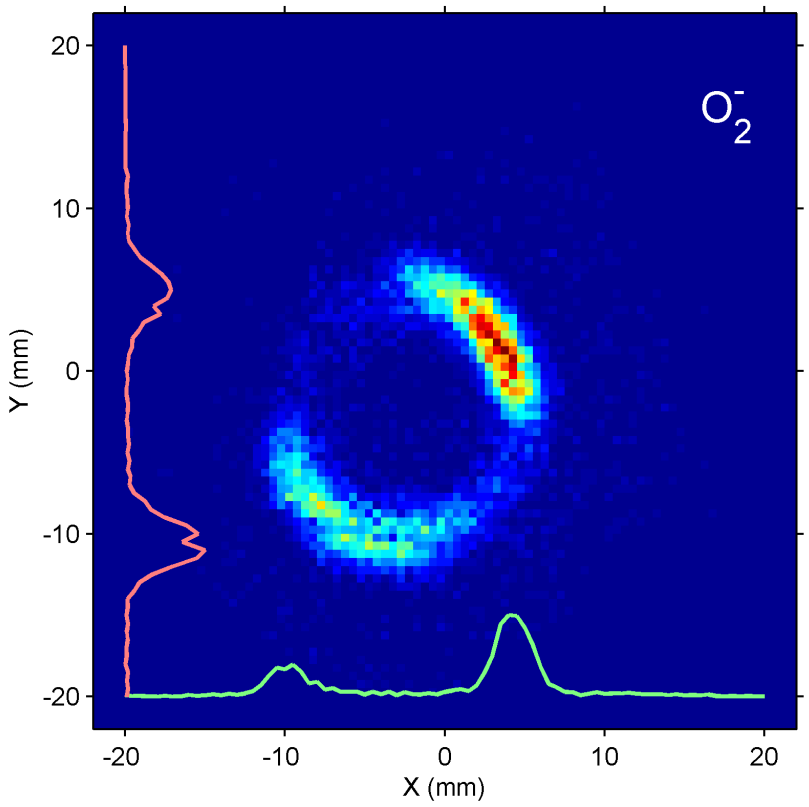

Figure 3.25: Prompt signal of the neutral profile of photo-detached O_2^- from the trap center for storage times between 0.01 s and 2 s applying trapping mode III. The clear observation of a ring shape is in excellent agreement with the predictions from the simulation (see Fig. 3.24).

3.5.4 The ring-shaped trapping mode

In the course of this study, a new trapping mode was discovered, which might have improved properties to the previously introduced one. Here, the ions are trapped with a smaller angular distribution in the phase space and at the same time maintain a feasible phase space volume. In figure 3.25, the neutral profile from trapped O_2^- ions under cryogenic trap conditions is shown applying the trapping mode III from table 3.2 and selecting only counts of the photo-detached O_2^- ions from the trap center.
Here, a clear ring shaped structure of the neutrals appears. The same trapping mode was also investigated by simulations obtaining the phase space distribution for mode III in Fig. 3.24. Here, the phase space is mainly divided into two islands with rather large transversal distances from the center. Due to the radial symmetry of the trap, the ions are stored in a halo without stable trajectories on the symmetry axis. Because of the small angular deviation of only $\sim \pm 6$ mrad for each island, a sharp projection of the halo from the trap center is observed as a ring in the neutral profile on the detector. The radius of the ring profile is found in good agreement with the simulations.

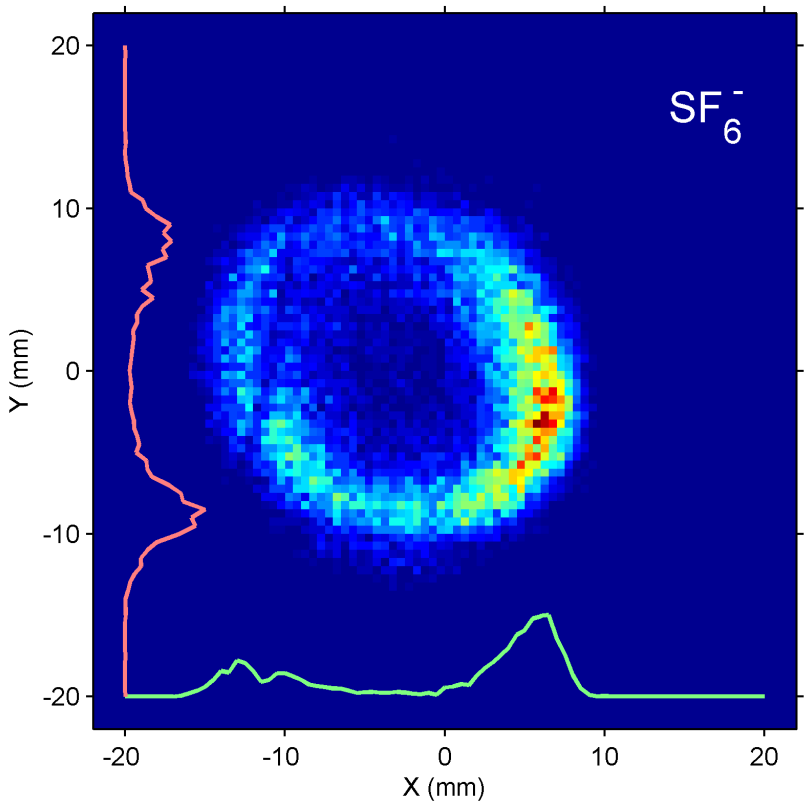

Figure 3.26: Prompt signal of the neutral profile from photo-destructed SF_6^- for storage times between 0.1 s and 2 s applying trapping mode III. The ring shaped profile exhibits a slightly larger extension compared to the profile from O_2^- in Fig. 3.25.

The asymmetric intensity in Fig. 3.25 is generated by the beam profile of the injected ions to either of the two sides; the upper right or lower left side. In this way a higher amount of ions can be stored compared to an ion injection into the trap center. The overlaid profiles in Fig. 3.25 were obtained as previously by summing the counts over a width of ±2 mm around the center of the ring in perpendicular direction.
In contrast to the previously discussed trapping mode II, a localized structure of neutrals is obtained on the detector, which is supposed to enhance the sensitivity for signatures of a kinetic energy release in fragmentation. In this case, an additional broadening of the distribution is expected depending on the value of the KER.
As a test measurement, SF_6^- was also trapped in mode III and photo-detached and photo-dissociated in the trap center. The derived data including statistics of one complete day, is presented in Fig. 3.26 for storage times between 0.1 s and 2 s using only the prompt neutrals after each laser shot. Also here the proposed ring shape for mode III is obtained and the asymmetry in the phase space occupation is rotated due to different injection settings.
Estimates on the value of KER for the dissociation channel $SF_6^- \rightarrow SF_5^- + F$ can be obtained by considering the energy thresholds, which are for instance displayed in Fig. 2.2. After the initial VAD decay is over, only SF_6^- ions with internal energies

below the electron affinity EA are left in the trapped ion ensemble. Thus, the maximum KER is found for SF_6^- ions with internal energies of EA and is KER_{max} = EA + E_{ph} − E_D = 0.755 eV, where the photon energy is E_{ph} = 1.165 eV, the dissociation threshold E_D = 1.44 eV and EA = 1.03 eV. However, as illustrated in Fig. 2.16, the maximum of the internal energy distribution after 100 ms is expected to be at about 0.5 eV due to the energy loss of the ions by radiative cooling. Here, the KER is found at only ∼0.2 eV. It is not unreasonable, that vibrational energy also remains in the SF_5^- product, as also more decay channels for excited SF_5^- are available and this further reduces the value for KER.
We will derive the maximum emission angle of the neutral fluorine for some values of the KER, thus for the case of a transversal dissociation with respect to the direction of the detector. Due to energy and momentum conservation in the dissociation process, the kinetic energy of the fluorine is $E_F = (m_F/m_{SF_6^-})\, E_{SF_6^-}$ = 871 eV. Using the longitudinal momentum of the neutral fluorine in the direction of the detector $p_F^s = (2\, m_F\, E_F)^{1/2}$ and the maximum transversal momentum $p_F^x = (2\, m_F\, m_{SF_5^-}/m_{SF_6^-})^{1/2} \times KER^{1/2}$, one finds the maximum transversal emission angle

$$\Theta_{max}^x = \frac{p_F^x}{p_F^s} = \left(\frac{m_{SF_5^-}}{m_{SF_6^-}} \frac{KER}{E_F} \right)^{1/2} . \tag{3.28}$$

Accordingly, for values of KER of 50 meV, 200 meV and 755 meV, transversal emission angles of the neutral fluorine are determined at 7 mrad, 15 mrad and 29 mrad, respectively. The projection of these emission angles on the detector, assuming a SF_6^- beam that is parallel to the symmetry axis of the trap, leads to radial distances of the neutral F of 6.5 mm, 13 mm and 26 mm from the symmetry axis. In conclusion, in case of a kinetic energy release and the detection of the neutral fluorine atoms, the observed ring profile of SF_6^- in Fig. 3.26 would become broader compared to the one from O_2^- in Fig. 3.25, however, the position of the rings should stay the same.
To characterize and compare both measurements, O_2^- and SF_6^-, the radial profiles were determined by deriving the distance $r = (x^2 + y^2)^{1/2}$ of each neutral count from the center of the ring and creating a histogram. The center was determined by comparing radial profiles for different proposed center positions and the narrowest radial profile was assumed to give the best approximation of the center position.
The results are given in Fig. 3.27, where one has to note that not the same center values has been derived for O_2^- and SF_6^-. As already visually observed in the neutral position image, the SF_6^- distribution exhibits a broader distribution indicating the presence of dissociation, but also a larger radius is observed. However, even though the differences are clearly visible in the radial profile, an enhanced uncertainty is expected from the determination of the ring centers. In section 4.3, a reasonable explanation will be found that the neutral dissociation product fluorine is detected with a reduced efficiency compared to the SF_6 from the detachment process. Thus, also in the measurement of the ring profile, the signatures of the dissociation might be obstructed by the detachment signal. To apply this method as a distinctive measurement between detachment and dissociation, further investigations have to be performed, in particular employing the trapping mode to a well-known model

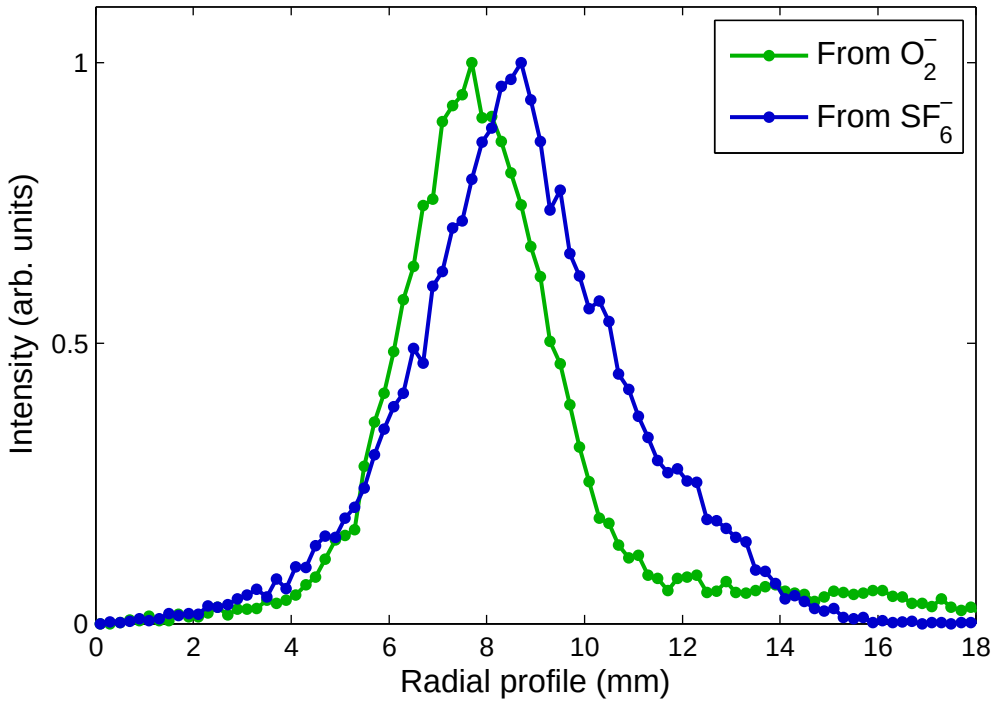

Figure 3.27: Comparison between the radial profiles from the ring shaped position images from Fig. 3.25 and Fig. 3.26. The profiles were derived by creating a histogram using the radial distances $r = (x^2 + y^2)^{1/2}$ for each neutral count from the center of the ring. Clear differences are observed, however, uncertainties are present due to the determination of the centers.

system.
In conclusion, different trapping modes have been investigated using the position sensitivity of the cryogenic detector. Influences on the injection parameters could convincingly be revealed in the neutral signal, but also pose the problem to apply reproducible, symmetric ion injection settings. The balance between the number of ions to be trapped for sufficient statistics and the localized neutral signal on the detector, led to the discovery of the ring shaped trapping mode. Here, ions are only trapped with an extended distance from the trap center, however, with a narrow angular uncertainty and thus, a well defined projection of the neutrals on the detector is obtained.
Signatures of the SF_6^- dissociation have been found, but the method is yet not evolved enough to clearly claim the observation. Similar experiments will be available under improved conditions in the Cryogenic Storage Ring CSR, as here phase space cooling can be applied with the electron cooler and a narrower ion distribution is obtained to start with.

Chapter 4

Experiments on SF_6^-

This chapter presents the experimental results obtained in this work with the Cryogenic Trap for Fast ion beams (CTF) in Heidelberg. The experimental setup has been introduced in the previous chapter 3.
First, the measurement procedure is described for the investigation of the process of vibrational electron auto-detachment (VAD) of SF_6^-, which was obtained with previously unattained precision and extended observation times exceeding ∼100 ms. Various systematic studies were performed to characterize the dependencies of this decay and theoretically reconstruct the decay curve of the VAD process for the first time using a microscopic model. The experimental results have motivated the choice of the applied detailed model which was introduced in chapter 2. In particular we will show that the adiabatic electron binding energy can be reliably extracted from the electron auto-detachment rates, which were measured at different ion source conditions. The second part of this section presents the experimental procedure for the measurements on laser-induced delayed electron detachment of SF_6^-.

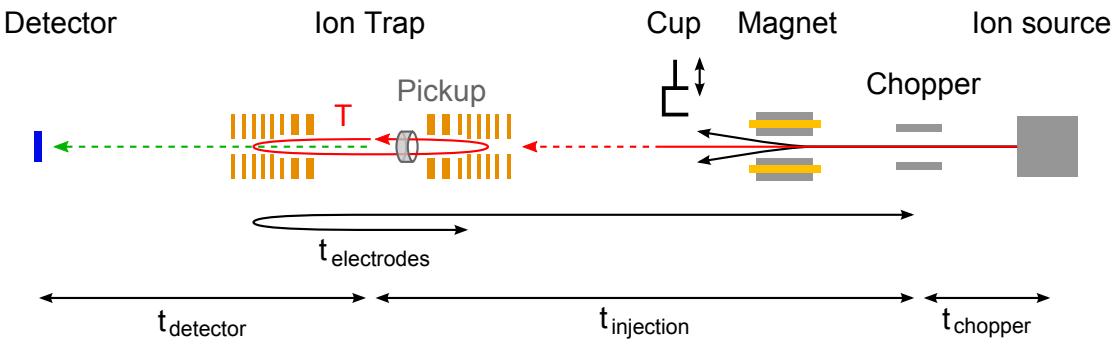

Figure 4.1: Schematic setup of the CTF and the ion injection (the detailed setup is displayed in Fig. 3.2 and Fig. 3.7); typical values for the propagation times t_x for SF_6^- ions and the oscillation time T are given in table 4.1.

Table 4.1: Characteristic values for the storage of SF_6^- ions; the ion propagation times t_x to elements x as labeled in Fig. 4.1 with frequency f and period T for the oscillation in the ion trap.

Property	Unit	Value
SF_6^- mass	u	145.963038
Kinetic energy	eV	6000
Velocity	mm/μs	89.064
T	μs	20.15
f	kHz	49.63
$t_{chopper}$	μs	7
$t_{injection}$	μs	48
$t_{detector}$	μs	10
$t_{electrodes}$	μs	65

4.1 Measurement procedure

A schematic representation of the CTF setup is depicted in Fig. 4.1, which includes only essential components such as the ion trap, the beam chopper and the dipole magnet. The corresponding characteristic time scales for the case of SF_6^- are summarized in table 4.1. Measurements were performed at 300 K and at 12 K trap temperature using SF_6^- ions with a kinetic energy of 6 keV.

4.1.1 Ion injection

Negative ions are produced in the MISS ion source (see Sec. 3.2.2) and immediately accelerated without accumulation. The measurement cycle itself is triggered by the signal used to activate the following beam chopper, which is located at a distance of 0.61 m from the source center. Up to the beam chopper a continuous ion beam is transported from the source, which experiences at first a 20 kV acceleration, focusing by an einzel lens, and then deceleration to the final kinetic energy of 6 keV. The approximate flight duration of the extracted ions between the source target and the beam chopper is $t_{chopper} \sim 7$ μs for SF_6^-.
The beam chopper consists of two opposing horizontal plates, to which a set of voltages is applied, to deflect the ion beam. By quickly switching these voltages between a "pass" and a "block" setting, a short ion pulse of a few microseconds is transmitted. While ion pulses of approximately 20 μs duration are needed for the experiment, for diagnostic purposes a d.c.-beam is transmitted, which is then observed on the Faraday Cup behind the dipole magnet (see Fig. 3.7). A step-wise variation of the magnetic field strength enables a scan over the different ion masses produced by the source and their selection for the experiment. More precisely, the mass over charge ratio m/q is determined, but small multiply charged negative ions are very rare and would require special care in the production or a certain minimum

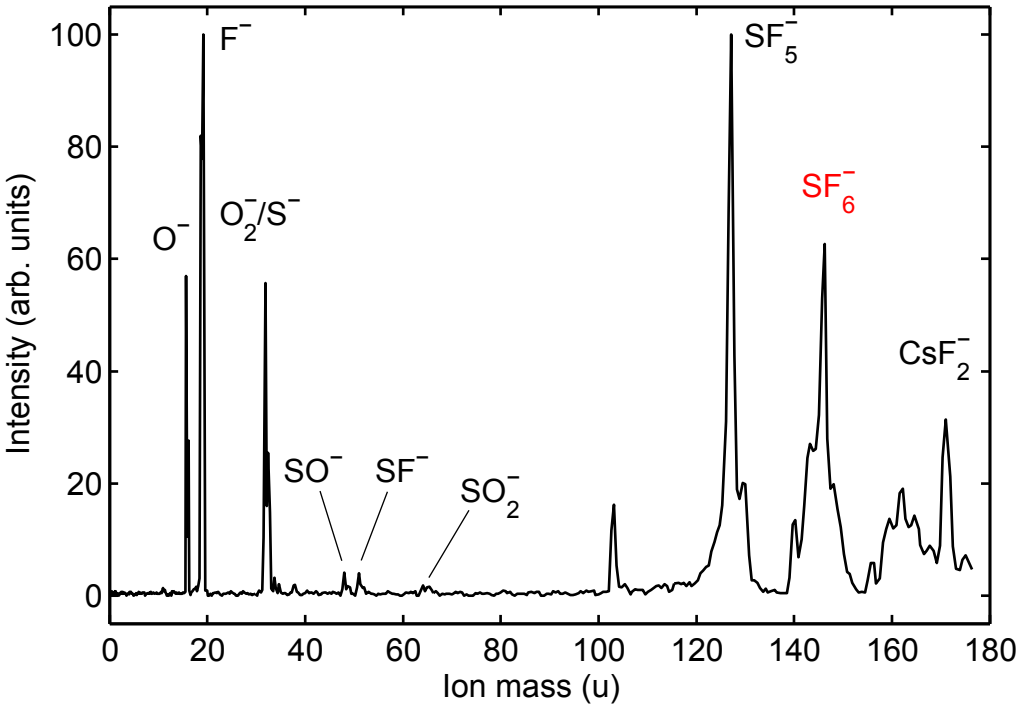

Figure 4.2: Wide range mass scan with the dipole magnet using a 6 keV ion beam: Besides SF_6^-, anions composed of sulfur and fluorine from the SF_6 production gas and a contamination from oxygen are observed.

cluster size [126–128], so that the selection of m/q effectively translates to a mass selection.

4.1.2 Mass selection

A sample mass scan of a 6 keV ion beam from the cesium sputter ion source MISS with a drilled molybdenum target and SF_6 as a production gas is shown in Fig. 4.2. Oxygen is usually found as a contamination coming from oxidized surfaces or from water, however, its abundance in the beam reduces during operation. On the other hand, small atomic anions are very valuable for test measurements, where high currents and ions without internal excitation are required. Besides different anions composed of sulfur and fluorine also SF_5^- is found in high amounts, supporting the later assumption of high excitation energies in the ion production process which leads to dissociation of the SF_6^-. While no atomic Cs^- has been observed, a contribution of CsF_2^- has tentatively been identified by its mass.

4.1.3 Ion trapping

For ion trapping, the beam chopper is used to create an ion bunch of a few microseconds, which is then guided to the ion trap. After it has passed the initially grounded entrance mirror of the trap, its voltages are switched on before the reflected ions can leave the trap (depicted by $t_{electrodes}$ in Fig. 4.1). The typical time

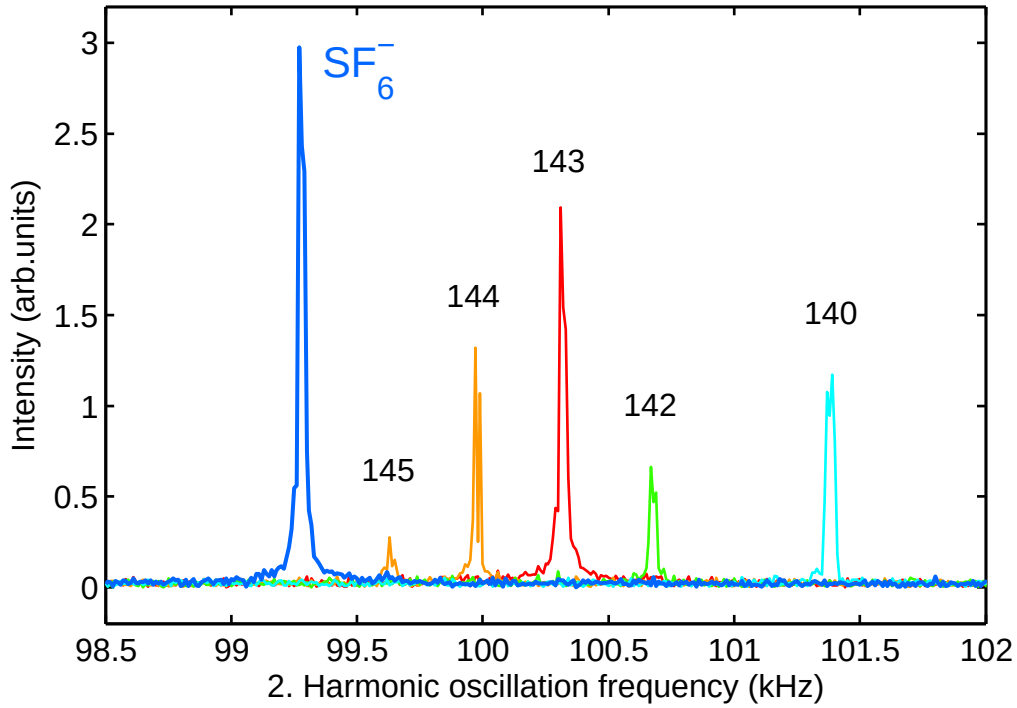

Figure 4.3: Fast Fourier transform of the amplified pickup signal for a stored SF_6^- beam and other neighboring ion masses taken by independent measurements. The lower masses could be combinations of SF_5^- with water, OH and O, respectively. An impurity in the peak with the mass 146 (SF_6^-) is not expected.

scales for SF_6^- are given in table 4.1. The ion bunch length defined by the chopper is usually chosen almost as long as the oscillation period ($T \sim 20\ \mu s$) to ensure high ion numbers in the trap. Ions situated *in* the entrance mirror when the voltages are switched on experience an acceleration and will be lost from the trap. Thus, the trap is never entirely filled longitudinally upon an injection, which can be interpreted as a very long bunch being stored in the trap. The dispersion of the bunch due to space charge effects, the energy spread of the beam and different path lengths of the ion trajectories in the trap will lead to a continuously filled trap within a few milliseconds. Except for measurements with the laser, the ions were always stored in the self-synchronizing trapping mode (mode I in table 3.2 and Fig. 3.24).

4.1.4 Pickup signal

The number of trapped ions can be non-destructively monitored by the mirror charge they induce on a cylindrical pickup electrode close to the center of the trap. The amplified signal is observed on an oscilloscope to determine the position of the ion bunch and the frequency spectrum is obtained by a numerical fast Fourier transform (FFT) of the signal.
A small part of the frequency spectrum of a trapped SF_6^- beam is presented in Fig. 4.3 together with the spectra from the storage of other neighboring ion masses. Here, each color corresponds to a different setting of the dipole magnet as set in the

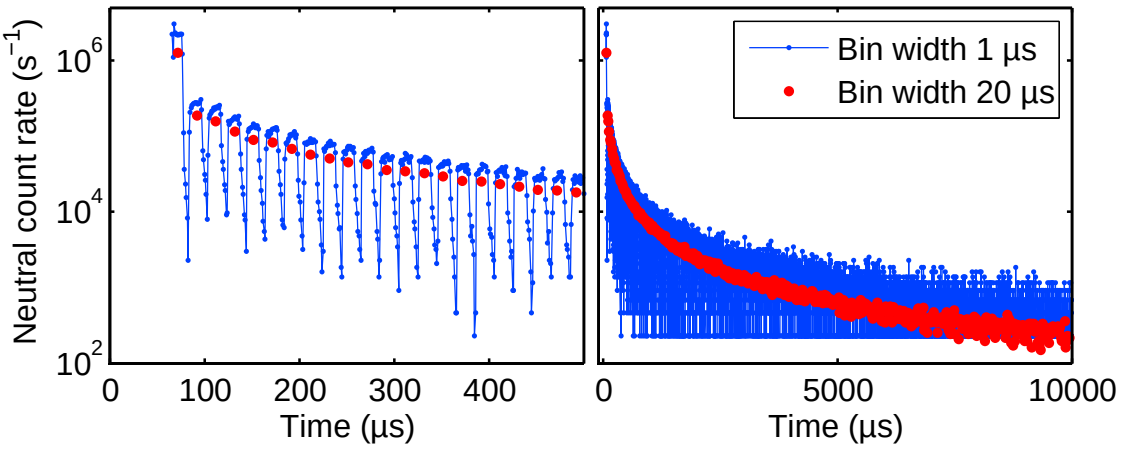

Figure 4.4: Neutral detector count rate for a trapped SF_6^- beam in the first 500 μs and 10 ms revealing the bunch structure for early trapping times.

separate measurements. Thus, through the monitoring of the oscillation frequencies a possible contamination can be identified. The lower ion masses next to SF_6^- could be combinations of SF_5^- with water, OH and O, respectively, however, they do not influence the mass signal at 146 u (SF_6^-). One should also note that this analysis is always performed at the second harmonic frequency of the signal, which usually shows the strongest amplitude since the beam crosses the pick-up twice each orbit.

4.1.5 Detector count rate

The primary experimental observable for the VAD process of SF_6^- is the count rate of neutral particles on the micro-channel plate (MCP) detector placed behind the trap exit mirror in a distance of ∼87 cm from the trap center. In this detection scheme, half of the resultant neutral SF_6 are moving towards the detector; the other half is moving towards the entrance mirror and cannot be detected. Otherwise, all neutrals which are created in the field free region between the trap mirrors are expected to arrive on the detector. This can be seen from the spatial distribution of particle hits on the detector plane (compare figures 3.4 and 3.10).
On the other hand, in the trap lenses and near the ion turning points in trap mirrors, the angular distribution widens and the ion kinetic energy is reduced, suppressing the detection of neutral decay products originating from these locations. Typical MCP detection efficiencies are found to be rather independent of the particle mass or charge [75, 76], but are energy dependent with approximately 50% for an energy of 6 keV and about 10% at 1 keV.
The neutral detector count rate as a function of time for the first 500 μs of the ion storage is shown on the left in Fig. 4.4 and for 10 ms on the right. The neutral count rate is recorded as explained in Sec. 3.3, usually with a 1 MHz clock frequency resulting in a time resolution of 1 μs, which is sufficient for the purpose of the measurement. The periodic structure in the neutral count rate seen in Fig. 4.4 is determined by the trapped ion bunches. The first, more intense, neutral bunch at

$\sim$70 μs is caused by collisional induced neutralization of ions in the relatively high-pressure of the injection beam line as well as by neutralization due to the higher VAD rate for earlier times (as caused by initially high internal energies of the SF_6^- ions, see below).
The full-resolution count rate (in blue) is compared in Fig. 4.4 to the count rate binned with a bin width of 20 μs (in red), which corresponds to the ion oscillation time and eliminates a beating between the bunch structure and the binning, while grouping data points to reduce the statistical error. In the measurements below, thousands of ion injection and trapping cycles are typically performed for a specific setting to obtain appropriate statistics. The count rates are averaged over the number of injections and presented as a rate per second. The right plot in Fig. 4.4 shows the neutral rate over a longer time window and reveals the power-law character of the SF_6^- VAD, which will be discussed in detail in Sec. 4.2.

4.1.6 Storage lifetimes caused by residual gas collisions

Residual gas induced limitation of the lifetime of stored ions in the trap is reflected in an exponential decay characteristic of the neutral count rate $R(t)$ at long times ($t > 1$s) by

$$R(t) = \epsilon \frac{N_0}{\tau_{rg}} e^{-t/\tau_{rg}}, \tag{4.1}$$

where τ_{rg} is the storage lifetime, i.e. the time after which a fraction of $1/e$ of the initial number of trapped ions N_0 has been lost from the beam, while ϵ denotes the detection efficiency.
A comparison of the exponential loss of trapped SF_6^- ions by these residual gas collisions at trap temperatures of 300 K and 12 K is shown in Fig. 4.5, which results in lifetimes of 29.0$\pm$0.3 s and 880$\pm$130 s, respectively. Here, the dark count rate of the detector is determined after each trapping cycle by ejecting the ions and continuing to measure the count rate without beam. For the depicted measurements, this dark count rate is found to be $\sim$7 counts/s for the room temperature measurement and only $\sim$1.5 counts/s for the cryogenic case, which for the latter one constitutes the strongest source of background in the experiment. The difference in the dark count rates is most likely due to lower thermal noise at cryogenic operation, as the detector has then a temperature of about 50 K.
A reliable measurement of the vacuum pressure could be obtained for the room temperature experiment with an ionization vacuum gauge, yielding $(1.0 \pm 0.1) \times 10^{-10}$ mbar. Thus, the residual gas density n can be determined with the ideal gas law $n = p/k_B T$, and enables to determine a collisional destruction cross section of $\sigma = 1/(n\tau\bar{v}) = (6.1 \pm 0.6) \times 10^{-16}$ cm^2 for collisions of SF_6^- with the residual gas particles, mainly hydrogen. For the velocity a calculated average value of 85% of the maximum velocity was used to account for the deceleration in the mirror potential.

For the cryogenic measurement the lifetime was found to be $\sim$900 s, where the decay tends to become slightly slower for larger times. This translates into an upper limit for the residual gas pressure at a trap temperature of 12 K of $< 3 \times 10^{-12}$ mbar. Here, the ideal gas law for a temperature of 300 K was used to obtain the room

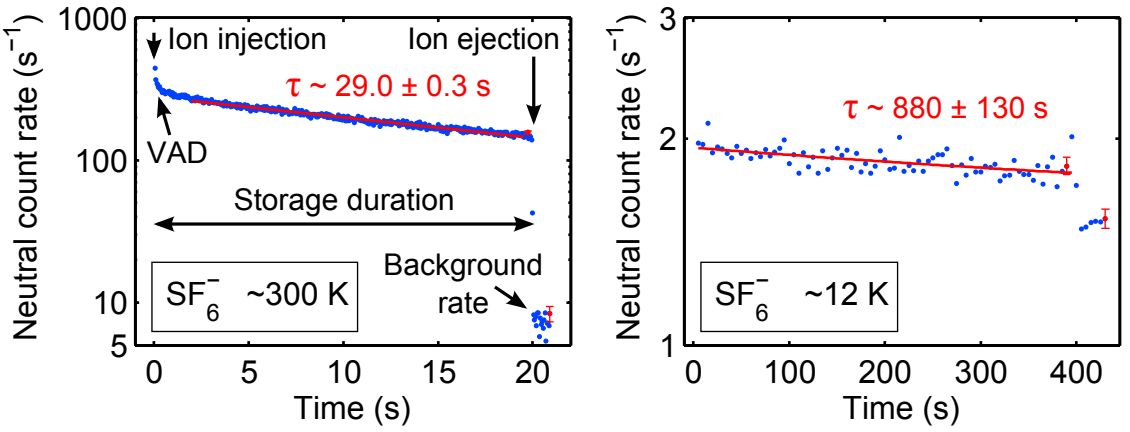

Figure 4.5: Collision-related trapping lifetimes of SF_6^- ions at 300 K and 12 K trap temperature corresponding to different residual gas pressures (see text).

temperature equivalent (RTE) pressure, instead of using the gas temperature of 12 K. As discussed in Ref. [8] the actual vacuum in the trap chamber might be even better as at these very long storage times also other pressure independent loss processes might occur. In any case, within the time window relevant for the VAD process of up to ∼100 ms, the rate of neutral particles from residual gas collisions is in very good approximation independent of time.

4.1.7 Additional background effects

To ensure a clean signal for the VAD process of SF_6^- at early times, possible additional disturbances were investigated with trapped O^- ions, as these do not exhibit VAD or other decays. In addition to the constant background from detector dark counts and the ion neutralization in residual gas collisions in the trap, an enhanced count rate was observed during the first hundreds of microseconds after the O^- injection. As shown in Fig. 4.6, the signal was even observed when the ions were not trapped, which was accomplished by increasing the trap electrode delay until the reflected ions could leave the trap unhindered.
On the other hand, the signal could be completely suppressed by applying a positive voltage of 1000 V on the repeller grid in front of the detector (see figures 3.13 and 3.11). Hence, we attribute the origin of this signal to a flux of low energetic positive ions originating from collisions of the injected ions with the inside surface of the small tube mounted at the entrance to the cryogenic trap, which was installed to reduce the gas flux into the trap and most of all efficiently absorb scattered IR radiation from the warm region by its rough oxidized surface.
Another possible disturbance of the count rate at very early storage times may be caused by ions injected on metastable trajectories which are rapidly lost from the trap and thus diminish the number of stored particles. Evidence for this process was observed through a variation of the injection settings by systematically misaligning the injected SF_6^- ion beam with respect to the trap axis using the beam chopper also as a static deflector. By this, more ions will end up on outer phase space trajectories, as indeed observed in Fig. 4.7. Proper injection settings are crucial

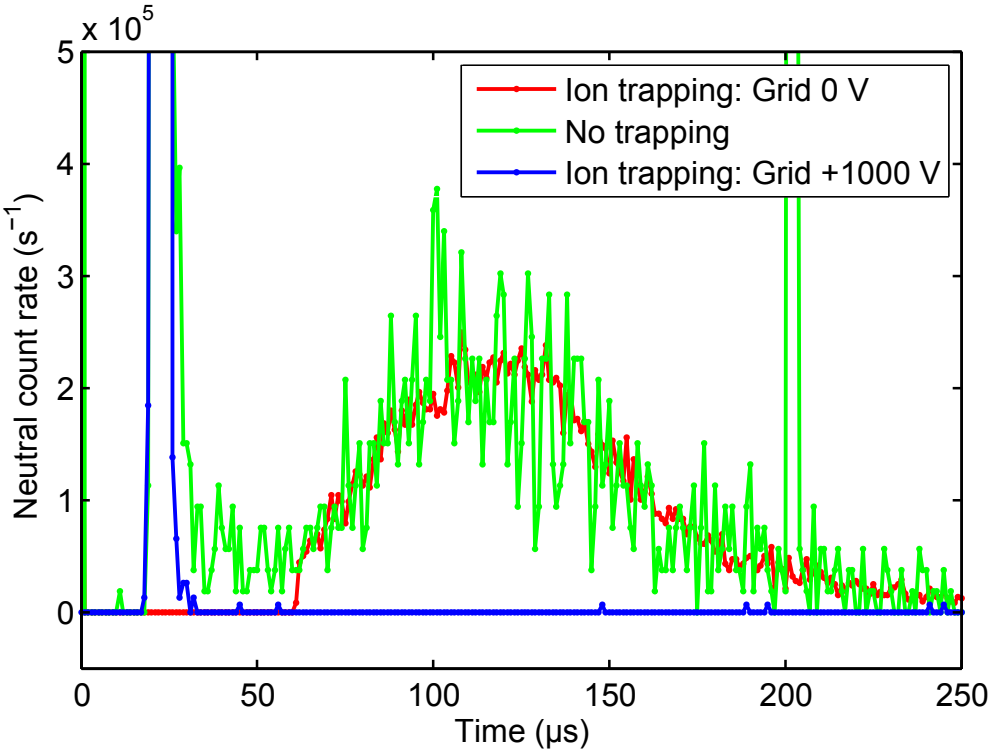

Figure 4.6: Background rate of positive slow ions created in the injection beam line by collisions with the chamber wall. The background rate could be suppressed by applying a voltage of +1000 V to the grid in front of the MCP detector (compare figures 3.13 or 3.11).

for clean undisturbed observations. However, signal contributions from ion loss via metastable trajectories cannot be excluded for observation times <500 μs. Thus, only storage times >500 μs are considered in the following analysis.

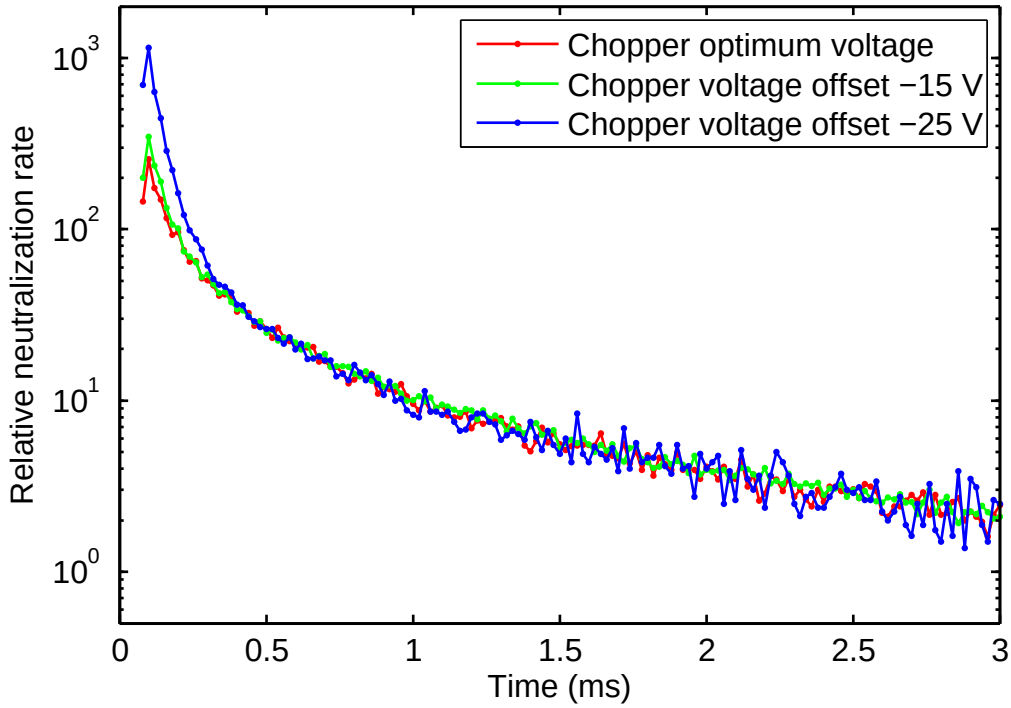

Figure 4.7: The fast depletion of ions from the trap could be influenced by changing the chopper voltage. During the first ∼500 μs this overlaps with the neutral count rate from other ion losses like VAD. For comparison, the relative neutralization rate was obtained by scaling the curves taken under different injection conditions, to the long time behavior of the decay.

4.2 Vibrational auto-detachment of excited SF_6^-

The VAD signal of stored SF_6^- ions could already be clearly seen in the brief discussion of measurements above (Fig. 4.4), where the background effects for very early times as well as the residual gas collision induced ion loss were also addressed. The highly excited SF_6^- ions injected from the ion source are denoted as $(SF_6^-)^*$. The VAD signal is found to exhibit a power function in time, with deviation towards a steeper dependence for later times (see figures 4.8 and 4.9). Previous studies of the VAD process of $(SF_6^-)^*$ were summarized in the introduction of Sec. 2.3. It should be recalled, that in a recent measurement with the electrostatic storage ring ELISA, a power law decay with a time dependence of $t^{-1.5}$ was reported from the observation of neutral decay products over the time span between hundred microseconds and ten milliseconds [25].
To yield a comprehensive understanding of the observed VAD signal, a detailed investigation covering a wide range of time scales is necessary, using existing VAD rate models. In the following measurements, a time range from hundreds of microseconds to in principle minutes is accessible. However, the steadily diminishing rate of the initial VAD decay becomes unobservable at around 100 ms. Systematic studies of the VAD decay curves were performed and are discussed within the framework of statistical models.

4.2.1 Characterizing the detachment signal

A double logarithmic presentation of the plotted decay curves is chosen to account for the steep shape of the decay, which clearly visualizes the wide range of time scales involved. However, the data representation in histograms with constant bin widths introduced before and shown for instance in Fig. 4.4, leads to problems in applying fit routines for this wide range of observation times due to the statistical error becoming comparable to the signal itself. Figure 4.8(a) shows the same measurement using bin widths of 100 μs and 1 ms, respectively, which is compared to a logarithmic binning in Fig. 4.8(b). For a constant binning with a small bin width, short times are well represented, but for later times discrete steps due to single counts appear. For larger bins, early times are represented in less detail.
The logarithmic binning (Fig. 4.8 b) is realized by introducing an equidistant binning to the logarithm of each particle arrival time instead of to the time itself, in this case 40 per decade. For example, the first bin at $t > 1$ ms is given by the counts between 10^{-3} s and $10^{-3+1/40}$ s. The scatter for very early times in the logarithmic binning stems from a beating between the early bunch structure of the ions in the trap and the logarithmic bin width. However, as mentioned before, these times are not further considered in the following analysis.
One has to note that time zero of the measurement is defined by the chopper switching when the ion bunch is released. Thus, a correction in the time scale of around 7 μs has to be applied to account for the flight time from the ion source to the chopper. On the other hand, the recorded detection time of a neutral contains a time of flight delay between the trap and the detector of about 10 μs, and is only known with an uncertainty of $\pm 1/4$ of the orbital period because the location of

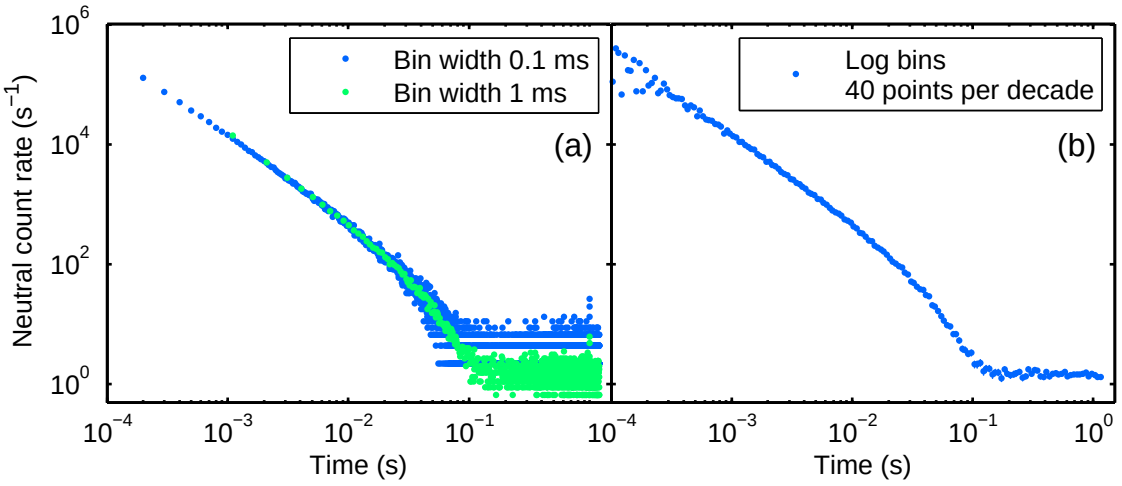

Figure 4.8: Comparison of a histograms of the decay rate with constant bin widths of 100 μs and 1 ms (a), and a logarithmically binned histogram with 40 bins per decade (b).

the detachment event along the trap axis is unknown. Both effects nearly compensate each other and the remaining small time shift and uncertainty is unimportant considering only times $t > 500$ μs.
The measurements performed with the CTF exhibit a power law behavior of the VAD rate $R(t)$ for early times t given by $R(t) \propto t^n$, with n being negative and varying between –1.5 and –1.0. In figure 4.9, the observed neutralization rate is shown for one measurement compared to a power law with an exponent of $n = -1.4$. In comparison to the recent ion storage ring measurement [25], the neutralization rate of SF_6^- anions by collisions with the residual gas could be reduced by a factor of $\sim 10^3$. Hence, while residual-gas neutralization limited the observation of the VAD neutralization rate to $t < 10$ ms in the previous ring experiment, the present work finds significant VAD signals up to $\sim$0.1 s.
To account for the strong deviations from the power law dependence after $\sim$10 ms, observed for the first time in the VAD rate for SF_6^- (compare Ref. [25]), a modified power law model is employed as a first step in this analysis. This model was introduced in Ref. [11] to describe the depletion of excited vibrational states by radiative cooling. We will use this empirical model to parametrize the observed decay shape and compare the different measurements. The model assumes the neutralization rates to be given by

$$R(t) = A\,(t/\tau)^{n+1}\frac{1}{e^{t/\tau}-1} + C, \tag{4.2}$$

where τ is the 'cooling' time, and A and C are rates. Note, that the function behaves like $\propto t^n$ for times $t \ll \tau$. C includes the detector dark count rate and accounts for the collisional-induced neutralization, which is assumed to be constant due to the long storage lifetime of the ions (see Fig. 4.5) as compared to the observation time of the VAD signal. The value of C is determined from the late part ($t > 0.2$ s) of the neutralization curve, where the MCP count rate is almost exclusively composed of background events. Although the interpretation of the fit parameter τ as a 'cooling' time is questionable (see later in Sec. 4.2.3 in the discussion with the detailed model),

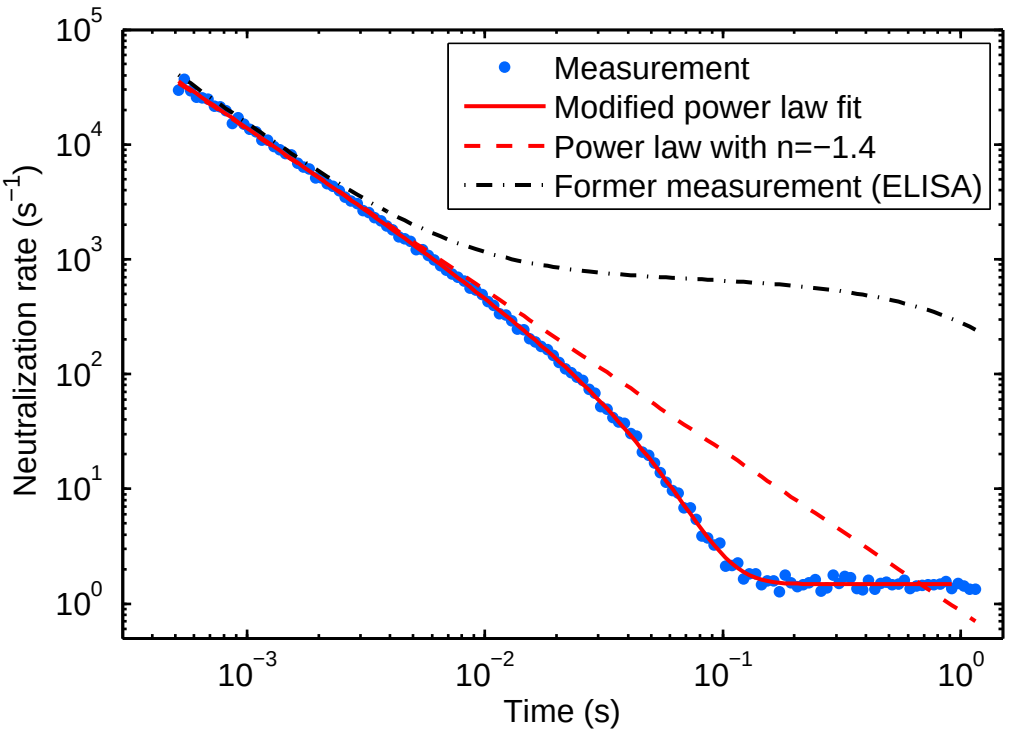

Figure 4.9: Neutralization decay rate of the VAD process of SF_6^- compared to a power law with $t^{-1.4}$ and to a curve approximating the former measurement [25], showing a dramatically higher background due to residual gas collisions. The displayed fit with the modified power law from Eq. (4.2) resulted in an exponent $n = -1.405 \pm 0.006$ and a cooling time $\tau = 22.8 \pm 0.6$ ms.

we will keep the phrase for the time being.
As can be seen in Fig. 4.9, Eq. (4.2) results in a very good description of the data with (for this particular data shown here) $n = -1.405 \pm 0.006$ and $\tau = 22.8 \pm 0.6$ ms. For comparison we also show in Fig. 4.9 the result of the measurement performed at the ELISA storage ring [25]. This measurement exhibited a similar exponent of –1.5, but a considerably higher collisional background corresponding to a mean ion storage time of 1.1 s, concealing the feature of the VAD process at times $\gtrsim$5 ms.

4.2.2 VAD-signal dependence on ion source settings

Systematic studies on the curve shape of the time varying VAD-signal of $(SF_6^-)^*$ were performed. During the CTF cool-down, taking usually a week, the neutralization process was investigated, but no dependence on the trap temperature could be observed besides a decreased dark count rate of the MCP detector. Influences of the ambient background radiation on the radiative cooling of $(SF_6^-)^*$ are actually not expected for times earlier than a few 100 ms even at temperatures of ∼300 K.
We also carefully investigated possible influences of the number of trapped ions on the neutralization decay rate. Keeping the neutral count rate below the saturation limit of the MCP detector, no change in the shape of the VAD signal was observed. However, we do expect the VAD signal to depend on the ion source parameters,

as the internal excitation of the $(SF_6^-)^*$ ions leaving the source will certainly be influenced by the way they are produced. A detailed description of the MISS ion source operation can be found in Sec. 3.2.2. In the present case, the tungsten filament is heated to temperatures in the range between 1000 and 1500 K. Cold (300 K) SF_6 gas is continuously delivered through the target bore and condensed at its surface, where the dominant part of the electron attachment occurs. This was confirmed by the sharp kinetic energy of the ions observed, when they experience the full acceleration potential, as discussed in Sec. 3.2.2.
As a first parameter, the heating current of the tungsten ionizer filament was varied by about ±20% as permitted while maintaining a stable operation of the source. A second source parameter, which was investigated for its influence on the neutralization rate, is the cathode voltage by which the cesium cations are accelerated onto the target. Here, they are suspected to release electrons and/or adsorbed SF_6 from the surface, which then recombine either upon release or in the gas phase. Impact energies of up to 2000 eV may lead to excitations of the SF_6^- and a variation of this parameter in the feasible range might be visible in the measurement.
The sputtering of ions from surfaces has been intensively investigated; high vibrational and rotational energies of the sputtered ions have been observed [113, 114], however, the ion creation from a gaseous target in this experiment differs significantly from the arrangement in these investigations and may lead to different results.
The influence of both parameters have been studied (1) for filament currents between 18 and 24 A and (2) for cathode voltages between 800 and 2000 V. For the first one, this translates into 60 and 110 W from the corresponding power supply and gives temperatures between 1400 K and 1700 K using the Stefan-Boltzmann-law with an approximate emissivity of ∼0.25 for tungsten [108]. Possibly higher ion currents were compensated by changing the slits in the injection beam line to avoid detector saturation.
The exponent n and the 'cooling' time τ obtained from the analysis of the measured neutralization rate decay curve using Eq. (4.2) are shown in Fig. 4.10 as a function of the filament current (1) and the cathode voltage (2), respectively. No systematic trend in the dependencies could be observed, although statistically significant variations between the measurements occur. Exponents between –1.45 and –1.1 and 'cooling' parameters τ from 10 ms to 25 ms were determined. The fact that different power laws were observed proves an influence of the ion preparation process on the VAD signal. Also other source parameters than those tested by this set of measurements might be responsible for the variations.
A parameter which cannot be directly monitored in our setup is the pressure in the ion source. This pressure is mainly determined by the flow of SF_6 gas fed into the source. The first possibility to obtain a rough measure of the source pressure is the pressure reading of the vacuum gauge connected to the beam chopper chamber ("chopper pressure"), which allows to observe and control at least relative changes of the source pressures. An attempt to estimate the absolute source pressure has been carried out in Sec. 3.2.4. According to this estimate the pressure in the source is about 6×10^3 higher than measured in the chopper chamber. However, we will continue to use the chopper pressure to characterize the source pressure, as it is the primary experimental parameter that was monitored.

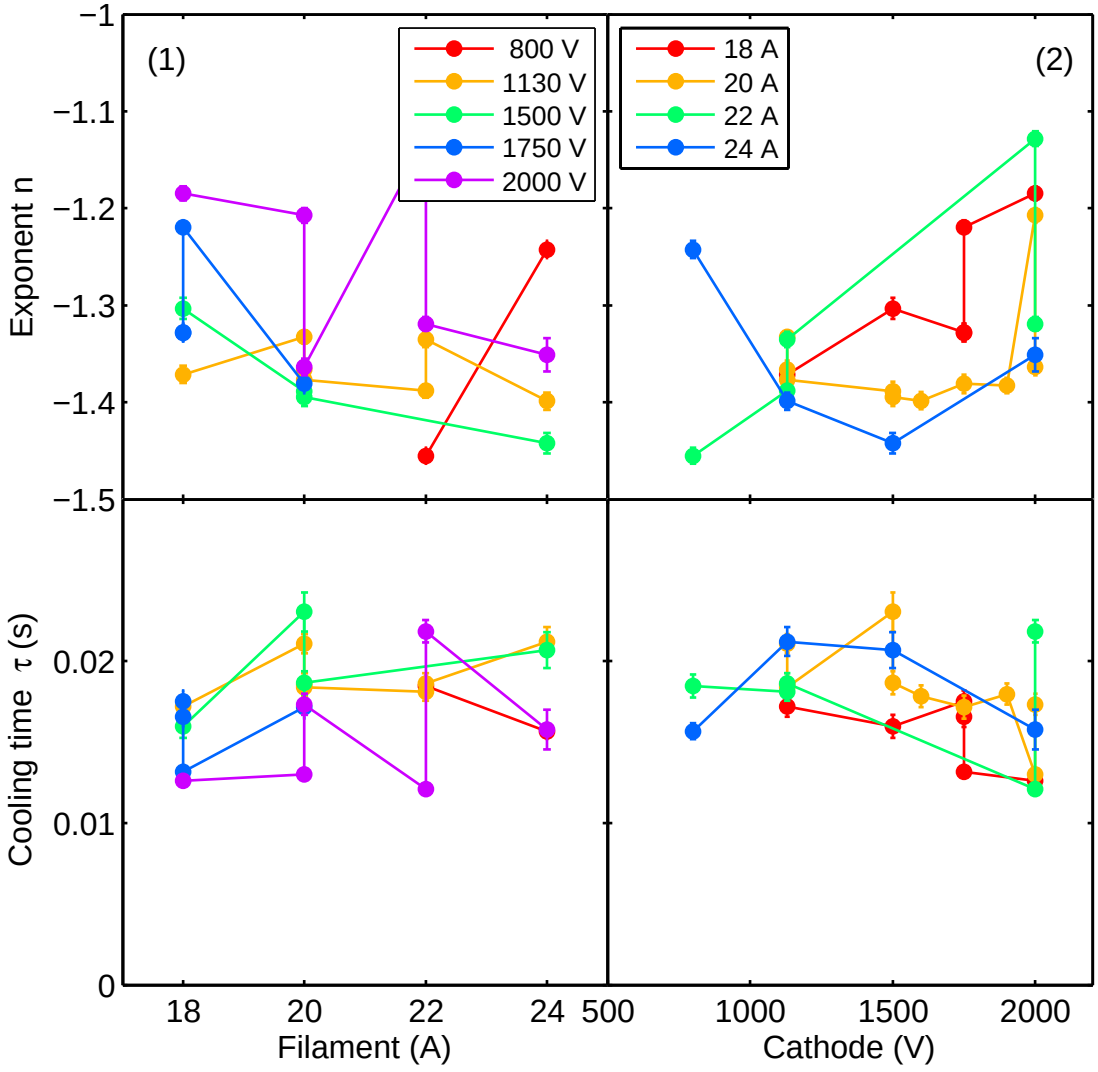

Figure 4.10: Fitted parameters using Eq. (4.2): Both sides show the same data set as a function of the filament current (1) and the cathode voltage (2). No systematic dependence on either of the parameters could be observed. The large variations of the parameters might be due changes in the ion source pressure, as for these measurements no particular care was taken to keep it constant.

In the study on the variation of the ion source pressure, much care was taken to keep the other source and ion injection parameters constant during the measurement period; this holds for instance, for the cathode voltage and the filament current, but also for the ion beam line including the dipole magnet and the positions of beam slits. Moreover, five measurements were taken during single days (thereby eliminating the effects of repeated ion source warm-up and shutdown procedures) in each case starting at a high pressure of $\sim 5 \times 10^{-6}$ mbar. Before each new measurement the pressure was decreased reducing the SF_6 gas flow and waiting for steady conditions. As for the maximum pressure the ion yields are highest, keeping this sequence in performing the study allowed all settings to be optimized at the highest occurring

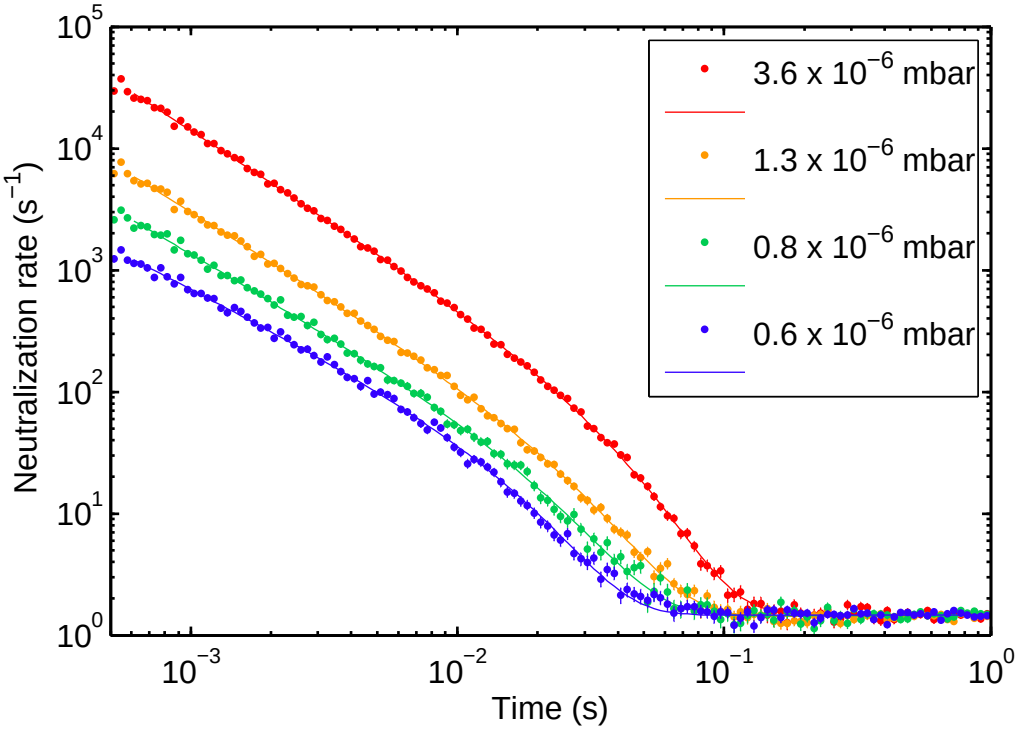

Figure 4.11: VAD neutralization rates, together with modified power function fits observed at different source pressures, which are indirectly measured by observing the residual gas pressures in the chopper chamber. The cathode voltage and filament current were kept constant at 800 V and 22 A, respectively.

beam intensity, making sure that no saturation effects affect the data. It was possible to decrease the ion source pressure stepwise by almost one order of magnitude to a final value of $\sim 6 \times 10^{-7}$ mbar.

Four of these neutralization curves measured for a cathode voltage of 800 V and a filament current of 22 A are shown in Fig. 4.11 together with the modified power function fits from Eq. (4.2). The intensity differences between measurements are entirely due to the increased ion yield at higher pressures. The fit parameters are summarized in Fig. 4.12 as a function of the pressure and compared to a second set of measurements on a different day using a cathode voltage of 2000 V and a filament current of 22 A. A clear trend of the fitted exponent n can be observed as a function of the pressure covering a range between roughly –1.5 and –1.0. Thus, for the highest pressure the steepest decay characteristics are found, which also indicates a higher internal excitation of the $(SF_6^-)^*$ because of the predicted energy dependence of the VAD rate coefficients.

The second fit parameter, the 'cooling' time τ, also exhibits a clear tendency on the pressure. This dependence is not expected for a radiative cooling process, which indicates that the deviation from the power function may arise from a different process. This is discussed in more detail in Sec. 4.2.3. Note that both fit parameters depend not only smoothly on the source pressure but also show a distinct dependence on the cathode voltage.

The influence of the pressure onto the VAD signal shape is likely due to collisional

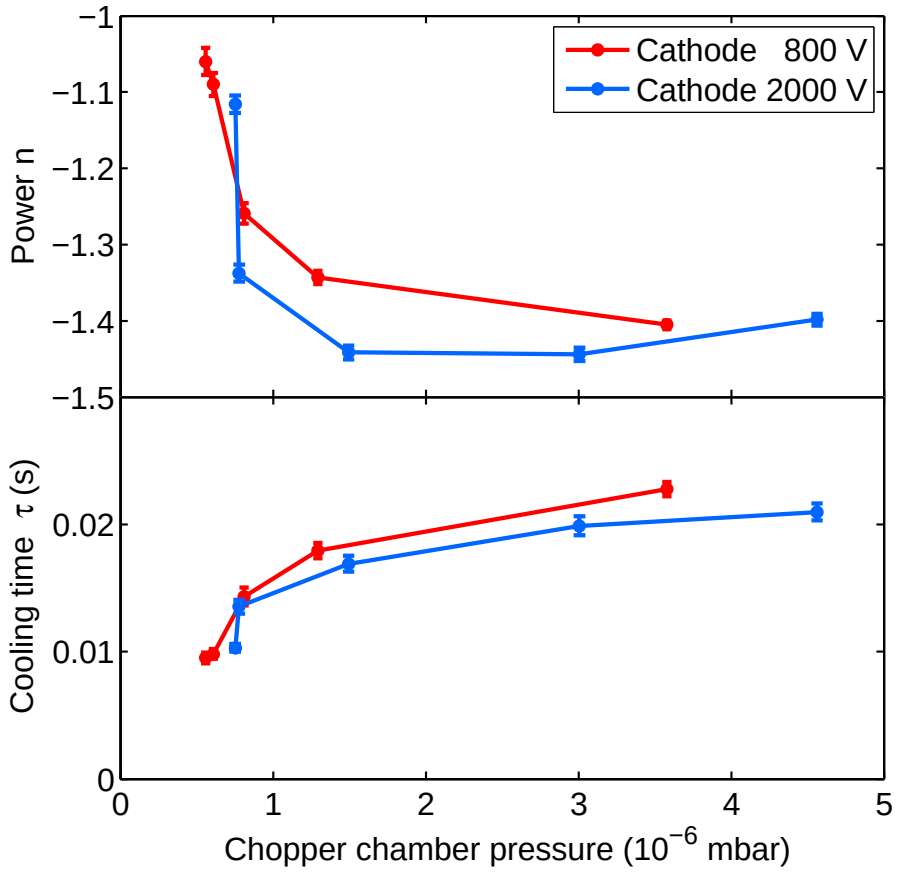

Figure 4.12: Parameters deduced from a fit of Eq. (4.2) to the VAD neutralization rate decays measured at different source pressures, but a constant filament current of 22 A and for two extreme cathode voltages. The parameters are plotted as a function of the chopper chamber pressure. The true source pressure was estimated (Sec. 3.2.4) to be a factor of $\sim 6 \times 10^3$ higher.

excitation during the acceleration process of the ions. Estimated collision rates in the source are given in table 3.1, where for the relevant pressure range average collision numbers of 0.5 up to 5 collisions of ions with SF_6 gas on the extraction path from the source were found. The increased collision rate at higher source pressure is expected to lead to an increased excitation, which is in turn leading to a faster VAD-decay and thus to a steeper power law.

4.2.3 Modeling the VAD decay with vibrational and rotational temperature distributions

Instead of the simple empirical model of the modified power function, a system specific detachment model is now applied to the data, which incorporates specific properties from SF_6 and SF_6^-. Further insight into the distribution of internal excitations as well as the validity of different model input parameters can be inferred by this model, which was derived in chapter 2.
Energy-dependent VAD rate coefficients $k(E)$ are applied, which were suggested by

Troe *et al.* [19, 22–24], but have not yet been confronted with the detailed information available from storage ring or trap experiments. As the rate coefficients depend on the total internal energy of $(SF_6^-)^*$, an integration over an energy distribution is performed yielding a neutralization rate, which reflects the neutral detection rate taken with the CTF (compare Eq. (2.25)). Temporal changes of the energy distribution lead to a variation of the VAD rate and hence to the measured neutralization rate decay curves. For the initial vibrational excitation a thermal, canonical energy distribution is applied, which assumes an initial thermalization of the SF_6^- ion ensemble before its injection to the trap. It is given by $f(E,T) \propto \rho(E)\exp(-E/k_BT_{vib})$, accounting for the statistic multiplicity for each energy by the density of states $\rho(E)$ and for its temperature-dependent initial population, as discussed in Sec. 2.4. Similarly, rotational excitation is considered by integrating over a rotational canonical energy distribution (see Sec. 2.4.2).

VAD model with EA 1.20 eV and symmetrical SF_6^- structure

At first, the detachment rate coefficients from [19, 22] are used, which are based on an electron affinity EA of 1.20 eV and on vibrational frequencies for SF_6 and SF_6^- taken from Gutsev and Bartlett [36]. Here and in the discussion of the applied models, we illustrate their typical matching with the data for single example curves only. Moreover, in Fig. 4.13 as well as in all following figures, the VAD neutralization rates are given after background subtraction (rate at 0.2 s $< t <$ 1.0 s) to illustrate the dependencies and agreement with the model for later times more clearly. The measurement is shown up to the times when the rate starts to scatter around zero, because then parts of the data cannot be displayed due to the logarithmic scale.
When fitting the model from Eq. (2.25) with EA = 1.20 eV, $T_{rot} = 0$ and $k_{rad} = 0$ by adjusting T_{vib} and the overall normalization, the slope of the power function can be well reproduced, whereas large deviations occur for times beyond 10 ms; the fit curve bends at earlier times than the data (red curve in Fig. 4.13). The fall-off in the VAD neutralization rate occurs at times corresponding to the inverse of the detachment rate coefficients $k(E)$ close to the threshold energy EA. Considering Fig. 2.7 this is given by $\sim$200 s^{-1} and thus a time of around 5 ms. Here, the deviation from the power law naturally occurs due to the low level density of SF_6 in the energy range where the excitation energy of SF_6^- approaches the threshold EA.
If one includes into the model with EA=1.20 eV the rotational excitation of the SF_6^- ensemble, as described by Eq. (2.32)-(2.35), the fit can be considerably improved. Due to the difference in the rotational constants of SF_6^- and SF_6, the presence of rotational excitation in the detachment process enhances the electron affinity to an effective value of $\mathrm{EA}(J) = \mathrm{EA} + \Delta E_R(J)$, and thus, the amplitudes of the detachment rate coefficients $k(E,J)$ at a given energy decrease. $\Delta E_R(J)$ is the rotational energy difference between SF_6 and SF_6^- for a given J, which has to be spent to ensure angular momentum conservation in the detachment process (see Sec. 2.4.2). If rotations are included, the model reproduces also the later times of the neutralization curve, where the fall-off is now shaped by the rotational excitation. However, also radiative cooling can be expected to become a relevant process at later times. The energy dependence of the radiative cooling rate $k_{rad}(E)$ has been estimated in the present work in Sec. 2.5.1, where the calculated integrated infrared

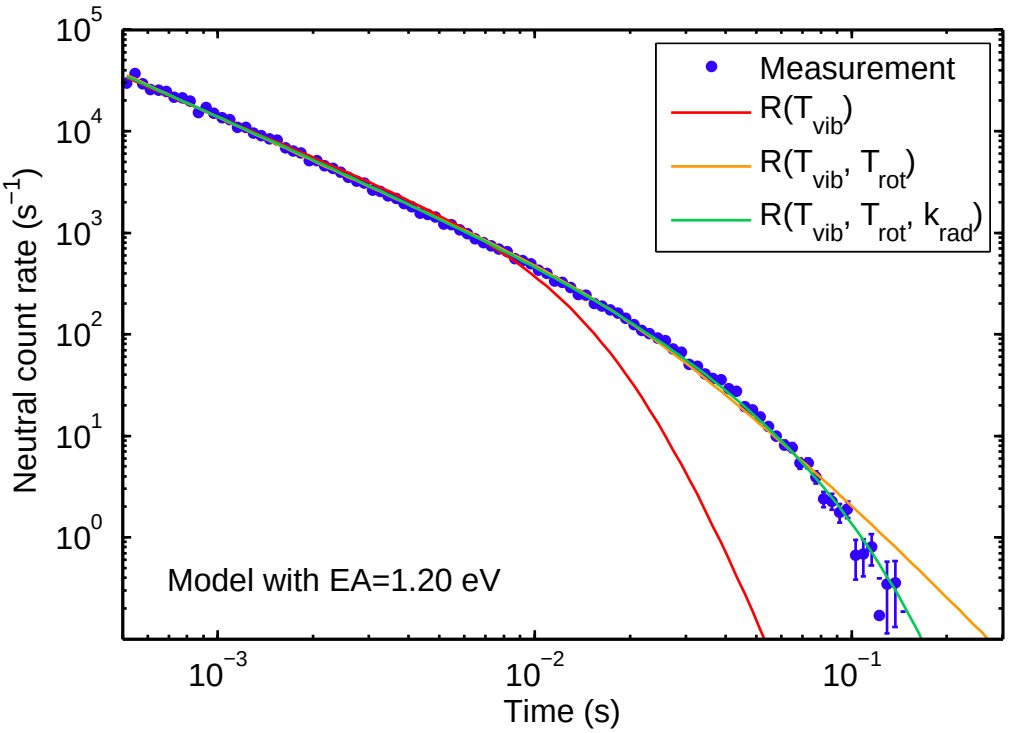

Figure 4.13: Comparison of VAD model fits (see the text) with an EA of 1.20 eV and symmetrical SF_6^- structure, subsequently including rotational excitation by T_{rot} and radiative cooling by k_{rad} in addition to the vibrational excitation (red: $T_{vib} = 2050$ K, $T_{rot} = 0$, $k_{rad} = 0$; orange: $T_{vib} = 5900$ K, $T_{rot} = 2500$ K, $k_{rad} = 0$); green: $T_{vib} = 8600$ K, $T_{rot} = 6400$ K, $k_{rad} = 28$ s^{-1}).

intensity of the strongest IR-active vibrational mode of SF_6^- [77] was used in a stochastical approximation. A value of $k_{rad} \approx 45$ s^{-1} (lifetime of 22 ms) is derived from Eq. (2.38) for an energy of about 1 eV (see also Fig. 2.15). It should be noted that significantly higher cooling rates for SF_6^- have been determined theoretically by Dunbar to 80 s^{-1} and experimentally by Troe *et al.* to 59 s^{-1} (both quoted in Ref.[19]), yielding cooling lifetimes of 12.5 ms and 17 ms, respectively.
Radiative cooling can be included into the model calculation as discussed in Sec. 2.4.2 by including the radiative rate coefficient k_{rad} in the total decay rate entering Eq. (2.25). The cooling rate k_{rad} is here assumed to be independent of the excitation energy as it only becomes significant when in the final phase of the VAD decay curve ions with excitation energies in a narrow range close to the EA contribute to the neutralization signal. For $k_{rad} = 28$ s^{-1}, the resulting fit curve leads to an excellent agreement with the data as shown by the green curve in Fig. 4.13. One has to note that here the radiative cooling lifetime $\tau_{rad} = k_{rad}^{-1}$ is not equal to the quantity τ, which was only used in Eq. (4.2) to parametrize the measurements. In any case it is seen that rotational excitation and radiative cooling are processes with opposite influence on the neutralization curve, and are thus 'competing' in the data fitting.
Figure 4.14 illustrates the fitted vibrational and rotational temperatures as a function of the chopper chamber pressure for the case without consideration of radiative

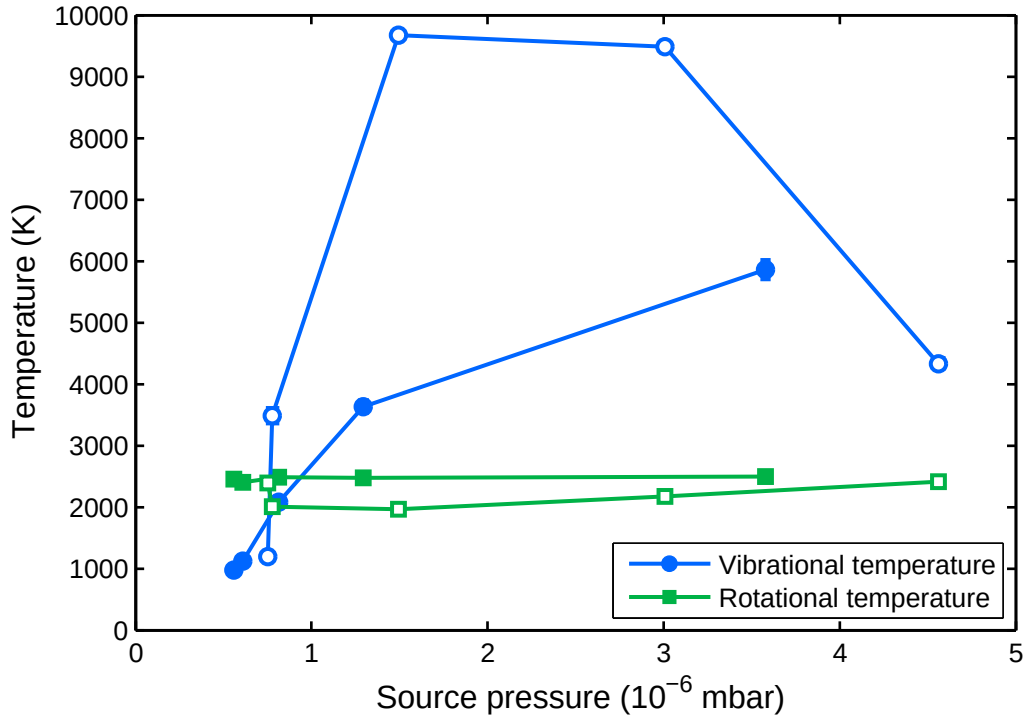

Figure 4.14: Vibrational and rotational temperatures as a function of the chopper chamber pressure (reflecting the source pressure variations) from fits using the VAD model and assuming EA = 1.20 eV. Full symbols are measurements with a cathode voltage of 800 V, open symbols for 2000 V.

cooling. The vibrational temperatures show an increasing dependence on the pressure reaching very high temperatures. The rotational temperature exhibits only small variations in the order of 2000 to 3000 K. The full symbols in Fig. 4.14 denote the measurements with a cathode voltage of 800 V, open symbols are for 2000 V. The difference of the results for the two cases shows also a variation of the neutralization rate on the cathode voltage, as it already became visible in Fig. 4.12. In the presence of radiative cooling, the rotational temperatures approach unrealistically high values, which is why they have not been included in Fig. 4.14.
It is well known that molecules become highly vibrationally and rotationally excited within the sputtering process in the ion source (see also Sec. 3.2.3). This was for instance investigated by Wucher *et al.* [113, 114], where temperatures in order of several thousands for rotations and vibrations have been found, with usually higher values for the rotations. The average internal energy was found to increase with the cluster size, which can be explained by the gained binding energy, when the larger clusters are formed by attaching atoms or small clusters. However, SF_6 molecules are already existing on the target surface and are assumed to be only desorbed by the sputtering cesium cations, besides attaching an electron. Hence, the observed vibrational temperatures of up to 9000 K obtained with this VAD model seem unrealistically high and this approach is ruled out as a reasonable description of the data.

VAD model with EA 1.03 eV and asymmetrical SF_6^- structure

The calculation of the detachment rate coefficients have been revised recently by Troe [24] using extensive calculations of the SF_6^- structure and of the vibrational frequencies [17]. In these calculations an asymmetric structure of SF_6^- in the ground state was found in contrast to the former assumption of an octahedral shape. Coming along with this, lower energetic vibrational modes are present which dominate and increase the density of states of SF_6^- (compare table 2.1). A new value for the electron affinity of 1.03 eV was determined by Troe [24] and the size of the detachment rate coefficients decreases considerably (Fig. 2.7).
The calculated VAD rate decay based on EA = 1.03 eV and the new vibrational frequencies for SF_6^- is fitted to the data at first considering only vibrational excitation. The neutralization rate extends to larger times and even exceeds the measurement at late times for the best fit value of $T_{vib} = 4900$ K (see Fig. 4.15). This overshoot cannot be corrected by the inclusion of rotational excitation as this would extend the fall-off region to even larger times as shown in Fig. 4.15. Good agreement is achieved by including also radiative cooling. This contribution is found to be crucial to obtain a reasonable fit result. To demonstrate the overall quality of agreement between data and model, the weighted residuals (compare Eq. (4.3)) are shown in Fig. 4.15. But also for these model calculations a competition between rotational excitation and radiative cooling is taking place.
Different approaches have been applied to constrain the two competing processes. For this purpose, the previously presented 10 measurements of the neutralization rate of SF_6^- under well-defined source and injection conditions are available, which are found to feature different vibrational and rotational energy distributions, and all of which will be used in the following analysis.
At first, the parameters resulting from fits assuming constant rotational temperatures are shown in Fig. 4.16, where the vibrational temperatures and the cooling rates as a function of the chopper pressure are plotted. The agreement of the fit model with the data is measured by χ^2, which is defined by

$$\chi^2 = \sum_{i=1}^{N} \frac{(f(x_i) - y_i)^2}{\sigma_i^2}, \tag{4.3}$$

where the summation goes over all N data points and the squared residual between measured value y_i and the model $f(x_i)$. The uncertainty of each data point σ_i was determined by the statistical error from the square root of the total counts. After normalization of χ^2 with the degrees of freedom (dof), which is N subtracting 1 and the number of fit parameters, χ^2/dof should be a value close to 1. For values much larger than 1, the model is found to be a bad description of the data and in case of much smaller values features of the model merely reproduce random fluctuations in the data.
The fitting was performed with MATLAB using a numeric fitting model with an energy resolution of 1 meV in $k(E)$ and $f(E,T)$, which turned out to be sufficient by a comparison to fits with higher energy resolution and still allowed reasonable array sizes in the calculation. For the rotational excitation, angular momentum numbers J up to 1000 were allowed.

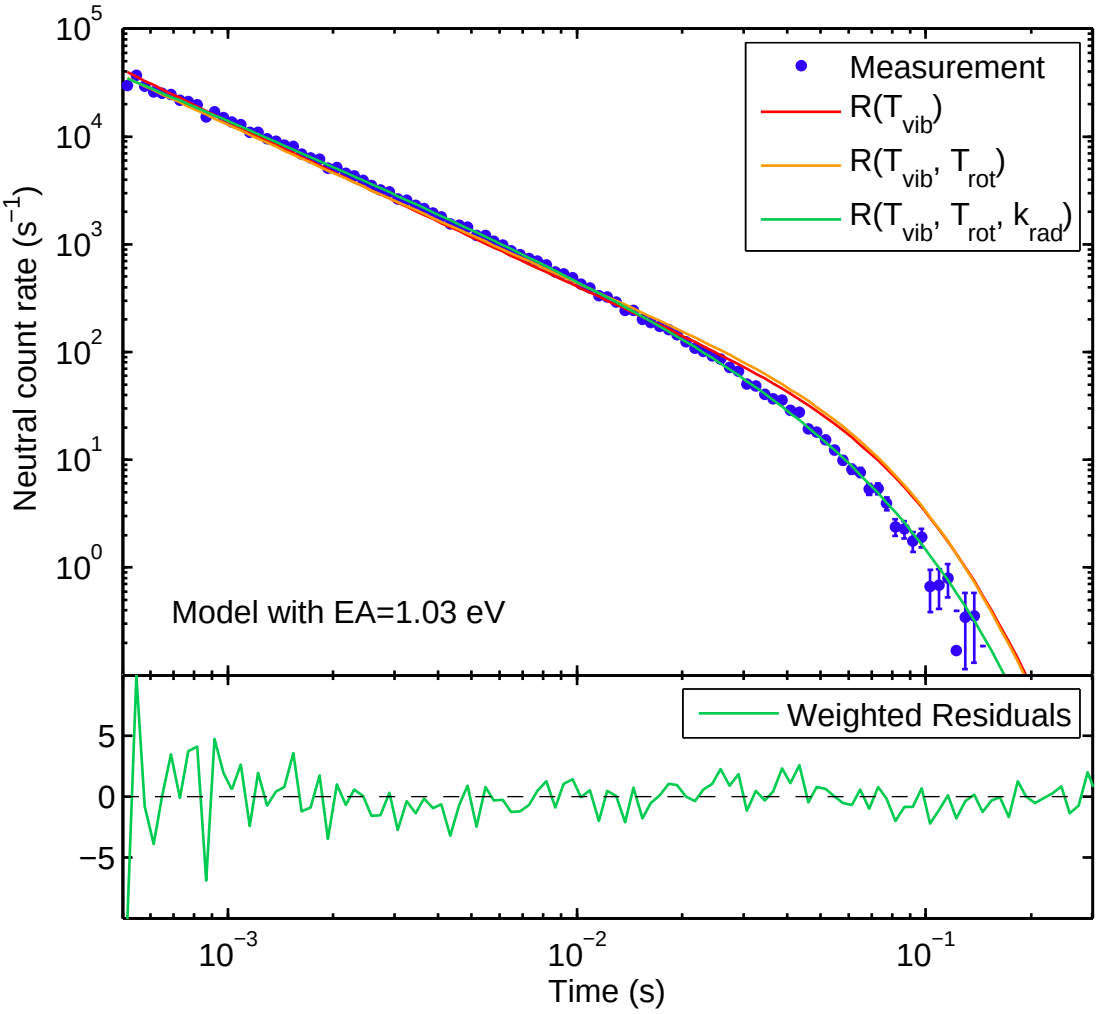

Figure 4.15: Comparison of VAD model fits with an EA of 1.03 eV including subsequently rotational excitation by T_{rot} and radiative cooling by k_{rad} to the vibrational excitation. The weighted residuals illustrate the overall conformity of the data to the model. (red: $T_{vib} = 4900$ K, $T_{rot} = 0$, $k_{rad} = 0$; orange: $T_{vib} = 2900$ K, $T_{rot} = 13$ K, $k_{rad} = 0$; green: $T_{vib} = 3300$ K, $T_{rot} = 5300$ K, $k_{rad} = 28$ s^{-1}).

In figure 4.16 the resulting χ^2/dof from these fits are found to be close to 1, indicating that a reasonable agreement can be achieved for all fits with constant rotational temperature between 500 and 4000 K. The vibrational temperatures vary only marginally for different values of T_{rot} and exhibit a clear increase with the pressure from 1000 to 4000 K. When compared to Fig. 4.12, one finds a relation between the exponent n and the vibrational temperatures, namely an exponent around $n = -1$ at $T_{vib} = 1000$ K and increasing to $n = -1.4$ at $T_{vib} = 4000$ K. Thus, a steeper decay curve corresponds to a higher excitation, which is consistent with the interpretation that states with higher energy and accordingly, higher detachment rate coefficients, are populated at 4000 K.
Similarly to the fit results with EA=1.20 eV, the vibrational temperature shows a strong dependence on the cathode voltage. For high impact energies of the cesium

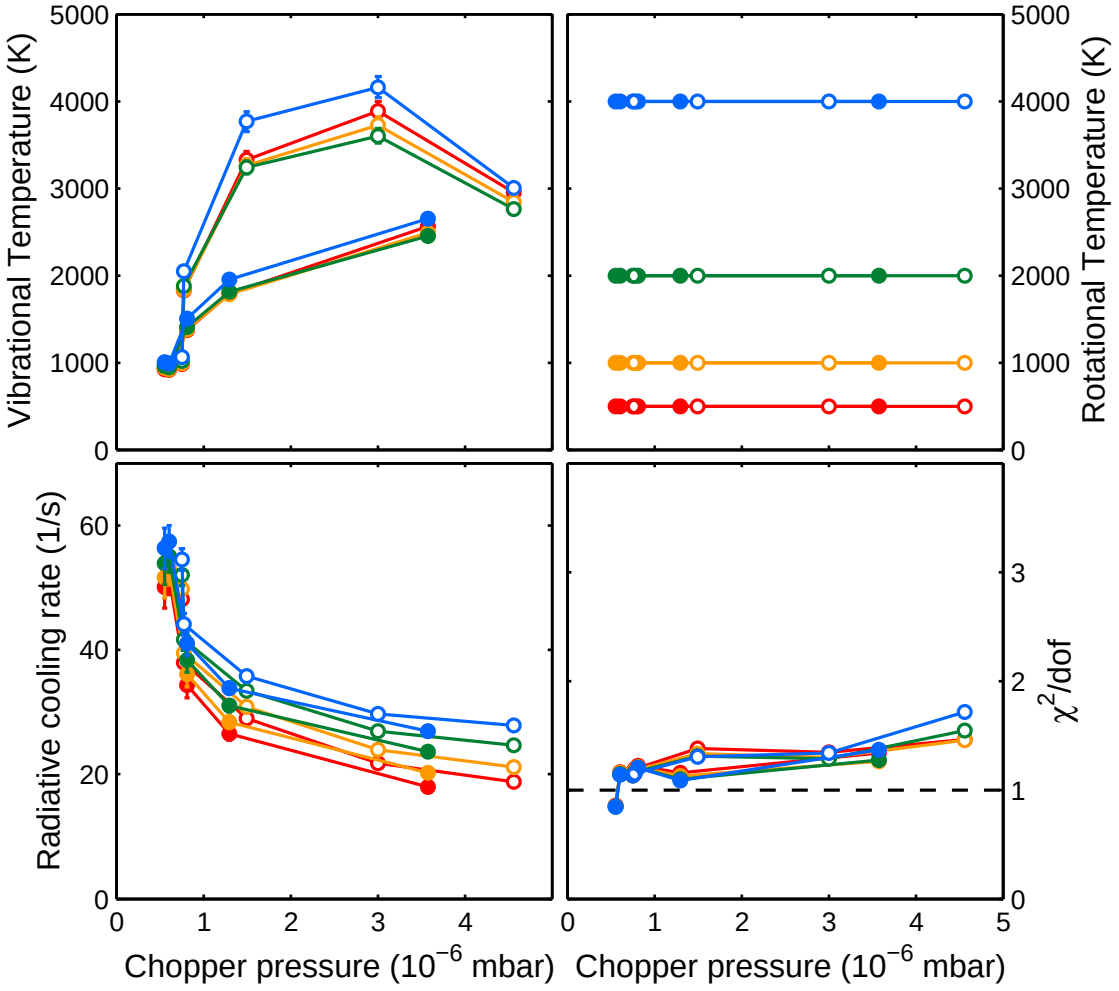

Figure 4.16: Fits with EA = 1.03 eV and fixed rotational temperatures (full symbols are for a cathode voltage of 800 V, open symbols for 2000 V).

cations onto the source target (cathode voltage of 2000 V), the highest vibrational temperatures are observed, where, however, very similar temperatures are found at low source pressures. As the negative ions are also pre-accelerated with the cathode voltage from the target to the extraction electrode (compare Fig. 3.8), the collision energy of the SF_6^- ions with SF_6 gas is enhanced for a higher cathode voltage. Thus, a higher internal excitation of the SF_6^- at higher cathode voltage can be well explained.

The assumption of a constant rotational temperature for all different measurements is somewhat artificial, it seems to be more reasonable to assume $T_{rot} \propto T_{vib}$. The fit parameters of the best fits obtained by assuming EA = 1.03 eV and $T_{rot} = T_{vib}$, and adjusting T_{vib} and k_{rad} are displayed in Fig. 4.17 (red curves). As other studies on internal excitation of ions produced in a sputter source found higher rotational than vibrational excitation, the fit was repeated for rotational temperatures twice as high as the vibrational one; the results are also shown in Fig. 4.17 (blue curves). The fit values show a similar shape as a function of the pressure, however, in the case of the

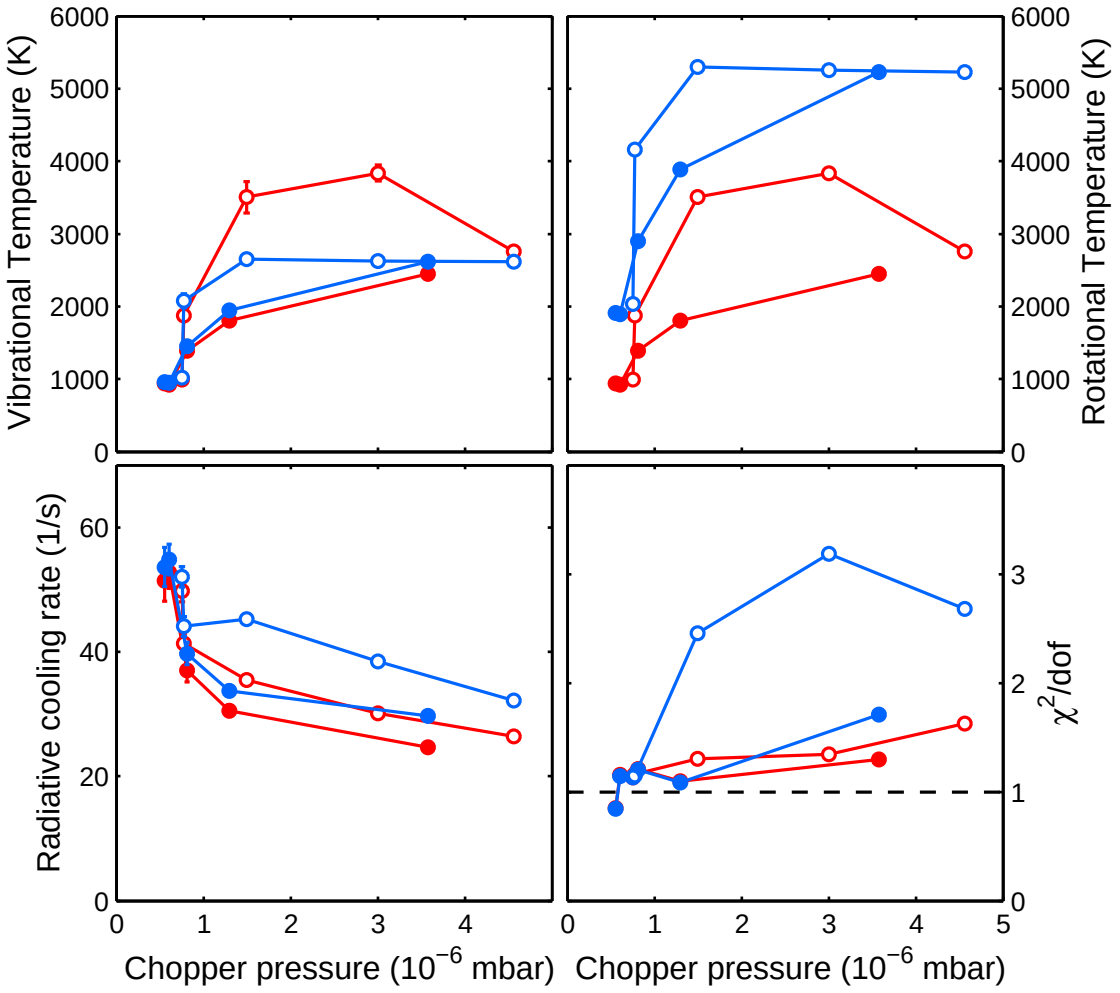

Figure 4.17: Fits with EA = 1.03 eV assuming $T_{rot} \propto T_{vib}$: red curves with $T_{rot} = T_{vib}$; blue curves with $T_{rot} = 2 \cdot T_{vib}$ (full symbols are for a cathode voltage of 800 V, open symbols for 2000 V).

higher rotational temperature the fit starts to get unacceptable for higher pressures.

The radiative cooling rate parameter in Fig. 4.16 shows only a weak dependence on the rotational temperature, but is found to depend strongly on the source pressure, which is not expected. When the cooling starts to become a competing process to the detachment ($t \gtrsim$10 ms), only the low energetic ions should be left in the ensemble and the cooling rates should be very similar to each other within the ensemble.
To investigate whether a reasonable description of the data assuming a constant radiative rate k_{rad} can be obtained for EA = 1.03 eV, corresponding fits were performed. The results for three cooling rates of 25 s^{-1}, 30 s^{-1} and 35 s^{-1} (corresponding to lifetimes of 40 ms, 33 ms and 29 ms) are shown in Fig. 4.18. One notices that for low ion source pressures only the highest cooling rate leads to a feasible fit result (red curve), illustrated by χ^2/dof. On the other hand, for these high cooling rates χ^2/dof is found to exceed a value of 3 for higher pressures, which is also noticeable

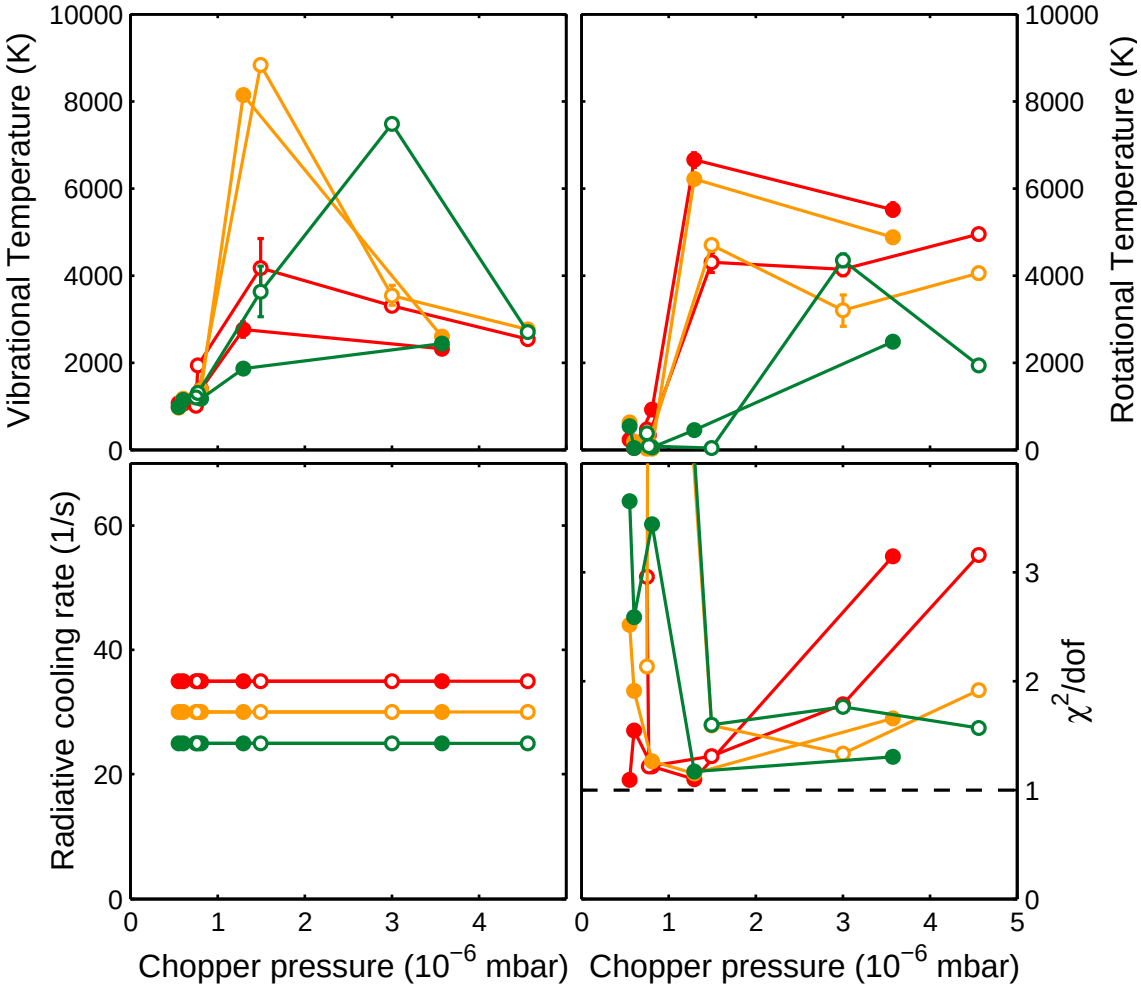

Figure 4.18: Fits with EA = 1.03 eV and fixed radiative cooling rates (full symbols are for a cathode voltage of 800 V, open symbols for 2000 V).

by a bad agreement in comparing the data and the fit curve for this case (not shown here). The same observation applies to the lower cooling rates with opposite dependencies in the pressure, and hence, no satisfying fit result can be achieved with a fixed cooling rate and EA = 1.03 eV.

While a cooling rate of the order of 30 s^{-1} is nearly consistent with the estimate given in Sec. 2.5.1, the failure of describing the data with a constant cooling rate might indicate that the parameter k_{rad} is compensating a yet unknown shortcoming of the underlying model or parameter assumption.

Summarizing the fit results with the microscopic detachment model, a good agreement of the model with EA = 1.03 eV and asymmetrical SF_6^- structure is achieved, showing reasonable fit values of the rovibrational temperatures and radiative cooling rates. This is in contrast to the model using EA = 1.20 eV and assuming symmetrical (octahedral) SF_6^-. Still, the radiative cooling rates k_{rad} vary by a factor of two, which is non-physical as at late times only excited states in SF_6^- close to the threshold contribute and k_{rad} should be independent of the initial energy distribution of

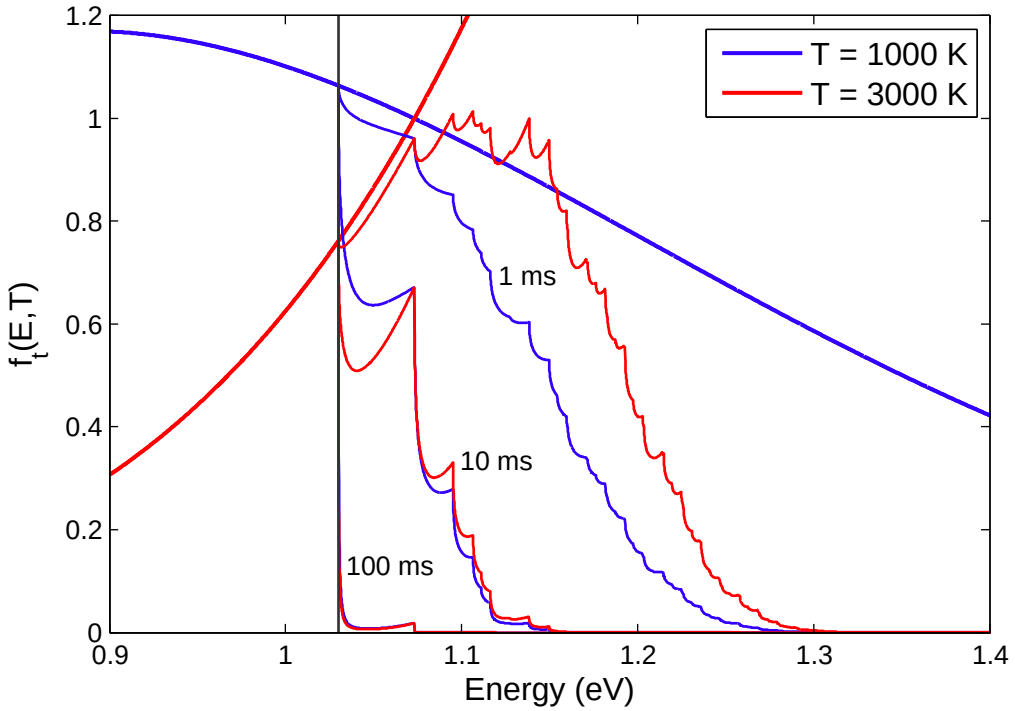

Figure 4.19: Vibrational energy distribution $f_t(E,T)$ of the stored SF_6^- ions at three different storage times of 1 ms, 10 ms, and 100 ms, assuming EA = 1.03 eV, $J = 0$, $k_{rad} = 0$ with vibrational temperatures of $T_{vib} = 1000$ K (blue lines) and 3000 K (red lines).

the ions.

This can also be illustrated by comparing the time dependence of the vibrational energy distribution for different initial temperatures. Figure 4.19 shows an initial thermal distribution $f_t(E,T)$ for $T = 1000$ K (blue curves) and $T = 3000$ K (red curves), respectively, and their time dependence for storage times of $t = 1$ ms, 10 ms and 100 ms obtained by multiplying the internal energy distribution with $\exp(-k(E)\,t)$ and using the values of $k(E)$ for EA = 1.03 eV. The initial distributions were scaled to cross each other at an energy of EA+0.043 eV (lowest vibrational frequency in SF_6) and facilitate their comparison. One notices that, even for the very different initial conditions, after 10 ms the distributions have reached very similar shapes and thus can be also expected to lead to neutralization rates close to each other.

4.2.4 Determination of the electron affinity of SF_6^-

In the prior analysis of the VAD-induced neutralization of SF_6^-, the value of the adiabatic electron affinity was kept constant at EA = 1.03 eV, which is the value determined by Troe [24]. However, a wide range of values were actually reported for the EA in the literature as summarized in Sec. 2.2.1 of this work. On the other hand, the presented VAD model based on calculated vibrational frequencies of asymmetric SF_6^- and measured electron capture cross sections of SF_6, which can also be applied using other EA values, and thus slightly different energy regimes of $\rho^-(E)$ of SF_6^-. We therefore performed some fits assuming different EA values to investigate whether the dependence of the extracted k_{rad} values on the source pressure could possibly be traced back to a failure of picking the right EA value. Figure 4.20 displays the results of this investigation for three EA values of 0.83 eV, 0.93 eV and 1.03 eV setting $T_{vib} = T_{rot}$ and treating T_{vib} and k_{rad} as free parameters to be determined by the fit. These results clearly show that the trend of the deduced k_{rad} value with increasing source pressure can be reversed when lowering the EA

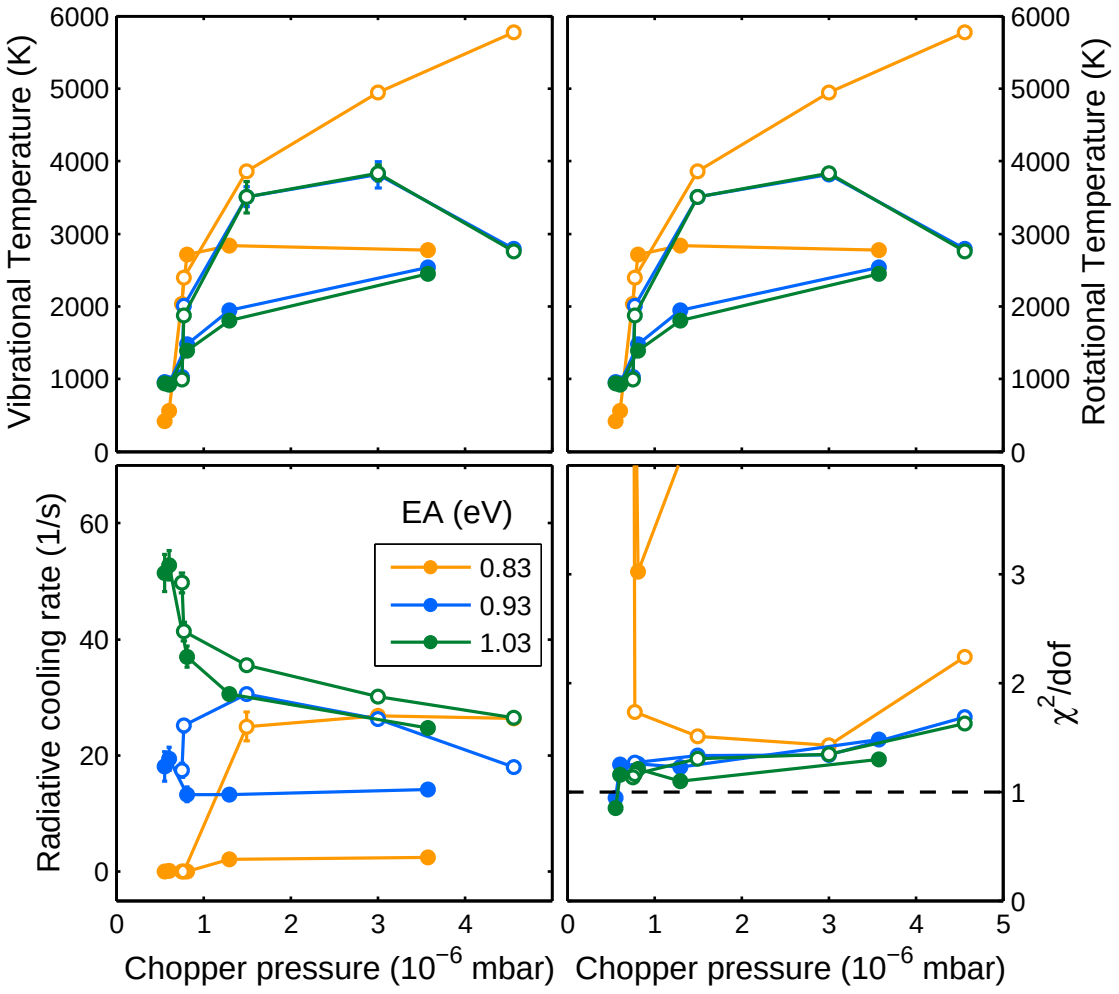

Figure 4.20: Fit results for different EA and assuming $T_{rot} = T_{vib}$ and adjusting T_{vib} and k_{rad} (full symbols are for a cathode voltage of 800 V, open symbols for 2000 V).

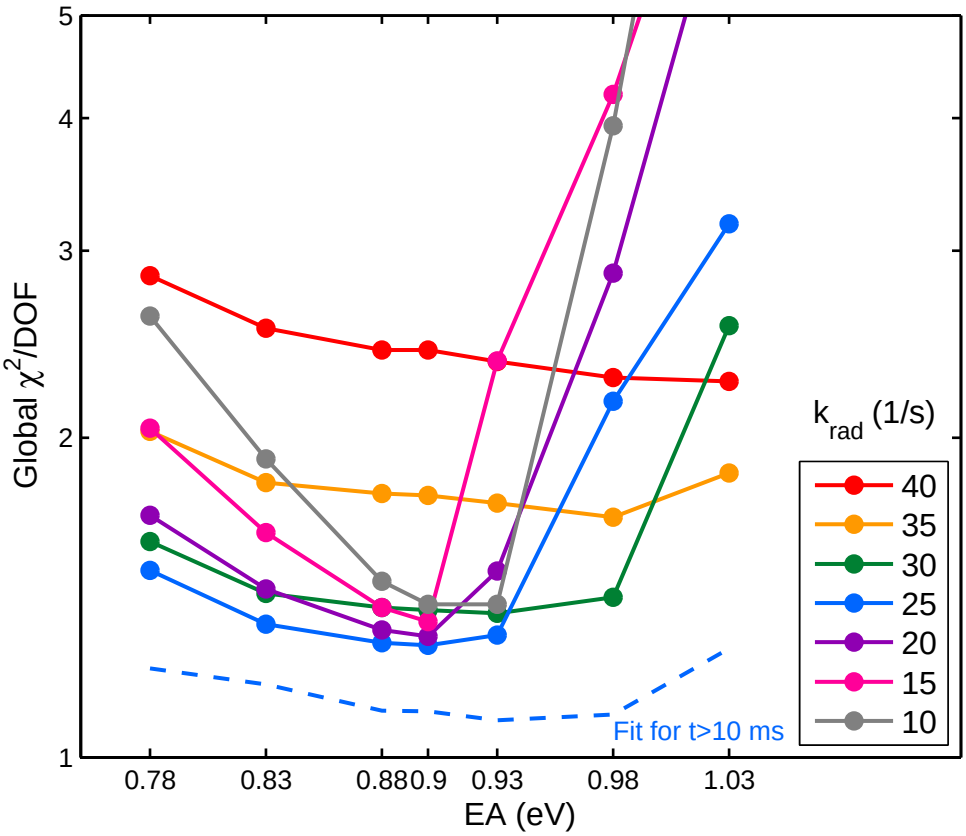

Figure 4.21: Global χ^2/DOF curves as a function of the adiabatic electron affinity, obtained by fitting the 10 measured VAD-neutralization rate curves for storage times >1 ms assuming different values for the radiative cooling rate k_{rad}, leaving only T_{vib} and T_{rot} together with the normalization to vary with the source pressure. The dashed line is the corresponding χ^2/DOF curve for $k_{rad} = 25$ s^{-1} but considering only storage times >10 ms.

value from 1.03 eV to 0.93 eV. This gives confidence that we might be able to deduce the value of the adiabatic electron detachment energy from a combined fit of the 10 individual measurements by requiring a constant radiative cooling rate; a requirement which is well justified as discussed above (see discussion of Fig. 4.19). Fits of the data were therefore performed with constant value for k_{rad} and EA, and again allowing to adjust the vibrational and rotational temperatures independently. Values for EA between 0.78 eV and 1.03 eV were used as well as k_{rad} between 10 s^{-1} and 40 s^{-1}. The global χ^2/DOF was obtained for each set of 10 fitted curves, using a sum over all residuals for χ^2 and normalizing with the total number of degrees of freedom by DOF $= \sum_i \mathrm{dof}_i$. Thus, a measure of the overall conformity between the model and the data for a set of the values of EA and k_{rad} is obtained. The global χ^2/DOF are shown as a function of EA in Fig. 4.21 and as a function of k_{rad} in Fig. 4.22. For both cases a clear minimum in the global χ^2/DOF is observed for values of EA = 0.90 eV and $k_{rad} = 25$ s^{-1} (blue curves).
The value of the global χ^2/DOF as a function of k_{rad} and EA has been examined by

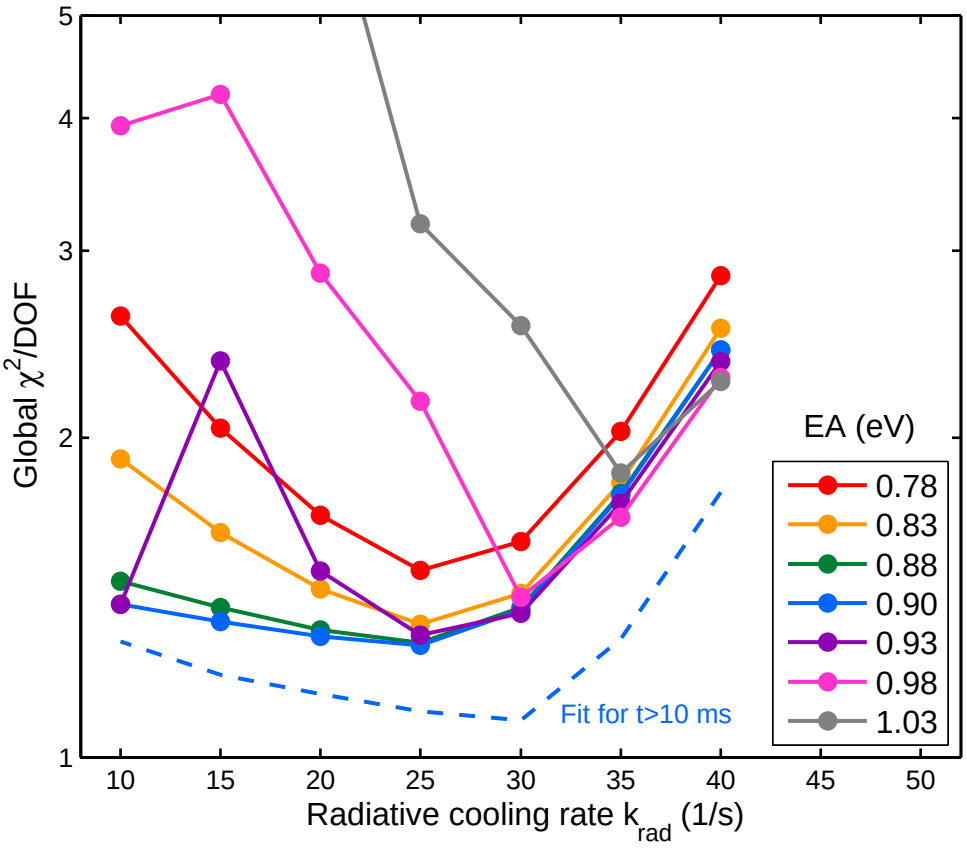

Figure 4.22: Global χ^2/DOF curves as a function of the radiative cooling rate, obtained by fitting the 10 measured VAD-neutralization rate curves for storage times >1 ms assuming different values for the radiative cooling rate k_{rad}, leaving only T_{vib} and T_{rot} together with the normalization to vary with the source pressure. The dashed line is the corresponding χ^2/DOF curve for EA = 0.90 eV but considering only storage times >10 ms.

fitting with a polynomial function. From this, the minimum global χ^2/DOF is found for values of EA $= 0.90 \pm 0.05$ eV and $k_{rad} = 25 \pm 5$ s^{-1}. Following Ref. [129], the statistical uncertainty of each value was found by the parameter range over which the global χ^2/DOF is smaller than $(\chi^2/\text{DOF})_{min} \times \{1 + 10p/\text{DOF}\}$, where p is the number of fit parameters for each of the 10 fits.

To estimate possible systematic errors, which might arise from assuming a thermal internal energy distribution of the nascent SF_6^- ions, we also performed fits restricting the fit range to storage times $t > 10$ ms. At these times the remaining population pattern is considerably less sensitive to the precise form of the initial distributions (see the populations in Fig. 4.19). Remarkably, these restricted fits result in very similar best values for EA and k_{rad}, namely EA $= 0.93 \pm 0.07$ eV and $k_{rad} = 30 \pm 7$ s^{-1} with similar statistical errors (see Fig. 4.21 and 4.22). We will take the average between the two values deduced for EA and k_{rad} as our final result, adding half the difference between the two individual values as systematic error to the statistical uncertainty.

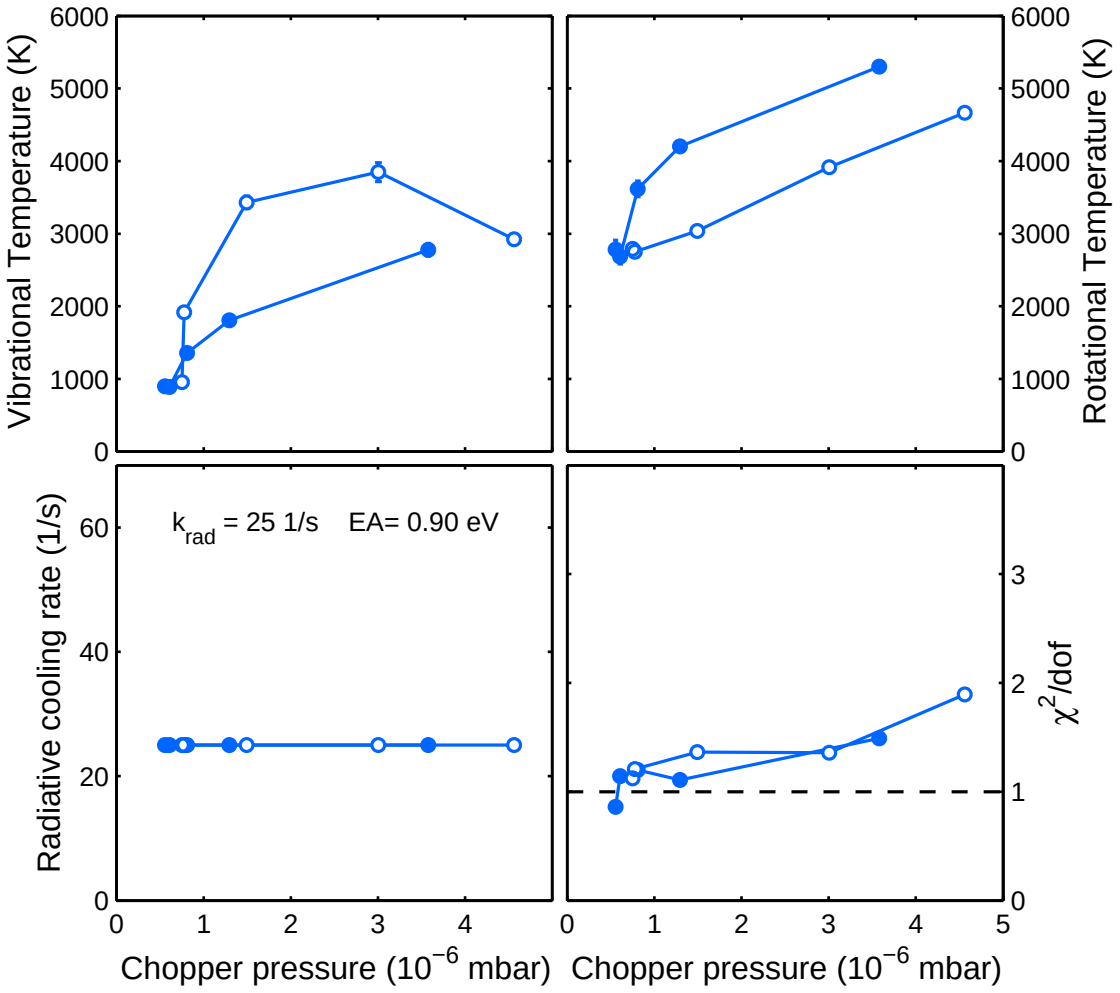

Figure 4.23: Vibrational and rotational temperatures for the best fit result with EA = 0.90 eV and $k_{rad} = 25\ \mathrm{s}^{-1}$ for a fit range of $t > 1$ ms (full symbols are for a cathode voltage of 800 V, open symbols for 2000 V).

The final value of the experimentally determined adiabatic electron affinity of SF_6^- including the statistical and systematic uncertainties is thus

$$\mathrm{EA} \;=\; 0.91 \pm 0.05\ \mathrm{eV}. \tag{4.4}$$

This value is in excellent agreement with the adiabatic electron affinity of SF_6^- of 0.9 ± 0.1 eV calculated in the paper of Eisfeld (2011) [18]. Considering the margin of the error ranges, the value slightly deviates from the recent experimental value of EA = 1.03 ± 0.05 eV from Troe (2012) [24] and the recent theoretical value of EA = 1.034 ± 0.030 eV from Karton and Martin (2012) [38].
For the radiative cooling rate of SF_6^- a value of

$$k_{rad} \;=\; 27 \pm 6\ \mathrm{s}^{-1} \tag{4.5}$$

is determined, which corresponds to the cooling at internal energies near the EA. The cooling rate was approximated in Sec. 2.5.1 and the energy dependent rates for

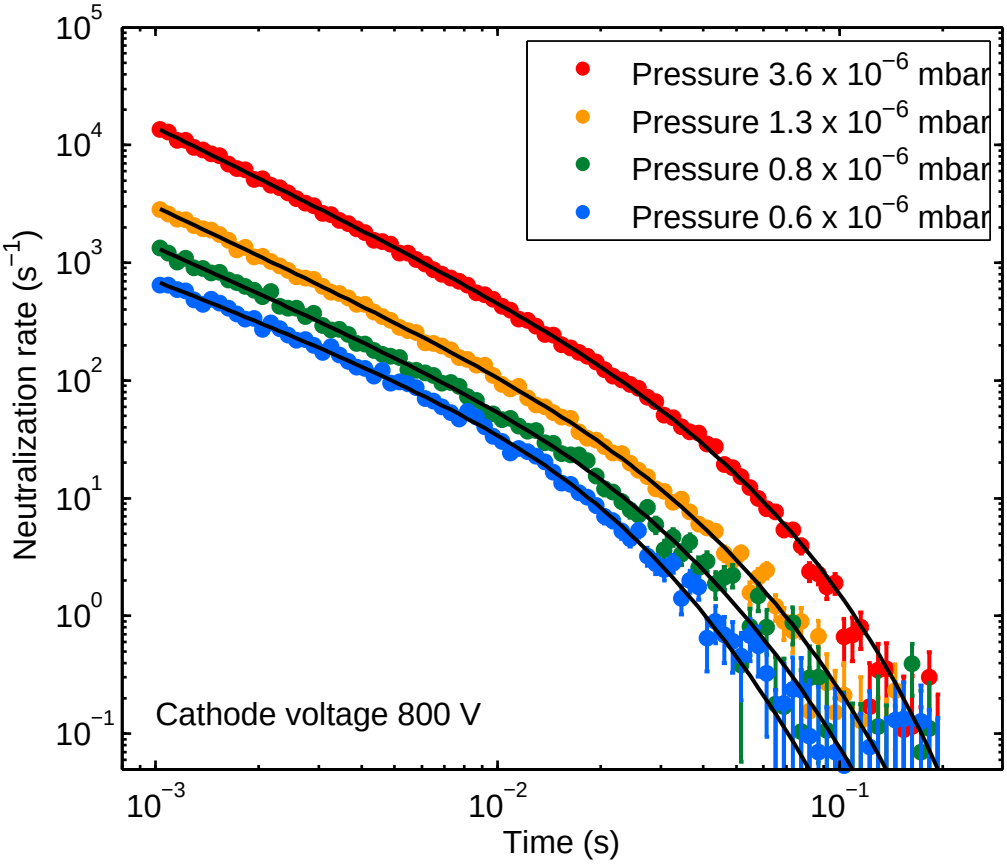

Figure 4.24: Best fit of the VAD-neutralization curves for a cathode voltage of 800 V using EA = 0.90 eV and $k_{rad} = 25$ s^{-1}; T_{vib}, T_{rot}, and the overall normalization were adjusted. The fit parameters are displayed in Fig. 4.23.

$k_{rad}(E)$ were displayed in Fig. 2.15. Here, for an energy of about 0.91 eV a value of 43 s^{-1} is estimated. Even though the value deduced in the present experiment is about 50% smaller, in view of the approximation entering the theoretical estimate this is still considered to be a reasonable agreement.
The vibrational and rotational temperatures resulting from this analysis for the fixed values of EA = 0.90 eV and $k_{rad} = 25$ s^{-1} are shown in Fig. 4.23, where T_{vib} and T_{rot} are found to lie in a plausible range. The vibrational temperature exhibits higher values for the measurements with a cathode voltage of 2000 V compared to 800 V, which is consistent with previous interpretations. At 2000 V, T_{rot} shows similar values as T_{vib}, while for 800 V the rotational temperatures is found twice as high as the vibrational one. However, the influence of rotational excitation is poorly reproduced by the VAD curves, as it was illustrated in Sec. 4.2.3. The χ^2 values are in an acceptable range considering the fact that the fit comprises five orders of magnitude in the VAD curve.
The high quality of the fits can also be judged from plots where the data are compared to the model curves for four of the measurements in each series performed at cathode voltages of 800 V (Fig. 4.24) and 2000 V (Fig. 4.25).

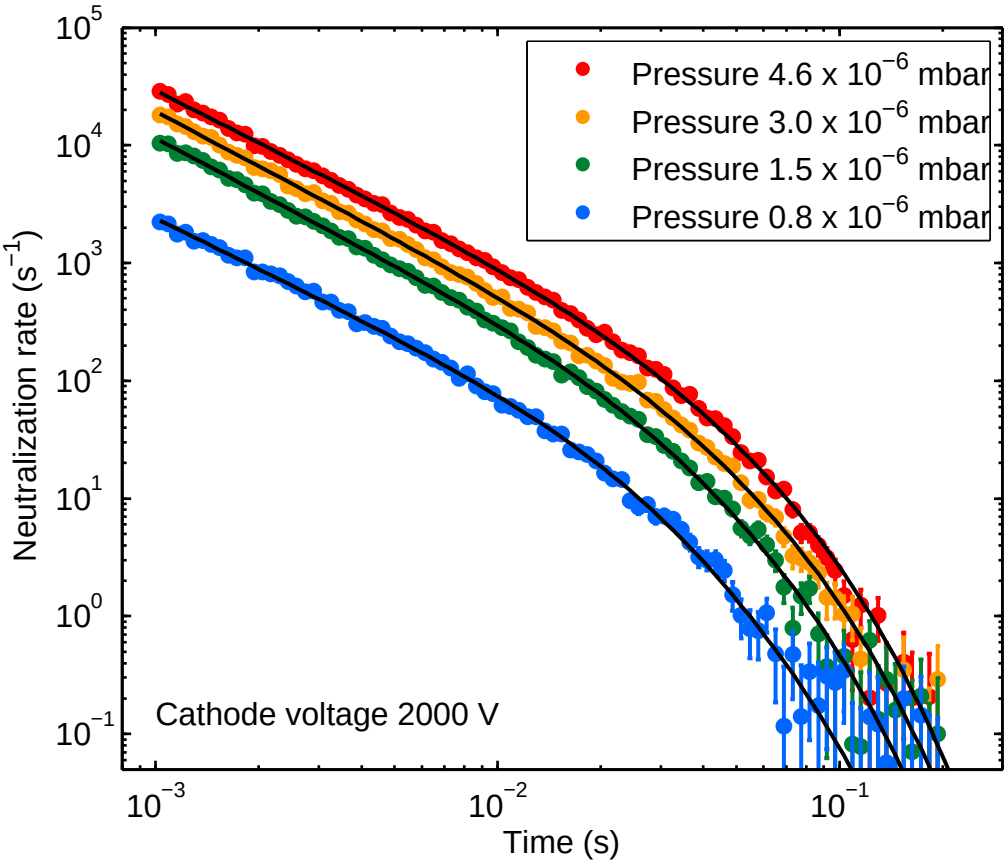

Figure 4.25: Best fit of the VAD neutralization curves for a cathode voltage of 2000 V using EA = 0.90 eV and $k_{rad} = 25$ s^{-1}; T_{vib}, T_{rot}, and the overall normalization were adjusted. The fit parameters are displayed in Fig. 4.23.

4.2.5 Alternative information about the initial SF_6^- energy distribution

In the following section we estimate the percentage of ions in the stored ensemble of SF_6^-, which have internal energies larger than the VAD-threshold energy EA, by comparing the VAD induced decays to those induced by residual gas collisions. Two measurements are presented, which have been performed at room temperature and under cryogenic trap conditions, respectively. These measurements were taken to determine the collisional lifetime of the stored SF_6^- under the respective conditions. Note that the ambient radiation field is not expected to affect the rate of neutral particle production in either of these measurements; 'warm' and 'cold' in the following will only be used to distinguish between the two measurements, which therefore essentially differ in the relative importance of residual gas collisions.
The number of ions which decayed by VAD can be determined by integrating the observed neutralization rate over the observation time. Moreover, after about 100 ms, the VAD process ceases and only those ions are left in the trap, which had initial internal energies below EA or decayed into this region radiatively. They contribute to the neutralization rate only via collisions with residual gas and in the following will be called 'stable'. To determine the total amount of stable ions, a reliable collisional lifetime fit is necessary which requires a long-time storage in the order of the expected lifetime.
A long-time measurement of the neutralization rate of SF_6^- at room temperature was already presented in Fig. 4.5(a), and a single exponential fit was applied to characterize the long-time ion loss and determine the collisional cross section. However, for the present purpose a good representation of the complete curve is required. For trapping times exceeding the VAD-decay between 100 ms and 1 to 2 seconds, an additional fast decay component was found and the fit was extended to a double ex-

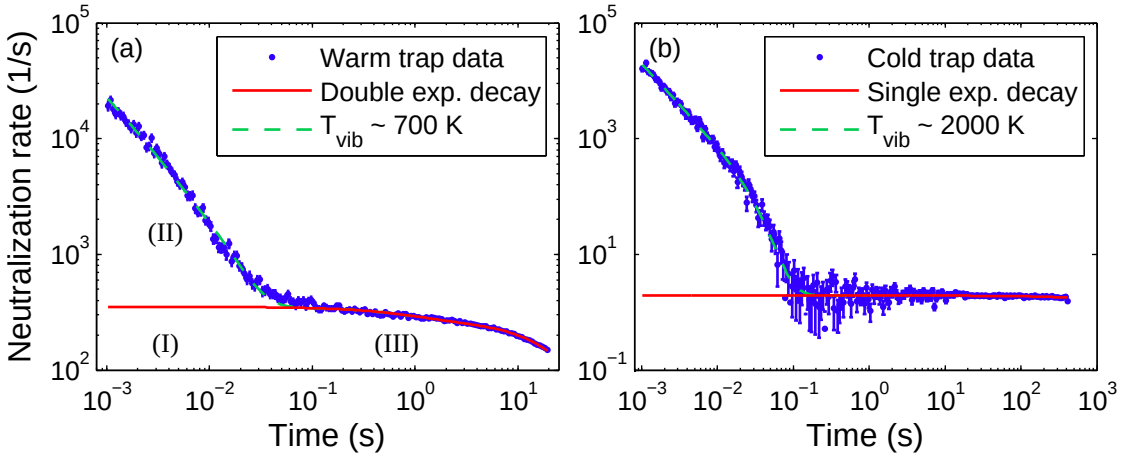

Figure 4.26: Long-time measurements of the neutralization rate of SF_6^-: (a) measurement with a warm ion trap and storage lifetimes of $\tau_1 \sim 29$ s and $\tau_2 \sim 900$ ms. (b) cold ion trap measurement with a storage lifetime of $\tau_1 \sim 840$ s. All fit values as well as the determined counts for the regions (I), (II) and (III) are summarized in table 4.2.

Table 4.2: SF_6^- count rate summary determined from fits and integrated rates; the labels 'warm trap' and 'cold trap' are to distinguish between the two measurements, no influence on the internal excitation of the ions by the ambient radiation field is expected

	Warm trap	**Cold trap**
Exponential fits of collisional-induced ion loss*		
N_1 (s^{-1})	7920 ± 120	322 ± 54
τ_1 (s)	29.3 ± 0.4	840 ± 140
N_2 (s^{-1})	65 ± 8	
τ_2 (s)	0.87 ± 0.09	
$C^\dagger$ (s^{-1})	7.36	1.55
Counts from the measurement		
(I)[a]	33.7 ± 1.3	0.038 ± 0.009
(II)[b]	80 ± 17	36.5 ± 0.5
(III)[c]	7950 ± 120	322 ± 54
Relative counts since t ≥1 ms		
(I)	0.0042 ± 0.0002	∼0
(II)	0.010 ± 0.002	0.102 ± 0.015
(III)	0.984 ± 0.020	0.898 ± 0.202
Estimated temperatures T_{vib}(K)		
From relative counts	∼600	∼850
Fit value [#]	∼700	∼2000

* Fit function: $R_{coll}(t) = N_1/\tau_1\ exp(-t/\tau_1) + N_2/\tau_2\ exp(-t/\tau_2)\ +\ C$

† Detector dark count rate

[a] Collisional-induced $1 \leq t \leq 100$ ms: $\int_{1\,\mathrm{ms}}^{100\,\mathrm{ms}} R_{coll}(t)dt$

[b] VAD-induced $1 \leq t \leq 100$ ms: $\int_{1\,\mathrm{ms}}^{100\,\mathrm{ms}} R_{VAD}(t)dt$

[c] Collisional-induced $t > 100$ ms: $\int_{100\,\mathrm{ms}}^{\infty} R_{coll}(t)dt$

[#] Fit using EA = 0.91 eV, times later than 1 ms and adjusting T_{vib}, k_{rad} and the normalization.

ponential function. Respective lifetimes of $\tau_1 \sim 29$ s and $\tau_2 \sim 900$ ms were obtained. Fit parameters and determined counts are summarized in more detail in table 4.2. At cryogenic temperatures, a long time measurement with a trapping duration of 400 s was chosen with a background measurement of 40 s after the ejection of the ions, from which a storage lifetime of $\tau_1 \sim 840$ s was found.
The neutralization rate curves of these measurements are plotted in Fig. 4.26(a) for the 'warm' trap and (b) for the 'cold' trap together with the fits of the exponential

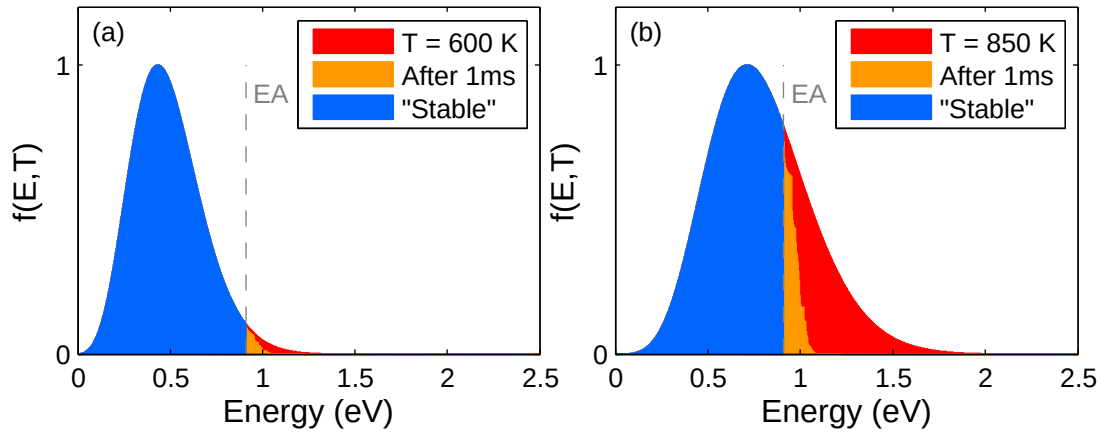

Figure 4.27: The thermal energy distributions for the 'warm' trap (a) and the 'cold' trap (b) with the same relative fraction above and below the EA after 1 ms as it was derived from the relative counts of the neutralization curves (Fig. 4.26 and table 4.2). The energy distributions show in blue the fraction below EA, in orange the contribution which is left with energies above EA after 1 ms and the sum of all curves including the red part is the initial distribution.

decays caused by residual gas collisions. Contributions of the collisional-induced ion loss for times 1 ms $\leq t \leq$ 100 ms (I) and $t >$ 100 ms (III) are obtained from the exponential parts of the fit function. The VAD part (II) is then derived by integrating over all counts for times 1 ms $\leq t \leq$ 100 ms and subtracting the collisional fraction and the detector dark counts. However, ions lost by collisions at times 1 ms $\leq t \leq$ 100 ms can have been either excited above the EA or stable. This was accounted for by a larger error in table 4.2 for the contribution (II).
Thus, for storage times later than 1 ms, the measured relative counts between excited ions and stable ions could be determined and are also summarized in table 4.2. In the warm trap measurement, ∼1% of the trapped SF_6^- are found to be excited above the VAD-threshold and ∼99% are stable. The cold trap measurement shows ∼10% excited SF_6^- and 90% stable ions.
From these values one realizes, that a large amount of the trapped ions are indeed not very highly excited and do not undergo VAD. This is a very important observation, as it gives information on the creation and excitation process of the ions in the source. In case of low-energy electron attachment to the neutral SF_6 without thermalization, the internal energy distribution of the SF_6 gas would be retained and only shifted towards higher energies by the electron affinity EA. Hence, all SF_6^- ions would have energies higher than the EA and would thus dominantly decay via VAD in the first 100 ms. However, this assumption is far off the observation, as the determined percentages illustrate.
On the other hand, if the ensemble of SF_6^- is thermalized in the source, the distribution can be described by a temperature as assumed when the VAD model is adjusted to the measurements. Figure 4.27(a) and (b) illustrates thermal energy distributions for both measurements which were chosen such that they contain the same relative fractions above and below the EA at the time $t = 1$ ms as were determined from the

relative counts (table 4.2). The whole envelope including the red, orange and blue areas displays the initial distribution at time zero with temperatures of ∼600 K in the case of the warm trap and ∼850 K for the cold trap measurement. The orange part shows the remaining energy distribution after the depletion due to the VAD process at a time $t = 11$ ms and for energies above the EA. The blue area is the fraction below EA, which is considered to be stable with respect to VAD, and can be assume to be the fraction, which is left after ∼100 ms.
Figure 4.26 displays also the result of the fits with the VAD model using EA = 0.91 eV. However, one has to note that because of the long storage duration, lower statistics are available for the VAD part of the neutralization curve compared to the measurements in the previous section. Nevertheless, the fitted temperature of T_{vib} ∼700 K for the warm trap is in good agreement with the temperature from the relative counts, however, larger discrepancies are found for the cold trap measurement with a fitted temperature of T_{vib} ∼2000 K.
As the main intention of these long-time storage measurements was to derive a reliable storage lifetime, it was not attempted to keep the ion source pressure at a constant value. On average the ion source pressure was higher in the cold trap measurement, which confirms the trend of the temperatures. For both measurements a cathode voltage of 2000 V and a filament current of 22 A were used.
Summarizing the observations, the relative amounts of excited and stable SF_6^- have been determined by a comparison of the neutral count rates between VAD and collisional-induced neutralization, and a relatively small fraction of the ions was found to be excited above the EA. An energy distribution defined by low-energy electron attachment without thermalization can thus be excluded from these observations. With the assumption of fully thermalized distributions in the ion source, some discrepancy is found between the temperature values considering on the one hand the ratio of the total decay counts at early and at late times, and on the other hand the initial (mainly short-time) VAD time-dependence (VAD model fits). An incomplete thermalization of the ions in the source leading to different shapes of the initial energy distribution than shown in Fig. 4.26, may explain the observed differences for these high temperatures.

4.3 Photo-detachment and delayed decay of SF_6^-

The cooling rate which was determined in the previous section indicates the influence of the radiative stabilization processes after the electron attachment to SF_6, as a competing process to VAD. However, after ∼100 ms the radiative cooling process can no longer be followed as the neutral rate from the VAD decay vanishes. Photo-excitation of SF_6^- gives access to the ion's internal cooling process even below the threshold EA, and performed in an ion beam trap at low pressure, this process can be investigated under isolated conditions without, e.g., collisional stabilization.
The remaining internal energy distribution, once the thermal VAD process has vanished, is here shifted upwards by the absorbed photon energy (see Sec. 2.5.3 and Fig. 2.17). The subsequent neutralization rate by VAD, as induced by the laser excitation, is used to draw conclusions on the internal energy of the ions prior to their photo-excitation. An introduction on this process can be found in Ref. [130]; similar measurements have been performed for instance on C_{60}^- [11] or aluminum clusters Al_n^- [131, 132].
A schematic view on the measurement in the CTF is shown in Fig. 4.28. Through a crossed ion-laser beam configuration in the trap center, a small fraction of the stored ions is photo-excited. As the ions are moving simultaneously in both directions, the excited ion fraction manifests itself in two short, counter-propagating "bunches" inside the unexcited trapped ions. The earliest neutral counts on the detector originate from the bunch moving towards the detector at the time of the excitation. Further delayed neutrals arrive each half oscillation period coming from either of the two excited ion bunches. Note that while neutral particles are created from the excited bunches continuously, they are born at near-identical velocities and hence arrive at the detector within a narrow time window.
As in the previous experiments, a 6 keV SF_6^- ion beam is trapped under cryogenic conditions at a trap temperature of ∼12 K. A trapping mode differing from the

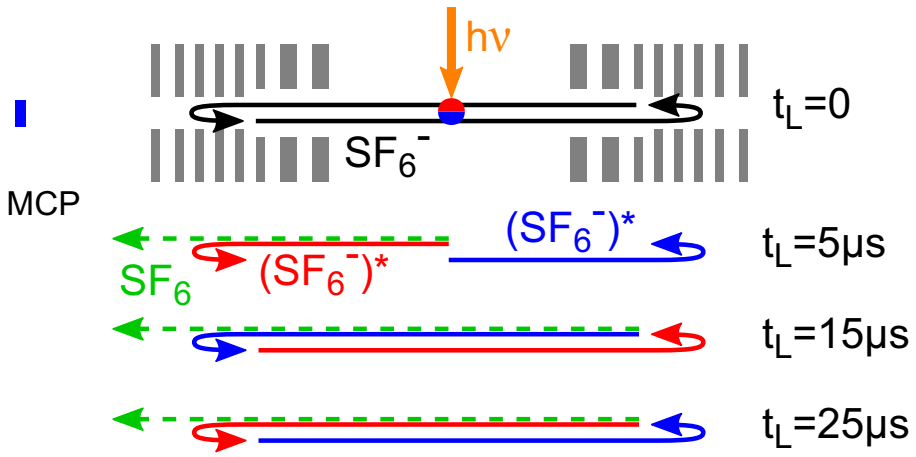

Figure 4.28: Schematic process of the laser excitation of a stored ion beam (not to scale): A small fraction of the beam is excited and moves as two excited bunches in opposite directions (red and blue). Neutral fragments are created and drift towards the detector (green) each half oscillation.

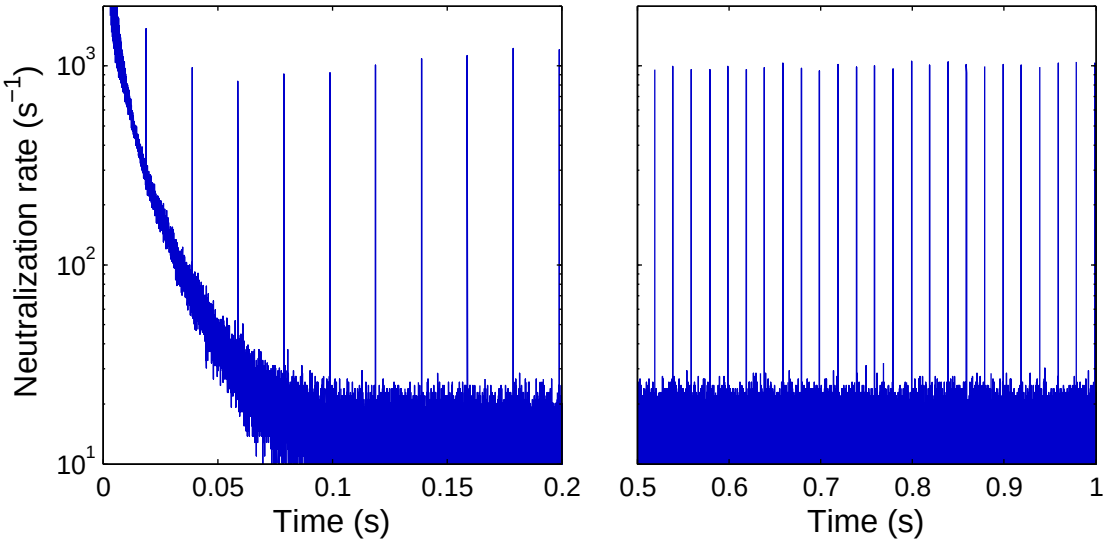

Figure 4.29: Neutralization rate of SF_6^- with enhanced signals from the photo-induced neutralization coinciding with the laser shots every 20 ms.

other modes discussed in Sec. 3.5.2 was employed using a positive η-parameter, which ensured a faster dispersion of the stored ion bunch. As in the previous mode the trap oscillation period was ∼20 μs. The ion source was operated with a cathode voltage of 2000 V, and a filament current of 26 A, while the vacuum pressure in the chopper chamber was kept at an intermediate value of $\sim 2 \times 10^{-6}$ mbar.
Photo-excitation is performed with the laser setup introduced in Sec. 3.4 using a 1064 nm (1.165 eV), pulsed Nd:YAG laser with a pulse repetition rate of 50 Hz and a pulse length between 15 ns and 20 ns. An average laser power of 1 W was used (corresponding to 20 mJ/pulse) and the laser beam was expanded to a diameter of about 15 mm providing a large overlap with the stored ion beam, but relatively low photon intensity. The applied photon energy was sufficient to excite all ions above the EA independent of their remaining internal energy, but also strongly suppressed the probability for direct vertical photo-detachment, which was observed at much higher photon energies of the order of ∼2.8 eV [5] to ∼3.27 eV [17].
During the first 100 ms to 200 ms of the ion storage the initial VAD process takes place, where almost all of the excited $(SF_6^-)^*$ with $E >$ EA neutralize and are lost from the trapped ion ensemble. However, as quantitatively discussed before, a large amount of the stored ions are not excited above the EA and remain stored, and are hence only affected by rare residual gas collisions.
The neutralization rate of a trapped SF_6^- beam with periodic photo-excitation is shown in Fig. 4.29 for storage times of up to 1 s and with time bins of 10 μs. A clear enhanced neutral signal is observed in pulses spaced by 20 ms corresponding to the laser repetition rate. For times shorter than 100 ms, the photo-excited signal overlaps with the initial VAD. These early pulses will not be considered in this analysis as the signal from photo-induced, delayed electron emission is influenced by the steeply changing background. The current data set includes an average over more than 10^5 injections, where signal amplitudes are given in units of counts per

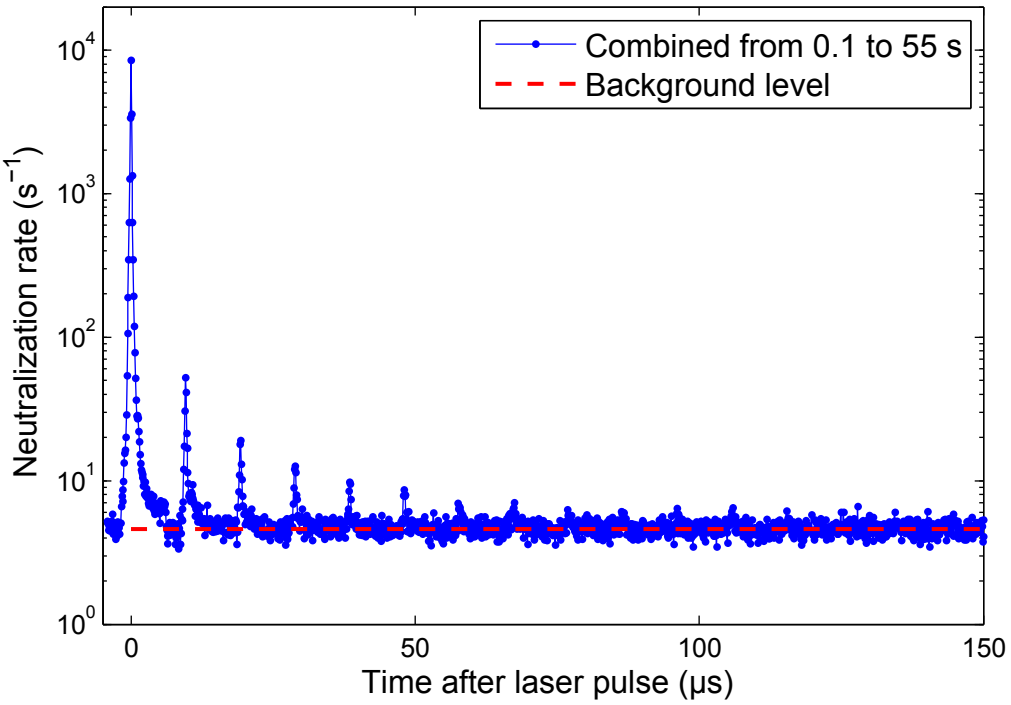

Figure 4.30: Combined neutralization signal from all laser shots between 0.1 s and 55 s of ion storage with a bin width of 100 ns

second and injection.
In the high resolution time spectrum with 0.1 μs binning, a small drift of the time differences between the peaks was observed as the laser clock and TDC clock were not properly phase-locked. However, the time of each laser shot was determined via a search algorithm for the intensity peaks. With this information the time windows following each laser shot were superimposed on each other. This combination of all laser shots from a large number of injections and summed over all storage durations of 0.1 s $< t <$ 55 s is presented in Fig. 4.30 as a function of the time after the laser shot. This representation reveals several equidistant neutral signals with a separation of 10 μs, i.e., half of the SF_6^- oscillation period in the trap. The background from ion loss by residual gas collisions was determined by an averages of the background rates between the individual laser shots which were fitted with an exponential decay function to account for the finite storage lifetime. In Fig. 4.30, these background rates were summed over the respective time window to illustrate the determined background level.
As illustrated in Fig. 4.28 and visible in Fig. 4.30, the first neutral signal, referred to as the prompt signal, originates from ions moving towards the detector at the time of the laser excitation. Because the exact decay time cannot be determined, the prompt signal can thus contain possible contributions from direct vertical photodetachment of excited SF_6^- in addition to the neutrals from the fastest VAD decays. The prompt signal represents the decay times between zero and 5 μs after the excitation, before the excited bunch is reflected by the trap mirror potential. All later peaks are due to delayed decays of the newly formed, metastable $(SF_6^-)^*$. Each

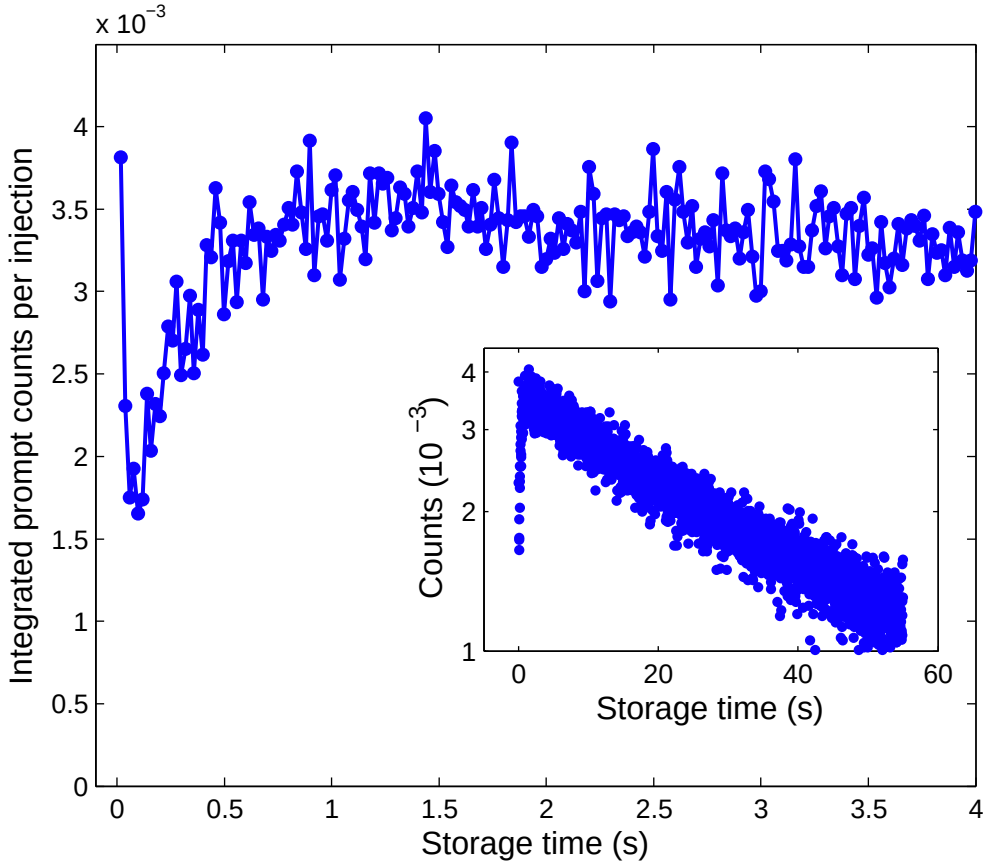

Figure 4.31: Integrated neutral counts for each prompt signal: The first few counts are from the overlap of the thermal and photo-induced SF_6^- decays. The low count rate at early storage times (∼0.1-0.5 s) is likely caused by a preference for photo-dissociation of the excited SF_6^-, which exhibits a low detection efficiency. Radiative cooling of the internal energy of SF_6^- changes the decay channel to photo-induced VAD for later storage times, which increases the count rate due to a high detection efficiency (compare Fig. 4.32 and see text for details). Residual gas collisional ion loss causes the exponential decline of the signal at times ∼2-55 s (see inset).

signal peak incorporates a decay duration of 10 μs, i.e., one trap passage of the ions in the direction towards the detector.

4.3.1 Prompt signal and photo-detachment cross section

A single neutral prompt signal without averaging over the storage duration was used in Sec. 3.5.2 to derive the (approximate) ion beam and laser beam overlap. For the averages shown here, the width of the neutral signal is dominated by the drift between the laser clock and TDC clock increasing for long storage times. The slightly asymmetric shape of each peak towards longer times in Fig. 4.30 is ascribed to ions decaying inside the mirror potential with a reduced velocity and thus arriving later on the detector. In any case, the exact decay time within the ion flight times of 5 μs for the prompt signal and of 10 μ for each delayed signal cannot be determined.

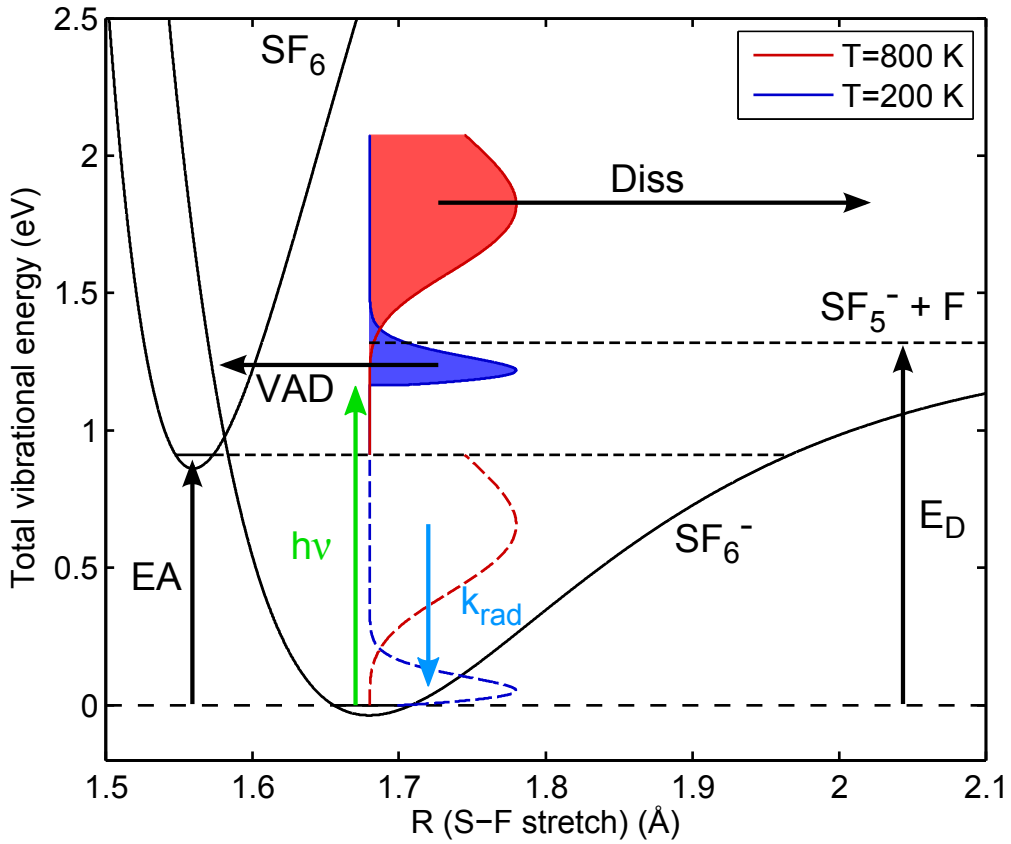

Figure 4.32: Schematic view of the potential curve of SF_6^-: Excited SF_6^- ions at 800 K (initial energy distribution represented by the dashed red line) are assumed to undergo dominantly dissociation after the absorption of the photon energy of 1.165 eV (green arrow; red area: projected energy distribution), whereas colder SF_6^- ions at 200 K (blue dashed line) stay mainly below the dissociation threshold of 1.32 eV and decay via VAD (blue area: projected energy distribution after photon absorption). Radiative cooling (cyan arrow) decreases the ion's temperature during the ion storage, which changes the decay process from photo-dissociation to photo-detachment. The lower detection efficiency for the neutral dissociation product fluorine compared to SF_6 leads to the lower neutral count rate for early storage times in Fig. 4.31.

The counts of the prompt signals integrated over the 5 μs time window directly following each laser shot are shown in Fig. 4.31 as a function of the ion storage time. The very low rate of only ~ 2 to 4×10^{-3} counts per laser shot indicates that no detector saturation effects are expected. The first few enhanced data points are due to the overlap of the photo-detachment with the initial VAD-decays and therefore cannot be determined with much precision. The increase of the neutral yield of about a factor of two over the first second indicates that the internal energy of the stored SF_6^- changes during this storage time interval. However, in case of radiative cooling during this storage time one would expect a decreasing neutral yield by VAD

as less ions would have enough energy after the photon absorption to decay by this process within the first 5 μs.
An explanation of the rise in the neutralization rate is obtained by considering the process of auto-dissociation of SF_6^-, which becomes a relevant process at these early observation times and high excitation energies (compare Fig. 2.8). The schematic view on the potential curve of SF_6^- for the stretch of a single S-F bond in Fig. 4.32 elucidates the competing processes of VAD, dissociation and radiative cooling. A value of EA = 0.91 eV is assumed for the electron affinity. According to the energy difference between the electron affinity and the dissociation energy of $E_D - \mathrm{EA} = 0.41$ eV, which was determined in Ref. [20], a dissociation threshold of $E_D = 1.32$ eV is considered in Fig. 4.32 as well as also for the later analysis.
A still hot SF_6^- ion ensemble at 800 K, as illustrated by the red dashed curve in Fig. 4.32, will be shifted by the absorbed photon energy of 1.165 eV dominantly above the dissociation threshold of 1.32 eV (red area). These ions will mainly decay via dissociation, but this fragmentation will be detected by the MCP detector with a reduced efficiency as the neutral fluorine atom from the dissociation process exhibits a laboratory kinetic energy of about 780 eV only (see Sec. 2.5.3). For longer storage times the energy distribution approaches lower temperatures due to the radiative cooling process, and an increasing amount of ions can only be photo-excited *below* the dissociation threshold. These SF_6^- ions will mainly decay via VAD and will be observed with a higher detection efficiency, which explains the rising prompt amplitude in Fig. 4.31 for later times.
For even longer storage times, the prompt signal exhibits an exponential decay, as depicted in the inset of Fig. 4.31, which can be dominantly assigned to trap ion loss due to residual gas collisions. The total number of ions decaying via residual gas collisions and counted on the detector can be extrapolated from an exponential fit of the neutral counts between each laser shot and leads to about 234 ions per injection. The exponential fit of the time dependence of the prompt signals only leads to ∼6 ions which decay per injection due to the photo-excitation.
These values can be used to approximate the photo-detachment cross section of SF_6^- at the laser wavelength of 1064 nm by $\sigma_{pd} = (N_{pd}/N_L) \cdot I_{ph}^{-1}$ and thereby exclude two-photon absorption processes in the measurement. N_{pd}/N_L is the fraction of electron-detached SF_6^- ions irradiated by the laser beam and I_{ph} is the photon intensity per unit area. The fraction of illuminated SF_6^- for each laser shot in the ion trap is about 1.7% of the trapped ions, which is obtained by comparing the ions' flight time through the laser beam of ∼15 mm diameter with the trap oscillation period. Thus, on average only about $N_L = 4$ of the 240 trapped ions are in the laser beam. The maximum number of counts per laser shot is determined from Fig. 4.31 by the amplitude of an exponential fit to about $N_{pd} \approx 3.6 \times 10^{-3}$. These extrapolated neutral counts are due to the VAD-decay with the same detection efficiency as for neutrals from the residual gas induced neutralization, and the detector efficiency cancels out for the ratio N_{pd}/N_L.
The average laser power was measured by a caloric laser power meter used as a beam dump after the laser beam left the ion trap and gives 1 W in the trap center after correction for the window transmission, which corresponds to 20 mJ per pulse inside the trap (see also Sec. 3.4). A photon intensity of $I_{ph} = 5.4 \times 10^{16}$ photons/cm^2 is

obtained with the beam diameter of 15 mm. Combining these values, one finds a photo-detachment cross section for SF_6^- of

$$\sigma_{pd} \approx 2 \times 10^{-20}\ \mathrm{cm}^2 \tag{4.6}$$

at a wavelength of 1064 nm. This is in a reasonable order of magnitude compared to measured photo-detachment cross sections of SF_6^- of $\sigma_{pd} \sim 10^{-18} - 10^{-19}$ cm^2 at wavelengths between 360-400 nm [133] and which are steeply falling towards longer wavelength. In addition, the small fraction of counts from the illuminated ions ($N_{pd}/N_L = I_{ph}\sigma_{pd}$) shows that two-photon processes can be neglected in the measurement, as the probability for this process scales with $(I_{ph}\sigma_{pd})^2$.

4.3.2 Delayed detachment after photo-excitation

Figure 4.33 displays the integrated neutral counts for the prompt and delayed signals after background subtraction and for storage times up to 2 s after summing up the laser shots inside the respective time windows following the laser excitation (compare Fig. 4.30). The first point at 2.5 μs is the prompt peak and the following delayed signals are separated by 10 μs. Time frames between 0.5 s and 2 s of ion storage exhibit similar time dependencies and are additionally combined as the red curve. A power function of $\propto t^{-1.2}$ is found to approximately describe the shape of this decay for about 10 μs $< t_L <$ 100 μs, except the data at 0.1-0.5 s of the storage time. The similarity of the different curves for $t_L > 0.5$ s indicates that the energy distribution does not change significantly during ion storage, and processes such as radiative cooling are already completed or proceed over much longer time scales.
However, the strong discrepancy observed for the first 0.1 to 0.5 s can be assigned to the radiative cooling process, which became already apparent in the increasing prompt intensity (see Sec. 4.3.1 and Fig. 4.31). This also showed that before radiative cooling, hot SF_6^- ions decay mainly via dissociation and only a smaller fraction is left for the delayed detachment process.
To investigate possible long-time dependencies of the radiative cooling process, the CTF capability of providing extremely high vacuum was used to store and laser irradiate the SF_6^- ions for as long as 55 s. Integrated delayed counts for longer storage times are shown in Fig. 4.34, where in (a) also the background level for each time period is indicated and in (b) the background was subtracted. Within the statistical error no time variation of the signal shape is found and the decrease of the amplitude in (a) is due to trap ion loss induced by residual gas collisions. Values below 10^{-6} counts per laser shot and injection are assumed to be consistent with the background due to their large statistical errors. For the further analysis of the decay shape following a laser pulse, the summed data for 1 s to 55 s of ion storage are used.
Models for the delayed neutralization rate of SF_6^- after photo-excitation were introduced in Sec. 2.5.3, where the rate $R_{ph}(t_L, t_i)$ is given as a function of the time after the laser shot t_L, which was obtained by integrating over the initial energy distribution $f_{t_i}(E - h\nu)$ after a storage time of t_i and shifted by the photon energy $h\nu$. Equation (2.42) accounts for the detected SF_6 neutrals after electron detachment by $k(E)$ and Eq. (2.43) for the detected fluorine atoms after the dissociation by

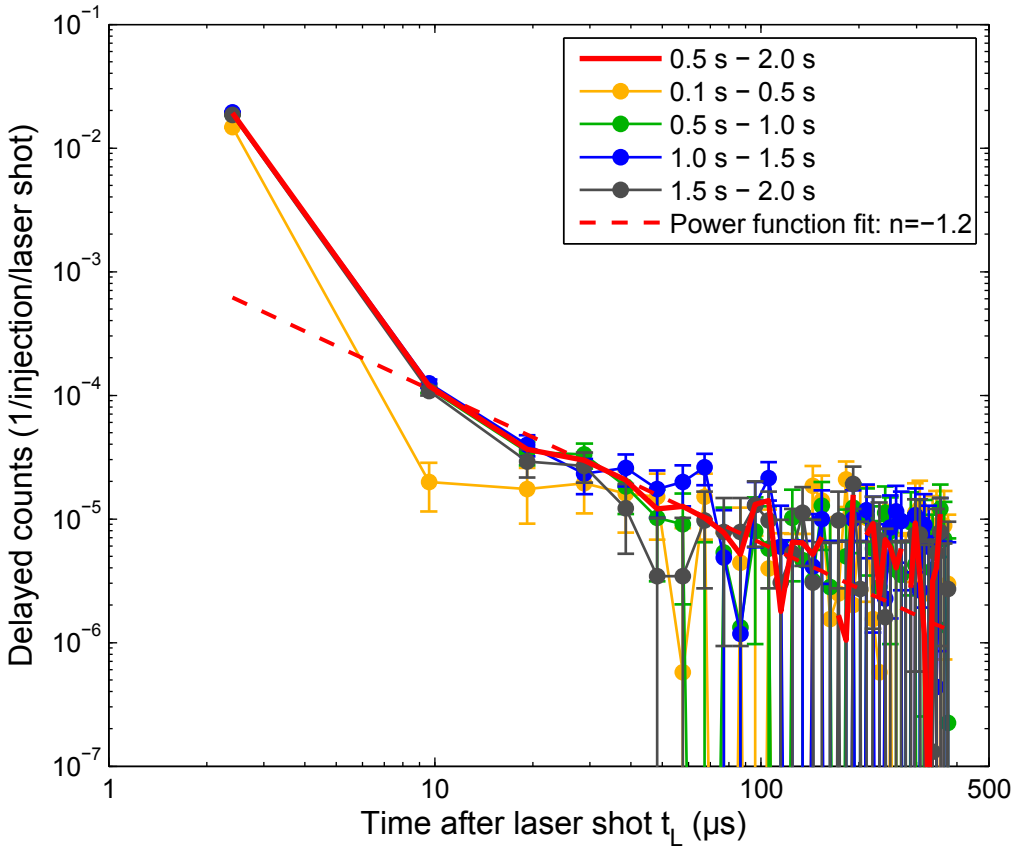

Figure 4.33: Neutral counts versus the time after laser excitation shown for different storage time intervals. The deviation in the first 0.5 s can be attributed to radiative cooling and a competition between VAD and auto-dissociation as shown in Fig. 4.31 and Fig. 4.32 and is described in the text. The difference in the prompt amplitude compared to Fig. 4.31 is due to a different measurement set, which here includes the data for storage times $t \geq$ 2 s with possibly different ion intensities.

$k_{diss}(E)$, where in each case both processes are present. In equation (2.44) the two competing processes are combined with different detection efficiencies ϵ and ϵ_{diss}.
It was also found that a simple radiative cooling model including only the strongest IR active mode and stochastical intramolecular vibrational redistribution (IVR), leads to energy distributions similar to thermal canonical distributions at varying temperatures (compare Fig. 2.16). Thus, IR cooling times and temperatures of the SF_6^- ions can be connected to each other.
In figure 4.35, the model from Eq. (2.42)-(2.44) with detection efficiencies of $\epsilon = 1$ and $\epsilon_{diss} = 0.2$ was adjusted to the delayed neutral counts by varying the temperature of the initial distribution; excluding the prompt signal at $t_L = 2.5$ μs from the analysis. As the carefully determined background level in Fig. 4.34 still seems to underestimate the background for late times, a new background for the analysis in Fig. 4.35 was determined from an average of the delayed signal for times $t > 150$ μs after the laser shot. Furthermore, for the displayed models in Fig. 4.35, values of EA = 0.91 eV and $E_D = 1.32$ eV were assumed for all curves, except for the dark

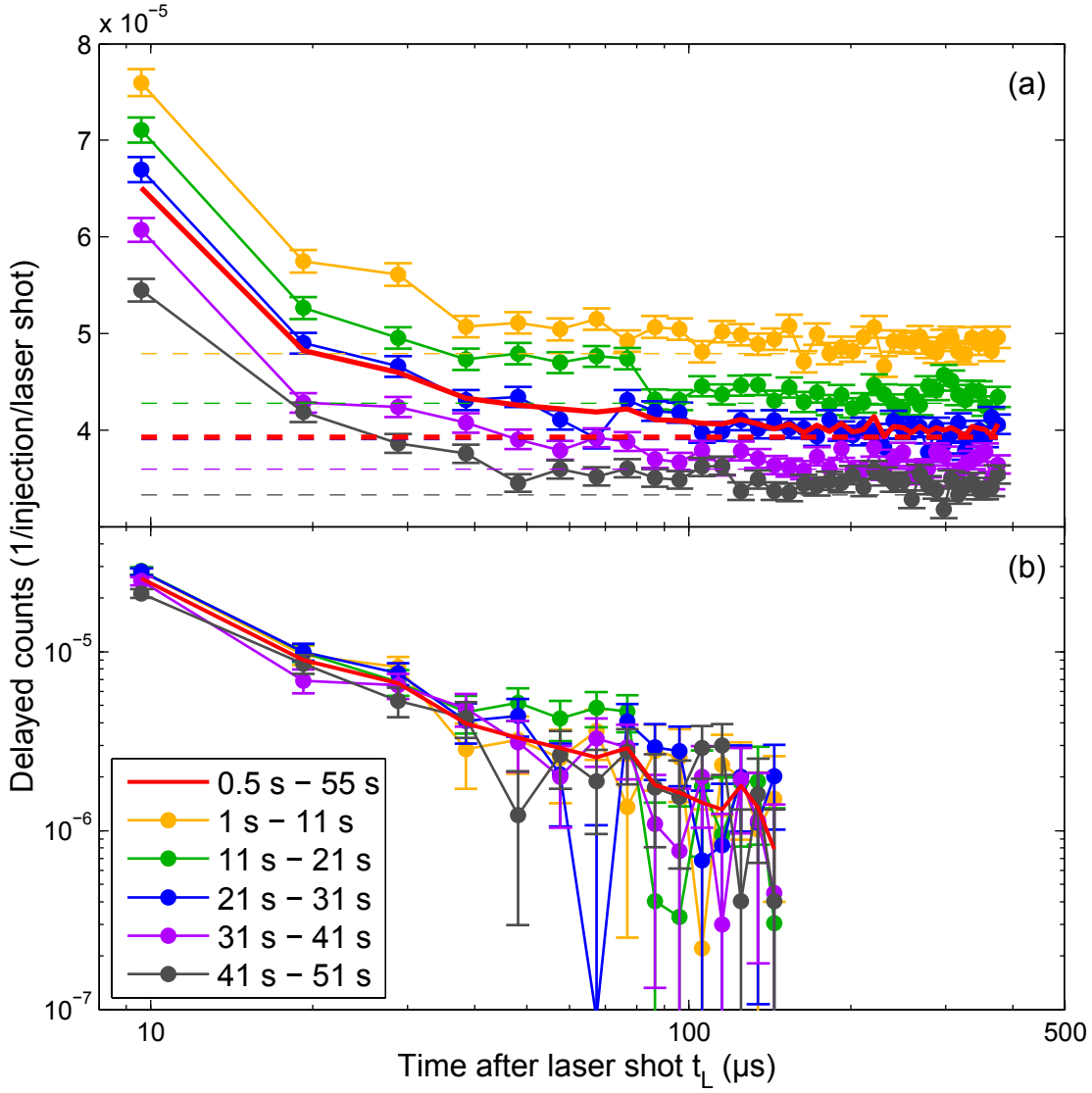

Figure 4.34: (a) Photo-induced delayed neutralization counts for times ($t_L > 5\mu s$) for storage times up to 55 s and corresponding background level for the time periods. (b) The same counts in a logarithmic scale and after background subtraction.

gray curve with EA = 1.03 eV and $E_D = 1.44$ eV from Ref. [24].
The model function was normalized to the first delayed peak, which exhibits the highest statistics. To account for the uncertainty of the ion decay time, the model curve was integrated over a time range of 10 μs around the times where the delayed peaks were observed. Hence, the prompt contains the integrated counts from zero to 5 μs, the first delayed signal from 5 μs to 15 μs, etc.
The best match between this model and the experimental data was found for temperatures of about $T_{vib} = 300$ K, whereas for higher temperatures such as 600 K a steeper decline of the delayed signal is predicted, while a flatter decline is predicted for $T_{vib} = 100$ K.
This result suggests that radiative cooling over storage times of up to 55 s does not

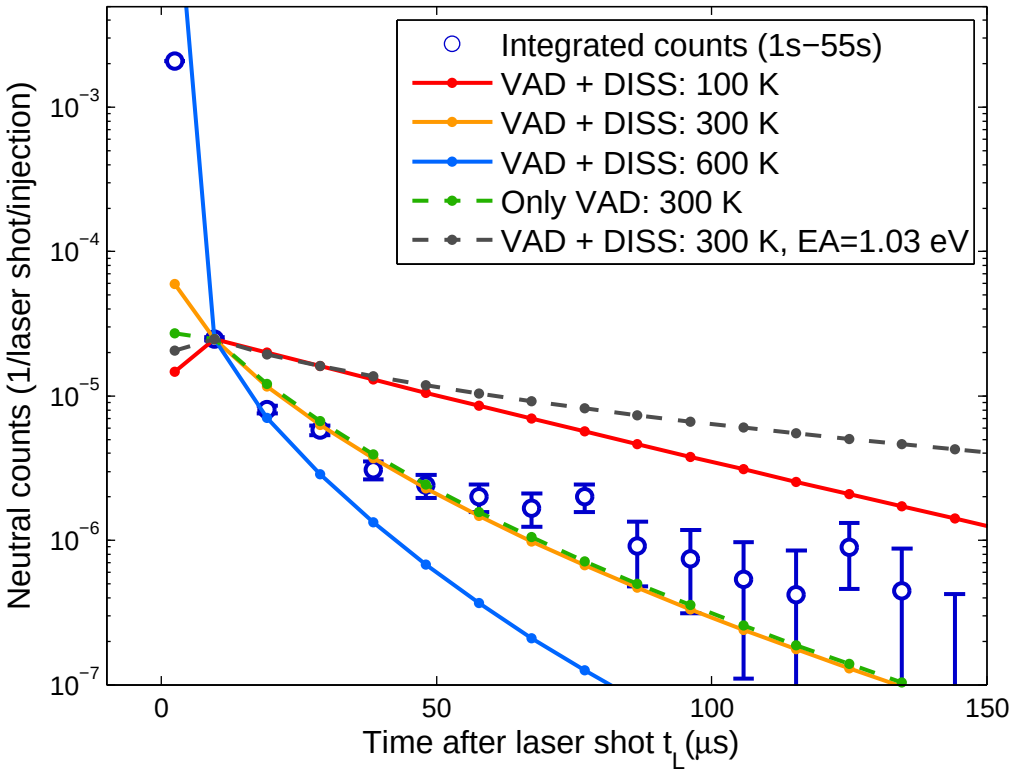

Figure 4.35: Photo-induced delayed neutralization signal after subtraction of the background, which was estimated from the data for times >150μs (see text). Model predictions for different vibrational temperatures using Eq. (2.42)-(2.44) with $\epsilon = 1$ for the VAD process and $\epsilon_{diss} = 0.2$ for auto-dissociation, and using EA = 0.91 eV and $E_D = 1.32$ eV (except for the gray curve with EA = 1.03 eV and $E_D = 1.44$ eV from Ref. [24]). The green curve is for the case of $k_{diss} = 0$ to illustrate the influence of dissociation.

yield vibrational temperatures of <300 K, much higher than the trap temperature of ∼12 K.

Although the internal energy remaining at 300 K in all 15 vibrational modes is sufficient to populate the strong IR active mode at 83 meV by IVR, the energy could at these lower internal energies also already be trapped in the non-IR-active modes with weak coupling to the other modes. Considering a very naive approximation, where all vibrational modes would be singly occupied except for the strong IR active modes at 671.1 cm^{-1} and 757.7 cm^{-1}, it is found that a total vibrational energy of 0.49 eV above the zero point energy would remain in the molecule. Most of the vibrational energy distribution for 300 K is thus found below this energy. On the other hand, the high energy part of the distribution is in any case not practically accessible in this measurement, as it is shifted by the absorbed photon energy of 1.165 eV to energies above 1.6 eV, so that it is contained in the prompt signal and hence excluded from analysis.

An a priori possible explanation of the high remaining internal energy by rotational

excitation can be ruled out within the context of this model assumption: We start by considering SF_6^- ions in the vibrational ground state, however with a high degree of rotational excitation (which because of angular momentum conservation requires the emission of many photons and hence has a long time constant).
The rotational excitation is here considered to be retained after the photon absorption and the photon energy to be transfered only to vibrational excitation. Hence, all ions would have equal vibrational energies, but ions with a high angular momentum J would decay with a reduced VAD rate $k(E, J)$ as it was discussed in Sec. 2.4.2 and illustrated in Fig. 2.12. The lower VAD rate for these SF_6^- ions with high J leads to an even shallower decay dependence, in contrast to the required steeper decay for a low vibrational temperature.
The result of the model with an energy distribution at 300 K, an electron affinity of EA = 1.03 eV and dissociation energy of 1.44 eV is also displayed in Fig. 4.35 for comparison, and shows a shallower dependence as a function of the time after the laser shot. Accordingly, much higher temperatures would be required to match the data with these values for the thresholds.
Finally, a vibrational temperature of T_{vib} = 300 K with EA = 0.91 eV exhibits the closest agreement of the model prediction with the observed prompt amplitude. Here, contributions from possibly direct photo-detachment or photo-dissociation could be contained in the prompt signal, being indistinguishable from decay processes with prior vibrational excitation. This would increase the observed prompt signal, but is not accounted for in the model.
In conclusion, the delayed neutralization rate of SF_6^- after photo-excitation can be used to determine the remaining energy content under isolated, undisturbed conditions. Vibrational temperatures for long storage times could be determined, but indicate vibrational excitation with $T_{vib} \sim 300$ K for cooling times as long as 55 s.

Chapter 5

Summary and prospects

5.1 SF_6^- studies at the cryogenic ion trap CTF

In the present studies, the vibrational auto-detachment (VAD) was investigated on an increasingly complex, but comprehensive studied molecule, the sulfur hexafluoride anion. Statistical models were employed to reproduce the observations. The excellent agreement with the measurements allowed to study contributions from various effects on the decay time-dependence.

On the one hand, for SF_6 a comprehensive knowledge about molecular structure, vibrational and rotational properties has been accumulated as well as far-reaching experimental investigations. The symmetric, octahedral structure of the neutral and the recently suggested, slightly distorted appearance of the anion [17] are well explored theoretically and vibrational frequencies like the prominent IR-active modes also experimentally observed [5]. On the other hand, besides the symmetric regular molecular appearance, statistical models are found to be applicable describing collective behavior as intramolecular vibrational redistribution (IVR) and their coupling to the electronic motion.
Considering in comparison for instance metal clusters, their nuclear structures are often less well known even at small sizes or exhibit strong isomerization between different geometries even at low excitation [134]. Accordingly, the vibrational motion leaves uncertainties and collective movements become apparent. In these systems, one is fully dependent on statistical methods and microscopic calculations, as still possible for SF_6^-, are hopeless.
For SF_6^- both conditions, well-known structure and properties and the applicability of statistical models, are rather well fulfilled and, as shown in the present investigation, can be applied to model even the complex process VAD. This was confirmed by the observation of a power-law time-dependence of the neutralization rate of trapped, highly excited $(SF_6^-)^*$ ions over several orders of magnitude in its size between hundreds of μs to over 100 ms. Previously unobserved deviations from the power-law towards later times were identified and could be characterized by applying a recent state-of-the-art model [19–24], which combines statistical approaches with experimental electron capture cross sections.
The deviation from the power-function behavior was found to manifest itself at time scales which correspond to the calculated VAD rate at the threshold EA. Only the

present, low background measurement could access these small decay rates, which otherwise would have been concealed in the background from collisional ion loss. Moreover, this observation most likely excludes other earlier models used in VAD calculations, which assumed an electron affinity EA of 1.20 eV [19–21] and also relied on former vibrational frequency calculations of SF_6 and SF_6^- [36]. In contrast, the recent model assuming a slightly asymmetric anion geometry [17], and a new value for EA of 1.03 eV [24] leads to a satisfying agreement with the data from the present work, already without considering further effects becoming important at the late times of the decay.

In describing the stochastical character of the $(SF_6^-)^*$ decay governed by significant IVR, a thermal vibrational energy distribution was chosen to account for the initial excitation constellation. Conversely, this provided a possibility to determine the vibrational temperature of the investigated system for the time prior to the decay, reflecting the ion source excitation. In terms of this, a variation of the excitation was observed in the obtained vibrational temperatures, scaling clearly with the SF_6 gas inlet pressure to the ion source. Hence, not only the matching between measurement and recent model could be demonstrated, but also an influence on the experimental preparation conditions of the observed decay could be affirmed, supporting the stochastical character of the decay and inferring vibrational temperatures between 1000 to 4000 K.

In addition, contributions from rotational excitation, reflecting the realistically expected conditions of the production process in the ion source, were also taken into account as well as radiative cooling, being predicted to occur at similar time scales. Most of the latter influences turned out to be crucial for the fitting between model and data and yielded radiative cooling rates k_{rad} between 20 and 60 s^{-1}, which are for the upper range in reasonable agreement with predictions (80 s^{-1} theoretically and 59 s^{-1} experimentally [19]).

The radiative cooling rates k_{rad} determined in the fit were found to depend significantly on the ion source conditions. In order to minimize this unphysical trend in the fitted cooling rates, also the value of the electron affinity EA was varied. This analysis was only enabled by considering that EA and k_{rad} are required to be independent of the initial excitation of SF_6^-, as they influence the decay curve only at late times, and thus, have to be equal for all the ten well-controlled measurements of the VAD decay. Using the minimum of the derived global χ^2 of the fits of these measurements, a new value of the adiabatic electron affinity of $EA = 0.91 \pm 0.05$ eV was thus determined in the present work, which is in excellent agreement with the calculation [18] by Eisfeld of 0.9 ± 0.1 eV. The former reported value by Troe of 1.03 ± 0.05 eV [24] and the calculation by Karton and Martin of 1.03 ± 0.03 eV [38] slightly deviate from the results of our analysis.

In the context of this investigation, also a value for the radiative cooling rate of SF_6^- close to the threshold EA of $k_{rad} = 27 \pm 6$ s^{-1} was determined, which is found to be lower than the value of ~ 43 s^{-1} calculated from a simplified model in this work, but still in an acceptable range.

In a second investigation, the extension towards even longer observation periods of the radiative cooling process of SF_6^- was achieved by probing the ions via photoexcitation at different trapping times. The stable SF_6^- ions, which remain trapped

after the thermal VAD stops, were re-excited via photon-absorption from a pulsed Nd:YAG laser at 1064 nm (1.165 eV), and the photo-induced, neutral producing decay process was observed. The direct continuation of the cooling beyond the initial VAD process could be observed as a function of storage time by measuring the neutral fragment yield occurring promptly after the laser pulses. The competition of VAD and auto-dissociation after the photo-excitation, considering their individual detection efficiencies, enabled this observation.
A steady state of the SF_6^- internal excitation was approached in the relaxation process after about 1 s and the photo-induced decay remained unchanged for ion storage times up to 55 s. Here, a remaining vibrational temperature in the SF_6^- of around 400 K was derived. However, it is questionable whether a temperature definition is applicable for these low excitations as the discrete nature of the vibrational states might become apparent.
A simplified cascade radiative cooling model, using only the strongest IR-active vibrational modes and statistical approaches, was compared to the result with a vibrational temperature distribution. Both models resulted in a similar shape of the energy distribution and thus, the cascade cooling model can be used to relate the remaining temperature to an effective radiative cooling time required for reaching a steady state configuration in SF_6^-. The noticeable vibrational energy content remaining in the SF_6^- ions, is tentatively assigned to energy trapped in non-IR active modes without vibrational redistribution.
The investigations on SF_6^- with the CTF showed that a statistical description for this symmetric model system is feasible at a significant level of numerical accuracy. The late deviations from the power-law behavior can be ascribed to a reduction of the vibrational level density in neutral SF_6 for energies close to the EA (finally reaching a discrete regime). In other investigated systems, this deviation has been usually fully assigned to radiative cooling [11], which here is found to be only partly responsible for the stagnation of the VAD decay. The statistical character of SF_6^- despite the near symmetric geometry might be found in the additional electron occupying a σ^* orbital [17], thus reflecting an electron delocalization with a coupling to the vibrational degrees of freedom.
Besides the fundamental observations, the results presumed here can have influence on the atmospheric modeling of the SF_6 degradation rates. In the sparse upper atmosphere, the radiative stabilization of the electron-attached $(SF_6^-)^*$ complex leads to a higher abundance of SF_6^- ions and thus, accesses a variety of reaction channels decomposing SF_6 [15].

Extended knowledge on the system is expected from well controlled ion production with low excitation energies. The creation of negative ions from a supersonic expansion ion source, which is currently being assembled and commissioned at the CTF setup, can be expected to produce rotationally and vibrationally much colder molecular and cluster ions (This ion source was provided in view of future collaborative work by the cluster chemistry group under supervision of Prof. Niedner-Schatteburg in Kaiserslautern, Germany). Here, the ionization process occurs prior to the supersonic cooling and the additional energy entry due to the electron attachment can thus largely be cooled away. This new ion source offers the production of ions from gaseous as well as solid targets for instance for metal clusters, by laser sputtering

from a target and simultaneous ionization through a plasma.
Other systems like negative copper and cobalt clusters are also currently being investigated in the CTF presently, produced with the cesium sputter ion source MISS preceding later intended work with the supersonic expansion ion source. Additionally, a new 20 Hz pulsed, optical parametric oscillator (OPO) laser system is currently being commissioned at the CTF, which covers tunable photon energies from 0.48 eV to 5.51 eV (2600 nm to 225 nm) and pulse intensities of up to 30 mJ. The wide range of photon energies will be used to identify unknown adiabatic electron affinities through the process of delayed electron detachment, as here, in contrast to photo electron spectroscopy, which probes the vertical detachment energy, the threshold after the completed IVR, corresponding to the adiabatic EA is probed. The variation of the photon energy over the range of the expected EA values offers such determinations even for less well investigated systems than SF_6^-. Additionally, the time-dependence of the VAD rate can be revealed for excitation by a range of photon energies above the EA.

5.2 Status of the Cryogenic Storage Ring

Outstanding opportunities for future experiments will also be provided by the new Cryogenic Storage Ring (CSR), currently being built at the Max-Planck-Institute for nuclear physics in Heidelberg. The experience gained from the construction, assembly and operation of the CTF as a prototype device confirmed many of the original design intentions for the CSR, but also triggered several crucial improvements [78]: An improved mechanical support concept will decouple the ion optical elements such as electrostatic deflectors and quadrupole lenses from the experimental vacuum chambers of the CSR in order to assure their proper alignment after the thermal shrinking at cryogenic temperatures. Furthermore, designated 2-K-cryo-condensation pumping units will be employed in contrast to the cooling units integrated in the vacuum chamber walls at the CTF.
The CSR will be the first electrostatic storage ring being cooled with supra-fluid helium below 2 K and it will consist of four linear sections for experiments. It will be capable of storing ions with kinetic energies between 20 and 300 keV/charge on an orbit with a circumference of 35 m. The purely electrostatic deflection of the stored ions in the CSR imposes no upper limit on the ion masses and thus provides excellent conditions for the investigation of large molecules, clusters and even bio-molecules. The relatively low kinetic energies compared to magnetic storage rings (>MeV/amu) allow the ion acceleration from a high-voltage platform, which is suitable for a careful production of large molecules. The expected long ion storage lifetimes also allow the undisturbed investigation of highly charged ions, in addition to offering sufficiently long times for radiative cooling of the ions to their vibrational ground states.
The first (room temperature) electrostatic storage ring ELISA was developed for similar purposes in Aarhus, Denmark in 1997 [81], and consists basically of two 180° bends accomplished by one 160° and two 10°-deflectors each and two straight sections. Similar designs were employed for the following rings at KEK [82] and TMU [83], where the latter one was upgraded to liquid nitrogen operations. A

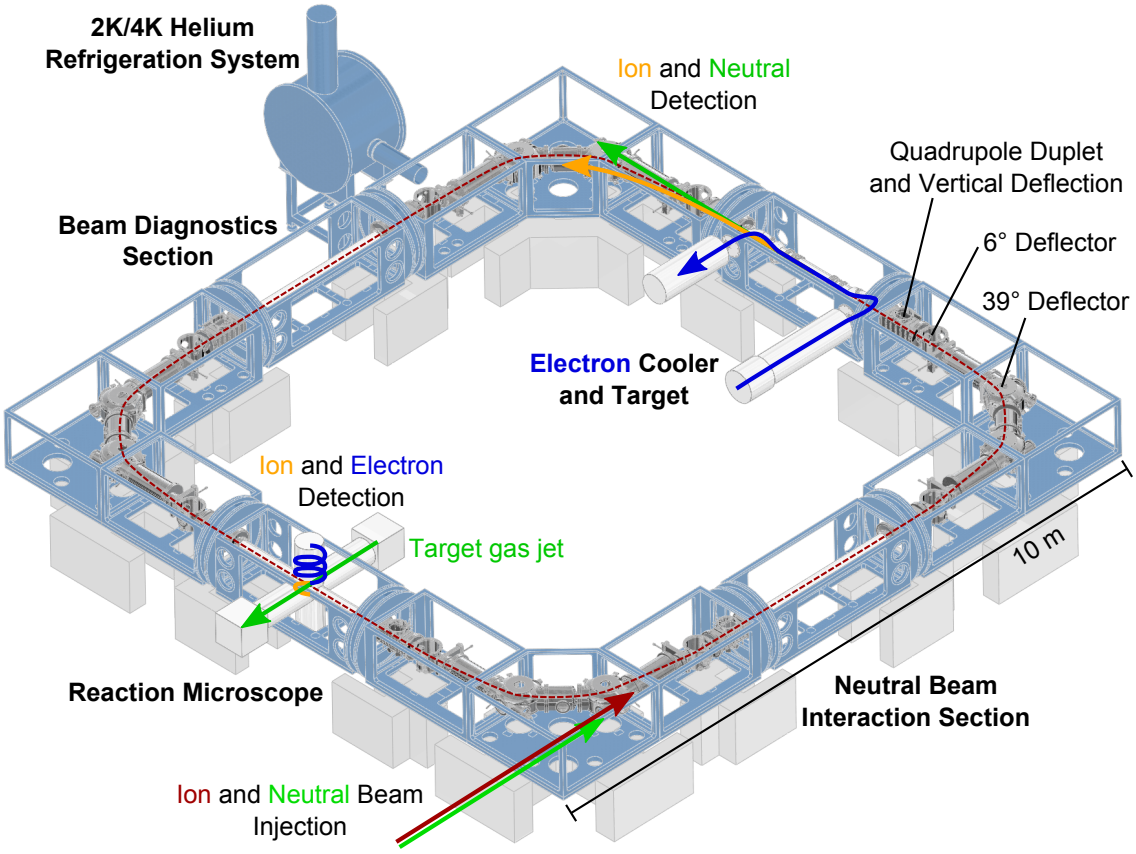

Figure 5.1: Schematic overview on the CSR

cryogenic electrostatic double-storage ring DESIREE for negative and positive ion collision reactions is currently under commissioning [135], but does not offer all the features of the CSR, most notably an electron-cooled beam.
The CSR is also expected to surpass these rings with respect to the extremely high vacuum and cold environment, and moreover by the larger dimensions and its planned array of more sophisticated particle detection systems. One linear section is designed to house an electron-cooler and target combination [136], where the stored ion beam is merged with a velocity matched, energy-sharp electron beam. The transversal and longitudinal phase space of the stored ion beam as well as the internal vibrational and rotational degrees of freedom [137] will be cooled by collisions with the cold electrons. Ion masses of even up to 200 amu are accessible by cooling, which is limited by the production of cold electrons down to 1 eV. However, used as an electron target the relative energies between the two merged beams can be sensitively varied obtaining resonance structures in recombination processes.
Another linear section is designated to the operation of a storage ring internal reaction-microscope [138], for investigations of collision processes with the COLTRIMS (Cold Target Recoil Ion Momentum Spectroscopy) technique, using a cold supersonic jet target and a measurement of the momentum vectors of all collision partners to obtain a kinematically complete experiment with particles in well-prepared quantum states. The diagnostics section of the CSR will house electrostatic beam position monitors and a low intensity beam current measurement using

Figure 5.2: Photo of the CSR construction site (as seen from the left side of Fig. 5.1): The helium refrigeration system on the left side is connected to the first finalized corner for cryogenic tests. Most isolation vacuum chambers are in place, and the inner vacuum chambers of these sections are presently being installed.

a SQUID. A straight section with a fast merged neutral particle beam produced by photo-detachment of an anion beam.
Thus, an extended field of research will be opened by the capabilities of the CSR, finding its applications in astrophysics, large molecule and cluster physics and research on bio-molecules or highly charged ions. Up to now, the cryogenic and high-voltage tests have been successfully carried out at the first ring corner, according modifications and improvements have already been included in the recent assembly of the remaining corners and linear sections. The commissioning, still without electron-cooler and reaction-microscope will take place in summer 2013. Further details on the developments are found in Ref. [79].

Appendix A

The appendix presents the theoretical background to derive the statistical models for unimolecular decays. At first, a short introduction to quantum mechanics will provide vibrational and rotational properties of molecules. However, for increasingly complex systems the deterministic models for single quantum states have to be replaced by stochastical approximations to obtain measurable quantities. The basic approaches to model unimolecular reaction rates will be illustrated.

A.1 Molecular properties

A.1.1 Born-Oppenheimer Approximation

Considering for simplicity a diatomic molecule, the stationary energy states E are determined by the time-independent Schrödinger equation [139]:

$$\hat{H}\Psi = E\Psi, \tag{A.1}$$

where $\hat{H}$ is the Hamilton operator containing kinetic and potential energy contributions of the system and Ψ is the wave-function. Neglecting particle spin, the Hamilton operator $\hat{H}$ of a molecular system can be separated into the following contributions [140]

$$\hat{H} = \hat{T}_N + \hat{T}_\mathrm{e} + \hat{V}_\mathrm{NN} + \hat{V}_\mathrm{ee} + \hat{V}_\mathrm{Ne}, \tag{A.2}$$

where $\hat{T}_\mathrm{N}$ and $\hat{T}_e$ are the kinetic energy operators of the nuclei (N) and electrons (e), respectively, and the potentials $\hat{V}$ are divided into repulsive interactions between nuclei (NN), electrons (ee) and the attractive potential between nuclei and electrons (Ne).
The molecular wave-function Ψ can be separated into nuclear and electronic motion using the different, specific propagation time scales of the electrons and the nuclei. Due to the smaller electron mass compared to the nuclei, the electrons can almost instantaneously follow the motion of the nuclei and hence, the electron dynamics can be considered for fixed positions of the nuclei. In addition, it is assumed that $\nabla_\mathbf{R}\Psi_\mathrm{e}(\mathbf{R},\mathbf{r}) = 0$, so that the nuclear kinetic energy operator does no longer act on Psi_e. This principle is well known as the Born-Oppenheimer approximation [141] and allows to write the total wave function as a product of an electronic and a nuclear wave function

$$\Psi(\mathbf{R},\mathbf{r}) = \Psi_\mathrm{e}(\mathbf{R},\mathbf{r})\Psi_\mathrm{N}(\mathbf{R}), \tag{A.3}$$

with the electronic $\Psi_{\mathrm{e}}(\mathbf{R},\mathbf{r})$ and nuclear wave functions $\Psi_{\mathrm{N}}(\mathbf{R})$, and the nuclei positions $\mathbf{R}$ as a parameter and variable $\mathbf{r}$ for the electron positions. The Schrödinger equation is solved for a fixed configuration of $\mathbf{R}$ by

$$(\hat{T}_{\mathrm{e}} + \hat{V}_{\mathrm{ee}} + \hat{V}_{\mathrm{NN}} + \hat{V}_{\mathrm{Ne}})\Psi_{\mathrm{e}}(\mathbf{R},\mathbf{r}) = E_{\mathrm{e}}(\mathbf{R})\Psi_{\mathrm{e}}(\mathbf{R},\mathbf{r}), \tag{A.4}$$

only taking contributions into account which apply to the electron wave function. The obtained electron energy eigenvalues $E_{\mathrm{e}}(\mathbf{R})$ for one specific nuclei configuration and the kinetic energies of the nuclei $\hat{T}_{\mathrm{N}}$ are applied to the nuclear wave-function $\Psi_{\mathrm{N}}(\mathbf{R})$ to determine the nuclear motion

$$(\hat{T}_{\mathrm{N}} + E_{\mathrm{e}}(\mathbf{R}))\Psi_{\mathrm{N}}(\mathbf{R}) = E_{\mathrm{N}}\Psi_{\mathrm{N}}(\mathbf{R}). \tag{A.5}$$

At the equilibrium distance $\mathbf{R}_{eq}$ the eigenvalue $E_{\mathrm{e}}(\mathbf{R})$ exhibits a minimum. In the energy eigenvalues for the nuclei E_{N}, the different contributions for translations, vibrational and rotational energies can be identified, however, a coupling between vibrational and rotational motion might be present (coriolis interactions). The translational part vanishes by using center of mass coordinates.
Deriving precise energy states usually needs the help of approximations and numerical approaches, which have to be chosen individually to accommodate the structure and symmetry of the specific molecule. Various procedures can be found elsewhere and are not discussed here. Additionally, the electronic excitation will not be addressed as the characteristic time scales of electronic excitation and de-excitation are much shorter than the typical time range in the performed experiment. Also the restriction to the symmetry properties of the investigated systems, namely SF_6 and SF_6^-, will be made.

Potential Energy Surface PES

The potential energy curve (for only one dimension in space) or the Potential Energy Surface (PES) is the connection between the potential energy of an molecule and its geometry. The potential is provided by the fast moving electrons for each nuclear configuration and is hence identical to the $\mathbf{R}$-dependent electronic energy eigenvalue $E_e(\mathbf{R})$ in Eq. (A.4). For non-linear molecules it is a function of $3N-6+1$ dimensions where N is the number of atoms subtracting 3 translational and 3 rotational degrees of freedom.
From this explanation it is clear that the PES determines the vibrational movement of the nuclei, which in the ground states has an energy close to the potential minimum, however always with a zero point energy. A brief summary of vibrational states are given below, followed by methods to calculate the vibrational density of states and rules for rotational energies.

A.1.2 Vibrational energy spectrum

The vibrational energy levels of a diatomic molecule can be approximated for low excitation with the Harmonic oscillator potential, which means that the true PES is approximated by a potential energy curve with only a quadratic dependence on

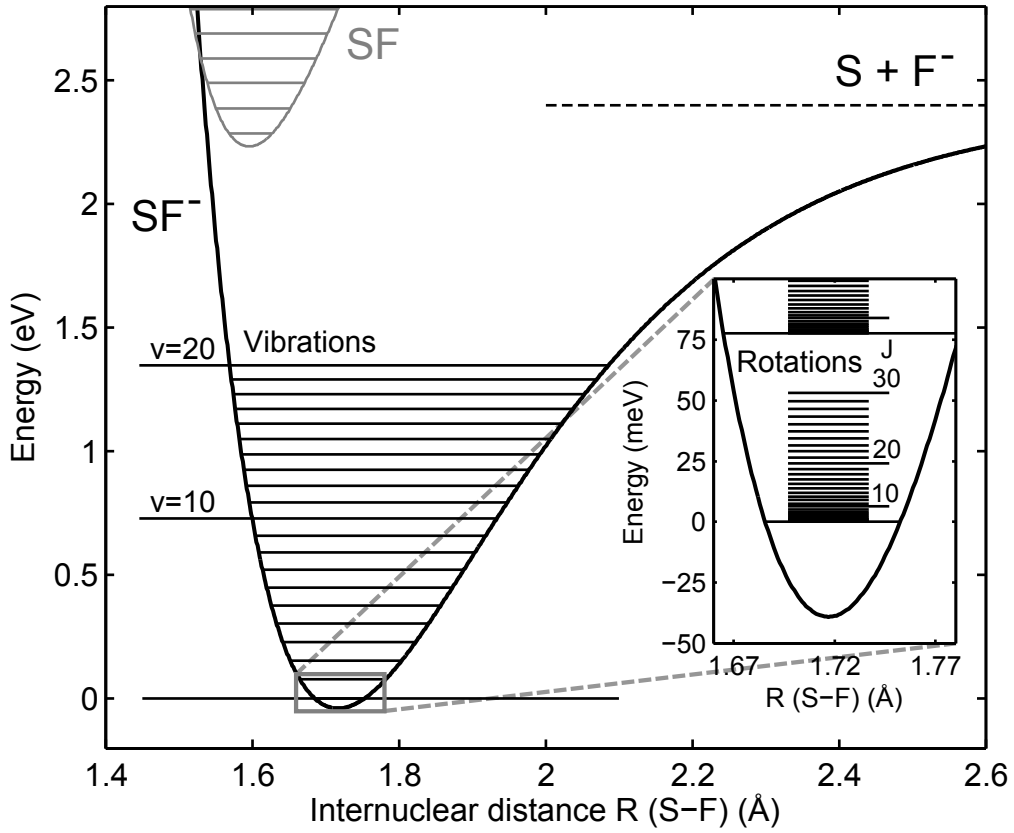

Figure A.1: Potential energy curves for the dimers SF^- and SF approximated by as a Morse-potential with their vibrational energy levels and rotational excitations of SF^- in the inset. Internuclear distances of 1.596 Å for SF and 1.717 Å for SF^-, vibrational energy values of $h\nu = 635$ cm^{-1} and $h^2\nu^2/4D_e = 4.34$ cm^{-1} for SF^- and $h\nu = 837.64$ cm^{-1} and $h^2\nu^2/4D_e = 4.46$ cm^{-1}, and the electron affinity of EA = 2.285 eV and the dissociation energy of $D_0 = 2.40$ eV of SF^- are taken from Ref. [142]. The dissociation energy $D_0 = 3.51$ eV for SF is from Ref. [143], and rotational constant of SF^- is from Ref. [144].

the nuclear distance. The energy Eigenstates are then given by

$$E_v = h\nu\left(v + \frac{1}{2}\right), \tag{A.6}$$

where h is Planck's constant, ν is the fundamental vibrational frequency, v the vibrational quantum number and the part $E_Z = 1/2h\nu$ is the zero-point energy. To account for deviations from the harmonic potential, which is for example necessary to describe the breaking of a chemical bond at a certain critical energy, an empirical potential called "Morse potential" can be used

$$V_R = D_e(1 - e^{-a(R-R_{eq})})^2, \tag{A.7}$$

where $D_0 = D_e - E_Z$ is the dissociation energy and $a = 2\pi\nu\sqrt{\mu/2D_e}$ is a measure of the curvature of the potential with the vibrational frequency ν and the reduced

mass μ of the two atoms. The corresponding vibrational energy levels in the Morse potential are then given by

$$E_v = h\nu\left(v+\frac{1}{2}\right) - \frac{h^2\nu^2}{4D_e}\left(v+\frac{1}{2}\right)^2. \tag{A.8}$$

Figure A.1 illustrates the Morse potential for the case of the sulfur fluorine anion SF^- together with the spacing of the vibrational energy levels.
In polyatomic molecules with symmetric top or spherical top geometry, the total vibrational energy in the harmonic approximation is given by a sum over all vibrational energies in the (3N-6)-vibrational modes (in the following $s = 3N-6$) by

$$E_{v_i} = \sum_{i=1}^{s} h\nu_i\left(v_i+\frac{1}{2}\right), \tag{A.9}$$

which not explicitly accounts for possible degeneracies of the vibrational frequencies ν_i, so that $\nu_i = \nu_j, i \neq j$ can occur. Anharmonicities can also be introduced to polyatomic molecules, but it will not be discussed here.

Fermi's Golden Rule

Another important aspect are the selection rules for the transitions between vibrational energy levels. For the harmonic case only transitions between neighboring levels are allowed, $\Delta v = \pm 1$, while for anharmonic potentials also higher steps are possible. The probability for a transition is important to estimate lifetimes of an excited state or the absorption of radiation.
In principle, the probability is given by the overlap between the wave functions of both energy levels in the context of the interaction. The transition matrix element $|V_{if}| = |\langle\psi_i|V_{if}|\psi_f\rangle|$ gives the coupling of the initial state i and the final state f. The transition rate W_{if} is then given by Fermis's Golden Rule as

$$W_{if} = \frac{2\pi}{\hbar}|V_{if}|^2\rho_f, \tag{A.10}$$

where ρ_f is the density of states for the final state and thus, weighting the transition rate with the number of available configurations. The density of states for vibrations will be determined below.
A dipole interaction can be used to approximate the transition strength with the dipole moment $\boldsymbol{\mu}=-e\mathbf{r}$, where $\mathbf{r}$ is the position vector of the affected electron, and the relation to the transition matrix element is given as

$$|V_{if}|^2 \propto |\boldsymbol{\mu}_{if}|^2. \tag{A.11}$$

Besides the interaction of the dipole with an external field, for instance a laser, and leading to the absorption of a photon, also the spontaneous emission of radiation can be given in terms of the transition matrix element as

$$A_{if} = \frac{8\pi^2}{3}\frac{\nu_{if}^3}{\epsilon_0 c^3\hbar}|\boldsymbol{\mu}_{if}|^2 = \frac{1}{\tau_{if}}, \tag{A.12}$$

where A_{if} is the Einstein coefficient for spontaneous emission. The lifetime τ_{if} of a state is directly connected to the transition matrix element of the two involved states and hence, a dipole moment has to be present for the specific mode to emit radiation. In the context of a vibrational mode, a permanent and/or induced dipole moment must be existing or at least generated in the excited case, to be infrared active (IR-active)(see for example in Ref. [145]):

$$\boldsymbol{\mu}(R) = \boldsymbol{\mu}(R_{eq}) + \frac{d\boldsymbol{\mu}(R_{eq})}{dR}(R - R_{eq}). \tag{A.13}$$

The first term is the permanent dipole moment at the equilibrium position and the second term is generated through an asymmetric vibrational movement of the molecule and its charge distribution. For a polyatomic molecule always an asymmetric stretch or bending mode exists that mediates IR absorption or emission.
In the case of radiative cooling, the energy loss of an excited molecule by the spontaneous emission of radiation, can only be induced by an IR-active mode and in particular, modes with high dipole moment and high frequencies are dominant (compare Eq. (A.12)).

A.1.3 Vibrational density of states

In preparation for the applied statistical methods in Sec. B.2, the concept of the phase space and the density of states are introduced, which are essential tools to describe the complexity in molecular systems. The vibrational phase space is spanned between the $s = 3N - 6$ dimensions of the position components q_i of the nuclei and their momentum components p_i and hence, has s^2 dimensions. A specific phase space volume can be imagined as a measure for the probability that the molecule exhibits the connected configuration, when the volume is compared to the total available phase space. In classical physics, the phase space volume is given by an integration along all dimensions up to a defined energy threshold, whereas in a molecule the volume can be directly related to a number of configurations due to the quantum nature of the system. Hence, the classical phase space volume is divided into areas defined by the uncertainty principle $\Delta q \Delta p \leq \hbar/2$, and the total number of states with energies up to a threshold value of E is given by the sum of states

$$N(E) = \frac{1}{h^s} \int_{H=0}^{H=E} dq_1 \cdots dq_s dp_1 \cdots dp_s, \tag{A.14}$$

where h is Planck's constant.
In contrast, the density of states $\rho(E)$ is derived by the integration of the phase space at a fixed energy $H = E$ by

$$\rho(E) = \frac{1}{h^s} \int_{H=E} dq_1 \cdots dq_s dp_1 \cdots dp_s \tag{A.15}$$

and the relation between both given quantities is

$$\rho(E) = \frac{dN(E)}{dE}. \tag{A.16}$$

The density of states is an important quantity for a micro-canonical system, as for instance a molecule, as it is also described by a defined internal energy.
Although these definitions include the quantum aspect of the system, for low energies the sum and density of states are not represented by continuous functions as it is indicated by the integral. Firstly, for a vanishing energy both quantities are not defined as the system has at least the zero-point energy, and secondly, states are only available at energies which are multiples of the vibrational modes. For $N(E)$, one obtains a step-function, which always increases at these energies, and $\rho(E)$ is a superposition of δ-functions with $\delta(E - E_V(\{v_i\}))$, where $E_V(\{v_i\})$ is a vibrational energy state and characterized by the ensemble of vibrational quantum numbers ν_i. Anyhow, for higher energies the spacing between the levels decreases and both quantities are fairly described by a continuous function.
For the classical harmonic oscillator the sum and density of states are given by

$$N(E) = \frac{E^s}{s! \prod_{i=1}^{s} h\nu_i}, \tag{A.17}$$

$$\rho(E) = \frac{E^{s-1}}{(s-1)! \prod_{i=1}^{s} h\nu_i}, \tag{A.18}$$

and this definition does not account for the zero-point energy.

Direct Count

An exact method to determine the density of states numerically is the Direct Count method by Beyer and Swinehart [66, 67] in 1973, whose accuracy is only limited by the chosen energy spacing ΔE and the precision of the available vibrational frequencies. Typical frequencies are provided as good as one cm^{-1} or one order of magnitude lower, however, an energy resolution of one cm^{-1} is usually feasible (conversion factor: 1 cm^{-1} $\approx$0.1239 meV). In this algorithm, an array of zeros according to the energy spacing and a selected maximum energy is initialized and the first entry is set to one to account for the ground state. A loop over all vibrational modes is executed and the array always increased at multiples of the vibrational energy by a number according to the degeneracy of the mode.

Whitten-Rabinovitch approximation

To obtain an analytic function for the density of states, an improved and established approach to the classical case was proposed by Whitten and Rabinovitch [146] in 1963, which does not only include the zero-point energy but also applies an empirical correction factor, which was derived by fits to computed densities of states of various polyatomic molecules:

$$\rho(E) = \frac{(E + a(E)E_Z)^{s-1}}{(s-1)! \prod_{i=1}^{s} h\nu_i}, \tag{A.19}$$

$$a(E) = 1 - \beta\omega(E), \tag{A.20}$$

$$E_Z = 1/2 \sum_{i=1}^{s} h\nu_i. \tag{A.21}$$

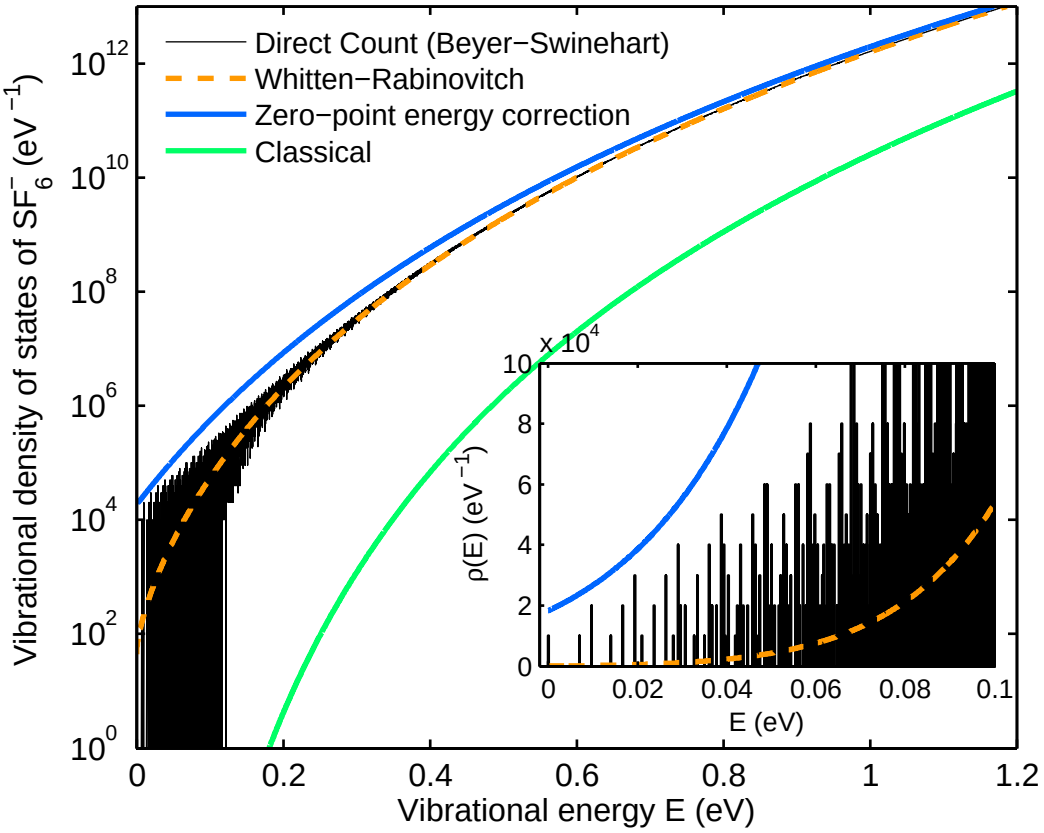

Figure A.2: The vibrational density of states for SF_6^- is shown as a comparison between different methods described in the text using vibrational frequencies from [17, 18]. The inset shows the low energy part on a linear scale where for the direct count (Beyer-Swinehart) method the individual vibrational levels are visible. Here, the Whitten-Rabinovitch approximation nicely describes the shape, but does not account for the discrete nature. For the direct count method an energy resolution of one cm^{-1} was used.

Using $a(E) = 1$, the function only takes the zero-point energy E_Z into account. The energy-dependent correction function $\omega(E)$ and the factor β only dependent on the vibrational modes and are given by

$$\log_{10}\omega \approx -1.0506(E/E_Z)^{0.25} \qquad at\ E > E_Z, \tag{A.22}$$

$$\omega^{-1} \approx 5(E/E_Z) + 2.73(E/E_Z)^{0.5} + 3.51 \qquad at\ E < E_Z, \tag{A.23}$$

$$\beta = \frac{(s-1) < \nu_i^2 >}{s < \nu_i >^2}, \tag{A.24}$$

where $< x >$ denotes the average value. One has to note, that both ways to determine the density of states define the energy scale with $E = 0$ being the zero-point energy. In figure A.2 the density of states for SF_6^- are illustrated and the result from different, introduced methods are compared.
Finally, the transition between micro-canonical and canonical systems will be illustrated. A micro-canonical system as depicted beforehand refers to a single molecule

with a fixed energy E and thus, an energy-dependent function as for instance the density of states $\rho(E)$ can be applied to describe the microscopic system. However, for statistical models, where a whole ensemble of molecules is characterized, not all molecules will have the same energy, but rather follow an energy distribution. If this system is also thermalized, meaning in an equilibrium by the interaction with the surroundings, the system is described by a temperature and a canonical energy distribution.
For a given temperature T, the energy distribution of the ensemble gives the probability to find a molecule with a specific energy E. Here, high energetic molecules are less likely as they would exchange energy with low energetic molecules, which is accounted for by Boltzmann's factor $exp(-E/k_BT)$. On the other hand, as shown by the density of states, a strongly increasing number of configurations are available for higher energies leading to an opposing energy-dependence as before. Combined, the canonical energy distribution $f(E,T)$ for the vibrational excitation is given by

$$f(E,T) = \frac{1}{Q(T)}\,\rho(E)\,e^{-\frac{E}{k_BT}}, \tag{A.25}$$

$$Q(T) = \int_0^\infty \rho(E)\,e^{-\frac{E}{k_BT}}\,dE, \tag{A.26}$$

where k_B is Boltzmann's constant ($\sim 8.617\times10^{-5}$ eV/K) and the canonical partition function $Q(T)$ accounts for the normalization of $f(E,T)$.
The maximum of this distribution, when only the zero-point energy is used in $\rho(E)$, thus Eq. (A.19) with $a(E)=1$, is given by the simple equation

$$E_{max} = (s-1)k_BT - E_Z. \tag{A.27}$$

For SF_6^- with the most recent vibrational frequencies from Ref. [17], the maximum is found at $E_{max}/\mathrm{eV} = 1.206\times10^{-3}\ T/\mathrm{K} - 0.364$. The canonical energy distribution can for instance be used to transform the energy-dependent rate coefficients $k(E)$ for a microscopic system to that of a canonical system as $k(T)$.

A.1.4 Rotational energy spectrum

For a rigid rotor diatomic molecule, the rotational energy levels are given by

$$E_r(J) = BJ(J+1), \tag{A.28}$$

where J is the angular momentum quantum number and B is the rotational constant, which can be calculated from the momentum of inertia $I = \mu\mathbf{r}^2$ with the reduced mass μ:

$$B = \frac{\hbar}{4\pi cI}. \tag{A.29}$$

For a fixed rotational energy in a diatomic molecule, the quantized projection onto an external axis with the quantum numbers $M_J = -J$, ..,–1, 0, +1, .., $+J$ leads to the degeneracy of $g(J) = 2J+1$. Selection rules for transitions are $\Delta J = 0, \pm1$. Taking into account the centrifugal stretching of the bonds, higher orders of $J(J+1)$ have to be also included into equation (A.28).

More complex systems, in particular non-linear molecules, can have three different rotational constants A, B and C. Considering the investigated molecules, SF_6^- and SF_6, the restriction to symmetric top molecules and the special case of spherical top will be shown. For a symmetric top molecule, two rotational constants are equal, $A = C$, and the resulting rotational energy can be written as

$$E_{JK} = BJ(J+1) + (A-B)K^2, \tag{A.30}$$

with the additional quantum number K, which stands for the projection onto the molecular symmetry axis (in addition to the projection on an external axis M_J). In the prolate top case ($A > B$) the rotational energy increases with K and reduces for oblate molecules ($A < B$). The degeneracy is thus given by $g(J) = 2\,(2J+1)$ (only for $K > 0$).
Selection rules for transitions are $\Delta J = \pm 1$ and $\Delta K = 0$, as per definition K is the projection on the symmetry axis of the molecule and has no net dipole moment. Here, also additional summands with higher orders in $J(J+1)$ and K can be introduced for the non-rigid case.
A special case of the symmetric top configuration is the spherical top, where all rotational constants are equal ($B = A = C$) and the dependence on K in the rotational energy is eliminated; thus Eq. (A.28) applies. However, the degeneracy is now found to be $g(J) = (2J+1)^2$ due to the removed dependence on K, which can take any value $-J, .., 0, .., +J$.
Also here a canonical energy distribution for the rotational energy can be defined using the degeneracy of the specific molecule structure

$$f_{rot}(E,T) = \frac{1}{Q_{rot}(T)}\, g(J)\, e^{-\frac{E(J)}{k_B T}}, \tag{A.31}$$

$$Q_{rot}(T) = \sum_{J=0}^{\infty} g(J)\, e^{-\frac{E(J)}{k_B T}}, \tag{A.32}$$

$$\tag{A.33}$$

and with the rotational partition function $Q_{rot}(T)$.

Appendix B

B.1 Chemical Reaction Dynamics

The chemical rate theory describes the time dependence of a chemical system, for example represented by

$$a\mathrm{A} + b\mathrm{B} \rightarrow c\mathrm{C} + d\mathrm{D}, \tag{B.1}$$

where A and B are the reactant species, C and D the product species and the lower-case letters denote the amount needed from the each species. In chemical reaction rates, the concentration of a species is depicted by squared brackets as $[A]$ and the time-dependence is presented by the derivative of that concentration $d[A]/dt$. Dependent on the amounts needed from a species, the reactions are categorized in orders.

B.1.1 First-Order Reactions

We will restrict this introduction to First-order reactions; they are in the simplest case represented as

$$\mathrm{A} \rightarrow \mathrm{B}, \tag{B.2}$$

the reaction rate is proportional to the available concentration $[A]$ of the species A and the well-known exponential dependence is derived for the reaction rate

$$R(t) = -\frac{d[A]}{dt} = k[A], \tag{B.3}$$

$$[A] = [A]_0 \, e^{-kt}. \tag{B.4}$$

The lifetime τ for this reaction, which means the depletion of the concentration to 1/e of the initial value, is simply given by

$$\tau = 1/k. \tag{B.5}$$

This introduction will be restricted to first-order reaction, however, more complex configurations can occur with several reaction steps. In a first-order reaction with two steps, the concentration of the last species $[C]$ depends on the previous concentration $[B]$, but also indirectly on the first $[A]$:

$$\mathrm{A} \xrightarrow{k_1} \mathrm{B} \xrightarrow{k_2} \mathrm{C}. \tag{B.6}$$

The concentration of $[A]$ still follows an exponential decay, however, the concentration of $[B]$ will be highlighted here as an intermediate concentration and follows as

$$[B] = [B]_0\, e^{-k_2 t} + \frac{k_1[A]_0}{k_2 - k_1}\,(e^{-k_1 t} - e^{-k_2 t}) \tag{B.7}$$

and as a special case of $k_2 = k_1$ the concentration of $[B]$ is given by

$$[B] = ([B]_0 + [A]_0\, k_1\, t)\, e^{-k_1 t}. \tag{B.8}$$

An extension of the previous reaction is found when two types of products can be created from $[B]$, like shown here:

$$\begin{aligned} \mathrm{A} \xrightarrow{k_1} \mathrm{B} \xrightarrow{k_2} \mathrm{C} \\ \mathrm{B} \xrightarrow{k_3} \mathrm{D} \end{aligned} \tag{B.9}$$

and hence, the reaction rate for $[B]$ is given by

$$\frac{d[B]}{dt} = k_1[A] - k_2[B] - k_3[B] \tag{B.10}$$

and the solution for the concentration of $[B]$ is

$$[B] = [B]_0 e^{-(k_2+k_3)t} + \frac{k_1[A]_0}{(k_2+k_3) - k_1}(e^{-k_1 t} - e^{-(k_2+k_3)t}) \tag{B.11}$$

Additional contributions by further products can be included into the reaction rate deriving the concentration of $[B]$.
Finally, also reversible reactions will be introduced where the products from the initial reactant can proceed to form the original species. In the simplest case, the reaction is then given by

$$\mathrm{A} \underset{k_{-1}}{\overset{k_1}{\rightleftarrows}} \mathrm{B} \tag{B.12}$$

where the index -1 denotes the inverse reaction of k_1. The rate equation is then given by

$$\frac{d[B]}{dt} = k_{-1}[B] - k_1[A] = -\frac{d[A]}{dt} \tag{B.13}$$

In general, any reaction in an isolated system has to be reversible due to the fundamental physical principle of invariance under time reversal, called microscopic reversibility, and the system reaches an equilibrium. Thus, the net reaction comes to a standstill and according to the principle of detailed balance, one finds

$$k_1[A]_{eq} = k_{-1}[B]_{eq}, \tag{B.14}$$

$$\frac{k_1}{k_{-1}} = \frac{[B]_{eq}}{[A]_{eq}} = K_{eq} \tag{B.15}$$

with the equilibrium concentrations $[A]_{eq}$ and $[B]_{eq}$ and the equilibrium constant K_{eq}. This principle can also be applied to the reversible processes of electron detachment and attachment, which is the main aspect of this work.

Furthermore, for a canonical system that is related to a reversible process, the temperature-dependence of the equilibrium constant K_{eq} is described by Van't Hoff's relation, which is given by

$$\frac{d(\ln(K_{eq}))}{dT} = -\frac{\Delta E}{k_B T^2}, \tag{B.16}$$

where ΔE is the energy difference between both states or configurations A and B. Inserting K_{eq} from equation (B.15), this relation splits up and can be transformed into two rate definitions for k_1 and k_{-1}, respectively, and in the general form it gives the Arrhenius law

$$k(T) = A\, e^{-\frac{E_0}{k_B T}}, \tag{B.17}$$

where E_0 is the activation energy that is necessary to populate the state and A is a frequency factor, which is in the order of the vibrational frequency ($\sim 10^{13}$ Hz) and is usually determined experimentally.
However, if the micro-canonical rate constant $k(E)$ as a function of the energy E can be calculated in detail by applying specific knowledge of the system, a transformation to the canonical rate $k(T)$ can be performed and leads to more accurate and molecule-specific rates by

$$k(T) = \int_{E_0}^{\infty} f(E,T)\, k(E)\, dE. \tag{B.18}$$

Here, an integration over the whole energy spectrum is performed and $k(E)$ is weighted with the canonical energy distribution from equation (A.25). For energies below the threshold E_0 no reaction is induced and it is $k(E) = 0$. In the following section, $k(E)$ will be derived by applying statistical methods.

B.2 Statistical unimolecular rate theory

The aim of this section is to provide a basic knowledge about the historical development of unimolecular rate theories, certainly not covering all the aspects and mathematical derivations, but presenting the important formulas and considerations. Further reading and background information can be found for instance in [140, 147, 148].
A unimolecular reaction is the simplest type of elementary reaction and describes an initially excited molecule evolving in time. Usually an activation energy E_0 is required to enable the reaction. In the case of isomerization only a part of the nuclei of the molecule move to different locations by consuming (temporarily) energy; for dissociation the activation energy can be associated with the breaking of a weak molecular bond (see Fig. B.1).
In an experiment, the molecule has to be initially prepared in an excited state, which can be realized, for instance, by thermal heating, energetic collisions or radiative excitation. Questions are how the molecule acquires the activation energy and how this energy is stored for the extended time period. Knowledge about the speed of the decay, the energy thresholds and the resulting products probably including their excitation should be gained. Some reactions exhibit an activation barrier to overcome and thus, also tunneling might be a competing process to take into account, although it will not be discussed here.

B.2.1 Lindemann's Mechanism

The activation energy, which is necessary to induce the unimolecular decomposition process, was proposed by Lindemann in 1922 to originate from bimolecular collisions [149] in contrast to radiative activation from the surroundings (radiation hypothesis). The mechanism for the reaction involves a reversible process of an activating and deactivating reaction, and a decomposition from the activated complex, which is given by

$$\mathrm{A} + \mathrm{M} \underset{k_{-1}}{\overset{k_1}{\rightleftarrows}} \mathrm{A}^* + \mathrm{M} \tag{B.19}$$

$$\mathrm{A}^* \xrightarrow{k_2} products \tag{B.20}$$

where A and A* are the relaxed and activated complexes, respectively, and M is the collision partner (can also be A). If the decomposition is slow compared to the reversible reaction, the steady-state productions of the concentration of A* can be applied, and leads to

$$\frac{d[A^*]}{dt} = k_1[M][A] - k_{-1}[M][A]^* - k_2[A^*] = 0, \tag{B.21}$$

and hence, the total reaction rate for the decomposition is expressed by

$$k_2[A^*] = \frac{k_1 k_2[M][A]}{k_{-1}[M] + k_2} = k_{uni}[A]. \tag{B.22}$$

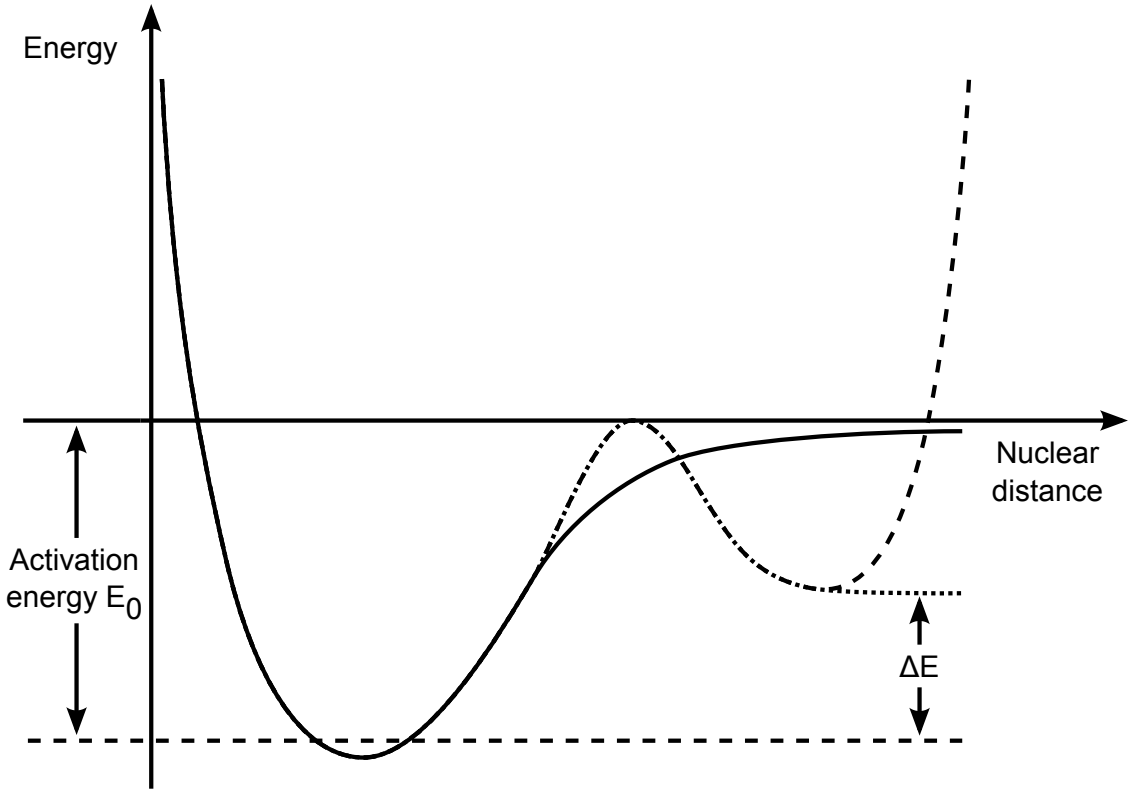

Figure B.1: Schematic potential energy curve for dissociation without barrier (solid line), dissociation with barrier (dotted line) and isomerization (dashed line) presented here with the same activation energy E_0.

Under high pressure conditions, $k_{-1}[M] \gg k_2$, the decomposition rate k_2 in the denominator is negligible and $k_\infty = k_1 k_2 / k_{-1}$ is obtained, whereas in the low pressure limit any activation process will directly lead to a decomposition with $k_0 = k_1[M]$. For collisions between ions and molecules the Langevin theory [150] describes the collisions with an effective interaction potential and averages over a Boltzmann-velocity distribution. The resulting Langevin rate constant reads as

$$k_L = \sqrt{\frac{4\pi^2 \alpha e^2}{\mu}}, \tag{B.23}$$

where α is the polarizability of the molecule and μ the reduced mass of the collision partners. However, here the focus will be on the decomposition rate and on the development of the applied models.

B.2.2 RRK Theory

One of the first statistical approaches to unimolecular reaction rates was carried out by Rice, Ramsperger and Kassel (1927/1928) [151, 152], and based on two assumptions. Firstly, the molecular system is described by a collection of s coupled identical harmonic oscillators with energy $h\nu$ ($s = 3N - 6$ vibrational degrees of

freedom). Secondly, the intramolecular vibrational redistribution (IVR), which is the exchange of energy between the vibrational oscillators, is much faster than the unimolecular decomposition, called the "ergodic hypothesis".
The total vibrational energy in the system is then given by $E = nh\nu$ with n vibrational quanta and the activation energy for the reaction might be written as $E_0 = mh\nu$. Due to the fast redistribution of the energy, there is a certain probability that the critical quanta m are populated, which can be defined purely stochastically. The ratio between distributing n quanta among s oscillators with at least m quanta in the critical oscillator, and the same distribution without the restriction reads as

$$\mathcal{P} = \frac{(n-m+s-1)!n!}{(n-m)!(n+s-1)!} \simeq \left(\frac{n-m}{n}\right)^{s-1}. \tag{B.24}$$

Here, large number approximations were used and when the definitions for E and E_0 from above are inserted, the energy-dependent reaction rate is

$$k(E) = \nu \left(\frac{E-E_0}{E}\right)^{s-1}, \tag{B.25}$$

where the vibrational frequency ν is here also used as a characteristic rate for the transfer.
Thus, the basic energy-dependence of the reaction rate is found to increase rapidly with the energy, however, some of the approximations might not be valid for the molecular systems. For instance, the large number approximation can not be applied for small molecules and furthermore, the model is restricted to identical oscillators and does not consider the zero-point energy.

B.2.3 RRKM Theory and TST

Marcus (1951) [62] included specific molecular properties into the RRK theory such as individual vibrational modes. In the spirit of the RRKM theory, unimolecular reactions can be imagined as a reaction flux in the phase space and accordingly, we will derived the reaction rate from this approach. One has to note that there are different ways obtain the reaction rate and also a parallel concept, the transition state theory (TST), was developed, which however leads finally to the same result.
The reaction rate will be obtained as an energy-dependent quantity, and thus describes a micro-canonical system. Due to the redistribution of energy between the vibrational modes, the location of the molecule in the phase space changes in the course of time, however, always at a fixed internal energy. Instead of one molecule passing through all configurations, one might also imagine a large ensemble of molecules N with fixed energy E, where each of them has a different configuration. One fraction of the phase space defines the critical region from which the reaction takes place, and is related to a fraction of molecules dN in this critical region. This part is compared to the total, available phase space volume at a fixed energy E and hence, to the density of states ρ as

$$\frac{dN}{N} = \frac{\text{fraction of molecules in critical region}}{\text{total number of molecules}} \propto \frac{d\rho}{\rho}, \tag{B.26}$$

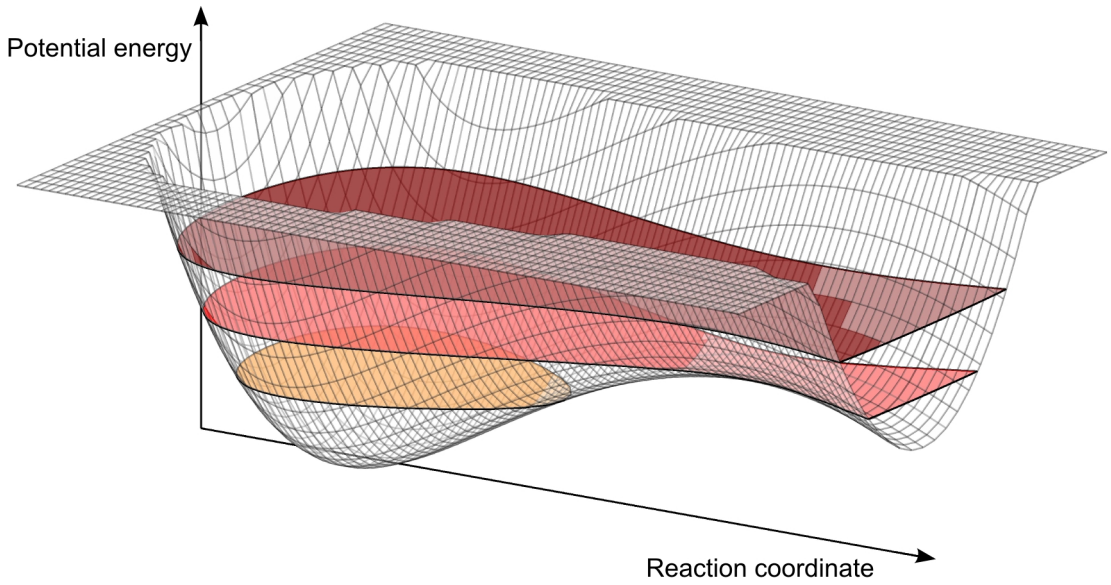

Figure B.2: Potential energy surface with a saddle point and the phase space for three different total internal energies. At the lowest energy the reaction cannot be induced, at higher energies the density of states at the saddle point determines the reaction rate when compared to the total phase space surface at this energy. The concept of the figure was adopted from Ref. [140].

where $d\rho$ denotes the density of states of the critical region.
To calculate this fraction, we define a reaction coordinate (denoted by ‡), a trajectory in the vibrational phase space along which the reaction takes place, which could be the direction of a critical bond (see also Fig. B.2). The energy in the product state is reduced by the activation energy E_0 and also by a translational energy $\epsilon_t^\ddagger$ along the reaction coordinate, which is necessary to transfer the system into this region of the phase space. The corresponding phase space volume is obtained by an integration at a fixed energy $H = E$ for ρ and at the reduced energy for the product $H = E - E_0 - \epsilon_t^\ddagger$ for $d\rho$, which leads to

$$\frac{dN}{N} = \frac{dq^\ddagger dp^\ddagger \int\limits_{H=E-E_0-\epsilon_t^\ddagger} dq_2 \cdots dq_n dp_2 \cdots dp_n}{\int\limits_{H=E} dq_1 \cdots dq_n dp_1 \cdots dp_n} = \frac{dq^\ddagger dp^\ddagger \; h^{n-1} \; \rho(E - E_0 - \epsilon_t^\ddagger)}{h^n \; \rho(E)}, \tag{B.27}$$

where in the second step the definition of the density of states was used from Eq. (A.15). The decay rate of the N molecules is then given by the time derivative of their number and using the relation $dq^\ddagger dp^\ddagger / dt = d\epsilon_t^\ddagger$, one obtains

$$\frac{dN}{dt} = N \, \frac{d\epsilon_t^\ddagger \, \rho(E - E_0 - \epsilon_t^\ddagger)}{h \; \rho(E)} = N dk(E, \epsilon_t^\ddagger), \tag{B.28}$$

where $dk(E, \epsilon_t^\ddagger)$ is the reaction rate, but still as a function of the translational energy. An integration over all possible translational energies $\epsilon_t^\ddagger$ from zero to $E - E_0$ leads

the RRKM reaction rate

$$k(E) = \frac{\int_0^{E-E_0} \rho(E - E_0 - \epsilon_t^\ddagger) d\epsilon_t^\ddagger}{h\ \rho(E)} = \frac{N^\ddagger(E - E_0)}{h\ \rho(E)}, \tag{B.29}$$

where $N^\ddagger(E - E_0)$ is the sum of states in the critical phase space area along the reaction coordinate.
The canonical reaction rate as a function of the temperature is obtained, equation (B.18) applies, and with the definition in equation (A.25) and performing the integration one obtains

$$k(T) = \frac{k_B T}{h} \frac{Q^\ddagger(T)}{Q(T)} e^{-\frac{E_0}{k_B T}}, \tag{B.30}$$

which exhibits an Arrhenius form. Both representations, Eq. (B.29) and (B.30), are also obtained from transition state theory in the microscopic or canonical approach, respectively. This derivation also comes close to the approaches from TST and the reaction coordinate can be identified with the transition state.
A variation of the RRKM theory is for instance the Statistical adiabatic channel model (SACM) [153–155] for the dissociation of a molecule, where the vibrational modes are distinguished between *conserved* and *disappearing* oscillators, respectively. The *conserved* modes exhibit similar vibrational frequencies in the reactant and product system, which correspond to the same symmetry operation. These modes are treated as being passive and not contributing energy to the reaction. The *disappearing* oscillators are modes, which correspond for example to the stretching motion of the breaking bond and will not be present in the product fragment.

B.2.4 Rotational excitation in RRKM

The treatment of rotational excitation in the RRKM theory or extended models is ambiguous [156–158]. Fundamentally, the rotational energy has less contribution to the total energy compared to the vibrational, however, with a high angular momentum considerable effects can occur. Regarding the total energy E in a molecule, the vibrational energy is reduced by the presence of rotational excitation as $E_{vib} = E - E_{rot}$.
One aspect is whether rotations should be treated as active or adiabatic degrees of freedom. The K quantum number, the projection of the total angular momentum J onto the symmetry axis of the molecule, can couple to the vibrational motion (Coriolis coupling). If the coupling is strong, the rotational degree of freedom has to be treated as active; for a weak coupling as adiabatic. In the latter case, the rotational quantum state is maintained during the reaction and no exchange of energy with other states takes place. Thus, the reaction rate can be obtained as a function of the total energy E, the total angular momentum J and the K rotor. Here, an explicit dependence on K can occur as this state is conserved. Hence, the reaction rate $k(E, J, K)$ is derived by using Eq. (B.29) with

$$\rho(E, J, K) = (2J + 1)\ \rho(E - E_r(J, K)), \tag{B.31}$$

$$N^\ddagger(E, J, K) = (2J + 1)\ N^\ddagger(E - E_0 - E_r(J, K)). \tag{B.32}$$

The prefactor originates from the M_J degeneracy. A summation over all K orientations $(-J, .., 0, .., +J)$ leads to $k(E, J)$, where each K is weighted by the probability $\mathcal{P}(K)$ as

$$k(E,J) = \sum_{K=-J}^{+J} \mathcal{P}(K)\ \rho(E,J,K), \tag{B.33}$$

$$\mathcal{P}(K) = \frac{\rho(E - E_r(J,K))}{\sum\limits_{K=-J}^{+J} \rho(E - E_r(J,K))}. \tag{B.34}$$

In the second approach, the active rotor, $\rho(E - E_r(J,K))$ is averaged over all orientations in K, as here an exchange of energy between the states is assumed. The same argumentation also holds for the treatment of $N^\ddagger$. If the averaged expressions are entered into Eq. (B.29), the same equation for $k(E, J)$ is obtained. Hence, in terms of the RRKM approach, no difference between active and adiabatic rotors is present. It might become important, if an anharmonic density of states has to be considered or if the coupling between rotations and vibrations is included in a more specific way.
However, for the spherical top molecule the K summation simplifies to an additional prefactor of $2J + 1$ as the rotational energy does not depend on K anymore. If in addition the angular momentum is conserved in the reaction, the reaction rate with dependence on J is given by

$$k(E,J) = \frac{N^\ddagger(E - E_0 - E_r^\ddagger(J))}{h\ \rho(E - E_r(J))}. \tag{B.35}$$

If both rotational energies are different, in particular considering the case where $E_r^\ddagger(J) > E_r(J)$, the threshold for a reaction is in general not reached, when the vibrational energy E_{vib} exceeds the activation energy E_0, as $E_{vib} = E - E_r(J) > E_0$. Due to the constraint from the rotational excitation, the vibrational energy also needs to account for the rotational energy difference $\Delta E_r(J) = E_r^\ddagger(J) - E_r(J)$, which increases the reaction threshold. This is especially important in the case of the electron detachment rates for SF_6^- in the presence of rotational excitation.

Bibliography

[1] V. Vuitton, P. Lavvas, R. Yelle, M. Galand, A. Wellbrock, G. Lewis, A. Coates and J.-E. Wahlund. Negative ion chemistry in Titan's upper atmosphere. *Planetary and Space Science*, 57(13):1558–1572, November 2009. doi:10.1016/j.pss.2009.04.004.

[2] M. C. McCarthy, C. A. Gottlieb, H. Gupta and P. Thaddeus. Laboratory and Astronomical Identification of the Negative Molecular Ion C_6H^-. *The Astrophysical Journal*, 652(2):L141–L144, December 2006. doi:10.1086/510238.

[3] S. Brünken, H. Gupta, C. A. Gottlieb, M. C. McCarthy and P. Thaddeus. Detection of the Carbon Chain Negative Ion C_8H^- in TMC-1. *The Astrophysical Journal*, 664(1):L43–L46, July 2007. doi:10.1086/520703.

[4] J. Cernicharo, M. Guélin, M. Agúndez, K. Kawaguchi, M. McCarthy and P. Thaddeus. Astronomical detection of C_4H^- , the second interstellar anion. *Astronomy and Astrophysics*, 467(2):L37–L40, May 2007. doi:10.1051/0004-6361:20077415.

[5] J. Bopp, J. Roscioli, M. Johnson, T. Miller, A. Viggiano, S. Villano, S. Wren and W. Lineberger. Spectroscopic characterization of the isolated SF_6 and $C_4F_8^-$ anions: Observation of very long harmonic progressions in symmetric deformation modes upon photodetachment. *The Journal of Physical Chemistry A*, 111(7):1214–1221, 2007. doi:10.1021/jp0665372.

[6] D. Zajfman, O. Heber and L. Vejby-Christensen. Electrostatic bottle for long-time storage of fast ion beams. *Physical Review A*, 55(3):1577–1580, 1997. doi:10.1103/PhysRevA.55.R1577.

[7] H. Wollnik and M. Przewloka. Time-of-flight mass spectrometers with multiply reflected ion trajectories. *International Journal of Mass Spectrometry and Ion Processes*, 96(3):267–274, April 1990. doi:10.1016/0168-1176(90)85127-N.

[8] M. Lange, M. Froese, S. Menk, J. Varju, R. Bastert, K. Blaum, J. R. C. López-Urrutia, F. Fellenberger, M. Grieser, R. von Hahn, O. Heber, K.-U. Kühnel, F. Laux, D. A. Orlov, M. L. Rappaport, R. Repnow, C. D. Schröter, D. Schwalm, A. Shornikov, T. Sieber, Y. Toker, J. Ullrich, A. Wolf and D. Zajfman. A cryogenic electrostatic trap for long-time storage of keV ion beams. *The Review of scientific instruments*, 81(5):055105, May 2010. doi:10.1063/1.3372557.

[9] K. Hansen, J. Andersen, P. Hvelplund, S. Møller, U. Pedersen and V. Petrunin. Observation of a 1/t Decay Law for Hot Clusters and Molecules in a Storage Ring. *Physical Review Letters*, 87(12):1–4, August 2001. doi:10.1103/PhysRevLett.87.123401.

[10] J. U. Andersen and E. Bonderup. Thermionic emission from clusters. *Journal of Physics B:*, 4075(02), 2002. doi:10.1088/0953-4075/35/5/201.

[11] J. U. Andersen, H. Cederquist, J. S. Forster, B. A. Huber, P. Hvelplund, J. Jensen, B. Liu, B. Manil, L. Maunoury, S. Brndsted Nielsen, U. V. Pedersen, H. T. Schmidt, S. Tomita and H. Zettergren. Power-law decay of collisionally excited amino acids and quenching by radiative cooling. *The European Physical Journal D - Atomic, Molecular and Optical Physics*, 25(2):139–148, August 2003. doi:10.1140/epjd/e2003-00093-9.

[12] M. Schneider, M. Arditi and M. B. Barrau. BR1: a new ultrasonographic contrast agent based on sulfur hexafluoride-filled microbubbles. *Investigative Radiology*, 30(8):451–457, August 1995. doi:10.1097/00004424-199508000-00001.

[13] L. G. Christophorou. Electron Interactions With SF_6. *Journal of Physical and Chemical Reference Data*, 29(3):267, May 2000. doi:10.1063/1.1288407.

[14] M. K. W. Ko, N. D. Sze, W.-C. Wang, G. Shia, A. Goldman, F. J. Murcray, D. G. Murcray and C. P. Rinsland. Atmospheric sulfur hexafluoride: Sources, sinks and greenhouse warming. *Journal of Geophysical Research*, 98 (D6):10499, 1993. doi:10.1029/93JD00228.

[15] T. Reddmann, R. Ruhnke and W. Kouker. Three-dimensional model simulations of SF_6 with mesospheric chemistry. *Journal of Geophysical Research*, 106(D13):14525, July 2001. doi:10.1029/2000JD900700.

[16] F. C. Fehsenfeld. Ion Chemistry of SF_6. *The Journal of Chemical Physics*, 54 (1):438, 1971. doi:10.1063/1.1674631.

[17] W. Eisfeld. Highly accurate determination of the electron affinity of SF6 and analysis of structure and photodetachment spectrum of SF_6^-. *The Journal of Chemical Physics*, 134(5):054303, February 2011. doi:10.1063/1.3544213.

[18] W. Eisfeld. Erratum: Highly accurate determination of the electron affinity of SF6 and analysis of structure and photodetachment spectrum of SF_6^- [J. Chem. Phys. 134, 054303 (2011)]. *The Journal of Chemical Physics*, 134(12): 129903, 2011. doi:10.1063/1.3575400.

[19] J. Troe, T. M. Miller and A. A. Viggiano. Low-energy electron attachment to SF_6. I. Kinetic modeling of nondissociative attachment. *The Journal of Chemical Physics*, 127(24):244303, December 2007. doi:10.1063/1.2804761.

[20] J. Troe, T. M. Miller and A. A. Viggiano. Low-energy electron attachment to SF_6. II. Temperature and pressure dependences of dissociative attachment. *The Journal of Chemical Physics*, 127(24):244304, December 2007. doi:10.1063/1.2804762.

[21] A. A. Viggiano, T. M. Miller, J. F. Friedman and J. Troe. Low-energy electron attachment to SF_6. III. From thermal detachment to the electron affinity of SF_6. *The Journal of Chemical Physics*, 127(24):244305, December 2007. doi:10.1063/1.2804764.

[22] J. Troe, T. M. Miller and A. A. Viggiano. On the accuracy of thermionic electron emission models. I. Electron detachment from SF_6^-. *The Journal of Chemical Physics*, 130(24):244303, July 2009. doi:10.1063/1.3149782.

[23] H.-J. Troe, G. Marowsky, N. S. Shuman, T. M. Miller and A. A. Viggiano. On the Temperature Dependence of the Thermal Electron Attachment to SF_6 , SF_5Cl, and $POCl_3$. *Zeitschrift für Physikalische Chemie*, 225(11-12):1405–1416, December 2011. doi:10.1524/zpch.2011.0187.

[24] J. Troe, T. M. Miller and A. A. Viggiano. Communication: Revised electron affinity of SF_6 from kinetic data. *The Journal of Chemical Physics*, 136(12): 121102, March 2012. doi:10.1063/1.3698170.

[25] J. Rajput, L. Lammich and L. Andersen. Measured Lifetime of SF_6^-. *Physical Review Letters*, 100(15):1–4, April 2008. doi:10.1103/PhysRevLett.100.153001.

[26] L. Andersen. Thermionic electron emission from SF_6. *Physical Review A*, 78 (3):1–5, September 2008. doi:10.1103/PhysRevA.78.032512.

[27] J. C. Rienstra-Kiracofe, G. S. Tschumper, H. F. Schaefer, S. Nandi and G. B. Ellison. Atomic and Molecular Electron Affinities: Photoelectron Experiments and Theoretical Computations. *Chemical Reviews*, 102(1):231–282, January 2002. doi:10.1021/cr990044u.

[28] X. Li, H. Wu, X.-B. Wang and L.-S. Wang. s-p Hybridization and Electron Shell Structures in Aluminum Clusters: A Photoelectron Spectroscopy Study. *Physical Review Letters*, 81(9):1909–1912, August 1998. doi:10.1103/PhysRevLett.81.1909.

[29] K. M. Eisele. SF_6, a Preferable Etchant for Plasma Etching Silicon. *Journal of The Electrochemical Society*, 128(1):123, 1981. doi:10.1149/1.2127351.

[30] S. Solomon, D. Qin, M. Manning, Z. Chen, M. Marquis, K. B. Averyt, M. Tignor and H. L. Miller. *IPCC, 2007: Climate Change 2007: The Physical Science Basis. Contribution of Working Group I to the Fourth Assessment Report of the Intergovernmental Panel on Climate Change*, volume Geneva. Cambridge University Press, 2007.
URL `http://www.ipcc.ch/publications_and_data/ar4/wg1/en/ch5s5-es.html`

[31] G. E. Streit. Negative ion chemistry and the electron affinity of SF_6. *The Journal of Chemical Physics*, 77(2):826, 1982. doi:10.1063/1.443898.

[32] C. Lifshitz. Electron affinities from endothermic negative-ion charge-transfer reactions. IV. SF_6, selected fluorocarbons and other polyatomic molecules. *The Journal of Chemical Physics*, 59(6):3182, 1973. doi:10.1063/1.1680459.

[33] P. W. Harland and J. C. J. Thynne. Autodetachment lifetimes, attachment cross sections, and negative ions formed by sulfur hexafluoride and sulfur tetrafluoride. *The Journal of Physical Chemistry*, 75(23):3517–3523, November 1971. doi:10.1021/j100692a005.

[34] E. P. Grimsrud, S. Chowdhury and P. Kebarle. Electron affinity of SF6 and perfluoromethylcyclohexane. The unusual kinetics of electron transfer reactions A+B=A+B, where A=SF_6 or perfluorinated cyclo-alkanes. *The Journal of Chemical Physics*, 83(3):1059, 1985. doi:10.1063/1.449468.

[35] E. C. M. Chen, J. R. Wiley, C. F. Batten and W. E. Wentworth. Determination of the electron affinities of molecules using negative ion mass spectrometry. *The Journal of Physical Chemistry*, 98(1):88–94, January 1994. doi:10.1021/j100052a016.

[36] G. Gutsev and R. Bartlett. Adiabatic electron affinities of PF_5 and SF_6: a coupled-cluster study 5 6. *Molecular Physics*, 94(1):121–125, May 1998. doi:10.1080/002689798168402.

[37] T. M. Miller, S. T. Arnold and A. Viggiano. G3 and G2 thermochemistry of sulfur fluoride neutrals and anions. *International Journal of Mass Spectrometry*, 227(3):413–420, July 2003. doi:10.1016/S1387-3806(03)00079-4.

[38] A. Karton and J. M. L. Martin. Comment on "Revised electron affinity of SF_6 from kinetic data" [J. Chem. Phys. 136, 121102 (2012)]. *The Journal of Chemical Physics*, 136(19):197101, May 2012. doi:10.1063/1.4719180.

[39] D. Bishop. *Group theory and chemistry*. Dover Publications, Mineola, 1993.

[40] P. J. Hay. Generalized valence bond studies of the electronic structure of sulfur difluoride, sulfur tetrafluoride, and sulfur hexafluoride. *Journal of the American Chemical Society*, 99(4):1003–1012, February 1977. doi:10.1021/ja00446a005.

[41] A. E. Reed and F. Weinhold. On the role of d orbitals in sulfur hexafluoride. *Journal of the American Chemical Society*, 108(13):3586–3593, June 1986. doi:10.1021/ja00273a006.

[42] W. Demtröder. *Experimentalphysik 3: Atome, Moleküle und Festkörper*. Springer-Verlag, 3. Auflage, 2005.

[43] N. N. Nath. The normal vibrations of molecules having octahedral symmetry. *Proceedings of the Indian Academy of Sciences - Section A*, 1(4):250–259, 1934. doi:10.1007/BF03035564.

[44] P. S. Drzaic and J. I. Brauman. Electron photodetachment study of sulfur hexafluoride anion: comments on the structure of sulfur hexafluoride anion. *Journal of the American Chemical Society*, 104(1):13–19, January 1982. doi:10.1021/ja00365a004.

[45] R. S. Mulliken. Report on Notation for the Spectra of Polyatomic Molecules. *The Journal of Chemical Physics*, 23(11):1997, 1955. doi:10.1063/1.1740655.

[46] K. Kim, R. S. McDowell and W. T. King. Integrated infrared intensities and transition moments in SF_6. *The Journal of Chemical Physics*, 73(1):36, 1980. doi:10.1063/1.439883.

[47] B. R. Miller. Mean amplitudes of vibration of SF6 and intramolecular multiple scattering. *The Journal of Chemical Physics*, 75(11):5326, 1981. doi:10.1063/1.441976.

[48] J. M. W. Chase. NIST-JANAF thermochemical tables, 4th Ed.,. *J. Phys. Chem. Ref. Data, Monograph 9*, 1998.

[49] R. S. McDowell and B. J. Krohn. Vibrational levels and anharmonicity in SF_6 - II. Anharmonic and potential constants. *Spectrochimica Acta Part A: Molecular Spectroscopy*, 42(2-3):371–385, January 1986. doi:10.1016/0584-8539(86)80200-8.

[50] J. K. Böhlke. Isotopic Compositions of the Elements, 2001. *Journal of Physical and Chemical Reference Data*, 34(1):57, 2005. doi:10.1063/1.1836764.

[51] R. S. Berry. Ionization of Molecules at Low Energies. *The Journal of Chemical Physics*, 45(4):1228, 1966. doi:10.1063/1.1727742.

[52] J. Simons. Propensity rules for vibration-induced electron detachment of anions. *Journal of the American Chemical Society*, 103(14):3971–3976, July 1981. doi:10.1021/ja00404a002.

[53] P. K. Acharya, R. A. Kendall and J. Simons. Vibration-induced electron detachment in molecular anions. *Journal of the American Chemical Society*, 106(12):3402–3407, June 1984. doi:10.1021/ja00324a003.

[54] D. Edelson, J. E. Griffiths and K. B. McAfee. Autodetachment of Electrons in Sulfur Hexafluoride. *The Journal of Chemical Physics*, 37(4):917, 1962. doi:10.1063/1.1733191.

[55] R. N. Compton. Nondissociative Electron Capture in Complex Molecules and Negative-Ion Lifetimes. *The Journal of Chemical Physics*, 45(12):4634, 1966. doi:10.1063/1.1727547.

[56] A. D. Appelhans and J. E. Delmore. Refinement of the autoneutralization lifetimes of short lived states of SF_6. *The Journal of Chemical Physics*, 88(9): 5561, 1988. doi:10.1063/1.454567.

[57] J.-L. LeGarrec, D. A. Steinhurst and M. A. Smith. Measurement of the autodetachment lifetime of SF_6^{-*} as a function of electron energy in a free jet expansion. *The Journal of Chemical Physics*, 114(20):8831, 2001. doi:10.1063/1.1368382.

[58] J. M. S. Henis. Determination of Autoionization Lifetimes by Ion Cyclotron Reonances Linewidths. *The Journal of Chemical Physics*, 53(8):2999, 1970. doi:10.1063/1.1674440.

[59] R. Odom, D. Smith and J. Futrell. A study of electron attachment to SF_6 and auto-detachment and stabilization of SF_6. *Journal of Physics B: Atomic and Molecular Physics*, 8:1349, 1975. doi:10.1088/0022-3700/8/8/026.

[60] M. S. Foster and J. Beauchamp. Electron attachment to sulphur hexafluoride: Formation of stable SF_6 at low pressure. *Chemical Physics Letters*, 31(3): 482–486, March 1975. doi:10.1016/0009-2614(75)85068-8.

[61] Y. Liu, L. Suess and F. B. Dunning. Rydberg electron transfer to SF_6: product ion lifetimes. *The Journal of Chemical Physics*, 122(21):214313, June 2005. doi:10.1063/1.1925276.

[62] R. A. Marcus and O. K. Rice. The Kinetics of the Recombination of Methyl Radicals and Iodine Atoms. *The Journal of Physical Chemistry*, pages 894–908, 1951. doi:10.1021/j150489a013.

[63] W. H. Miller. Semiclassical limit of quantum mechanical transition state theory for nonseparable systems. *The Journal of Chemical Physics*, 62(5):1899, 1975. doi:10.1063/1.430676.

[64] E. Vogt and G. Wannier. Scattering of Ions by Polarization Forces. *Physical Review*, 95(5):1190–1198, September 1954. doi:10.1103/PhysRev.95.1190.

[65] C. E. Klots. Rate constants for unimolecular decomposition at threshold. *Chemical Physics Letters*, 38(1):61–64, February 1976. doi:10.1016/0009-2614(76)80255-2.

[66] T. Beyer and D. F. Swinehart. Algorithm 448: number of multiply-restricted partitions. *Communications of the ACM*, 16:379, 1973.
URL `http://dl.acm.org/citation.cfm?id=362275`

[67] S. E. Stein. Accurate evaluation of internal energy level sums and densities including anharmonic oscillators and hindered rotors. *The Journal of Chemical Physics*, 58(6):2438, 1973. doi:10.1063/1.1679522.

[68] I. Fabrikant and H. Hotop. Low-energy behavior of exothermic dissociative electron attachment. *Physical Review A*, 63(2):1–10, January 2001. doi:10.1103/PhysRevA.63.022706.

[69] S. Dushman. Thermionic Emission. *Reviews of Modern Physics*, 2(4):381–476, October 1930. doi:10.1103/RevModPhys.2.381.

[70] C. E. Klots. Evaporation from small particles. *The Journal of Physical Chemistry*, 92(21):5864–5868, October 1988. doi:10.1021/j100332a005.

[71] C. E. Klots. Thermal kinetics in small systems. *The Journal of Chemical Physics*, 90(8):4470, 1989. doi:10.1063/1.456633.

[72] C. Lifshitz. Energy-entropy trade-offs in the unimolecular decompositions of sulfur hexafluoride anion (SF_6). *The Journal of Physical Chemistry*, 87(18): 3474–3479, September 1983. doi:10.1021/j100241a024.

[73] K. Hansen and O. Echt. Thermionic Emission and Fragmentation of C_{60}. *Physical Review Letters*, pages 2337–2340, 1997. doi:10.1103/PhysRevLett.78.2337.

[74] M. Froese, K. Blaum, F. Fellenberger, M. Grieser, M. Lange, F. Laux, S. Menk, D. Orlov, R. Repnow, T. Sieber, Y. Toker, R. von Hahn and A. Wolf. Thermionic power-law decay of excited aluminum-cluster anions and its dependence on storage-device temperature. *Physical Review A*, 83(2):1–5, February 2011. doi:10.1103/PhysRevA.83.023202.

[75] M. Barat, J. C. Brenot, J. A. Fayeton and Y. J. Picard. Absolute detection efficiency of a microchannel plate detector for neutral atoms. *Review of Scientific Instruments*, 71(5):2050, 2000. doi:10.1063/1.1150615.

[76] S. Hosokawa, N. Takahashi, M. Saito and Y. Haruyama. Absolute detection efficiencies of a microchannel plate detector for 0.5-5 keV neutrals. *The Review of scientific instruments*, 81(6):063301, June 2010. doi:10.1063/1.3442514.

[77] C. L. Lugez, M. E. Jacox, R. a. King and H. F. Schaefer. Experimental and ab initio study of the infrared spectra of ionic species derived from SF_6 and SF_4 and trapped in solid neon. *The Journal of Chemical Physics*, 108(23):9639, 1998. doi:10.1063/1.476440.

[78] R. von Hahn, F. Berg, K. Blaum, J. Crespo Lopez-Urrutia, F. Fellenberger, M. Froese, M. Grieser, C. Krantz, K.-U. Kühnel, M. Lange, S. Menk, F. Laux, D. Orlov, R. Repnow, C. Schröter, A. Shornikov, T. Sieber, J. Ullrich, A. Wolf, M. Rappaport and D. Zajfman. The electrostatic Cryogenic Storage Ring CSR Mechanical concept and realization. *Nuclear Instruments and Methods in Physics Research Section B: Beam Interactions with Materials and Atoms*, 269(24):2871–2874, December 2011. doi:10.1016/j.nimb.2011.04.033.

[79] F. Fellenberger. *Aufbau und Charakterisierung der ersten Ecke des kryogenen elektrostatischen Speicherringes CSR.* Dissertation, Ruperto-Carola-University of Heidelberg, Germany, 2012.
URL `http://pubman.mpdl.mpg.de/pubman/item/escidoc:1566170:2`

[80] S. Earnshaw. On the nature of the molecular forces which regulate the constitution of the luminferous ether. *Trans. Camb. Phil. Soc.*, 7(July):97–112, 1842.

[81] S. r. P. Møller. ELISA, and electrostatic storage ring for atomic physics. *Nuclear Instruments and Methods in Physics Research Section A*, 394(3):281–286, July 1997. doi:10.1016/S0168-9002(97)00673-6.

[82] T. Tanabe, K. Chida, K. Noda and I. Watanabe. An electrostatic storage ring for atomic and molecular science. *Nuclear Instruments and Methods in Physics Research Section A*, 482(3):595–605, April 2002. doi:10.1016/S0168-9002(01)01704-1.

[83] S. Jinno, T. Takao, Y. Omata, A. Satou, H. Tanuma, T. Azuma, H. Shiromaru, K. Okuno, N. Kobayashi and I. Watanabe. TMU electrostatic ion storage ring designed for operation at liquid nitrogen temperature. *Nuclear Instruments and Methods in Physics Research Section A: Accelerators, Spectrometers, Detectors and Associated Equipment*, 532(1-2):477–482, October 2004. doi:10.1016/j.nima.2004.06.070.

[84] W. H. Benner. A Gated Electrostatic Ion Trap To Repetitiously Measure the Charge and m / z of Large Electrospray Ions. *Analytical Chemistry*, 69(20): 4162–4168, October 1997. doi:10.1021/ac970163e.

[85] K. Kingdon. A Method for the Neutralization of Electron Space Charge by Positive Ionization at Very Low Gas Pressures. *Physical Review*, 21(4):408–418, April 1923. doi:10.1103/PhysRev.21.408.

[86] J. D. Alexander, C. R. Calvert, R. B. King, O. Kelly, W. A. Bryan, G. R. A. J. Nemeth, W. R. Newell, C. A. Froud, I. C. E. Turcu, E. Springate, P. a. Orr, J. Pedregosa-Gutierrez, C. W. Walter, R. A. Williams, I. D. Williams and J. B. Greenwood. Short pulse laser-induced dissociation of vibrationally cold, trapped molecular ions. *Journal of Physics B: Atomic, Molecular and Optical Physics*, 42(15):154027, August 2009. doi:10.1088/0953-4075/42/15/154027.

[87] H. Pedersen, S. Altevogt, B. Jordon-Thaden, O. Heber, M. Rappaport, D. Schwalm, J. Ullrich, D. Zajfman, R. Treusch, N. Guerassimova, M. Martins, J.-T. Hoeft, M. Wellhöfer and A. Wolf. Crossed Beam Photodissociation Imaging of HeH+ with Vacuum Ultraviolet Free-Electron Laser Pulses. *Physical Review Letters*, 98(22):1–4, June 2007. doi:10.1103/PhysRevLett.98.223202.

[88] R. N. Wolf, M. Eritt, G. Marx and L. Schweikhard. A multi-reflection time-of-flight mass separator for isobaric purification of radioactive ion beams. *Hyperfine Interactions*, 199(1-3):115–122, April 2011. doi:10.1007/s10751-011-0306-8.

[89] D. A. Dahl. SIMION for the personal computer in reflection. *International Journal of Mass Spectrometry*, 200(1-3):3–25, December 2000. doi:10.1016/S1387-3806(00)00305-5.

[90] F. Hinterberger. *Physik der Teilchenbeschleuniger und Ionenoptik*. Springer Berlin Heidelberg, 2008. doi:10.1007/978-3-540-75282-0.

[91] A. Kechler. *Untersuchungen zur Massenauflösung in einer elektrostatischen Falle für schnelle Ionenstrahlen*. Bachelor's thesis, Ruperto-Carola-University of Heidelberg, Germany, 2011.

[92] D. Strasser, T. Geyer, H. Pedersen, O. Heber, S. Goldberg, B. Amarant, A. Diner, Y. Rudich, I. Sagi, M. Rappaport, D. Tannor and D. Zajfman. Negative Mass Instability for Interacting Particles in a 1D Box: Theory and Application. *Physical Review Letters*, 89(28):2–5, December 2002. doi:10.1103/PhysRevLett.89.283204.

[93] D. Strasser, O. Heber, S. Goldberg and D. Zajfman. Self-bunching induced by negative effective mass instability in an electrostatic ion beam trap. *Journal of Physics B: Atomic, Molecular and Optical Physics*, 36(5):953–959, March 2003. doi:10.1088/0953-4075/36/5/314.

[94] P. Bolotskikh, D. Grinfeld, A. Makarov and M. Monastyrskiy. Coulomb dynamics of ion bunches in multi-reflection electrostatic traps. *Nuclear Instruments and Methods in Physics Research Section A: Accelerators, Spectrometers, Detectors and Associated Equipment*, 645(1):146–152, July 2011. doi:10.1016/j.nima.2010.12.170.

[95] M. W. Froese, M. Lange, S. Menk, M. Grieser, O. Heber, F. Laux, R. Repnow, T. Sieber, Y. Toker, R. von Hahn, A. Wolf and K. Blaum. The decay of ion bunches in the self-bunching mode. *New Journal of Physics*, 14(7):073010, July 2012. doi:10.1088/1367-2630/14/7/073010.

[96] S. Menk. *A cryogenic trap for fast ion beams*. Diploma thesis, University of Heidelberg, 2009.
URL `http://pubman.mpdl.mpg.de/pubman/item/escidoc:914615:1`

[97] M. W. Froese. *A cryogenic electrostatic ion trap and first experiments on delayed emission of aluminum anion clusters and self-bunching*. Phd thesis, University of Heidelberg, Germany, 2010.
URL `http://pubman.mpdl.mpg.de/pubman/item/escidoc:912040:1`

[98] R. J. Donnelly and C. F. Barenghi. The Observed Properties of Liquid Helium at the Saturated Vapor Pressure. *Journal of Physical and Chemical Reference Data*, 27(6):1217, 1998. doi:10.1063/1.556028.

[99] T. Sieber, K. Blaum and M. Grieser. Beam diagnostics for the prototype of the Cryogenic Storage Ring CSR. In *Proceedings of EPAC08, Genoa, Italy*, pages 1287–1289, 2008.
URL `http://epaper.kek.jp/e08/papers/tupc097.pdf`

[100] R. Middleton. A versatile high intensity negative ion source. *Nuclear Instruments and Methods in Physics Research*, 214(2-3):139–150, September 1983. doi:10.1016/0167-5087(83)90580-X.

[101] R. E. Smalley, L. Wharton and D. H. Levy. The fluorescence excitation spectrum of rotationally cooled NO_2. *The Journal of Chemical Physics*, 63(11): 4977, 1975. doi:10.1063/1.431244.

[102] D. H. Levy. Laser Spectroscopy of Cold Gas-Phase Molecules. *Annual Review of Physical Chemistry*, 31(1):197–225, October 1980. doi:10.1146/annurev.pc.31.100180.001213.

[103] M. Herman, R. Georges, M. Hepp and D. Hurtmans. High resolution Fourier transform spectroscopy of jet-cooled molecules. *International Reviews in Physical Chemistry*, 19(2):277–325, April 2000. doi:10.1080/01442350050020905.

[104] J. Fenn, M. Mann, C. Meng, S. Wong and C. Whitehouse. Electrospray ionization for mass spectrometry of large biomolecules. *Science*, 246(4926): 64–71, October 1989. doi:10.1126/science.2675315.

[105] M. Karas and F. Hillenkamp. Laser desorption ionization of proteins with molecular masses exceeding 10,000 daltons. *Analytical Chemistry*, 2301(29): 2299–2301, 1988. doi:10.1021/ac00171a028.

[106] K. Tanaka, H. Waki, Y. Ido, S. Akita, Y. Yoshida, T. Yoshida and T. Matsuo. Protein and polymer analyses up tom/z 100 000 by laser ionization time-of-flight mass spectrometry. *Rapid Communications in Mass Spectrometry*, 2(8): 151–153, August 1988. doi:10.1002/rcm.1290020802.

[107] I. Manisali, D. D. Chen and B. B. Schneider. Electrospray ionization source geometry for mass spectrometry: past, present, and future. *TrAC Trends in Analytical Chemistry*, 25(3):243–256, March 2006. doi:10.1016/j.trac.2005.07.007.

[108] E. W. M. Haynes. *CRC Handbook of Chemistry and Physics, 92nd Edition (Internet Version 2012)*. CRC Press/Taylor and Francis, Boca Raton, FL, 2012.

[109] M. Yu. Work-function dependence of negative-ion production during sputtering. *Physical Review Letters*, (9), 1978. doi:10.1103/PhysRevLett.40.574.

[110] G. D. Alton. Semi-empimcal mathematical relationships for electropositive adsorbate induced work function changes. *Surface Science*, 175(1):226–240, September 1986. doi:10.1016/0039-6028(86)90094-4.

[111] G. D. Alton. Recent advancements in sputter-type heavy negative ion sources. In *Proceedings of the 1989 IEEE Particle Accelerator Conference, Accelerator Science and Technology*, number 3, pages 1112–1116. IEEE, 1989. doi:10.1109/PAC.1989.73368.

[112] P. Fayet, J. Wolf and L. Wöste. Temperature measurement of sputtered metal dimers. *Physical Review B*, 33(10):6792–6797, May 1986. doi:10.1103/PhysRevB.33.6792.

[113] A. Wucher and B. J. Garrison. Cluster formation in sputtering: A molecular dynamics study using the MD/MC-corrected effective medium potential. *The Journal of Chemical Physics*, 105(14):5999, 1996. doi:10.1063/1.472451.

[114] A. Wucher, A. Bekkerman, N. Dzhemilev, S. Verkhoturovb and I. Veryovkin. Internal energy of sputtered clusters: The influence of bombarding conditions. *Nuclear Instruments and Methods in Physics Research Section B: Beam Interactions with Materials and Atoms*, 140(3-4):311–318, May 1998. doi:10.1016/S0168-583X(98)00010-X.

[115] A. Wucher, C. Staudt, S. Neukermans, E. Janssens, F. Vanhoutte, E. Vandeweert, R. E. Silverans and P. Lievens. On the internal energy of sputtered clusters. *New Journal of Physics*, 10(10):103007, October 2008. doi:10.1088/1367-2630/10/10/103007.

[116] A. Wucher. Formation of atomic secondary ions in sputtering. *Applied Surface Science*, 255(4):1194–1200, December 2008. doi:10.1016/j.apsusc.2008.05.252.

[117] M. Wutz. *Handbuch Vakuumtechnik*. Vieweg Verlag, 1997.

[118] J. Ladislas Wiza. Microchannel plate detectors. *Nuclear Instruments and Methods*, 162(1-3):587–601, June 1979. doi:10.1016/0029-554X(79)90734-1.

[119] U. Spillmann, O. Jagutzki, L. Spielberger, R. Dörner, V. Mergel, K. Ullmann-Pfleger and H. Schmidt-Böcking. A Novel Delay-Line Anode Design for Position and Time Sensitive Read-Out of MCP-Based Detectors. *Physica Scripta*, T92(1):225–226, 2001. doi:10.1238/Physica.Topical.092a00225.

[120] P. Roth and G. Fraser. Microchannel plate resistance at cryogenic temperatures. *Nuclear Instruments and Methods in Physics Research Section A: Accelerators, Spectrometers, Detectors and Associated Equipment*, 439(1):134–137, January 2000. doi:10.1016/S0168-9002(99)00792-5.

[121] K. U. Kühnel, C. D. Schröter and J. Ullrich. Operating MCP Detectors at Cryogenic Temperatures. *Proceedings of EPAC08, Genoa, Italy*, pages 1179–1181, 2008.
URL `https://accelconf.web.cern.ch/accelconf/e08/papers/tupc055.pdf`

[122] O. Jagutzki, V. Mergel, K. Ullmann-Pfleger, L. Spielberger, U. Spillmann, R. Dörner and H. Schmidt-Böcking. A broad-application microchannel-plate detector system for advanced particle or photon detection tasks: large area imaging, precise multi-hit timing information and high detection rate. *Nuclear Instruments and Methods in Physics Research Section A: Accelerators, Spectrometers, Detectors and Associated Equipment*, 477(1-3):244–249, January 2002. doi:10.1016/S0168-9002(01)01839-3.

[123] K. M. Ervin, I. Anusiewicz, P. Skurski, J. Simons and W. C. Lineberger. The Only Stable State of O_2^- Is the $X_2\Pi_g$ Ground State and It (Still!) Has an

Adiabatic Electron Detachment Energy of 0.45 eV. *The Journal of Physical Chemistry A*, 107(41):8521–8529, October 2003. doi:10.1021/jp0357323.

[124] C. Blondel. Recent experimental achievements with negative ions. *Physica Scripta*, T58:31–42, January 1995. doi:10.1088/0031-8949/1995/T58/004.

[125] G. Doucas. The energy spread of some negative ions from a sputter source. *Revue de Physique Appliquée*, 12(10):1465–1469, 1977. doi:10.1051/rphysap:0197700120100146500.

[126] K. Leiter, W. Ritter, A. Stamatovic and T. Märk. Observation of dinegatively charged oxygen cluster ions $(O_2)_x^2$ (x = 3, 5, 7, 9). *International Journal of Mass Spectrometry and Ion Processes*, 68(3):341–346, February 1986. doi:10.1016/0168-1176(86)87058-6.

[127] S. Schauer, P. Williams and R. Compton. Production of small doubly charged negative carbon cluster ions by sputtering. *Physical Review Letters*, 65(5): 625–628, July 1990. doi:10.1103/PhysRevLett.65.625.

[128] N. Walsh, F. Martinez, G. Marx and L. Schweikhard. Multiply negatively charged aluminium clusters. *The European Physical Journal D*, 43(1-3):241–245, May 2007. doi:10.1140/epjd/e2007-00114-9.

[129] D. Cline and P. Lesser. Error estimation in non-linear least squares analysis of data. *Nuclear Instruments and Methods*, 82:291–293, May 1970. doi:10.1016/0029-554X(70)90366-6.

[130] E. E. Campbell and R. D. Levine. Delayed ionization and fragmentation en route to thermionic emission: statistics and dynamics. *Annual review of physical chemistry*, 51(1):65–98, January 2000. doi:10.1146/annurev.physchem.51.1.65.

[131] Y. Toker, O. Aviv, M. Eritt, M. Rappaport, O. Heber, D. Schwalm and D. Zajfman. Radiative cooling of Al_4 clusters. *Physical Review A*, 76(5):1–6, November 2007. doi:10.1103/PhysRevA.76.053201.

[132] M. Lange, M. W. Froese, S. Menk, D. Bing, F. Fellenberger, M. Grieser, F. Laux, D. A. Orlov, R. Repnow, T. Sieber, Y. Toker, R. von Hahn, A. Wolf and K. Blaum. Radiative cooling of Al_4^- and Al_5^- in a cryogenic environment. *New Journal of Physics*, 14(6):065007, June 2012. doi:10.1088/1367-2630/14/6/065007.

[133] P. Datskos, J. Carter and L. Christophorou. Photodetachment of SF_6^-. *Chemical Physics Letters*, 239(1-3):38–43, June 1995. doi:10.1016/0009-2614(95)00417-3.

[134] S. Zhao, Y. Ren, J. Wang and W. Yin. A density functional study of the interaction of NCO with small copper clusters. *The Journal of Physical Chemistry A*, 113(6):1075–85, February 2009. doi:10.1021/jp8059757.

[135] R. D. Thomas, H. T. Schmidt, G. Andler, M. Björkhage, M. Blom, L. Brännholm, E. Bäckström, H. Danared, S. Das, N. Haag, P. Halldén, F. Hellberg, A. I. S. Holm, H. A. B. Johansson, A. Källberg, G. Källersjö, M. Larsson, S. Leontein, L. Liljeby, P. Löfgren, B. Malm, S. Mannervik, M. Masuda, D. Misra, A. Orbán, A. Paál, P. Reinhed, K.-G. Rensfelt, S. Rosén, K. Schmidt, F. Seitz, A. Simonsson, J. Weimer, H. Zettergren and H. Cederquist. The double electrostatic ion ring experiment: a unique cryogenic electrostatic storage ring for merged ion-beams studies. *The Review of scientific instruments*, 82(6):065112, June 2011. doi:10.1063/1.3602928.

[136] A. Shornikov. *An electron cooler for ultra-low energy cryogenic operation.* Dissertation, Ruperto-Carola-University of Heidelberg, Germany, 2012. URL `http://pubman.mpdl.mpg.de/pubman/item/escidoc:1481450:1`

[137] S. Krohn, Z. Amitay, A. Baer, D. Zajfman, M. Lange, L. Knoll, J. Levin, D. Schwalm, R. Wester and A. Wolf. Electron-induced vibrational deexcitation of H_2^+. *Physical Review A*, 62(3):032713, August 2000. doi:10.1103/PhysRevA.62.032713.

[138] J. Ullrich, R. Moshammer, A. Dorn, R. Dörner, L. P. H. Schmidt and H. Schmidt-Böcking. Recoil-ion and electron momentum spectroscopy: reaction-microscopes. *Reports on Progress in Physics*, 66(9):1463–1545, September 2003. doi:10.1088/0034-4885/66/9/203.

[139] E. Schrödinger. Quantisierung als Eigenwertproblem. *Annalen der physik*, 286(18):109, 1926. URL `http://onlinelibrary.wiley.com/doi/10.1002/andp.19263851302/abstract`

[140] T. Baer and W. Hase. *Unimolecular reaction dynamics: theory and experiments.* Oxford University Press, New York/Oxford, 1996. doi:10.1002/0470845015.cua001.

[141] M. Born and J. Oppenheimer. Quantum theory of molecules. *Ann. Phys.*, 84 (20):0457, 1927.

[142] M. L. Polak, M. K. Gilles and W. C. Lineberger. Photoelectron spectroscopy of SF. *The Journal of Chemical Physics*, 96(9):7191, 1992. doi:10.1063/1.462526.

[143] D. L. Hildenbrand. Mass spectrometric studies of some gaseous sulfur fluorides. *The Journal of Physical Chemistry*, 77(7):897–902, March 1973. doi:10.1021/j100626a008.

[144] S. Midda and A. K. Das. Spectroscopic constants and molecular properties of CN^-, SiH^-, PO^-, SO^-, SF^-, and SiS^-: Density functional study. *International Journal of Quantum Chemistry*, 98(5):447–455, 2004. doi:10.1002/qua.20001.

[145] P. Bunker. Allowed transitions and the dipole moment of HD+. *Chemical Physics Letters*, 27(3):322–324, August 1974. doi:10.1016/0009-2614(74)90233-4.

[146] G. Z. Whitten and B. S. Rabinovitch. Accurate and Facile Approximation for Vibrational Energy-Level Sums. *The Journal of Chemical Physics*, 38(10): 2466, 1963. doi:10.1063/1.1733526.

[147] J. I. Steinfeld, J. S. Francisco, W. L. Hase and P. Hall. *Chemical Kinetics and Dynamics 2nd ed.* Prentice-Hall, Inc., a Simon & Schuster company, 1998.

[148] S. K. Upadhyay. *Chemical Kinetics and Reaction Dynamics*, volume 129. Springer Netherlands, September 2006. doi:10.1007/978-1-4020-4547-9_4.

[149] F. A. Lindemann, S. Arrhenius, I. Langmuir, N. R. Dhar, J. Perrin and W. C. McC. Lewis. Discussion on the radiation theory of chemical action. *Transactions of the Faraday Society*, 17:598, 1922. doi:10.1039/tf9221700598.

[150] Langevin. P. *Ann. Chim. Phys.*, 5:245–288, 1905.

[151] O. Rice and H. Ramsperger. Theories of unimolecular gas reactions at low pressures. *Journal of the American Chemical Society*, 49:1617–1629, 1927. doi:10.1021/ja01406a001.

[152] L. Kassel. Studies in Homogeneous Gas Reactions. II. Introduction of Quantum Theory. *The Journal of Physical Chemistry*, 225, 1928. doi:10.1021/j150289a011.

[153] M. Quack and J. Troe. Specific Rate Constants of Unimolecular Processes II. Adiabatic Channel Model. *Berichte der Bunsengesellschaft für physikalische Chemie*, 78(3):240–252, March 1974. doi:10.1002/bbpc.19740780306.

[154] J. Troe. Statistical adiabatic channel model for ionmolecule capture processes. *The Journal of Chemical Physics*, 87(5):2773, 1987. doi:10.1063/1.453701.

[155] J. Troe. Statistical adiabatic channel model for ionmolecule capture processes. II. Analytical treatment of iondipole capture. *The Journal of Chemical Physics*, 105(15):6249, 1996. doi:10.1063/1.472479.

[156] J. Troe. Specific rate constants k(E, J) for unimolecular bond fissions. *The Journal of Chemical Physics*, 79(12):6017, 1983. doi:10.1063/1.445784.

[157] L. Zhu and W. L. Hase. Comparison of models for calculating the RRKM unimolecular rate constant k(E, J). *Chemical Physics Letters*, 175(1-2):117–124, November 1990. doi:10.1016/0009-2614(90)85528-K.

[158] U. Lourderaj and W. L. Hase. Theoretical and computational studies of non-RRKM unimolecular dynamics. *The Journal of Physical Chemistry A*, 113 (11):2236–53, March 2009. doi:10.1021/jp806659f.

Danksagung

Auf dieser letzten Seite möchte ich mich gerne bei allen Personen herzlich bedanken, die einen großen Anteil am Gelingen dieser Arbeit hatten. Ich bedanke mich deshalb bei:

Andreas Wolf, Klaus Blaum und Robert von Hahn für die herzliche Aufnahme in der Arbeitsgruppe, die gute fachliche Führung und die angenehme Arbeitsatmosphäre.

Alexander Dorn für die Bereitschaft die Zweitkorrektur dieser Arbeit zu übernehmen.

Dirk Schwalm für die engagierte Beratung und motivierenden Diskussionen im Rahmen dieser Arbeit.

Herrn Prof. Jürgen Troe danke ich für die freundlichen Diskussionen und Hilfe bei der Einführung in die Theorie zu Beginn meiner Datenanalyse.

Des Weiteren danke ich dem CTF-Team, allen voran Michael Lange und Mike Froese, mit denen ich viel Zeit im Labor aber auch private Momente erleben durfte, sowie den neueren Mitgliedern des CTF-Teams Christian Breitenfeldt und Sebastian George.

Hiermit sind schon viele Büro- und Nachbarbürokollegen abgedeckt, nicht unerwähnt bleiben dürfen hier jedoch Florian Fellenberger, Felix Berg und Felix Laux, die mir fachlich immer zur Seite standen und für ein entspanntes Büroklima gesorgt haben.

Manfred Grieser und Roland Repnow danke ich für die fachliche Beratung in Bezug auf Ionenquellen und Ionenoptik.

Des Weiteren danke ich den Werkstattmitarbeitern und Elektronikern für die Unterstützung beim Aufbau und Wartung unserer Ionenfalle; hierbei besonders Dirk Kaiser, Michael Frauenfeld, Oliver Koschorrek und Rolf Epking.

Ich danke allen weiteren aktiven und ehemaligen Mitgliedern sowie Gästen dieser Arbeitsgruppe:

Arno Becker, Max Berg, Dennis Bing, Swarup Das, Christian Domesle, Florian Grussie, Philipp Herwig, Jens Homann, Brandon Jordan-Thaden, Claude Krantz, Holger Kreckel, Michael Lestinsky, Mario Mendes, Manas Mukherjee, Yuji Nakano, Christian Nordhorn, Olda Novotnŷ, Annemieke Petrignani, Andrey Shornikov, Kaija Spruck, Jule Stützel, Stephen Vogel

für die angenehme Arbeitsatmosphäre, den unterhaltsamen Austausch am Kaffeetisch und die meist gelungenen Speisen in unserer Kochgruppe.

Außerdem möchte ich der Arbeitsgruppe am Weizmann Institut in Israel um Daniel Zajfman, Oded Heber, Michael Haas und Dirk Schwalm für das Ermöglichen meines Forschungsaufenthaltes am Weizmann-Institut danken, bei dem leider nicht alle Experimente gelungen sind, ich aber viel durch den fachbezogenen aber auch privaten Austausch gelernt habe.

Zuletzt danke ich meinen Eltern und meiner Schwester für ihre Unterstützung in den letzten Jahren, und insbesondere meiner Freundin Steffi für die Geduld und Liebe in der Endphase dieser Arbeit.